



Chair of Physical Metallurgy and Metallic Materials

Doctoral Thesis



Development of TiAl alloys on the demand
of additive manufacturing and high-
temperature application

Dipl.-Ing. David Wimler, BSc

April 2021



MONTANUNIVERSITÄT LEOBEN
www.unileoben.ac.at

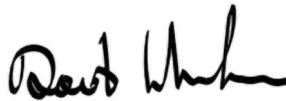
AFFIDAVIT

I declare on oath that I wrote this thesis independently, did not use other than the specified sources and aids, and did not otherwise use any unauthorized aids.

I declare that I have read, understood, and complied with the guidelines of the senate of the Montanuniversität Leoben for "Good Scientific Practice".

Furthermore, I declare that the electronic and printed version of the submitted thesis are identical, both, formally and with regard to content.

Date 01.04.2021

A handwritten signature in black ink, appearing to read 'David Wimler'.

Signature Author
David Wimler

The research in this dissertation was conducted at the Department of Materials Science at the Montanuniversität Leoben, Austria, under the supervision of Univ.-Prof. Dr. mont. Helmut Clemens and assoc. Prof. Dr. mont. Svea Mayer.

This work was financially supported by the BMBF project "NextTiAl" (03XP0088C), Germany. This multi-annual BMBF project focused on the development of γ -TiAl based alloys especially suitable for additive manufacturing.

Danksagung

An dieser Stelle möchte ich mich recht herzlich bei meiner Doktormutter assoz.Prof. Dr. mont. Svea Mayer und Univ.-Prof. Dr. mont. Helmut Clemens für die Möglichkeit und die Unterstützung bei der Durchführung dieser Dissertation am Department Werkstoffwissenschaft bedanken. Durch die zahlreichen Diskussionen und Korrekturen war es mir möglich mich wissenschaftlich weiterzuentwickeln.

Ebenfalls bedanken möchte ich mich bei Prof. Dr.-Ing. Carolin Körner von der FAU Erlangen-Nürnberg, welche sich bereit erklärt hat, die Mentorinnenschaft meiner Dissertation zu übernehmen und mir darüber hinaus Einblicke in die Prozesssimulation ermöglicht hat.

Seitens des "NextTiAl" Projekts möchte ich mich beim gesamten Konsortium recht herzlich für die erfolgreiche Zusammenarbeit bedanken. Bei Dipl.-Ing. Melissa Allen und Dr. Volker Güther von der GfE Metalle und Materialien GmbH, Nürnberg, möchte ich mich für die unzähligen chemischen Analysen sowie den interessanten fachlichen Meetings in immer bester Atmosphäre bedanken. Bei Dr. Alexander Kirchner und Dr. Burghardt Klöden vom Fraunhofer Institut IFAM Dresden möchte ich mich für die erhellenden Prozesseinblicke in die Additive Fertigung bedanken. Seitens der NMF GmbH, Fürth, bedanke ich mich bei Dipl.-Ing. Marcel Reith und Dr. Martin Franke für die interessanten und anregenden Diskussionen über Scanstrategien. Bei Dr. Wilfredo Garcia Vargas, TLS Technik GmbH & Co. Spezialpulver KG, Bitterfeld bedanke ich mich für die unkomplizierte Zurverfügungstellung von TiAl Pulver.

Mein Dankeschön geht an die GfE Fremat GmbH, Brand-Erbisdorf, für den finanziellen Beitrag an der Dissertation. Hierbei gilt mein ganz besonderer Dank Dr. Janny Lindemann, mit der ich sehr viele ergebnisreiche Diskussionen geführt habe. Sie leistete somit einen wertvollen Beitrag an meiner Dissertation.

Im Zuge des NextTiAl Projekts möchte ich mich für die finanzielle Basis der Dissertation bei der MTU Aero Engines AG bedanken. Dabei gilt mein Dank insbesondere Projektleiter Dr. Martin Schloffer für die erfolgreiche Zusammenarbeit und die vielen fachlichen Diskussionen, welche zur Erstellung interessanter wissenschaftlicher Arbeiten geführt hat.

Danke an alle Co-Autorinnen und Co-Autoren meiner Veröffentlichungen, durch welche ich in unzähligen Besprechungen und Messsitzungen ein tieferes Verständnis der verwendeten Methoden erlangt habe. Dabei möchte ich vor allem Dr. Christoph Gammner und Dr. Thomas Kremmer meinen Dank aussprechen für die Beantwortung meiner TEM Fragestellungen.

Den Kolleginnen und Kollegen am Department Metallkunde möchte ich für die ständige Hilfsbereitschaft und tolle Zusammenarbeit danken. Durch das sehr gute Arbeitsklima, welches von zutiefst fachspezifischen Diskussionen bis hin zum Planen der nächsten Wanderung geprägt wurde, war es mir möglich die notwendige Ausgewogenheit für ein wissenschaftliches Arbeiten sicherzustellen. Ein großer Dank gilt dabei meinen die Kollegen der HEAT-Group. Durch sie wurde ein jeder Tag im Büro erfolgreicher und lustiger.

Ein großer Dank gilt meinem treuen Freundeskreis meiner Heimat, welcher mittlerweile weit verstreut ist, jedoch immer antwortet. Durch ihre stetige selbstaufopfernde Bereitschaft sich auf ein Bier zu treffen, schufen sie Abwechslung, damit der Dissertationsalltag wieder fokussiert ablaufen konnte.

Mein allergrößter Dank gilt meiner Familie, welche immer größer wird: meinen Eltern, Marianne und Karl, die mich schon mein ganzes Leben unterstützen und mich immer motivieren meine Ziele zu erreichen. Dasselbe gilt für meine Schwestern, Marlene und Angelika. Sie alle haben mir die notwendige Zielstrebigkeit beigebracht und gaben mir uneingeschränkten Rückhalt, alles zu erreichen. Gleichzeitig wurde mir von meiner Familie auch der notwendige Ausgleich gezeigt, um die wichtigen Dinge, fernab von Atomen und Flugzeugen, nicht zu vergessen. Daran haben in den letzten Jahren auch meine Nichten, Mona & Linda, und Neffen, Maximilian & Ludwig, einen sehr großen Anteil gehabt.

Am Ende darf ich mich noch bei meiner Freundin Lea bedanken, die mir immer ihr Ohr für Beschwerden leiht, mir aufmunternde Worte schenkt oder mit mir schöne gemeinsame Tage teilt.

Vielen Dank!

Contents

Abstract	ix
Kurzfassung	xi
List of abbreviations, acronyms and symbols	xiii
1 Motivation and scope	1
2 State of the art	5
2.1 Intermetallic Ti-Al alloys for high-temperature application	5
2.1.1 Four generations of γ -TiAl based alloys	5
2.1.2 Link between microstructure and mechanical properties	8
2.1.3 Near- α alloys with intermetallic α_2 phase	9
2.2 Advanced powder metallurgical technologies	10
2.2.1 Production of metal powder by gas atomization	10
2.2.2 Spark plasma sintering	11
2.2.3 Electron beam melting	12
3 Summary of publications	15
3.1 High-quality powders as starting material	15
3.2 Tailor-made alloys for high-temperature applications	17
3.3 Overcoming the challenges of electron beam melting	21
	vii

4	Summary and outlook	25
5	List of publications	29
5.1	Publications included in this thesis	29
5.2	Publications related to this thesis	31
5.3	Conference contributions	31
5.4	Supervised academic works	32
	References	33
	Appendices	43
A	Aspects of powder characterization for additive manufacturing	43
B	Microstructural evolution and mechanical properties of an advanced γ -TiAl based alloy processed by spark plasma sintering	57
C	Novel intermetallic-reinforced near- α Ti alloys manufactured by spark plasma sintering	75
D	Designing advanced intermetallic titanium aluminide alloys for additive manufacturing	101
E	How electron beam melting tailors the Al-sensitive microstructure and mechanical response of a novel γ -TiAl based alloy	127
F	Microstructure and mechanical properties of novel TiAl alloys tailored via phase and precipitate morphology	157

Abstract

In the last decades, the successful alloy development in the field of titanium aluminides (TiAl) has led to the replacement of heavy Ni-base alloys in aerospace and automotive propulsion systems. Thereby, the used TiAl alloys, based on the intermetallic γ -TiAl phase, reach maximum service temperatures of about 750 °C and are manufactured via casting and/or forging. To increase the field of application for γ -TiAl based alloys, this thesis aims for higher application temperatures as well as new processing routes, i.e. predominantly powder metallurgical approaches like additive manufacturing.

However, the additive manufacturing via electron beam melting (EBM) of established alloys presents process-related challenges. Therefore, the thesis deals with the process-microstructure-property relationship of EBM-manufactured TiAl and uses this knowledge to design new process-adapted TiAl alloys of the 4th generation. This required a detailed microstructural characterization of the samples built with different process parameters with advanced methods as transmission electron microscopy, high-energy X-ray diffraction studies, energy dispersive X-ray spectroscopy, and mechanical testing up to 850 °C. The results show that the new alloys were chemically as well as microstructurally isotropic after manufacturing EBM samples with optimized parameters and a designed subsequent heat treatment.

In parallel, the alloy powders were investigated after densification via spark plasma sintering (SPS), a manufacturing method that allows the evaluation of new alloys and their microstructures completely on solid-state processes without re-melting and, more specifically, the impact of varying Al contents, as it is pronounced in EBM specimens. Based on ex- and in-situ experiments, the kinetic and stability of nm-sized precipitates could be established for optimal high-temperature properties.

Finally, the entire gained knowledge enabled the manufacturing of a resilient prototype of a new γ -TiAl based alloy of the 4th generation for high-temperature aerospace applications.



Online version of the thesis at
pure.unileoben.ac.at/portal

Kurzfassung

Entwicklung von TiAl-Legierungen für die Anforderungen der additiven Fertigung und Hochtemperaturanwendung

In den letzten Jahrzehnten haben die erfolgreichen Legierungsentwicklungen auf dem Gebiet der Titanaluminide (TiAl), als Ersatz für die schweren Ni-Basislegierungen, zum Einsatz in Antriebssystemen der Luftfahrt und Automobilindustrie geführt. Dabei erreichen die eingesetzten TiAl-Legierungen auf Basis der intermetallischen γ -TiAl Phase maximale Einsatztemperaturen von ca. 750 °C und werden durch Guss und/oder Schmieden hergestellt. Um den Einsatzbereich von γ -TiAl Legierungen zu erweitern, zielt diese Arbeit auf höhere Einsatztemperaturen sowie auf neue Verarbeitungswege ab, letzteres vor allem in Richtung Pulvermetallurgie, wie der additive Fertigung.

Jedoch weist die additive Fertigung mittels Elektronenstrahlschmelzen (EBM) von etablierten Legierungen prozessbedingte Herausforderungen auf. Daher beschäftigt sich diese Arbeit mit der Prozess-Mikrostruktur-Eigenschafts-Beziehung von EBM-gefertigtem TiAl und nutzt dieses Wissen zur Entwicklung neuer prozessangepasster TiAl-Legierungen der 4. Generation. Dies erforderte eine detaillierte mikrostrukturelle Charakterisierung der Proben, welche mit unterschiedlichen Prozessparametern hergestellt wurden, durch moderne Methoden wie Transmissionselektronenmikroskopie, Hochenergie-Röntgenbeugungsstudien, energiedispersiver Röntgenspektroskopie und mechanischer Prüfung bis zu 850 °C. Die Ergebnisse zeigen, dass die neuen Legierungen nach der Herstellung von EBM-Proben mit optimierten Prozessparametern und einer anschließenden Wärmebehandlung sowohl chemisch als auch mikrostrukturell isotrop sind.

Parallel wurden die Pulver der Legierungen mittels Spark-Plasma-Sintering konsolidiert und anschließend untersucht. Diese Fertigungsmethode ermöglicht die Bewertung neuer Legierungen und deren Gefüge ohne den Einfluss von variierenden Al-Gehalten, wie es in EBM gefertigten Proben ausgeprägt ist. Basierend auf ex- und in-situ Experimenten konnte die Kinetik und Stabilität von nm-großen Ausscheidungen für optimale Hochtemperatureigenschaften ermittelt werden.

Schließlich konnte durch die gewonnenen Erkenntnisse die Herstellung eines belastbaren Prototypen aus einer neuen γ -TiAl Legierung der 4. Generation für die Hochtemperaturanwendungen in der Luft- und Raumfahrt durchgeführt werden.

List of abbreviations, acronyms and symbols

α -Ti	Disordered hexagonal α -Ti(Al) phase (A3 structure)
α_2 -Ti ₃ Al	Intermetallic ordered Ti ₃ Al phase (D0 ₁₉ structure)
β -Ti	Disordered body-centered cubic β -Ti(Al) phase (A2 structure)
β_o -TiAl	Intermetallic ordered TiAl phase (B2 structure)
γ -TiAl	Intermetallic ordered TiAl phase (L1 ₀ structure)
γ_g	Globular γ
ζ -Ti ₅ Si ₃	Intermetallic Ti ₅ Si ₃ silicide (D8 ₈ structure)
AM	Additive manufacturing
at.%	Atomic percent
b	Burgers vector
bcc	Body-centered cubic
BMBF	Bundesministerium für Bildung und Forschung engl.: Federal Ministry of Education and Research, Germany
BSE	Backscattered electrons
BDTT	Brittle-to-ductile-transition-temperature
E_A	Area energy
E_L	Line energy
EBM	Electron beam melting
EDX	Energy dispersive X-ray spectroscopy
EIGA	Electrode induction melting gas atomization
FL	Fully lamellar
GE	General Electric, United States of America
HD	Hatching distance
HEXRD	High-energy X-ray diffraction

HIP	Hot isostatic pressing
I	Beam current
L	Liquid
LMP	Larson Miller parameter
LOM	Light optical microscope
m.%	Mass percent
MMC	Metal matrix composite
NL	Nearly lamellar
NL10 γ	Nearly lamellar microstructure consisting of 10 vol.% globular γ
NG	Near gamma
SCI	Science citation index
SEM	Scanning electron microscope
SE	Secondary electrons
SLM	Selective laser melting
SPS	Spark plasma sintering
$T_{\gamma, solv}$	Solvus temperature of the γ phase
T_{eu}	Eutectoid temperature, where $\alpha \rightarrow \alpha_2 + \gamma$
TEM	Transmission electron microscope
Ti6242S	Ti-base near- α alloy containing Al, Sn, Zr, Mo and Si
TiAl	Titanium aluminide
TiB	Intermetallic TiB boride phase (B27 structure)
TNB	TiAl alloy with an elevated Nb content and B
TNM	TiAl alloy with Nb, Mo and B
TNM ⁺	TNM alloy with additions of C and Si
v	Deflection speed of the electron beam
Ti-48-2-2	TiAl alloy with Nb and Cr
ODS	Oxide dispersion strengthened
p-Ti ₃ AlC	Intermetallic Ti ₃ AlC carbide (E2 ₁ structure)
PM	Powder metallurgy
RE	Rare earth elements
RT	Room temperature
U	Acceleration voltage of the electron beam
XRD	X-ray diffraction

Motivation and scope

Research and development of materials and technologies have always been driven by the pursuit of efficiency. Thus, aerospace and automotive propulsion systems become lighter and reach higher service temperatures every day, due to the introduction of novel tailor-made materials. Such improvements are essential to respond to the climate crisis in a significant way.

One promising class of materials, which is capable of satisfying these demands for improving efficiency, is the category of intermetallic titanium aluminides (TiAl). TiAl alloys based on the γ -TiAl phase are lightweight, i.e. a density of roughly $4\text{ g}\cdot\text{cm}^{-3}$, and possess excellent high-temperature properties, i.e. strength and creep resistance up to $750\text{ }^\circ\text{C}$ [1, 2]. Consequently, those alloys have already entered application as turbine blades [3, 4] in aircrafts as well as valves [5, 6] or turbocharger turbine wheels [7, 8] in automotive engines. One example is the TNM alloy consisting of $\text{Ti-43.5Al-4Nb-1Mo-0.1B}$ in at.%, which successfully substituted the twice as heavy blades of Ni-base alloys in low-pressure turbines [3]. Besides the excellent mechanical properties of the TNM alloy, the success of this alloy rests upon its manufacturing via casting and subsequent forging under near-conventional conditions, due to the specific process-adapted design of the alloy composition, which was developed at the Department of Materials Science, Montanuniversität Leoben [9–12]. This γ -TiAl based alloy of the 4th generation, the so-called process-adapted TiAl alloys, reach service temperatures up to $750\text{ }^\circ\text{C}$, which represents the maximum in the application of this class of materials [2, 5, 13].

Currently, powder metallurgical approaches such as additive manufacturing (AM) are on the rise, attempting to substitute investment casting and forging of TiAl alloys by the near-net-shape manufacturing of components [14, 15]. Thereby, the AM technique of electron beam melting (EBM) is mainly used to additively manufacture well-known alloys, like the well-known Ti-48Al-2Cr-2Nb (Ti-48-2-2, in at.%) alloy and the TNM alloy, which are originally developed for processing by means of investment casting and forging, respectively. Thus, certain challenges arise during the additive manufacturing of those conventional TiAl alloys,

e.g. an inhomogeneous phase distribution as well as the formation of a texture [16–20]. Those challenges have to be understood and further overcome by thorough investigation to ensure a successful manufacturing of a resilient TiAl component for application in propulsion systems.

The service temperature limit, as well as the processability by AM of TiAl alloys, provoked the scope of this thesis: on the one hand to exceed the current application limitations of state-of-the-art TiAl alloys, e.g. the TNM alloy, and on the other hand, to overcome previously mentioned challenges of the powder metallurgical approach to build a resilient TiAl prototype by EBM. The investigations carried out for this purpose were part of the "NextTiAl" project (03XP0088C), which was funded by the Federal Ministry of Education and Research (Bundesministerium für Bildung und Forschung, BMBF), Germany [21]. Three alloys emerged from this project: so-called BMBF1, BMBF2, and BMBF3, designed in cooperation with the Montanuniversität Leoben. The alloys are part of this thesis whose entire scope is shown in Fig. 1.1 in a schematic flowchart. The workflow starts on the left-hand side with the characterization of the start material and its properties for the manufacturing process, i.e. the high-quality TiAl powder, which is emphasized in **Publication A**¹.

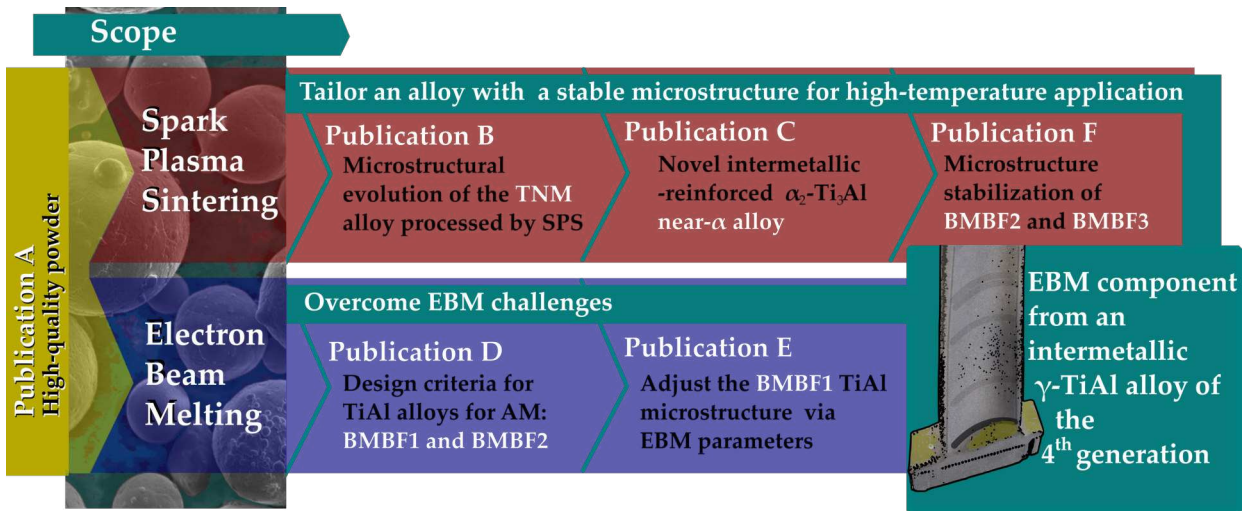


Figure 1.1: Schematic illustration of the thesis scope; the flowchart shows the two powder metallurgical approaches, i.e. spark plasma sintering (SPS) and EBM, supplied with high-quality powder. The SPS publications¹ were used to investigate alloys tailor-made for high-temperature application regarding chemical composition and microstructure, whereas the EBM publications aim to identify and overcome process-related challenges for the manufacturing of resilient TiAl components.

The powder metallurgical SPS process was used to densify alloy powder for detailed characterization, regarding microstructure evolution and stability as well as mechanical

¹The capital letters refer to the bibliographic detail of the publication in chapter 5.1 as well as to the respective sections A–F in the appendix.

properties. The advantage of this process is that it needs just small amounts of powder and is only minor influenced by the process itself when compared to the EBM process. At first, **Publication B** evaluates the SPS process by investigating the TNM alloy as a benchmark. Then, in **Publication C**, SPS was used to generate and concurrently evaluate a novel alloy, i.e. a high Al containing near- α Ti-base alloy reinforced with intermetallic Ti_3Al phase, which exceeds its former service temperature limit. Finally, two novel TiAl alloys were evaluated in **Publication F** regarding their potential to overcome the current application limits of TiAl alloys, i.e. high-temperature resistance by maintaining room temperature (RT) ductility.

Parallel, the BMBF alloys were investigated with respect to their processability via EBM. **Publication D** demonstrates the design criterion for γ -TiAl based alloys to prevent the formation of anisotropic properties as most components experience multiaxial stress during application. **Publication E** focuses on the EBM process itself and the resulting process-microstructure-property relationship.

The gained knowledge should finally merge in a novel process-adapted γ -TiAl alloy of the 4th generation, which enlarges the field of application and allows the production of TiAl components via AM.

State of the art

2.1 Intermetallic Ti-Al alloys for high-temperature application

2.1.1 Four generations of γ -TiAl based alloys

Alloys based on the intermetallic γ -TiAl phase are used in structural high-temperature application in the automotive and aerospace industry due to their low density, high specific strength as well as good creep and corrosion resistance at their service temperatures up to 750 °C. Therefore, this material class succeeded to substitute the twice as heavy Ni-base alloys as valves, turbocharger wheels and turbine blades to enhance the efficiency of propulsion systems [3, 5, 8, 22].

The base of TiAl alloys forms the binary Ti-Al phase diagram established by Schuster and Palm [23], shown in Fig. 2.1. Therein, binary alloys with an Al content between 42-48 at.% provide the 1st generation of engineering TiAl alloys [1]. At elevated temperature, two disordered phases exist for these alloys in the binary phase diagram: the hexagonal α -Ti(Al) (A3 structure) and the body-centered cubic (bcc) β -Ti(Al) phase (A2 structure). Whereas at lower temperatures, e.g. service temperature, these binary alloys consist of two ordered phases: the hexagonal α_2 -Ti₃Al phase (D0₁₉ structure), which is the ordered counterpart of α , and the face-centered tetragonal γ -TiAl phase (L1₀ structure), which denominates the material class [1, 23, 24]. The γ phase is the main phase of γ -TiAl alloys and carries the plastic deformation by the motion of ordinary dislocations with the Burgers vector $\mathbf{b} = 1/2 \langle 110 \rangle$ and mechanical twinning with $\mathbf{b} = 1/6 \langle 11\bar{2} \rangle$ on $\{111\}$ planes [25–29].

Based on the phase diagram in Fig. 2.1, the engineering γ -TiAl alloys, i.e. 42-48 at.% Al, can be distinguished by their solidification paths. Below 45 at.% Al, the alloy solidifies through the single β phase field region, i.e. $L \rightarrow L + \beta \rightarrow \underline{\beta} \rightarrow \beta + \alpha \rightarrow \dots$. For casting of TiAl alloys, this solidification ensures a fine grain and isotropic microstructure [30–32] due to the random

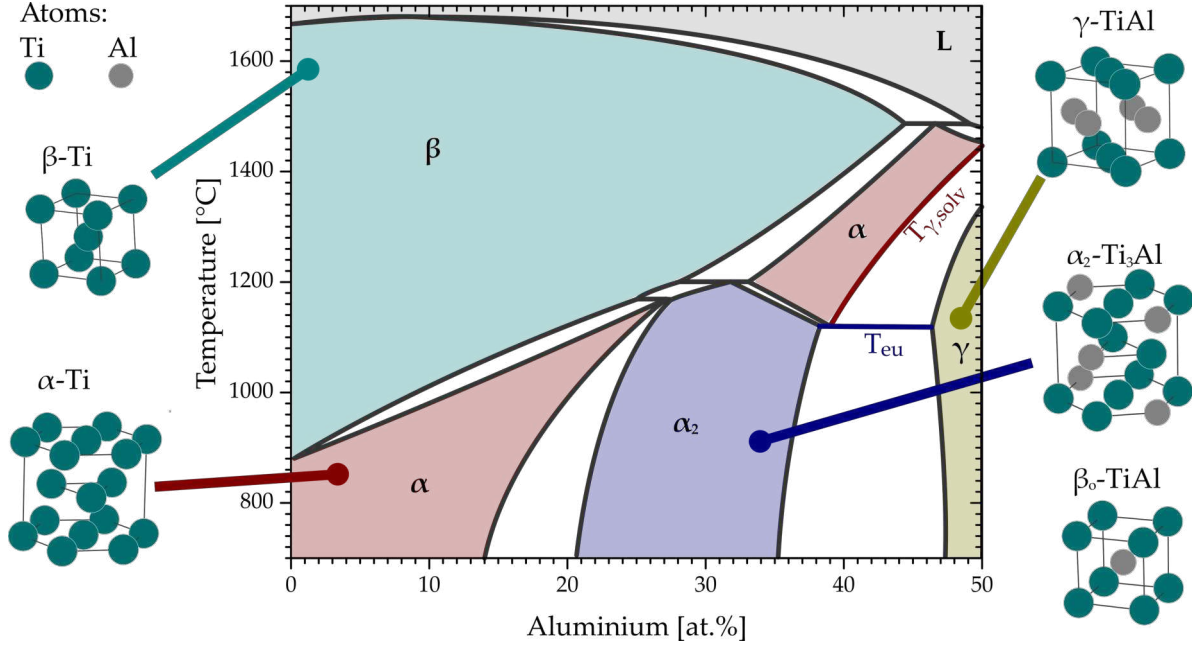


Figure 2.1: The binary Ti-Al phase diagram according to Schuster and Palm [23] wherein the single phase field regions are colored and the corresponding crystal structures are illustrated. Note that the β_o phase is introduced too, due to its relevance for non-binary alloys, see text.

transformation of α from β by 12 possible crystal orientation transformations according to Burgers [33]. On the contrary, binary TiAl alloys with higher Al contents solidify peritectic, i.e. $L \rightarrow L + \beta \rightarrow \alpha(+\beta) \rightarrow \dots$, which is prone to segregation and crystalline anisotropy [30, 34, 35]. However, those binary alloys of the 1st generation with only small quantities of alloying elements did not satisfy the requirements for application regarding strength, creep and oxidation resistance. Therefore, the impact of further alloying elements was considered. As a consequence, the 2nd generation of γ -TiAl alloys was introduced and their composition can be summarized as follows:

$$\text{Ti} - (45 - 48)\text{Al} - (1 - 3)X - (2 - 5)Y - (< 1)Z, \quad (2.1)$$

where $X = \text{Cr, Mn, V}$; $Y = \text{Nb, Ta, W, Mo}$; and $Z = \text{Si, B, C}$ (in at.% unless stated otherwise). In the framework of extensive research, the X elements lead to an increase in ductility [1, 24], whereas the heavy Y elements benefit the creep resistance due to their sluggish diffusion. Besides, Y elements act as strong β stabilizers, which means that the addition of those elements increases the stability range of the bcc β phase in the phase diagram [1, 36]. Therefore, in Al lean γ -TiAl alloys, it is also possible that β is stable down to RT, however, in course of cooling, an ordering reaction according to $\beta \rightarrow \beta_o$ -TiAl (B2 structure) takes place. The β_o phase is still bcc [37, 38], as shown in Fig. 2.1, but the long-range-order reinforces the phase, thus decreases the ductility [39, 40]. Hence, the appearance of the β_o phase is prevented in 2nd generation alloys. Finally, the Z elements were introduced to form precipitates to either improve the creep resistance, i.e. Si for silicides ζ -Ti₅Si₃ (D8₈

structure) [41–44] and C for carbides p-Ti₃AlC (E2₁ structure) [43, 45–47], or to refine the microstructure via heterogeneous nucleation, i.e. B for borides TiB (B27 structure) [1, 48]. The most prominent alloy in the 2nd generation is the Ti-48Al-2Cr-2Nb alloy. It gained its recognition through its installation as cast blades in the last stage of the low-pressure turbine of the GEnX jet engine from General Electrics (GE) in 2011 [3]. Nevertheless, despite excellent material properties, the service temperature of the 2nd generation Ti-48-2-2 alloy was limited to about 700 °C [13, 49, 50].

In order to exceed this temperature limitation, the content of the alloy elements was adjusted in the 3rd generation of the γ -TiAl alloys, which is written as follows:

$$\text{Ti} - (42 - 48)\text{Al} - (0 - 10)\text{X} - (0 - 3)\text{Y} - (0 - 1)\text{Z} - (0 - 0.5)\text{RE}, \quad (2.2)$$

where $X = \text{Cr, Mn, Nb, Ta}$; $Y = \text{W, Mo, Zr}$; $Z = \text{Si, B, C}$ and RE , which denotes rare earth elements [22]. Besides the already mentioned effects of the alloying elements, Zr can be addressed as an effective solid solution strengthener for γ -TiAl based alloys as Zr tends to partition rather into the γ phase than β_o , thus showing the opposite behavior than W and Mo [36, 51, 52]. Furthermore, the element C is also added due to its stabilizing effect of the α/α_2 phase, thus increasing the single α phase field region and minimizes the lamellar spacing, i.e. crucial for the creep strength [53–55], discussed in detail in section 2.1.2. Examples of a 3rd generation alloy are the so-called TNB alloys with high contents of Nb (5-10 at.%) and small amounts of B and C. These alloys exhibit tensile strength values up to 1000 MPa at RT and the high amount of Nb acts beneficial for creep resistance by impeding diffusion [48, 56, 57] as well as Nb improves the oxidation resistance by its integration into the protective oxide-layer [58–60]. In addition, up to 2% plastic strain can be maintained by facilitating mechanical twinning within the γ phase by decreasing the stacking fault energy with Nb additions [56, 61]. However, the lack of presenting a reliable processing route for this kind of high strength alloys leads to one further consideration in the design of γ -TiAl alloys: the processibility. Therefore, the engineering β -solidifying TNM alloy was developed with a nominal composition of Ti-43.5Al-4Nb-1Mo-0.1B, which, although chemically a 3rd generation alloy, represents a 4th generation TiAl alloy, the so-called process-adapted γ -TiAl based alloys. The TNM alloy was adapted to be forgeable in the as-cast state under near-conventional conditions by utilizing the 12 independent slip systems of the bcc β phase [9, 22]. The success of this approach led to the introduction of forged TNM blades into the Geared-Turbofan engine built by Pratt & Whitney and MTU in 2014 [4]. Further investigations on the TNM alloy result in the development of the TNM⁺ alloy, whose creep resistance exceeds those of the TNM alloy through the addition of C and Si [42, 62].

To this day, the TNM and TNM⁺ alloy represent the state of the art for high-temperature application of TiAl alloys and act as a common benchmark for the research and development of new γ -TiAl based alloys and novel processing routes, e.g. Refs. [5, 19, 63–68].

2.1.2 Link between microstructure and mechanical properties

Besides the chemical composition, the microstructure is key for the successful technical application of TiAl alloys. Usually, the microstructure is adjusted via a two-step heat treatment: The first step is set around the solvus temperature of the γ phase ($T_{\gamma, solv}$) and the second step below the eutectoid temperature (T_{eu} , where $\alpha \rightarrow \alpha_2 + \gamma$) and, concurrently, above the aimed service temperature to ensure microstructural stability [22, 69]. A large number of microstructures can be adjusted depending on the temperature of the first step, e.g. near gamma (NG), nearly lamellar gamma (NL γ), duplex (D), . . . , which are described in detail in Refs. [10, 69–72]. The highest creep resistance can be achieved through a so-called fully lamellar (FL) microstructure consisting solely of α_2/γ colonies and occasional precipitates, as illustrated in Fig. 2.2. This FL microstructure is adjusted above $T_{\gamma, solv}$ within the single α phase field region, see Fig. 2.1. Within a single phase field region, chemical inhomogeneities dissolve, which is particularly relevant in EBM manufactured TiAl samples, where Al variations arise, as explained in detail in section 2.2.3. However, during this heat treatment within the single α phase field region, the α grains tend to coarsen extensively, resulting in a low ductility at RT [73, 74]. Therefore, Kasthuber et al. [62] proposed the so-called "Si-effect" in TiAl alloys, where ζ -silicides as well as other stable precipitates, e.g. borides, impede grain boundary movement, thus keeping the colony size below 100 μm in the FL microstructure. Besides the prevention of grain growth during the heat treatment, a fine-grained starting microstructure is a beneficial precondition for the adjustment of a fine-grained FL microstructure [75, 76], as for example it is provided by EBM, as well as by SPS due to short dwell times. During cooling from the single α phase field region,

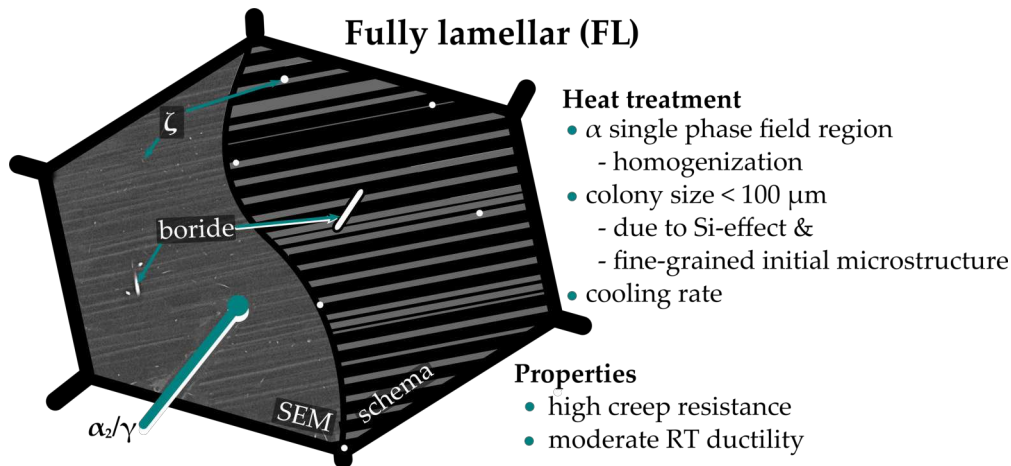


Figure 2.2: Scanning electron microscope (SEM) image and schematic illustration of a α_2/γ colony with occasional precipitates in a FL microstructure, adjusted within the single α phase field region followed by a specific cooling rate. Due to a fine initial microstructure as well as the Si-effect, a colony size below 100 μm can be maintained for a high creep resistance at service temperature and moderate ductilities at RT. See text for more details.

the α phase transforms into lamellar α_2/γ colonies according to the Blackburn orientation relationship [77]. Since this transformation is diffusion controlled, it applies that the higher the cooling rate, the finer the resulting lamellae in the colonies, thus higher strength and creep resistance is achieved [74, 78]. However, an extremely fine lamellar spacing facilitates the formation of cellular reaction (CR) at service temperature, which is the decomposition of the lamellae to minimize surface energy, starting at the colony boundaries according to $\alpha_2/\gamma \rightarrow \alpha_2 + \gamma + \beta_o$. Then, this fine-grained CR acts as a glide agent between the colonies, thus deteriorates the creep resistance [62, 79]. For example, although the FL microstructure of the TNM and TNM⁺ alloy provides excellent creep resistance up to 800 °C, its fine-lamellar microstructure decomposes by the CR, also encouraged by the low Al content of the TNM alloy, which benefits the β_o formation. Therefore, given the fact that the FL microstructure is designated as the most creep resistant microstructure, its stability has to be taken in consideration in the course of the alloy design. Furthermore, the single α phase field region has to be present, as it is not the case for the nominal TNM alloy [69], to adjust a creep resistant FL microstructure via heat treatment to exceed the current temperature limit of TiAl alloys.

2.1.3 Near- α alloys with intermetallic α_2 phase

At last, another material class of high-temperature Ti-base alloys should be mentioned in the course of this thesis, the near- α alloys, such as the Ti6242S alloy with a nominal composition of Ti-10.6Al-0.8Sn-2.1Zr-1Mo-0.2Si (Ti-6Al-2Sn-4Zr-2Mo-0.1Si m.%, so-called Ti6242S). Although it is not a TiAl alloy, the alloy achieves a temperature stability up to 550 °C [80–83]. The Al content improves the oxidation resistance as well as the strength. The latter stems from forming intermetallic α_2 -Ti₃Al in the α matrix. Those precipitates form during a final aging step around 600 °C in nanometer-size and are effective barriers for dislocation glide, i.e. during tensile tests, and climb, i.e. during creep tests [80, 84, 85]. The addition of solid solution strengthening elements, such as Sn, Zr or Mo, further improves the strength of near- α alloys. Besides, those alloys benefit from a RT ductility of more than 10%. However, state-of-the-art Ti-based alloys, as the Ti6242S alloy, disintegrated above 600 °C, regardless of which microstructure. Due to the fact that Ti-base alloys are currently under consideration to be manufactured via AM as well [16, 86, 87], there is also a demand for new process-adapted alloys for higher service temperatures. First attempts to increase their field of application were the development of so-called near- α_2 alloys with an elevated Al and Nb content [88, 89]. Therefore, the investigations overlap with the aims of the TiAl research.

2.2 Advanced powder metallurgical technologies

2.2.1 Production of metal powder by gas atomization

Currently, new processing approaches are under evaluation for industrial-scale manufacturing of high-temperature components in aerospace and automotive industries, by SPS or EBM. Their process-related features need to be researched in detail, to utilize their characteristics with new process-adapted 4th generation γ -TiAl alloys as well as new Ti-base alloys in the near future.

Metal powder is the starting material for the manufacturing of components via SPS or EBM. The technique of gas atomization is a common method to produce spherical metal powder on an industrial scale [90]. Since molten γ -TiAl and Ti-base alloys are highly reactive, the crucible-free EIGA (electrode induction melting gas atomization) technology has been applied to atomize these alloys. Thereby, small amounts of molten material form by inductively heating the tip of the rotating electrode, see Fig. 2.3a [91–94]. The TiAl ingots used as electrodes have to be free of large-scale segregations in order to produce homogeneous powder as no homogenization takes place in the small amount of molten material on the tip. The resulting melt jet from the tip is dispersed by Ar-inert gas into melt droplets, which solidify into spherical powder [93, 95]. Figure 2.3b shows the corresponding particle size distribution of EIGA-processed TiAl powder [91] and a SEM image of such powder particles. The high purity and roundness of the powder particles are a precondition for γ -TiAl and Ti-base powder to manufacture high-quality components. This means that high amounts of interstitial impurities, e.g. O, decrease the plasticity of the alloys [96–98], whereas

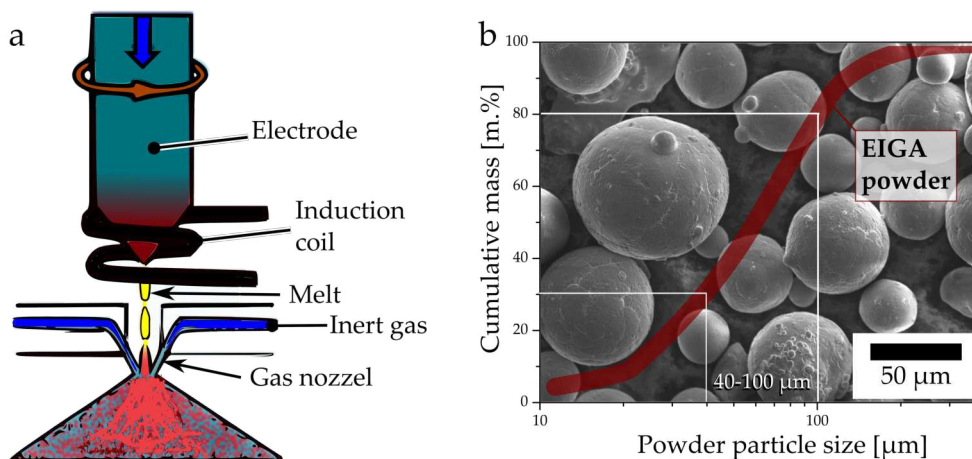


Figure 2.3: a) Schematic illustration of the EIGA process according to Ref. [91]. The EIGA technology is used for the manufacturing of high-purity TiAl or Ti-base alloy powder by using Ar as inert gas. b) SEM image of the spherical EIGA powder together with the cumulative particle size distribution [91], wherein the recommended powder particle range of the EBM process is entered.

misshaped powder particles decrease the flowability and bulk density, which complicates the even application of powder, e.g. during EBM [99–101]. Besides, the size of the powder particles is decisive for the processing technology, whereby the recommended range for EBM is between 40 - 100 μm [16, 102, 103] and for SPS $< 200 \mu\text{m}$ [104]. Those demands on size ensure a stable processing, discussed in detail in the next sections. However, those requirements limit the valuable fraction of the EIGA powder. In case of the EBM process solely 50 m.% is used (see Fig. 2.3b), whereas for SPS almost 100 % can be processed. The evaluation of those powder properties as well as their influence on the finished component is addressed further in detail in this thesis in **Publication A** and in chapter 3.1.

2.2.2 Spark plasma sintering

The technique of SPS consolidates metal powder into bulk or even near-net-shape components, as demonstrated in Refs. [105–107] on the basis of a TiAl turbine blade. In general, for the manufacturing via SPS, the powder is inserted into a graphite die and uni-axial stress together with pulsed electric current is applied in a water-cooled vacuum chamber [104], as schematically illustrated in Fig. 2.4. The quantity of necessary powder corresponds to the cavity of the graphite die. In the first stage of the powder consolidation, the pulsed electric current leads to a micro-spark discharge in the gaps between adjacent powder particles, whereby high temperatures are reached and, thus, the formation of sinter necks between the particles begins. Besides, it was originally claimed that plasma is formed between the powder particles during SPS which cleans the powder particle surface from oxides, which, however, is still under debate. Nevertheless, both aspects, the sparks as well as the claimed plasma, nominate the SPS manufacturing. After the first stage, where the powder particles connect via sinter necks, the porous bulk is heated via Joule heating, thus the bulk sinters below the solidus temperature of the alloy to its final density [104, 107]. Thereby, different dwell temperatures and times can be chosen, which facilitate the adjustment of different microstructures within the SPS unit, as shown for γ -TiAl based alloys [108–110]. Thereby, it could be shown that due to the short processing times achievable by SPS, i.e. heating rates of up to 1000 K/min and dwell times of single minutes, grain growth can be restricted, which is crucial for the ductility of TiAl. However, concurrently, these short processing times are only achievable by moderate sample sizes due to a necessary homogeneous thermal distribution within the sample. Moreover, the larger the samples the lower is the cooling rate, which is an essential parameter for adjusting a high-strength and creep resistant microstructure in γ -TiAl based alloys, as already explained in chapter 2.1.2 [111]. Nevertheless, the consolidation of powders into bulk discs with up to 80 mm in diameter allows the characterization and evaluation of alloys on a microstructural and mechanical scale as shown by Couret et al. [49]. Besides the consolidation of pre-alloyed powder, the technique of SPS allows the use of powder blends. Thus, TiAl and ODS

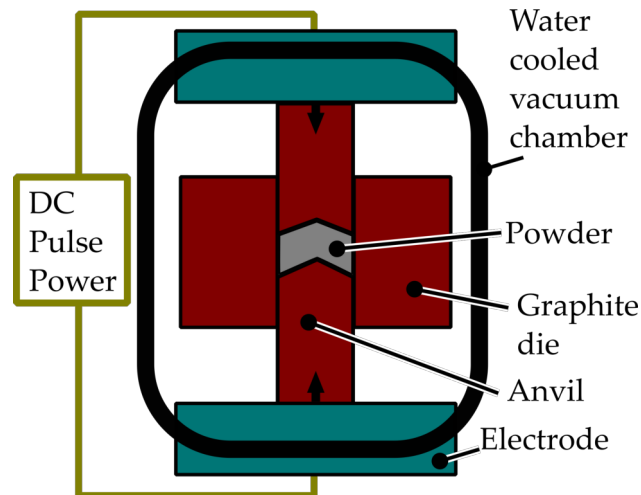


Figure 2.4: Schematic illustration of the densification of metal powder via the technique of SPS under applied uni-axial load and pulsed electric current.

(oxide dispersion strengthened) particle blends could be characterized [112] or new near- α Ti alloys could be generated [113] in a straightforward manner, not possible via casting. Other promising examples for SPS are Ti metal matrix composites (Ti-MMC), which show enhanced mechanical properties [114–119]. Ozerov et al. [114] could manufacture a Ti-MMC by solely blending a near- α Ti and a TiB_2 powder. Those examples show that SPS is a rather fast and independent method to consolidate powder for the design and investigation of γ -TiAl based alloys and Ti-alloys as it is also shown in **Publication B, C** and **F**.

2.2.3 Electron beam melting

AM of metal components is a strong driving force in research and development [16, 120, 121]. On the one hand, new functionalities can be introduced in components on a scale and flexibility which was not possible before, e.g. amorphous composites [122, 123] or near-net-shape Ni-base single crystals [124–126]. On the other hand, a new freedom of design was facilitated, which was inconceivable with conventional industrial casting, e.g. the manufacturing of bionic geometries to make components lighter, as shown by Refs. [127, 128]. For γ -TiAl alloys in particular, the declared goal is near-net-shape manufacturing of components, such as turbine blades, to decrease the buy-to-fly ratio of components by a material-efficient production [3, 15, 129–131].

In general, two AM techniques are currently used to build near-net-shape metal components based on a powder-bed: selective laser melting (SLM) [131–134] and EBM [102, 103, 132]. SLM uses a laser beam in an inert gas atmosphere, whereas EBM requires a vacuum condition to operate the utilized electron beam. However, EBM facilitates to defocus the electron beam via electromagnetic lenses to preheat the powder bed and the component. This standard option of preheating the component is the main reason, why EBM is the AM technique of

choice for γ -TiAl based alloys, which suffer from low ductility below the brittle-to-ductile-transition-temperature (BDTT) of 700-900 °C [1]. Therefore, the preheating above BDTT prevents thermal cracking by residual stress. Figure 2.5a shows a schematic illustration of an EBM unit and its main components whose function is described in the following. In principle, the EBM process can be represented as a cyclical sequence of four steps: i) powder deposition, ii) preheating, iii) selective melting and iv) lowering of the platform, schematically illustrated in Fig. 2.5b. In detail, during i), powder stored in the hopper is deposited by the so-called rake. Thereby, the rake moves from left and right and vice versa until the powder layer is evenly applied. Emphasize that a low flowability of the powder can impede the formation of an even powder-bed, which can result in critical bonding faults [101]. In step ii) the electron beam is defocused via electromagnetic lenses and the scanning speed is increased to preheat the powder bed with low energy input. Thereby, the temperature of a thermocouple attached below the start plate acts as a control value. During the manufacturing of γ -TiAl alloys, the preheating temperature is above 1000 °C to exceed BDTT. In addition, the preheating results in the slight sintering of the powder, which is essential to prevent the abrupt dusting of the negatively charged powder particles. This phenomenon, so-called smoke, aborts the building job and occurs especially when the powder contains a high fraction of fine particles, i.e. smaller than 40 μm . Next, iii), the focused electron beam selectively melts the powder on locations where the component has to be built. Thereby, a lot of process parameters can

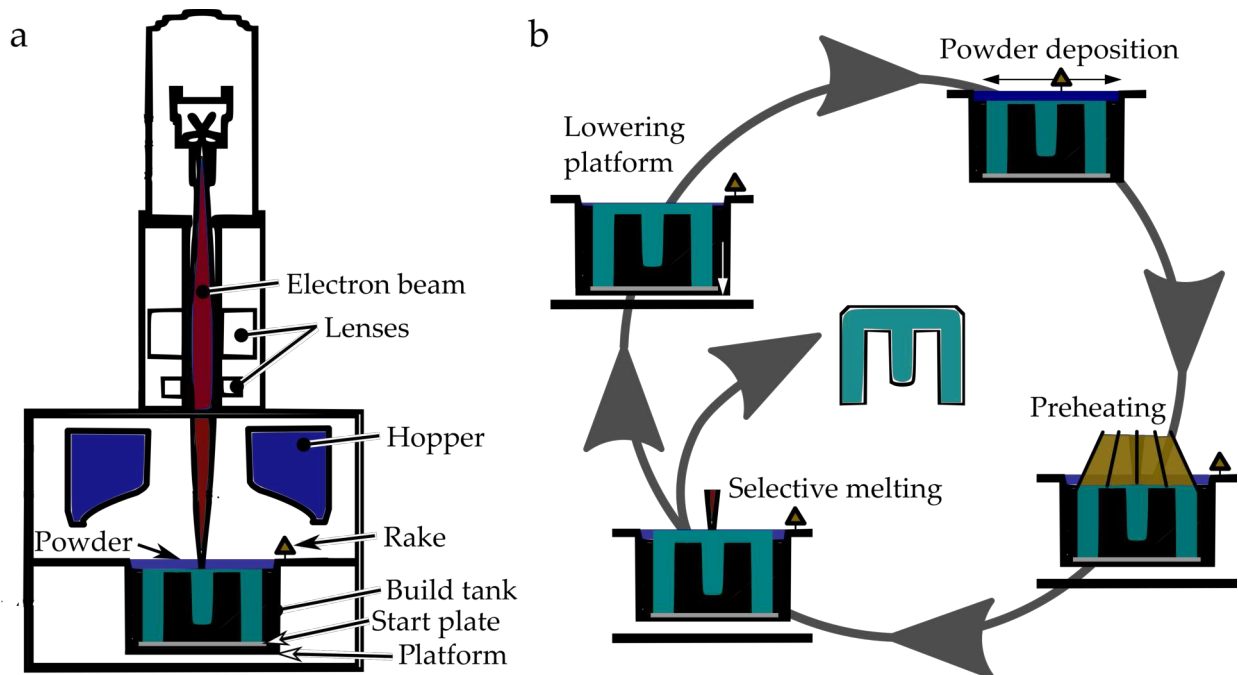


Figure 2.5: Schematic illustration of a) an EBM unit and b) the cyclical sequence to build an EBM component, described in detail in the text.

be set: the scan strategy, the hatching distance (HD), the deflection speed (v) and the beam current (I). The HD , v and I can be summarized by the area energy (E_A):

$$E_A = \frac{U \cdot I}{v \cdot HD} = \frac{E_L}{HD}, \quad (2.3)$$

where U is the constant acceleration voltage (60kV) and E_L is the line energy, which is also often used as an energy value. After selective melting, in step iv), the platform with the start plate, the component, and the powder is lowered by an individual layer thickness (t). In case of EBM, t is between 75 and 150 μm . Afterwards, the sequence starts continuously until the component is finished. The final component is enclosed in a so-called powder-cake, i.e. sintered powder, which is removed during post-processing via powder-blasting using the same powder to prevent cross-contamination.

The near-net-shape manufacturing of TiAl turbine blades or turbocharger wheels was already accomplished via EBM [14, 15, 135]. However, for the production of TiAl components on an industrial scale, specific challenges still need to be overcome. For example, the Al evaporation in the range of 0.5-8 at.% is a permanent issue of additively manufactured γ -TiAl components [103, 136–138]. This is crucial in Al-sensitive TiAl alloys, since Al shifts phase fractions and transition temperatures significantly when considering the phase diagram in Fig. 2.1 as guidance. Another issue regarding the processing via EBM is the formation of a solidification texture. This concerns mainly the manufacturing of Ni-base and Ti-base alloys [16, 87, 124–126, 139] with high E_A , because of steep thermal gradients and either no phase transformation in Ni-base alloys or only one in Ti-base alloys between the solidification and the RT microstructure. So far, in γ -TiAl alloys, where two phase transformations take place, i.e. $\beta \rightarrow \alpha \rightarrow \gamma$, only Ref. [19] documented signs of a solidification texture in the remaining β_o phase. So far, no one was capable to track it into the γ -phase, which carries mainly the plastic deformation [1, 140]. These EBM issues, i.e. Al content and texture formation, have to be understood and further overcome with the simultaneous optimization of the alloys and the process, addressed in **Publication D** and **E**, and in chapter 3.3.

Summary of publications

3.1 High-quality powders as starting material

Since AM became a topic for the processing of high-quality components on an industrial scale, the demand for metal powders has increased too. However, the requirements for AM powder are different from those powders dedicated for the processing via HIP or SPS. Those aspects are the focus of **Publication A**¹ (see chapter 5.1 for bibliographic details of the publication).

Technological parameters were evaluated on EIGA-manufactured TiAl powder, e.g. bulk density, tap density and flow behavior. Those technological test methods are standardized to prevent an influence by factors such as moisture level and test arrangement. The resulting bulk density of the TiAl powder was determined to be 2.3 g/cm³, i.e. 55 % when compared to the dense material. This technological parameter is important for the powder metallurgical approach, because of the shrinkage during sintering or melting. Other technology parameters such as tap density and flow behavior were also determined, pointing to good workability for HIP, SPS and AM. However, due to the complexity of the AM process, in particular the application of powder by the rake, such common technological test methods may be insufficient for the evaluation of AM powder [101, 141]. Therefore, the powder was investigated in more detail via light optical and electron microscopy on fractionated powder, see graphical abstract in Fig. 3.1.

The fractionation was conducted with standardized sieves. Image analysis of the powder cross-sections reveals gas pores within the spherical particles. The trapped gas is Argon, which became encapsulated during the EIGA process due to its insolubility in metals. The results show that the number of gas pores increases with increasing size of the particles. Such Argon pores limit the use of powder in AM, SPS or HIP: During EBM, some Ar pores

¹D. Wimler et al., Aspects of powder characterization for additive manufacturing, Practical Metallography 55 (2018) 620.

3.1 High-quality powders as starting material

cannot escape from the short existing melt pool into the vacuum chamber, thus remain in the final component [142]. Otherwise, during the consolidation of the powder via SPS and HIP, the pores can be closed by the external pressure at elevated temperature, but can open up again during a subsequent heat treatment, so-called thermally induced porosity, which deteriorates the static and dynamic mechanical properties [143, 144].

A close investigation of the powder surface by electron microscopy reveals satellites at the powder particles. Those can affect the properties negatively in two manners: First, they decrease the flowability. Secondly, satellites can detach during processing, thus increase the fine powder particle fraction, which leads to a further decrease of the flowability and, especially for the EBM process, an increase of the smoke-likeness. Besides, the powder surface shows a dendritic structure that continues into the TNM powder interior. This dendritic structure forms during solidification via the β phase, whose solubility in Al is limited. Therefore, the light element Al segregates in front of the solid/liquid interface. The Al rich liquid melt solidifies last and appears dark in the BSE SEM images. Such inhomogeneities appear mostly on a μm -scale but can enlarge if inhomogeneous EIGA feedstock material is used. Then, this can affect the microstructure of SPS and HIP processed components drastically due to locally different chemical compositions as there is no melting during the densification, thus no homogenization takes place.

Finally, the powder handling has to be considered; especially for the manufacturing of γ -TiAl based alloys. These alloys suffer from low ductility at room temperature, thus pores as well as impurities introduced by cross-contamination or handling at atmosphere embrittle the material irreversible [96–98].

In a nutshell, a top-quality powder in terms of processability and purity is the precondition for the manufacturing of top-quality TiAl components.

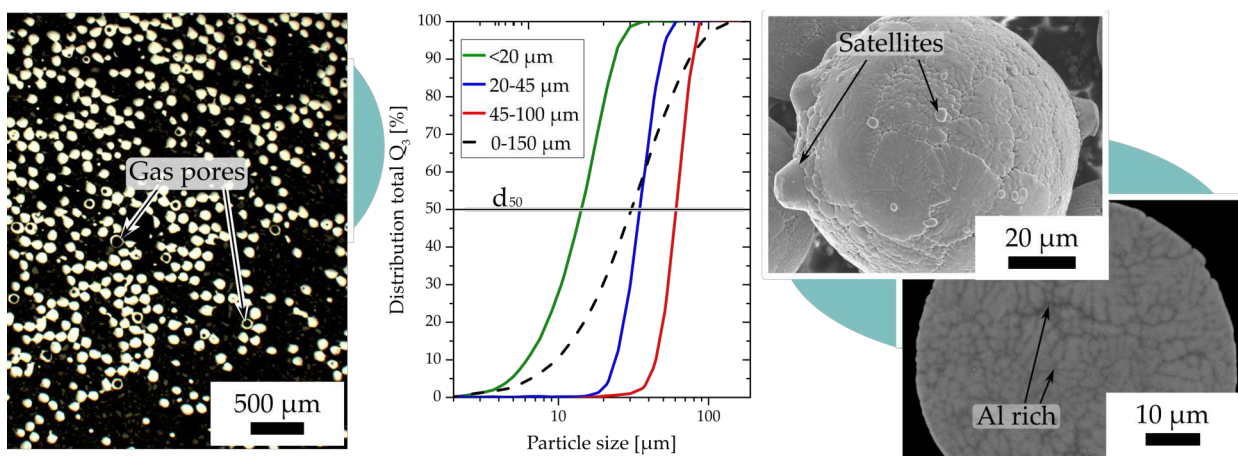


Figure 3.1: Graphical abstract assembled from **Publication A**: Aspects of powder characterization for additive manufacturing.

3.2 Tailor-made alloys for high-temperature applications

As soon as small quantities of metal powder are available, the SPS technique is an option to densify powder into bulk with different geometrical forms and sizes. Thus, alloys can be microstructurally and mechanically characterized, as it was done in **Publication B** as a benchmark study for SPS for the well-established TNM alloy. The same straightforward densification and subsequent characterization was also applied to new, tailor-made alloys for high-temperature application whether it is an improved near- α alloy in **Publication C** or a 4th generation γ -TiAl alloy in **Publication F** (see chapter 5.1 for bibliographic details of the publications).

The manufacturing of γ -TiAl based alloys via SPS enables an in-situ microstructure adjustment by sintering at different dwell times and temperatures. However, current SPS devices allow only cooling by natural convection, i.e. slow and geometry dependent. Consequently, the full potential of the processing-microstructure-property relationship can not be reached for TiAl alloys, as the cooling step is crucial for the formation of creep-resistant fine lamellar α_2/γ colonies. **Publication B**² addresses this concern by the densification of gas atomized TNM powder via SPS and designs subsequent multi-step heat treatments to optimize the mechanical properties for high-temperature applications, when compared to the as-SPS condition, which is summarized in the graphical abstract to the publication in Fig. 3.2. In as-SPS condition, the microstructure is called NL γ + β_0

²D. Wimler et al., Microstructural evolution and mechanical properties of an advanced γ -TiAl based alloy processed by spark plasma sintering, Materials 12 (2019) 1523.

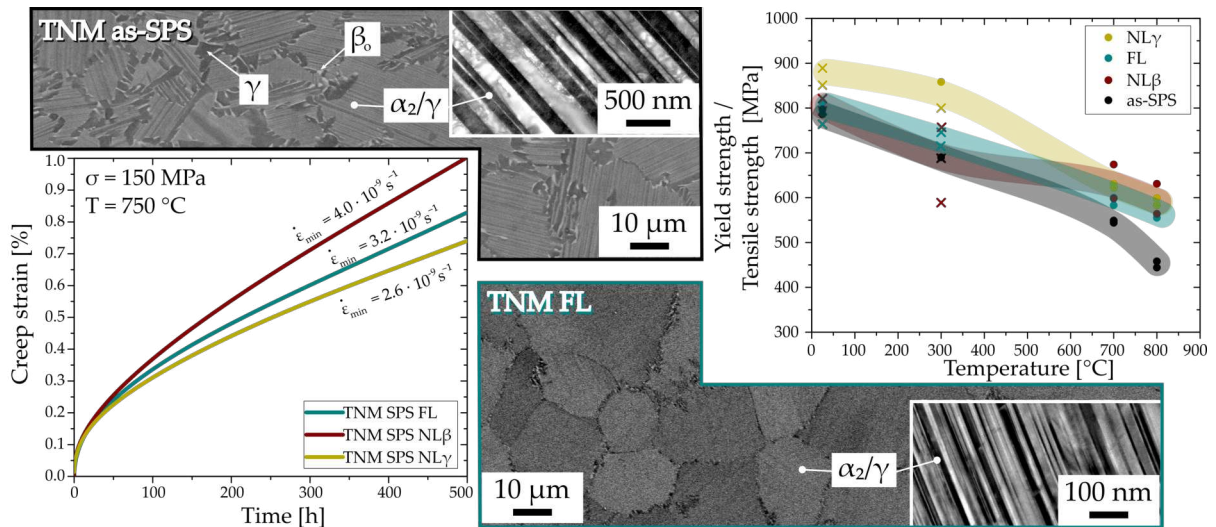


Figure 3.2: Graphical abstract assembled from **Publication B** entitled: Microstructural evolution and mechanical properties of an advanced γ -TiAl based alloy processed by spark plasma sintering.

with an average colony size below 20 μm . This fine microstructure stems from the short dwell time during SPS, i.e. 1300 $^{\circ}\text{C}$ for 3 min. However, due to the slow cooling rate of about 90 K/min the average lamellar width is 80 nm within the α_2/γ colonies. Therefore, three subsequent multi-step heat treatments were designed to adjust a NL γ , FL and NL β microstructure, whereby their average lamellar spacing was decreased to about 10 nm. As a consequence, hardness measurements at RT show an increase of about 70-90 HV10. However, this strengthening was not passed on the tensile test at temperatures below 600 $^{\circ}\text{C}$. The strength levels of the heat-treated microstructure could be maintained when compared to the as-SPS condition, but the ductility decreases. It is argued that the Oxygen content of 1300 m.ppm embrittles the alloy, which leads to an early failure of the tensile samples; except for the more ductile NL γ microstructure. However, the high-temperature yield strength could be increased significantly when compared to the as-SPS condition, i.e. from 450 MPa in the as-SPS condition to about 600 MPa in case of the NL β microstructure. Therefore, the creep tests at 150 MPa and 750 $^{\circ}\text{C}$ reveal excellent results, i.e. the plastic creep strain was kept below 1 % after 500 h under applied load and temperature. Thereby the NL γ microstructure, which shows the largest colony size with about 45 μm , performed best. In comparison to the TNM alloy processed via conventional processing routes, i.e. casting and subsequent heat treatments [69], an equal level of mechanical properties can be achieved.

To sum up, Publication B shows the potential of the SPS processing route as either an alternative powder metallurgical approach for the manufacturing of γ -TiAl alloys or for the research and development of alloys on a scale where microstructural and mechanical characterization is already possible.

The technique of SPS facilitates the development and processing of so-called metal matrix composites (MMC) and new alloys, as it was shown in **Publication C**³. Figure 3.3 shows the corresponding graphical abstract. The aim of this publication was to investigate new near- α alloy concepts to exceed current application limits of about 550 $^{\circ}\text{C}$.

For the Ti-MMC, the matrix alloy was the well-known near- α alloy Ti6242S (Ti-6Al-2Sn-4Zr-2Mo-0.1Si, in m.%) and the matrix-reinforcement was powder particles smaller than 20 μm of the engineering TNM alloy with a nominal composition in m.% of Ti-28.6Al-9Nb-2.3Mo-0.03B. The used powder blends were sintered either at 1100 $^{\circ}\text{C}$ or 1150 $^{\circ}\text{C}$ into the bulk material, whereon a complete microstructural as well as mechanical characterization was conducted. Due to the different sintering temperatures of the Ti6242S+TNM powder blends, the microstructures differ from each other: Sintering at 1100 $^{\circ}\text{C}$ reveals a Ti-MMC of Ti6242S matrix and TNM alloy powder particles, whereas sintering at 1150 $^{\circ}\text{C}$ generates a homogeneous fully lamellar microstructure without any TNM particles present. As a result of the dissolution of the TNM powder particles within the Ti6242S alloy, a novel near- α

³D. Wimler et al., Novel intermetallic-reinforced near- α Ti alloys manufactured by spark plasma sintering, *Materials Science and Engineering: A* (2020) 139798.

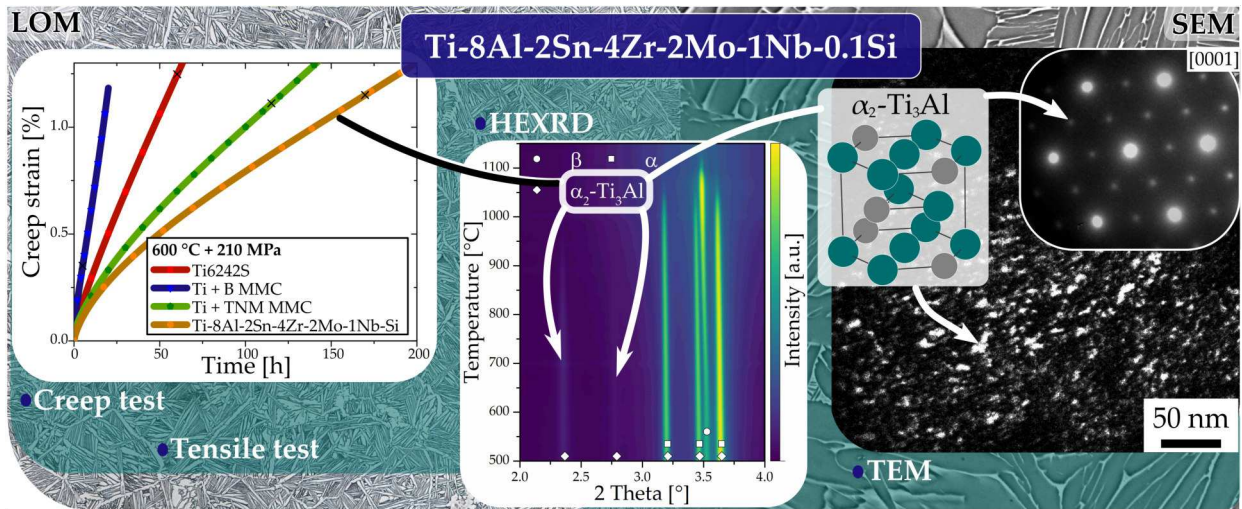


Figure 3.3: Graphical abstract assembled from **Publication C**: Novel intermetallic-reinforced near- α Ti alloys manufactured by spark plasma sintering.

Ti-base alloy was obtained with a composition of Ti-8Al-2Sn-4Zr-2Mo-1Nb-0.1Si in m.%, called Ti8242NbS.

In addition, the matrix Ti6242S powder was solely consolidated as a benchmark as well as pre-alloyed Ti6242+1 m.% B, which is a common Ti-MMC.

The microstructural characterization with the light optical microscope (LOM) and SEM reveals a fully lamellar microstructure in the Ti6242S as well as in both Ti6242S+TNM bulks, whereas the Ti6242+B MMC appears rather fine and globular and contains numerous TiB monoborides. Due to its microstructural fineness, the Ti6242+B MMC shows poor creep properties at 600 °C, which corresponds to the desired service temperature. Otherwise, the Ti6242S+TNM powder blends sintered at two different temperatures show enhanced properties during creep and tensile tests, when compared to the Ti6242S alloy. To understand this behavior, High-energy X-ray diffraction (HEXRD) and transmission electron microscopy (TEM) experiments were conducted at the novel Ti8242NbS alloy. The results reveal the presence of the intermetallic ordered hexagonal α_2 -Ti₃Al phase with a domain size of 10 nm surrounded by disordered α phase. Thus, the α_2 phase reinforces the microstructure by inhibiting the motion of dislocations within the majority α matrix. In-situ HEXRD reveals the complete α_2 -phase stability up to 670 °C, which proves that this novel near- α alloy, so-called Ti8242NbS, can be used at temperatures around 600 °C. As a result, the novel alloy exceeds the service temperature limit of 550 °C established by Ti-6 m.% Al base near- α alloys.

Currently, the material class of lightweight high-temperature alloys based on the intermetallic ordered γ -TiAl phase reaches temperatures of about 750 °C in service, as the engineering

TNM alloy [13]. Aiming for higher service temperatures, **Publication F**⁴ investigates two new alloys regarding their mechanical properties as well as their microstructural stability, see corresponding graphical abstract in Fig. 3.4. The two alloy powders, i.e. the so-called BMBF3 alloy: Ti-47.4Al-5.6Nb-0.4W and BMBF2 alloy: Ti-48.6Al-4.1Nb-0.7W-0.4Si-0.5C-0.1B (in at.%) were powder metallurgically manufactured via SPS and a subsequent heat treatment was established. For the BMBF3 alloy, the heat-treated microstructure consists of lamellar α_2/γ colonies surrounded by 10% globular γ (γ_g) phase, thus called NL10 γ , whereas for the BMBF2 alloy a NG as well as a FL microstructure were adjusted. Note that the NL and the FL microstructure of both alloys were stabilized at 900 °C for 240 min before tensile and creep testing. The results were compared with SPS-manufactured TiAl alloys of the 2nd generation, i.e. the Ti-48-2-2 alloy [49], as well as the 4th generation TNM alloy [Publication B]. The comparison shows that the NL10 γ condition of BMBF3 alloy is more ductile at RT and reaches better creep resistance at 750 °C than the TNM alloy in FL condition. The NG BMBF2 microstructure appears fine-grained and contains β_o and ζ phase, which increase the tensile strength but reduce the plastic strain to fracture below < 0.1%. On the contrary, the FL microstructure of the BMBF2 alloy with a colony size above 100 μm and an average lamellar spacing of 120 nm maintains RT ductility and shows superior creep resistance up to 850 °C, for which the additions of C and Si were responsible; similar to the TNM⁺ alloy [62].

Further investigations regarding the stability of the FL microstructure of the BMBF2 alloy were conducted. The microstructure was adjusted within the SPS unit, thus as-SPS and no subsequent heat treatment, exhibiting a lamellar spacing of about 310 nm. This microstructure was further stabilized at 800, 900 and 1000 °C for 10, 100 or 240 min.

⁴D. Wimler et al., Microstructure and mechanical properties of novel TiAl alloys tailored via phase and precipitate morphology, submitted to SCI Journal, (2021).

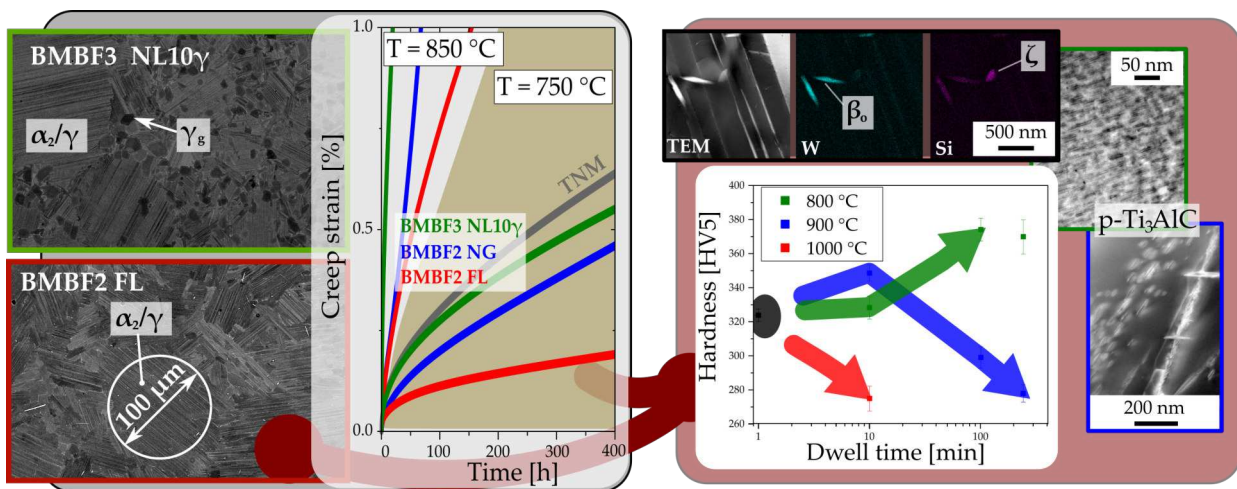


Figure 3.4: Graphical abstract of **Publication F**: Microstructure and mechanical properties of novel TiAl alloys tailored via phase and precipitate morphology.

The resulting microstructures show no significant difference in the SEM images, but in the hardness, X-ray diffraction (XRD) and TEM results. Based on those investigations, it was concluded that the as-SPS condition was in disequilibrium, thus α_2 phase dissolved during stabilization heat treatments between 800 and 1000 °C. Since the α_2 phase solves C, the dissolution of the α_2 lamellae within the α_2/γ colonies leads to the formation of perovskitic p-Ti₃AlC carbides in the γ phase. Depending on their size and distribution within the γ phase, those p-carbides result in a strengthening of the TiAl alloys by minimizing the mean free path of dislocations in the γ phase. In case of the sample stabilized at 800 °C, p-carbides appear in the TEM images as few atomic layer thick precipitates and are dispersed in the entire γ phase, thus increasing the hardness up to 15 %. Otherwise, stabilized at 900 °C, a softening appears due to coarse p-carbides in the center of γ lamellae. Besides, discontinuous coarsening of the γ laths additionally contributes to a decrease in hardness.

In summary, the BMBF2 alloy stabilized at 900 °C for the subsequent mechanical tests exhibits excellent creep resistance up to 850 °C. However, the alloy would be even better suited after stabilization at 800 °C, as the p-carbides appear finer and thus strengthen the γ phase more effectively. In contrast, the precipitation-free BMBF3 alloy, i.e. no Si and C was added, shows a reduced creep resistance, when compared to the BMBF2 alloy, regardless of the microstructure. However, the creep results exceed those of Ti-48-2-2 and TNM alloy in a comparable microstructure, and concurrently shows a better RT ductility than the TNM alloy.

3.3 Overcoming the challenges of electron beam melting

The additive manufacturing of near-net-shape γ -TiAl components is considered a promising method to substitute conventional investment casting and/or forging of γ -TiAl on an industrial-scale. First efforts to additively manufacture via EBM point out that near-net-shape turbocharger wheels [14, 135] and turbine blades [15, 145] are producible in a dense manner. However, these attempts already show first issues that EBM of γ -TiAl has to deal with, namely Al evaporation or the formation of a solidification texture [16–20]. To overcome these challenges and to use the full potential of the combination: AM and TiAl, more knowledge has to be gained regarding the interaction of γ -TiAl alloys and the EBM process to design a process-adapted γ -TiAl alloy of the 4th generation. These concerns are addressed in **Publication D** and **Publication E** (see chapter 5.1 for bibliographic details).

A solution to deal with the inhomogeneous Al evaporation in EBM manufactured γ -TiAl components is shown in **Publication D**⁵, whose graphical abstract is presented in Fig. 3.5. While the well-known Ti-48-2-2 alloy is presently used worldwide for AM, the approach

⁵D. Wimler et al., Designing advanced intermetallic titanium aluminide alloys for additive manufacturing, *Intermetallics* 131 (2021) 107109.

of this work was to develop new process-adapted γ -TiAl based alloys. Two advanced intermetallic TiAl alloys were designed to satisfy the demands of the EBM process as well as high-temperature application. The solution was to generate alloys with a large single α phase field region, due to two reasons: i) A heat treatment within a single phase field region enables a homogenization of the spatial distributed Al atoms, caused by Al evaporation during the EBM process, discussed in detail later. ii) During cooling from the single α phase field region, the α phase transforms into α_2/γ colonies, adjusting a so-called fully lamellar microstructure, which is considered to exhibit excellent creep resistance. Furthermore, additional alloying elements should reinforce the microstructure by solid solution and/or precipitation hardening. With these goals in mind, two alloys were chosen with the nominal composition of Ti-44.9Al-4Nb-0.7W-0.1B-1Zr-0.4Si-0.5C, the so-called BMBF1 alloy and Ti-48.4Al-4Nb-0.7W-0.1B-0Zr-0.4Si-0.5C, the so-called BMBF2 alloy (in at.%). In these alloys in particular, the C increases the single α phase field region, whereas Si is added to impede the α grains to grow by forming ζ -(Ti,Zr)₅Si₃ silicides.

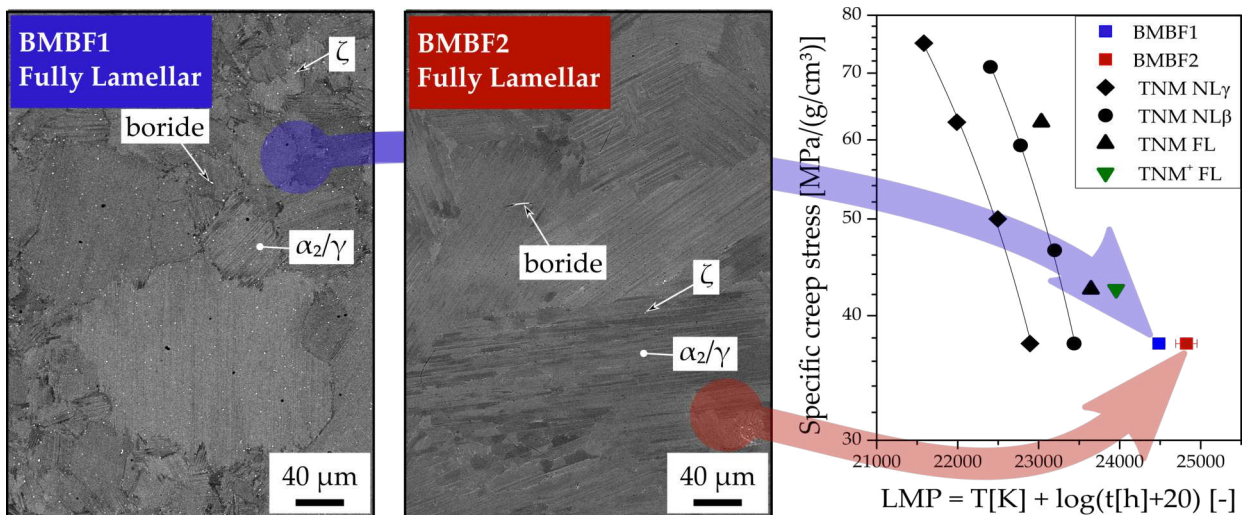


Figure 3.5: Graphical abstract assembled from **Publication D**: Designing advanced intermetallic titanium aluminide alloys for additive manufacturing.

The alloys were manufactured with different sets of parameters to find their feasible process window. This window is limited by the swelling phenomenon at high energy inputs and porosity at low energy inputs. Within the process window, the total Al content decreases with increasing E_L , which has an effect on the transformation temperatures. In addition, the microstructures of samples built with high E_L shows lines enriched with β_o phase, which stems from local high Al evaporation. Those lines vanish at low E_L in the as-EBM microstructure. Nevertheless, minor Al-variations remain in the dense specimens, thus the samples were heat-treated to adjust a FL microstructure in order to achieve the previously mentioned effects. No columnar or banded microstructural features could be determined in the FL microstructure. Further, the FL microstructure exhibits excellent

isotropic creep resistance up to 850 °C, thus exceeding those of the engineering TNM alloy [62, 146]. Therefore, it is concluded that the first attempt to design 4th generation γ -TiAl-based alloys adapted for the EBM process is rated successful. This design criterion of a γ -TiAl alloy with a FL microstructure will form a basis for producing TiAl components in the near future.

A dense γ -TiAl component can be built with different sets of EBM process parameters, whose impact on the final part regarding the microstructure is evaluated barely. Therefore, in **Publication E**⁶, four different sets of parameters were used to build cuboid samples of the Ti-44.8Al-4.1Nb-0.7W-1.1Zr-0.4Si-0.5C-0.1B (at.%) alloy, the so-called BMBF1 alloy. The characterization of the samples was conducted in detail via electron microscopy and diffraction experiments supported by numerical simulation, summarized in the graphical abstract shown in Fig. 3.6.

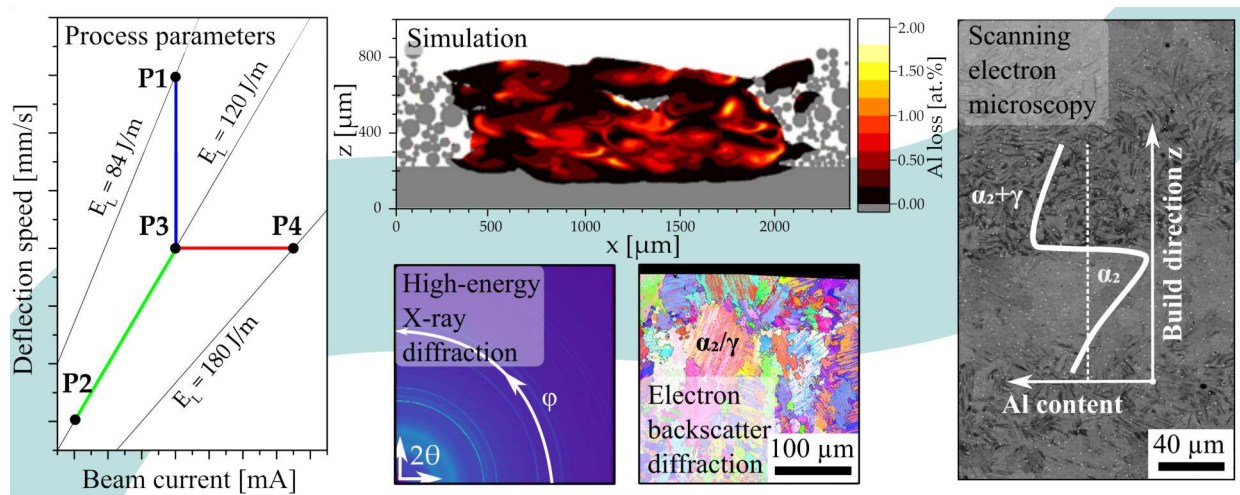


Figure 3.6: Graphical abstract from **Publication E**: How electron beam melting tailors the Al-sensitive microstructure and mechanical response of a novel γ -TiAl based alloy.

The evaluation of the Al content shows that Al differs up to 0.6 at.% between the built samples and up to 1.8 at.% when compared to the used powder. It was shown that an increase of E_L (Eq. 2.3) leads to lower Al contents. The variation of Al content in the samples is also reflected in the phase distribution of the as-EBM samples as well as in the samples heat-treated near the solvus temperature of the γ phase, $T_{\gamma, solv}$. The phase distribution confirms that the lower the Al content in the additively manufactured samples, the lower the γ phase fraction in the entire samples. Furthermore, an inhomogeneous Al distribution was observed through alternating banded phase distributions: In Al-lean bands, the α_2 phase dominates in the heat-treated condition. Otherwise, i.e. in the Al-rich bands, the γ phase is most present. As a consequence, the heat-treated microstructures show hardness values,

⁶D. Wimler et al., How electron beam melting tailors the Al-sensitive microstructure and mechanical response of a novel process-adapted γ -TiAl based alloy, submitted to SCI-journal.

which strongly scatter across these bands, i.e. soft in the γ rich bands and vice versa. The decreased Al content originates from the local Al evaporation on the top of the melt pool. Despite the short lifetimes of the melt pools, the combination of the high temperature of the molten material, the high evaporation pressure of Al and the prevailing vacuum in the EBM chamber results in Al evaporation. This Al evaporation becomes stronger with higher E_L due to higher temperatures of the melt.

Investigations of the crystal orientation in as-EBM condition via electron backscatter diffraction and high-energy X-ray diffraction reveal a preferred orientation in the majority phase γ : about 45° in building direction when E_L is high. It is concluded after the investigation of the topmost layer, that a strong thermal gradient towards the building direction forces a $\langle 001 \rangle_\beta$ solidification texture. This preferred orientation of β is subsequently inherited into the γ phase via the Burgers and Blackburn crystal orientation relationship. Since γ carries the plasticity in TiAl alloys, forcing a γ texture may lead to mechanical anisotropy.

Hence, the results show that the specific issues of EBM, i.e. Al content and texture, can not only be mastered by understanding the interaction between the process and the alloy, but can also be used in a targeted manner to adjust a wide range of material's properties.

Summary and outlook

The powder metallurgical approaches, SPS and EBM, are promising processes to manufacture components in near-net-shape geometries. Together with the development of new process-adapted TiAl alloys, which exceed the mechanical properties of state-of-the-art alloys, these approaches attempt to substitute established cost-intensive processes as investment casting and/or forging.

In order to realize this exchange, this thesis has been conducted to investigate the microstructural and mechanical properties of TiAl alloys as well as the technological influence of the EBM process, to end up with fundamental process-microstructure-property relationships for future improvements. This was established by the following investigations.

- A novel near- α alloy (Ti-8Al-2Sn-4Zr-2Mo-1Nb-0.1S in m.%), the well-known TNM alloy (Ti-43.5Al-4Nb-1Mo-0.1B in at.%), as well as two new TiAl alloys, so-called BMBF2 (Ti-48.6Al-4.1Nb-0.7W-0.4Si-0.5C-0.1B in at.%) and BMBF3 (Ti-47.4Al-5.6Nb-0.4W in at.%) were manufactured via SPS.

The novel near- α alloy shows enhanced high-temperature properties, i.e. via creep and tensile tests, as current near- α alloy, e.g. 550 °C for the Ti-6Al-2Sn-4Zr-2Mo-1Nb-0.1S alloy (in m.%), due to the α_2 reinforcement.

In case of γ -TiAl based alloys, the TNM alloy, applicable up to 750 °C, was manufactured via SPS and subsequent heat treatment as a benchmark for current state-of-the-art TiAl alloys. For the BMBF2 and BMBF3 alloy, subsequent heat treatments were designed to adjust a FL and NL γ microstructure, respectively. The evaluation of BMBF2 and BMBF3 microstructure shows superior creep properties, when compared to the TNM alloy. The BMBF2 alloy even remains below 1% creep strain after 100 h at 850 °C and 150 MPa because of p-type carbides and silicides, but behaves brittle at RT, while the BMBF3 alloy provides a higher ductility at RT than the TNM alloy. Besides, those investigations confirm that SPS is a rather fast and straight forward

4. Summary and outlook

method to investigate and develop novel alloys, due to the small amounts of required powder and no process-related impact when compared to EBM.

- The BMBF1 (Ti-44.8Al-4.1Nb-0.7W-1.1Zr-0.4Si-0.5C-0.1B in at.%) and BMBF2 alloy were manufactured via EBM. The microstructure appears with no columnar microstructure and no preferred crystal orientation by using the optimized set of process parameters. However, high energy inputs in the Al-low BMBF1 alloy forces a solidification texture of the β phase.

The process-related inhomogeneous Al content across the layers, although minimally pronounced, restricts the adjustment of a homogeneous microstructure, thus mechanical properties are anisotropic. Therefore, the inhomogeneous Al content was handled by adjusting a FL microstructure by heat treatments within the single α phase field region where a homogenization can take place. The established microstructure reveals excellent creep resistances up to 850 °C as well as an isotropic behavior in any building direction.

- Within the framework of the "NextTiAl" project (03XP0088C) [21], wherein the investigations were partly conducted, the BMBF3 alloy showed the best properties for further additively manufacturing of high-temperature γ -TiAl based alloys via EBM, i.e. better ductility and creep resistance than the TNM alloy. Therefore, this alloy was accepted as the so-called NextTiAl alloy with the nominal composition of Ti-47.5Al-5.5Nb-0.5 W (at.%). Within the project, Reith et al. [147] verified the good processability via EBM of cylindrical samples, thus confirming the NextTiAl alloy as process-adapted 4th generation TiAl alloy. Furthermore, the alloy was already manufactured into defect-free turbine blade blanks for the aerospace industry, see Fig 4.1 [148].



Figure 4.1: Novel process-adapted γ -TiAl based alloys, microstructurally and mechanically investigated in detail, produced by SPS and EBM, for the high-temperature application as turbine blades in aerospace propulsion systems. Blade blank image [148].

Although such components are still away from serial production, after post-processing of the pictured blade blanks in Fig 4.1, i.e. free from support structures, a heat treatment under pressure and removal of the surface roughness, EBM turbine blades may be introduced into the low-pressure turbines of the future.

List of publications

5.1 Publications included in this thesis

Publication A¹

Aspects of powder characterization for additive manufacturing

D. Wimler, S. Kardos, J. Lindemann, H. Clemens, S. Mayer, *Practical Metallography* 55 (2018) 620.

Publication B

Microstructural evolution and mechanical properties of an advanced γ -TiAl based alloy processed by spark plasma sintering

D. Wimler, J. Lindemann, H. Clemens, S. Mayer, *Materials* 12 (2019) 1523.

Publication C

Novel intermetallic-reinforced near- α Ti alloys manufactured by spark plasma sintering

D. Wimler, J. Lindemann, C. Gammer, P. Spoerk-Erdely, A. Stark, H. Clemens, S. Mayer, *Materials Science and Engineering: A* (2020) 139798.

Publication D

Designing advanced intermetallic titanium aluminide alloys for additive manufacturing

D. Wimler, J. Lindemann, M. Reith, A. Kirchner, M. Allen, W. Garcia Vargas, M. Franke, B. Klöden, T. Weißgärber, V. Güther, M. Schloffer, H. Clemens, S. Mayer, *Intermetallics* 131 (2021) 107109.

Publication E

How electron beam melting tailors the Al-sensitive microstructure and mechanical response of a novel process-adapted γ -TiAl based alloy

D. Wimler, K. Käsznar, M. Musi, C. Breuning, M. Markl, J. Keckes, H. Clemens, C. Körner, S. Mayer, submitted to SCI-journal, under review.

¹The capital letters refer to the respective sections A–F in the appendix

Publication F

Microstructure and mechanical properties of novel TiAl alloys tailored via phase and precipitate morphology

D. Wimler, J. Lindemann, T. Kremmer, H. Clemens, S. Mayer, submitted to SCI-journal, under review.

Remarks:

In the appended publications A-F, all experiments, the data analyses and the composition of the publications were performed by myself, D. Wimler, with the following exceptions:

- A** J. Lindemann evaluated the technological parameters and did the writing of the corresponding part. The analysis of the LOM images was performed by S. Kardos.
- B** The tensile tests were conducted and evaluated by J. Lindemann.
- C** The tensile tests were conducted and evaluated by J. Lindemann. The TEM experiments were performed by C. Gammer. Complementary, HEXRD measurements and the corresponding evaluation were done by A. Stark and P. Spoerk-Erdely, respectively.
- D** The production of the new TiAl alloy powders was carried out by M. Allen, V. Güther, and W. Garcia Vargas. The optimization of the EBM process parameters to additively manufacture a dense component was established by M. Reith, M. Franke, A. Kirchner, B. Klöden, and T. Weißgärber. The tensile tests were conducted and evaluated by J. Lindemann.
- E** The HEXRD experiments and their corresponding evaluation was done by J. Keckes and M. Musi, respectively. The numerical simulation and its analysis were performed by C. Breuning, M. Markl and C. Körner. The heat treatments and the determination of the corresponding phase fractions were conducted by K. Käsznar.
- F** The tensile tests were performed and evaluated by J. Lindemann. The TEM experiments were conducted by T. Kremmer.

5.2 Publications related to this thesis

An atomistic view on oxygen, antisites and vacancies in the γ -TiAl phase.

V. Razumovskiy, W. Ecker, D. Wimler, F.D. Fischer, F. Appel, S. Mayer, H. Clemens, submitted to SCI-journal, under review.

Metallography of intermetallic titanium aluminides – the (additive) manufacturing makes the difference.

S. Mayer, D. Schimbäck, R. Wartbichler, D. Wimler, H. Clemens, Practical Metallography 56 (2019) 567.

5.3 Conference contributions

Euro PM2019 - Maastricht *Oral presentation and proceedings*

High-resolution characterization of intermetallic TiAl-powder for additive manufacturing

D. Wimler, C. Gammer, J. Eckert, F. Mendez-Martin, J. Lindemann, H. Clemens, S. Mayer, Proceedings in: European Powder Metallurgy Association (Ed.), Euro PM 2019 International Conference and Exhibition: Maastricht, Shrewsbury UK, 2019.

Materials Science and Engineering 2018 - Darmstadt *Oral presentation*

Microstructural evolution and mechanical properties of TiAl-powder densified by spark plasma sintering

D. Wimler, J. Lindemann, H. Clemens, S. Mayer.

Most of the conferences were cancelled in 2020 because of the Covid-19 pandemic [149].

5.4 Supervised academic works

Thermomechanical processing and high-temperature behavior of the spark-plasma-sintered near- α Ti8242NbS alloy, David Obersteiner, Master thesis, Montanuniversität Leoben (scheduled 2021).

The influence of 2 at.% to 4 at.% Zirconium on phase equilibria in γ -based Ti-Al alloys, Stefan Kardos, Master thesis, Montanuniversität Leoben (2021).

Einfluss von EBM Parametern auf die γ -Solvustemperatur in einer experimentellen TNM-Legierung, Katharina Käschnar, Bachelor thesis, Montanuniversität Leoben (2019).

Teilchenkontrolliertes Kornwachstum in γ -TiAl Hochtemperaturlegierungen für die Additive Fertigung, Gloria Graf, Master thesis, Montanuniversität Leoben (2019).

Interaction between additive manufacturing process parameters and the microstructure of an advanced TiAl alloy, Fabian Lindlbauer, Bachelor thesis, Montanuniversität Leoben (2019).

Pulvercharakterisierung mittels Lichtmikroskopie für die additive Fertigung, Stefan Kardos, Bachelor thesis, Montanuniversität Leoben (2018).

References

For the available DOI and URL, the reader is referred to the online version as those are linked at the respective reference.

- [1] F. Appel, J. Paul, and M. Oehring, *Gamma titanium aluminide alloys: science and technology* (Wiley-VCH, Germany, 2012).
- [2] F. Appel, H. Clemens, and F. D. Fischer, *Progress in Materials Science* **81**, 55 (2016).
- [3] B. P. Bewlay, S. Nag, A. Suzuki, and M. J. Weimer, *Materials at High Temperatures* **33**, 549 (2016).
- [4] U. Habel, F. Heutling, C. Kunze, W. Smarsly, C. Das, and H. Clemens, in *13th World Conf on Titanium*, edited by V. Venkatesh, A. L. Pilchak, J. E. Allison, S. Ankern, R. Boyer, J. Christodoulou, H. L. Fraser, M. A. Imam, Y. Kosaka, H. J. Rack, A. Chatterjee, and A. Woodfield (2016).
- [5] M. Burtscher, T. Klein, J. Lindemann, O. Lehmann, H. Fellmann, V. Güther, H. Clemens, and S. Mayer, *Materials* **13** (2020).
- [6] S. Hurta, H. Clemens, G. Frommeyer, and H. P. Nicolai, in *Titanium 95*, Book - Institute of Materials, edited by P. A. Blenkinsop (Univ. Press, Cambridge, 1996) pp. 97–104.
- [7] T. Tetsui, *Advanced Engineering Materials* **3**, 307 (2001).
- [8] P. McQuay, in *Structural intermetallics 2001*, edited by K. J. Hemker (Minerals Metals & Materials Society, Warrendale, Pa., 2001) pp. 83–90.
- [9] W. Wallgram, T. Schmölzer, L. Cha, G. Das, V. Güther, and H. Clemens, *International Journal of Materials Research* **100**, 1021 (2009).
- [10] H. Clemens, W. Wallgram, S. Kremmer, V. Güther, A. Otto, and A. Bartels, *Advanced Engineering Materials* **10**, 707 (2008).

REFERENCES

- [11] M. Achtermann, W. Fürwitt, V. Güther, and H.-P. Nicolai, *Method for producing of gamma-TiAl base alloy*, EP2342365 (2011).
- [12] V. Güther, M. Allen, J. Klose, and H. Clemens, *Intermetallics* **103**, 12 (2018).
- [13] H. Clemens and S. Mayer, *Materials at High Temperatures* **33**, 560 (2016).
- [14] G. Baudana, S. Biamino, B. Klöden, A. Kirchner, T. Weißgärber, B. Kieback, M. Pavese, D. Ugues, P. Fino, and C. Badini, *Intermetallics* **73**, 43 (2016).
- [15] G. Baudana, S. Biamino, D. Ugues, M. Lombardi, P. Fino, M. Pavese, and C. Badini, *Metal Powder Report* **71**, 193 (2016).
- [16] T. DebRoy, H. L. Wei, J. S. Zuback, T. Mukherjee, J. W. Elmer, J. O. Milewski, A. M. Beese, A. Wilson-Heid, A. De, and W. Zhang, *Progress in Materials Science* **92**, 112 (2018).
- [17] J. Schwerdtfeger and C. Körner, *Intermetallics* **49**, 29 (2014).
- [18] M. Todai, T. Nakano, T. Liu, H. Y. Yasuda, K. Hagihara, K. Cho, M. Ueda, and M. Takeyama, *Additive Manufacturing* **13**, 61 (2017).
- [19] R. Wartbichler, H. Clemens, and S. Mayer, *Advanced Engineering Materials* (2019).
- [20] H. Yue, Y. Chen, X. Wang, S. Xiao, and F. Kong, *Journal of Alloys and Compounds* **766**, 450 (2018).
- [21] Bundesministerium für Bildung und Forschung, ed., *Deutschland druckt dreidimensional: Additive Fertigung revolutioniert die Produktion*, accessed 01.2021 (Berlin, 2020).
- [22] H. Clemens and S. Mayer, *Advanced Engineering Materials* **15**, 191 (2013).
- [23] J. C. Schuster and M. Palm, *Journal of Phase Equilibria and Diffusion* **27**, 255 (2006).
- [24] Y.-W. Kim and D. M. Dimiduk, *Journal of Materials* **43**, 40 (1991).
- [25] F. Appel, U. Lorenz, M. Oehring, U. Sparka, and R. Wagner, *Materials Science and Engineering: A* **233**, 1 (1997).
- [26] Z.-W. Ji, S. Lu, Q.-m. Hu, D. Kim, R. Yang, and L. Vitos, *Acta Materialia* **144**, 835 (2018).
- [27] U. Fröbel and F. Appel, *Acta Materialia* **50**, 3693 (2002).
- [28] H. Inui, M. H. Oh, A. Nakamura, and M. Yamaguchi, *Acta Metallurgica et Materialia* **40**, 3095 (1992).

-
- [29] M. A. Morris, *Intermetallics* **4**, 417 (1996).
- [30] M. Oehring, V. Küstner, F. Appel, and U. Lorenz, *Materials Science Forum* **539**, 1475 (2007).
- [31] D. R. Johnson, H. Inui, and M. Yamaguchi, *Acta Materialia* **44**, 2523 (1996).
- [32] J. Zollinger, J. Lapin, D. Daloz, and H. Combeau, *Intermetallics* **15**, 1343 (2007).
- [33] W. G. Burgers, *Physica* **1**, 561 (1934).
- [34] J. Kuang, R. Harding, and J. Campbell, *Materials Science and Engineering: A* **329**, 31 (2002).
- [35] J. Lapin and K. Kamyshnykova, *Intermetallics* **98**, 34 (2018).
- [36] R. Kainuma, Y. Fujita, H. Mitsui, I. Ohnuma, and K. Ishida, *Intermetallics* **8**, 855 (2000).
- [37] T. Schmoelzer, K.-D. Liss, P. Staron, S. Mayer, and H. Clemens, *Advanced Engineering Materials* **13**, 685 (2011).
- [38] R. Kainuma, I. Ohnuma, K. Ishikawa, and K. Ishida, *Intermetallics* **8**, 869 (2000).
- [39] M. Schloffer, F. Iqbal, H. Gabrisch, E. Schwaighofer, F.-P. Schimansky, S. Mayer, A. Stark, T. Lippmann, M. Göken, F. Pyczak, and H. Clemens, *Intermetallics* **22**, 231 (2012).
- [40] M. Kolb, J. M. Wheeler, H. N. Mathur, S. Neumeier, S. Korte-Kerzel, F. Pyczak, J. Michler, and M. Göken, *Materials Science and Engineering: A* **665**, 135 (2016).
- [41] T. Noda, M. Okabe, S. Isobe, and M. Sayashi, *Materials Science and Engineering: A* **192**, 774 (1995).
- [42] T. Klein, B. Rashkova, D. Holec, H. Clemens, and S. Mayer, *Acta Materialia* **110**, 236 (2016).
- [43] P. I. Gouma and M. Karadge, *Materials Letters* **57**, 3581 (2003).
- [44] A. Dlouhý and K. Kuchařová, *Intermetallics* **12**, 705 (2004).
- [45] F. Appel, J. D. H. Paul, M. Oehring, U. Fröbel, and U. Lorenz, *Metallurgical and Materials Transactions A* **34**, 2149 (2003).
- [46] H. Gabrisch, A. Stark, F.-P. Schimansky, L. Wang, N. Schell, U. Lorenz, and F. Pyczak, *Intermetallics* **33**, 44 (2013).

REFERENCES

- [47] C. Scheu, E. Stergar, M. Schober, L. Cha, H. Clemens, A. Bartels, F.-P. Schimansky, and A. Cerezo, *Acta Materialia* **57**, 1504 (2009).
- [48] R. M. Imayev, V. M. Imayev, M. Oehring, and F. Appel, *Intermetallics* **15**, 451 (2007).
- [49] A. Couret, D. Reyes, M. Thomas, N. Ratel-Ramond, C. Deshayes, and J.-P. Monchoux, *Acta Materialia* **199**, 169 (2020).
- [50] Y.-K. Kim, J. K. Hong, and K.-A. Lee, *Intermetallics* **121**, 106771 (2020).
- [51] J. Bresler, *Einfluss der Legierungselemente Niob, Tantal und Zirkonium auf das Hochtemperaturverhalten volllamellarer Titanaluminide*, Ph.D. thesis, FAU University Press (2020).
- [52] D. Holec, R. K. Reddy, T. Klein, and H. Clemens, *Journal of Applied Physics* **119**, 205104 (2016).
- [53] W. H. Tian and M. Nemoto, *Intermetallics* **5**, 237 (1997).
- [54] E. Schwaighofer, B. Rashkova, H. Clemens, A. Stark, and S. Mayer, *Intermetallics* **46**, 173 (2014).
- [55] J. Lapin, K. Kamyshnykova, T. Pelachová, and Š. Nagy, *Intermetallics* **128**, 107007 (2021).
- [56] F. Appel, M. Oehring, J. Paul, C. Klinkenberg, and T. Carneiro, *Intermetallics* **12**, 791 (2004).
- [57] H. F. Chladil, H. Clemens, G. A. Zickler, M. Takeyama, E. Kozeschnik, A. Bartels, T. Buslaps, R. Gerling, S. Kremmer, L. Yeoh, and K.-D. Liss, *International Journal of Materials Research* **98**, 1131 (2007).
- [58] J. W. Fergus, *Materials Science and Engineering: A* **338**, 108 (2002).
- [59] R. Pflumm, A. Donchev, S. Mayer, H. Clemens, and M. Schütze, *Intermetallics* **53**, 45 (2014).
- [60] S. L. Draper and D. Isheim, *Intermetallics* **22**, 77 (2012).
- [61] P. Dumitraschkewitz, H. Clemens, S. Mayer, and D. Holec, *Applied Sciences* **7**, 1193 (2017).
- [62] M. Kastenhuber, T. Klein, H. Clemens, and S. Mayer, *Intermetallics* **97**, 27 (2018).
- [63] J. A. Stendal, M. Eisentraut, M. Imran, I. Sizova, S. Bolz, S. Weiß, and M. Bambach, *Journal of Materials Processing Technology* **291**, 116999 (2021).

-
- [64] S.-K. Rittinghaus, J. Schmelzer, M. W. Rackel, S. Hemes, A. Vogelpoth, U. Hecht, and A. Weisheit, *Materials* **13** (2020).
- [65] J. Bieske, M. Franke, M. Schloffer, and C. Körner, *Intermetallics* **126**, 106929 (2020).
- [66] S. Mayer, D. Schimbäck, R. Wartbichler, D. Wimler, and H. Clemens, *Practical Metallography* **56**, 567 (2019).
- [67] S.-K. Rittinghaus, U. Hecht, V. Werner, and A. Weisheit, *Intermetallics* **95**, 94 (2018).
- [68] D. Bernal, X. Chamorro, I. Hurtado, and I. Madariaga, *Intermetallics* **124**, 106842 (2020).
- [69] E. Schwaighofer, H. Clemens, S. Mayer, J. Lindemann, J. Klose, W. Smarsly, and V. Güther, *Intermetallics* **44**, 128 (2014).
- [70] Y.-W. Kim, *Acta Metallurgica et Materialia* **40**, 1121 (1992).
- [71] Y.-W. Kim, *Intermetallics* **6**, 623 (1998).
- [72] Y.-W. Kim and S.-L. Kim, *Journal of Materials* **70**, 553 (2018).
- [73] K. Maruyama, R. Yamamoto, H. Nakakuki, and N. Fujitsuna, *Materials Science and Engineering: A* **239-240**, 419 (1997).
- [74] M. Beschliesser, A. Chatterjee, A. Lorich, W. Knabl, H. Kestler, G. Dehm, and H. Clemens, *Materials Science and Engineering: A* **329**, 124 (2002).
- [75] W. Li and K. Xia, *Materials Science and Engineering: A* **329-331**, 430 (2002).
- [76] I. Andersen and Ø. Grong, *Acta Metallurgica et Materialia* **43**, 2673 (1995).
- [77] S. Banerjee and P. Mukhopadhyay, *Phase transformations: Examples from titanium and zirconium alloys*, Pergamon materials series, Vol. 12 (Elsevier, Amsterdam and Oxford, 2007).
- [78] M. Takeyama, M. Nakamura, T. Kumagai, and M. Kikuchi, in *Proc First Int Symp Struct Intermet* (Minerals, Metals & Materials Soc (TMS), 1993) pp. 167–176.
- [79] S. Mitao and L. A. Bendersky, *Acta Materialia* **45**, 4475 (1997).
- [80] G. Lütjering and J. C. Williams, *Titanium* (Springer, Berlin Heidelberg, 2013).
- [81] W. Sha and S. Malinov, *Titanium alloys: Modelling of microstructure, properties and applications*, Woodhead Publishing in materials (Woodhead Pub, Cambridge, 2009).
- [82] Titanium Metals Corporation, *Timet - Datasheets* (accessed 01.2021).

REFERENCES

- [83] D. Eylon, S. Fujishiro, and F. H. Froes, *High Temperature Materials and Processes* **6**, 1685 (1984).
- [84] A. Popov, N. Rossina, and M. Popova, *Materials Science and Engineering: A* **564**, 284 (2013).
- [85] W. Jia, W. Zeng, and H. Yu, *Materials & Design* **58**, 108 (2014).
- [86] E. Hernández-Nava, P. Mahoney, C. J. Smith, J. Donoghue, I. Todd, and S. Tammas-Williams, *Scientific reports* **9**, 4070 (2019).
- [87] P. Barriobero-Vila, J. Gussone, A. Stark, N. Schell, J. Haubrich, and G. Requena, *Nature communications* **9**, 3426 (2018).
- [88] C. Leyens and M. Peters, *Titanium and titanium alloys: fundamentals and applications* (Wiley-VCH, Weinheim and Chichester, 2003).
- [89] G. Proske, G. Lütjering, J. Albrecht, D. Helm, and M. Daeubler, in *High Temperature Aluminides and Intermetallics*, edited by C. T. Liu, D. P. Pope, and S.-H. Whang (Elsevier, London, 1992) pp. 310–316.
- [90] J. Dawes, R. Bowerman, and R. Trepleton, *Johnson Matthey Technology Review* **59**, 243 (2015).
- [91] R. Gerling, H. Clemens, and F. P. Schimansky, *Advanced Engineering Materials* **6**, 23 (2004).
- [92] G. Chen, S. Y. Zhao, P. Tan, J. Wang, C. S. Xiang, and H. P. Tang, *Powder Technology* **333**, 38 (2018).
- [93] A. Lawley, *Journal of Materials* **33**, 13 (1981).
- [94] Werner Schatt, Klaus-Peter Wieters, Bernd Kieback, *Pulvermetallurgie: Technologien und Werkstoffe* (Springer, Germany, 2002).
- [95] A. Allimant, M. P. Planche, Y. Bailly, L. Dembinski, and C. Coddet, *Powder Technology* **190**, 79 (2009).
- [96] H. Ding, G. Nie, R. Chen, J. Guo, and H. Fu, *Materials & Design* **41**, 108 (2012).
- [97] R. Gaddam, B. Sefer, R. Pederson, and M.-L. Antti, *Materials Characterization* **99**, 166 (2015).
- [98] B. K. Kad and H. L. Fraser, *Philosophical Magazine Letters* **70**, 211 (1994).
- [99] A. M. Rausch, V. E. Küng, C. Pobel, M. Markl, and C. Körner, *Materials* **10** (2017).

-
- [100] A. M. Rausch, M. Markl, and C. Körner, *Computers & Mathematics with Applications* **78**, 2351 (2018).
- [101] A. B. Spierings, M. Voegtlin, T. Bauer, and K. Wegener, *Progress in Additive Manufacturing* **1**, 9 (2016).
- [102] M. Galati and L. Iuliano, *Additive Manufacturing* **19**, 1 (2018).
- [103] C. Körner, *International Materials Reviews* **61**, 361 (2016).
- [104] P. Cavaliere, *Spark plasma sintering of materials: advances in processing and applications* (Springer International Publishing, 2019).
- [105] A. Couret, T. Voisin, M. Thomas, and J.-P. Monchoux, *Journal of Materials* **69**, 2576 (2017).
- [106] T. Voisin, J.-P. Monchoux, L. Durand, N. Karnatak, M. Thomas, and A. Couret, *Advanced Engineering Materials* **17**, 1408 (2015).
- [107] N. F. Mogale and W. R. Matizanhuka, *Metals* **10**, 1080 (2020).
- [108] T. Voisin, L. Durand, N. Karnatak, S. Le Gallet, M. Thomas, Y. Le Berre, J.-F. Castagné, and A. Couret, *Journal of Materials Processing Technology* **213**, 269 (2013).
- [109] T. Voisin, J.-P. Monchoux, M. Perrut, and A. Couret, *Intermetallics* **71**, 88 (2016).
- [110] D. Wang, H. Yuan, and J. Qiang, *Metals* **7**, 201 (2017).
- [111] T. Voisin, J.-P. Monchoux, M. Hantcherli, S. Mayer, H. Clemens, and A. Couret, *Acta Materialia* **73**, 107 (2014).
- [112] C. Kenel, K. Dawson, J. Barras, C. Hauser, G. Dasargyri, T. Bauer, A. Colella, A. B. Spierings, G. J. Tatlock, C. Leinenbach, and K. Wegener, *Intermetallics* **90**, 63 (2017).
- [113] S. Decker, J. Lindemann, and L. Krüger, *Materials Science and Engineering: A* **674**, 361 (2016).
- [114] M. Ozerov, M. Klimova, A. Kolesnikov, N. Stepanov, and S. Zherebtsov, *Materials & Design* **112**, 17 (2016).
- [115] W. Lu, Di Zhang, X. Zhang, Y. Bian, R. Wu, T. Sakata, and H. Mori, *Journal of Materials Science* **36**, 3707 (2001).
- [116] X. Guo, L. Wang, M. Wang, J. Qin, Di Zhang, and W. Lu, *Acta Materialia* **60**, 2656 (2012).
- [117] H. T. Tsang, C. G. Chao, and C. Y. Ma, *Scripta Materialia* **37**, 1359 (1997).

REFERENCES

- [118] T. Saito, *Journal of Materials* **56**, 33 (2004).
- [119] X. Tao, Z. Yao, and S. Zhang, *Materials Letters* **225**, 13 (2018).
- [120] T. Wohlers, R. I. Campbell, and O. Diegel, *Wohlers report 2020: 3D printing and additive manufacturing state of the industry* (2020).
- [121] D. Herzog, V. Seyda, E. Wycisk, and C. Emmelmann, *Acta Materialia* **117**, 371 (2016).
- [122] Y. Zhang, J. Zhang, Q. Yan, L. Zhang, M. Wang, B. Song, and Y. Shi, *Scripta Materialia* **148**, 20 (2018).
- [123] Y. Zhang, X. Lin, X. Gao, X. Su, S. Guo, and W. Huang, *Journal of Alloys and Compounds* **819**, 153013 (2020).
- [124] E. Chauvet, C. Tassin, J.-J. Blandin, R. Dendievel, and G. Martin, *Scripta Materialia* **152**, 15 (2018).
- [125] R. R. Dehoff, M. M. Kirka, F. A. List, K. A. Unocic, and W. J. Sames, *Materials Science and Technology* **31**, 939 (2014).
- [126] M. M. Kirka, P. Nandwana, Y. Lee, and R. R. Dehoff, *Scripta Materialia* **135**, 130 (2017).
- [127] L. E. Murr, *Journal of Materials Research and Technology* **9**, 1087 (2020).
- [128] C. Emmelmann, P. Sander, J. Kranz, and E. Wycisk, *Physics Procedia* **12**, 364 (2011).
- [129] R. Huang, M. Riddle, D. Graziano, J. Warren, S. Das, S. Nimbalkar, J. Cresko, and E. Masanet, *Journal of Cleaner Production* **135**, 1559 (2016).
- [130] A. Timmis, A. Hodzic, L. Koh, M. Bonner, C. Soutis, A. W. Schäfer, and L. Dray, *The International Journal of Life Cycle Assessment* **20**, 233 (2015).
- [131] A. Gisario, M. Kazarian, F. Martina, and M. Mehrpouya, *Journal of Manufacturing Systems* **53**, 124 (2019).
- [132] L. Yang, K. Hsu, B. Baughman, D. Godfrey, F. Medina, M. Menon, and S. Wiener, *Additive manufacturing of metals: The technology, materials, design and production*, Springer Series in Advanced Manufacturing (Springer International Publishing, Cham and s.l., 2017).
- [133] M. Markl and C. Körner, *Annual Review of Materials Research* **46**, 93 (2016).

-
- [134] D. Schimbäck, J. Braun, G. Leichtfried, H. Clemens, and S. Mayer, *Materials & Design* **201**, 109506 (2021).
- [135] V. Juechter, M. M. Franke, T. Merenda, A. Stich, C. Körner, and R. F. Singer, *Additive Manufacturing* **22**, 118 (2018).
- [136] L. E. Murr, S. M. Gaytan, A. Ceylan, E. Martinez, J. L. Martinez, D. H. Hernandez, B. I. Machado, D. A. Ramirez, F. Medina, and S. Collins, *Acta Materialia* **58**, 1887 (2010).
- [137] D. Cormier, O. Harrysson, T. Mahale, and H. West, *Research Letters in Materials Science* **2007** (2008).
- [138] S. Biamino, A. Penna, U. Ackelid, S. Sabbadini, O. Tassa, P. Fino, M. Pavese, P. Gennaro, and C. Badini, *Intermetallics* **19**, 776 (2011).
- [139] S. S. Al-Bermani, M. L. Blackmore, W. Zhang, and I. Todd, *Metallurgical and Materials Transactions A* **41**, 3422 (2010).
- [140] P. Erdely, P. Staron, E. Maawad, N. Schell, H. Clemens, and S. Mayer, *Acta Materialia* **158**, 193 (2018).
- [141] S. Vock, B. Klöden, A. Kirchner, T. Weißgärber, and B. Kieback, *Progress in Additive Manufacturing* **67**, 544 (2019).
- [142] K. Cho, R. Kobayashi, J. Y. Oh, H. Y. Yasuda, M. Todai, T. Nakano, A. Ikeda, M. Ueda, and M. Takeyama, *Intermetallics* **95**, 1 (2018).
- [143] G. Wegmann, R. Gerling, and F.-P. Schimansky, *Acta Materialia* **51**, 741 (2003).
- [144] S. Tammam-Williams, P. J. Withers, I. Todd, and P. B. Prangnell, *Scripta Materialia* **122**, 72 (2016).
- [145] H. Yasuda, K. Cho, M. Todai, M. Ueda, D. Kondo, S. Morkoshi, A. Ikeda, M. Takeyama, and T. Nakano, *Journal of Smart Processing* **8**, 78 (2019).
- [146] M. Schloffer, *Gefüge und Eigenschaften der intermetallischen TNM-Legierung*, Dissertation, Montanuniversität Leoben, Leoben (Juli 2013).
- [147] M. Reith, M. Franke, M. Schloffer, and C. Körner, *Materialia* **14**, 100902 (2020).
- [148] B. Klöden and A. Kirchner, “Blade blanks manufactured with “EBM only” from TiAl alloy,” (30.1.2020).

REFERENCES

- [149] J. Burns, A. Movsisyan, J. M. Stratil, M. Coenen, K. M. Emmert-Fees, K. Geffert, S. Hoffmann, O. Horstick, M. Laxy, L. M. Pfadenhauer, P. von Philipsborn, K. Sell, S. Voss, and E. Rehfues, The Cochrane database of systematic reviews **10**, CD013717 (2020).

Aspects of powder characterization for additive manufacturing

D. Wimler^{a*}, S. Kardos^a, J. Lindemann^b, H. Clemens^a, S. Mayer^a

^a Department of Materials Science, Montanuniversität Leoben, 8700 Leoben, Austria

^b GfE Fremat GmbH, 09618 Brand-Erbisdorf, Germany

* Corresponding author

<https://doi.org/10.3139/147.110547>

Practical Metallography (2018) 55, 620

open access: CC BY 4.0



Keywords:

Powder; chemical analysis; technological parameters; fractionation; morphology

Abstract

“Top-quality powder is a precondition for additive manufacturing of quality components.” This paper covers the powder characterization of high-melting and highly reactive intermetallic γ -TiAl powders by combining technological and metallographic examinations. Measurements of tap density, bulk density, flow behaviour, particle size distribution and sphericity of the powder will reveal characteristic parameters which have an effect on process stability. The subsequent analysis of the powder microstructure will show possible gas inclusions or defects which may negatively affect the mechanical properties of the manufactured component. Each of these factors presents a quality criterion, which is also applicable – irrespective of the alloy system – to other materials systems.

A.1 Introduction

Over the past few decades, mainly melting metallurgical processes have been developed for the production of high-quality primary material for intermetallic titanium aluminides (TiAl) and titanium alloys. This primary material is then processed into components by means of investment casting and hot working, respectively. To this day, however, powder-metallurgical (PM) manufacturing processes have been limited to few niche applications. The introduction of powder-based manufacturing methods, e.g. additive manufacturing (AM), combined with the availability of high-quality metal and alloy powders pave the way for completely new approaches to materials processing and component design. Decisive advantages are that neither set-up times nor tool manufacturing are required and that alloying elements which have previously complicated production through the casting or forging route may now be used purposefully. Additive manufacturing thus pushes a paradigm shift with regard to materials and design and to new approaches to the manufacture of semi-finished products and components as well as their properties and design. In addition to the manufacture of complex components in large numbers which, in many cases, requires no mechanical post-processing, a biologically inspired approach to component design may be implemented, allowing the designer of the future to consider entirely new and thus unconventional design options. Furthermore, lattice structures may be achieved inside the component, which allow aspects of lightweight design to be realized efficiently and sustainably [1, 2]. It is precisely this multitude of new opportunities that has contributed to the “scientific and technological hype” surrounding AM technology. However, in the field of (inter)metallic materials – one example is the chemically reactive TiAl which is brittle at room temperature – Selective Laser Melting (SLM) as well as Electron Beam Melting (EBM) have become established [3]. One important criterion is the quality of the powder that is used as it has a direct effect on the production process with regard to process stability and the properties of the component [4]. Comprehensive characterization of the powder may be used to prevent issues of this kind, which is one of the incentives for writing this paper.

In the case of TiAl and Ti alloys, respectively, powder production involves the atomization of the molten material, which, technologically, is a very demanding process not only because of the high melting point but also because the process has to be “ceramicfree“, i.e. it has to take place under inert gas or in a vacuum. The reason for this is that the molten material is highly reactive and thus would react with almost any kind of crucible material. During the PIGA (Plasma Melting Induction Guiding Gas Atomization) process, a part of the molten material to be atomized is solidified on the wall of a water-cooled copper mould, so that the homogenous and still liquid molten material is protected against contamination with impurity atoms [5]. EIGA (Electrode Induction Melting Gas Atomization) completely abandons the use of a crucible. In this case, a bar-shaped ingot is smelted by slowly rotating it in an induction coil. The melting process focuses exclusively on the tip of the ingot and

the amount of molten material is kept at a low level, presenting safety-related benefits. It is not possible, however, to achieve a homogenization of the molten material; therefore, this process requires segregation-free ingots in order to obtain a chemically homogenous powder [1, 2, 5]. The powder characterized for this paper was produced by means of EIGA.

Due to the high affinity of TiAl alloys for the interstitial impurities oxygen, nitrogen and carbon, atomization of the molten material takes place under inert gas (argon), otherwise embrittling effects may occur [5]. It is possible, for example, to produce TiAl powders with oxygen contents of some 100 m.ppm [1, 5] but storage, handling and powder recycling may lead to local oxygen enrichment [6, 7]. Furthermore, atomization using inert gas yields a high powder sphericity [1, 2] which has a positive effect on the preparation of the powder bed in the AM production facility, where good flowability is required in order to apply uniform layers of powder [1, 4]. It should be noted, however, that gas inclusions may occur in the case of bigger powder particles and that the atomizing gas argon has no solubility in TiAl [5, 8]. These hollow spheres affect the density of the powder particles and subsequently the density and the mechanical properties of the additively manufactured component [8]. Porosity can almost be completely eliminated by Hot Isostatic Pressing (HIP). Subsequent heat treatments or mechanical loads at high temperatures, however, may cause these pores to reappear again, a process known as Thermally Induced Porosity (TIP) [9, 10]. Furthermore, atomization using inert gas achieves cooling rates of 10^4 up to 10^6 K/s during the solidification of the particles [1, 5, 11], causing TiAl alloys with Al contents <48 at.% to solidify dendritically to form a body-centred cubic (bcc) β phase, which has a low solubility for Al. Despite the high cooling rates, light elements such as Al may segregate. Those segregations can be effectively eliminated by subsequent HIP, however [12].

“The quality of the powder provides the basis for the manufacture of high-quality components”. From this point of view, this paper combines individual steps in the characterization of inert gas atomized TiAl powder by defining quality criteria with the aim of deducing resulting influences on the production of and the AM component itself.

A.2 Chemical analysis

The chemical composition of the powder plays a crucial role with regard to the phase distribution in the AM component. For this paper, powder of the β -solidifying TNM alloy with a nominal composition of Ti-43.5Al-4Nb-1Mo-0.1B (in at.%) was examined [13]. The quantitative elemental analysis for Ti, Al, Nb and Mo [11] was carried out using X-ray fluorescence spectroscopy (XRF). Atomic Emission Spectroscopy (AES) using Inductively Coupled Plasma (ICP) was used in order to detect non-metal elements such as B, Si and C which are added in small amounts to TNM-based alloy variants [14, 15]. Interstitially dissolved elements (H, O, N) were determined by means of Carrier Gas Hot Extraction

[14, 15]. However, the oxygen content in the powder does not remain constant due to storage, handling and powder recycling; for this reason, accompanying measurements are carried out during the process [6, 7].

A.3 Technological parameters

In order to guarantee process reliability, technological test methods in the field of PM have become established. Those tests are standardized in most cases as they are dependent on factors such as test arrangement and moisture levels. Direct results of these tests provide technological parameters which are comparable among each other for different materials systems [1].

A.3.1 Bulk density and tap density

In order to determine the bulk density of metal powders the mass of an amount of powder which – “as poured” – completely fills a cup with a specified volume is measured (DIN EN ISO 3923). Pouring the powder into the measuring vessel is achieved by directing it through a funnel with a defined orifice. Very fine powders are directed through an oscillating funnel or through a funnel with an additional baffle box containing inclined glass plates (Scott-Volumeter). The bulk density is determined by the particle shape and particle size distribution of a powder. Thus, spherical powders have – due to their increased mobility – a higher packing density than unevenly shaped particles. With regard to particle size, it applies that due to their increased surface and therefore higher friction values, fine powders show lower bulk densities than coarse powders.

The space required by a poured powder may be reduced by tapping or vibrations. In order to determine the tap density of a powder a specified amount of powder is densified by means of a tapping apparatus until no further decrease in the volume takes place (DIN EN ISO 3953). The difference between bulk density and tap density depends on the friction conditions within the powder (particle shape and particle surface texture). So, particles with a relatively high bulk density (spherical, coarser particles) usually show a smaller increase in density by tapping than powders with a low bulk density. Typical values for the bulk and tap density of spherical TiAl powders in additive manufacturing using EBM (particle fraction 45–120 μm) are a bulk density of 2.3 g/cm^3 – corresponding to about 55 % of the density of the compact material – and a tap density of 2.6 g/cm^3 [1, 16].

A.3.2 Flow behaviour

The workability of a powder is determined by the homogeneity and density of the powder bed applied in layers and thus by the flow behavior of the powder. It does not only depend

on the powder but to a great extent on the type of powder application. In addition, moisture also has an effect on flowability. The so-called Hausner ratio and the Carr index are reliable indicators when it comes to the evaluation of powder flowability. Both numbers may be calculated from bulk density and tap density, respectively [16, 17]. For TiAl EBM powders, the Hausner ratio is calculated to be 1.13 and the Carr index is 10. Both values indicate good flow behavior of the powder (Hausner ratio ≤ 1.25 and Carr index < 15). A standardized test method for the determination of the flowability of metal powders is the determination of the flow rate by means of a calibrated funnel (DIN EN ISO 4490). This method measures the time which is required for 50 g of metal powder to flow through the test orifice (diameter of 2.5 mm) of a Hall flowmeter. For the TiAl EBM powder, this time was measured to be about 33 s (residual moisture of 0.15 %). At double the residual moisture, the flow time increases to as much as 43 s. A more recent test method which is supposed to be more suitable for the determination of the flow behavior of powders is powder characterization by means of a so-called Revolution Powder Analyzer. It measures the flow behavior of a powder while rotating in a drum. Overall, current test methods only allow an estimation of the flowability of powders. Due to the complex correlations, a conclusive evaluation of the workability may only be carried out after testing the powders in AM machines [1, 16].

A.4 Fractionation

In most cases, fractionation of an atomized powder is required in order to use a specific fraction for the AM process [4, 18] or to determine the effect of powder size on the microstructure [5, 12]. Fractionation relies on different techniques which make use of the relevant physical properties of the powders. A classification according to density and shape is employed in air separation for example [1]. Standardized sieves are used to classify powders according to powder diameter (DIN EN ISO 3310-1) [1]. By means of sieve analysis the TNM alloy was separated into four fractions: $< 20 \mu\text{m}$, $20\text{--}45 \mu\text{m}$, $45\text{--}100 \mu\text{m}$ and $> 100 \mu\text{m}$. The mass fractions of the size fractions were determined and added up to a distribution total (Q_3) (see black graph in Fig. A.1). The type and parameters of atomization affect the position and shape of the distribution, which defines the output of individual fractions [1]. Table A.1 also includes the output of the four fractions given in m.%, as determined from Fig. A.1. The results of the sieve analysis for the fractions $< 20 \mu\text{m}$, $20\text{--}45 \mu\text{m}$ and $45\text{--}100 \mu\text{m}$ are also shown in Fig. A.1. From the distribution total, one can determine the d_{50} diameter which indicates when 50 m.% of the powder is larger and 50 m.% of the powder is smaller than a particle with the diameter d_{50} . The d_{50} values are also shown in Table A.1 and serve as characteristic values for the powder distribution. The graphs plotted in Fig. A.1 overlap slightly, despite fractionation. The reason for this is that not all powder particles are perfectly spherical, a fact that will be discussed in more detail in chapter A.5.1.3. In

addition, sieving quantity and time have a strong impact on the accuracy of fractionation and analysis.

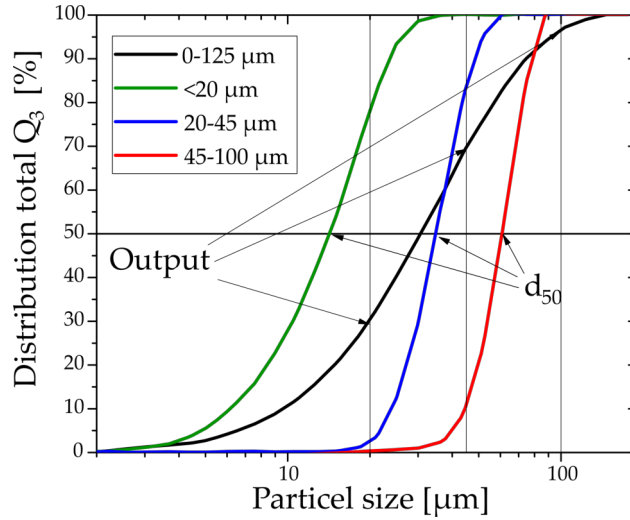


Figure A.1: Distribution total of the mass fractions as a function of their particle size for TiAl TNM powders, determined by sieve analysis (see text).

Table A.1: Results of sieve and image analyses for TiAl powder of the intermetallic TiAl TNM alloy (see text).

Particle size μm	Sieve analysis		Image analysis			
	Output m.%	d_{50} μm	$d_{F,max}$ μm	$d_{F,med}$ μm	H %	F -
<20	30	14	21	4	<0.1	0.90 ± 0.10
20-45	40	35	35	16	0.5	0.89 ± 0.10
45-100	25	61	95	50	4.0	0.83 ± 0.11
>100	5	-	169	82	5.7	0.82 ± 0.13

A.5 Morphology and microstructure

For the examination of the powder's morphology and microstructure, metallographic microsections were prepared. For this purpose, sieved hot mounting resin Polyfast by Struers ($<10 \mu\text{m}$) was mixed with a powder fraction. The ratio to be achieved has to be higher than 3 to 1 in order to avoid powder breaking out during the grinding process. A small amount of the TNM powder/Polyfast mixture is placed in a hot mounting press and the remaining quantity is topped up with commercially available Polyfast. Then, the mounted sample was grinded and polished using 1200, 2000 and 4000 grit SiC grinding paper as well as DP suspension M ($3 \mu\text{m}$) and OP-S ($0.04 \mu\text{m}$). After that, the sample was cleaned in an ultrasonic cleaner

using isopropyl alcohol as a solvent in order to remove traces of contamination prior to Light Optical Microscopy (LOM) and Scanning Electron Microscopy (SEM).

A.5.1 Light optical microscopy

LOM images were obtained using the Axio Imager M1 m by Zeiss. Figure A.2 shows such an image of the powder fraction $>100\ \mu\text{m}$. The generated image was then transferred to the image analysis software Stream Motion 1.9.3 by Olympus which is able to detect powder particles on the basis of their grey levels. The Feret diameter, circumference, (pore) area and form factor of the detected particles were determined by means of image analysis (see following subchapters for more details). For each powder fraction, at least 1500 powder particles were analyzed.

Feret diameter

Sieve analysis relies on the smallest powder diameter (d_{min}) as long as the powder particle has a convex shape. If a neck with an outer, concave radius forms between two particles as shown in Fig. A.3a, d_{min} will no longer be determinable by means of sieving. Alternatively, the diameter may be determined using image analysis software. For this purpose, the Feret diameter (d_F) of a 2D section of a powder particle is measured; the Feret diameter is defined as the distance between two parallel tangential lines (Fig. A.3a). Table A.1 compares the results of image analysis, showing the smallest ($d_{F,min}$), greatest ($d_{F,max}$) and mean ($d_{F,med}$) Feret diameter. The $d_{F,max}$ values approximately correspond to the greater particle sizes; however, $d_{F,med}$, and d_{50} are not comparable to one other as $d_{F,med}$ is the median for the number distribution (Q_0) and d_{50} is the median for the mass distribution Q_3 , explaining the

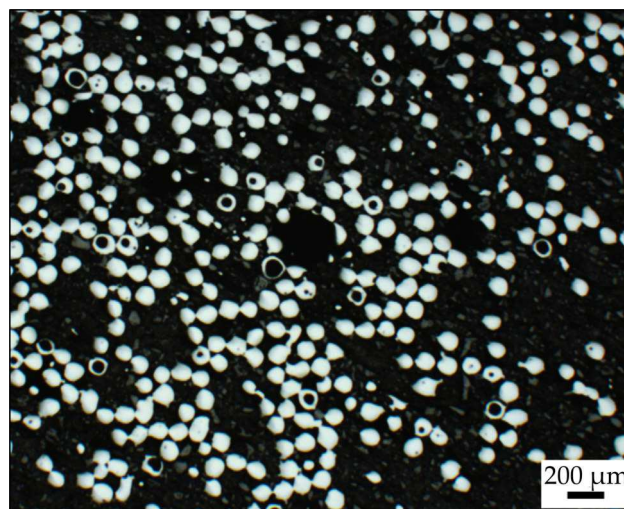


Figure A.2: LOM image of a cross section of the powder fraction $>100\ \mu\text{m}$ of a TiAl TNM powder. Hollow spheres appear as a ring.

comparatively smaller $d_{F,med}$ as described in Reference [19]. Furthermore, image analysis relies on a 2D section of a powder particle so that the size of the actual 3D particle is generally underestimated.

Circumference and area of the powder particle

Figure A.3a is a schematic depiction of a partially ground hollow powder particle. The area (A) corresponds to the reflecting area of a particle under the light microscope and U is its circumference. If a detected particle exhibits a pore as shown in Fig. A.3a, the pore area (A_P) will not be included in A . The sum of A and A_P is the total area (A_{Ges}). Figure A.4 shows A_P against A_{Ges} for the examined TNM powder. The straight line with a slope of 0.5 indicates that there are no particles with a pore area of 50%. This might be caused by the low strength levels of hollow particles so that those “fragile” particles are destroyed during atomization or sample preparation. According to the number of porous particles (N_P) and the total number of detected particles (N_{Ges}), the hollow sphere fraction (H) is calculated as follows:

$$H = \frac{N_P}{N_{Ges}} \cdot 100 \%. \quad (\text{A.1})$$

The results are summarized in Table A.1, showing that the number of hollow spheres rises in tandem with an increase in the size of the powder fraction. Gerling et al. [20] presented lower porosity results in his paper but also a similar trend which has already been observed multiple times in the literature on TiAl powders [1, 5, 20, 21]. Absolute numbers, however, vary greatly with regard to atomization and process parameters [1].

Increasing gas porosity limits the use of large powder fractions in AM as not all Ar gas pores can rise through the molten material to the surface of the melt pool during the short melting process. The solidified microstructure thus shows spherical pores which impair static and

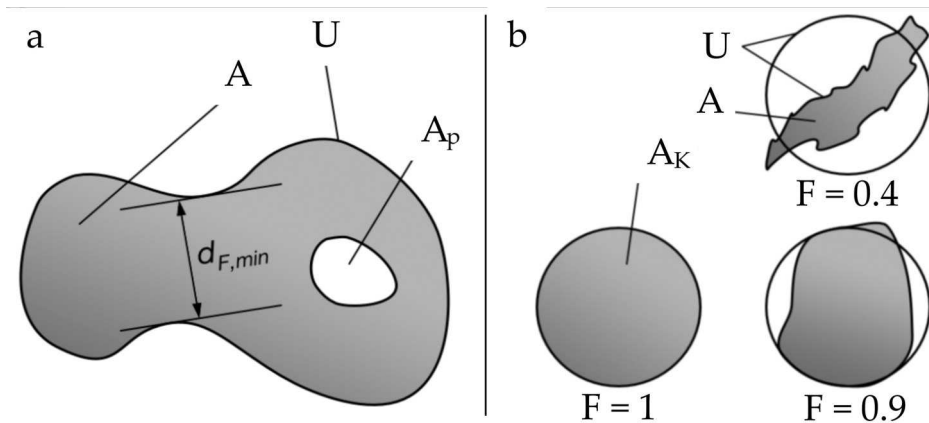


Figure A.3: a) Schematic depiction of a hollow powder particle; b) comparison of three individual powder particles with an identical circumference U , identical area of a circle with an identical circumference A_K with the diameter D , but a different form factor F and area A .

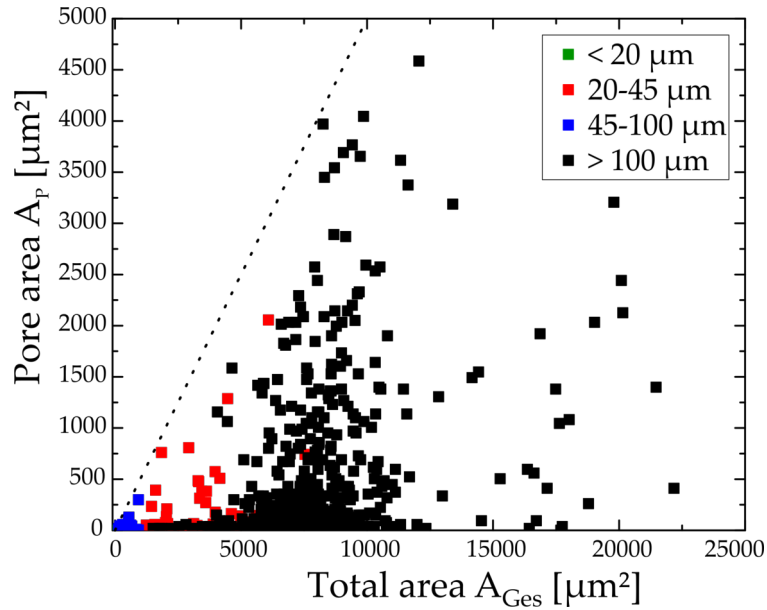


Figure A.4: Graph showing the pore area A_P of all identified particles from four fractions against the total area A_{Ges} , including a straight line with a slope of 0.5.

dynamic properties [8]. Subsequent HIP treatment reduces porosity. During a subsequent pressureless heat treatment, however, gas pores may reach a critical size again due to the gas pressure existing inside the pore [9, 10]. Those issues occur especially in components manufactured using EBM, where a powder fraction of 50 – 150 μm is used [4, 18]. The SLM process uses powder sizes of less than 50 μm [22], thus alleviating this problem. Even though processes such as Spark Plasma Sintering (SPS) use powder sizes of up to 200 μm , a porosity of less than <1% is achieved by means of mechanical compacting during sintering [23, 24].

Form factor

For the purpose of reliable process control, SLM and EBM require spherical particles in order to guarantee high flow rates and bulk densities. The sphericity of a particle may be described by the form factor (F) which is determined by means of image analysis of a 2D powder particle polish. The form factor is defined as the ratio of A_{Ges} to the area of a circle with an identical circumference (A_K) with the diameter D , which is referred to as equivalent diameter [1]. A perfectly spherical particle thus has the form factor $F = 1$, see Fig. A.3b. The less spherical the powder, the smaller this value will become. The mean and standard deviation of the four fractions are given in Table A.1 as well. The results show that the form factor decreases as the size of the fraction increases. A decreasing form factor entails a drop in the technological parameters which are relevant for the stability of the AM process [16].

A.5.2 Scanning electron microscopy

By means of the SEM, the surface as well as the microstructure of the powder may be examined, see Fig. A.5. The powder particles are either glued onto an electrically conductive specimen stub using silver paint or they are vapor-plated with gold. On the one hand, these procedures keep the powder particles in place and on the other hand achieve conductivity between the particles, thus preventing any charging effects. In this case, silver paint by Plano, Germany, was used.

In Fig. A.5a, several TNM powder particles of the fraction 45 – 100 μm are visible. This shows that not all particles have an ideally spherical shape. At higher magnification of the powder surface, see Fig. A.5b, satellites negatively affecting the AM process are visible. Those satellites do not only impair the technological properties but may also detach, thus increasing the fine content. Furthermore, the powder surface exhibits a dendritic structure which continues towards the center of the particle, see Fig. A.5c. During dendritic solidification, light elements in the powder may segregate. The segregation of Al is clearly recognizable by SEM contrast. The light dendritic areas indicate the starting point for solidification of the disordered bcc β phase which has a low solubility for Al. Therefore, the Al content during solidification is high in front of the solidification front. In the solidified powder, the interdendritic area is thus enriched with Al and appears dark under the SEM in BSE contrast mode [12, 25]. The variable Al contents within the powder do not affect the AM process due to the high mobility of light Al atoms.

In addition to that, contamination caused by impurity atoms may be detected during SEM analysis and Energy-Dispersive X-ray Spectroscopy. This kind of contamination, however, rarely occurs during the EIGA process and therefore could not be detected during these analyses.

A.6 Summary

For this paper, a comprehensive examination of an intermetallic TiAl powder from the TNM alloy family was carried out. Established technological test methods were used for this purpose, e.g. methods to determine the flow behavior, tap and bulk density, which are responsible for stable AM processes. In addition, the sphericity, gas inclusions and diameter of the particles could be determined by means of image analysis carried out on metallographic powder polishes and based on different powder fractions. Furthermore, it was shown that an increase in powder size causes a drop in sphericity and an increase in gas inclusions. Finally, SEM images showed segregations in the powder's microstructure. However, there were no traces of contamination caused by impurity atoms. Even though additive manufacturing is a promising manufacturing process of the 21st century, metallographic techniques will contribute sustainably to the introduction of this novel process technology, built upon the

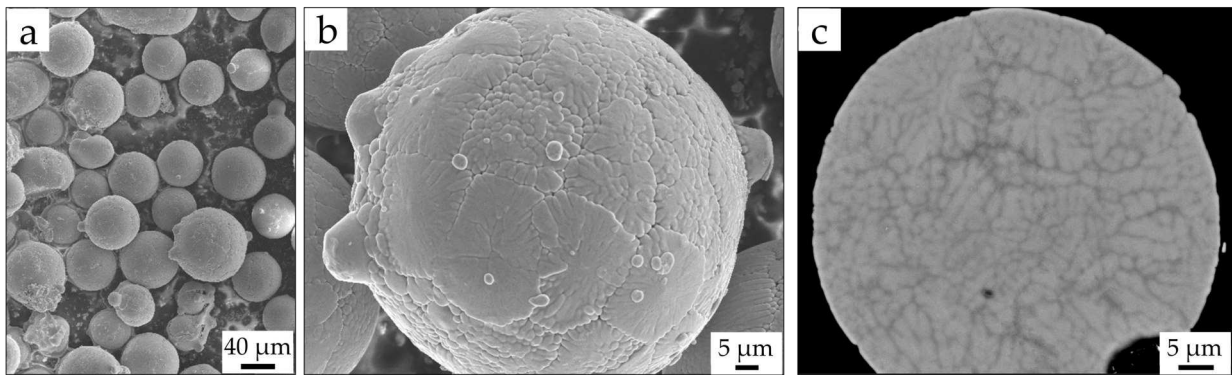


Figure A.5: SEM images of the TiAl TNM powder of the fraction 45–100 μm showing a) multiple powder particles; b) magnification of the powder surface together with dendritic structures and adhering satellites, which developed due to collisions during atomization; c) transverse section of a powder particle with dendritic structures, with dark areas indicating a high Al content and light areas indicating a low Al content. Images a) and b) were obtained using secondary electrons, whereas image c) utilized backscattered electron contrast.

quality of the starting powder, and to quality control efforts accompanying the individual process steps.

Acknowledgments

This work was carried out within the scope of the ProMat 3D project NextTiAl 03XP0088C of the Federal Ministry of Education and Research (BMBF) of the Federal Republic of Germany.

A.7 References

- [1] Schatt, W.; Wieters, K.-P.; Kieback, B.: *Pulvermetallurgie: Technologien und Werkstoffe*, 2. Auflage, Springer, Berlin, Deutschland, 2002
- [2] Gessinger, G. H.: *Powder Metallurgy of Superalloys*, Butterworths, Michigan, United States, 1984
- [3] Clemens, H.; Mayer, S.: *BHM* 160 (2015), 10–11, 513–516
- [4] Schwerdtfeger, J.; Körner, C.: *Intermetallics* 49 (2014), 29–35, DOI: 10.1016/j.intermet.2014.01.004
- [5] Gerling, R.; Clemens, H.; Schimansky, F. P.: *Adv. Eng. Mater.* 6 (2004), Nr. 12, 23–38
- [6] Wei, C.; Ma, X.; Yang, X.; Zhou, M.; Wang, C.; Zheng, Y.; Zhang, W.; Li, Z.: *Mater. Lett.* 221 (2018), 111–114, DOI: 10.1016/j.matlet.2018.03.124
- [7] Tang, H. P.; Qian, M.; Liu, N.; Zhang, X. Z.; Yang, G. Y.; Wang, J.: *JOM* 67 (2015), Nr. 3, 555–563
- [8] Cho, K.; Kobayashi, R.; Oh, J. Y.; Yasuda, H. Y.; Todai, M.; Nakano, T.; Ikeda, A.; Ueda, M.; Takeyama, M.: *Intermetallics* 95 (2018), 1–10, DOI: 10.1016/j.intermet.2018.01.009
- [9] Wegmann, G.; Gerling, R.; Schimansky, F.-P.: *Acta Mater.* 51 (2003), Nr. 3, 741–752
- [10] Tamas-Williams, S.; Withers, P. J.; Todd, I.; Prangnell, P. B.: *Scripta Mater.* 122 (2016), 72–76, DOI: 10.1016/j.scriptamat.2016.05.002
- [11] Appel, F.; Paul, J. D. H.; Oehring, M.: *Gamma titaniumaluminide alloys*, Wiley-VCH, Weinheim,

Deutschland, 2009

- [12] Kasthuber, M.; Klein, T.; Rashkova, B.; Weißensteiner, I.; Clemens, H.; Mayer, S.: *Intermetallics* 91 (2017), 100–109, DOI: 10.1016/j.intermet.2017.08.017
- [13] Clemens, H.; Mayer, S.: *MSF* 879 (2016), 113–118, DOI: 10.4028/www.scientific.net/MSF.879.113
- [14] Kasthuber, M.; Klein, T.; Clemens, H.; Mayer, S.: *Intermetallics* 97 (2018), 27–33, DOI: 10.1016/j.intermet.2018.03.011
- [15] Klein, T.; Rashkova, B.; Holec, D.; Clemens, H.; Mayer, S.: *Acta Mater.* 110 (2016), 236–245, DOI: 10.1016/j.actamat.2016.03.050
- [16] Spierings, A. B.; Voegtlin, M.; Bauer, T.; Wegener, K.: *Prog. Addit. Manuf.* 1 (2016), 1–2, 9–20
- [17] Emery, E.; Oliver, J.; Pugsley, T.; Sharma, J.; Zhou, J.: *Powder Technol.* 189 (2009), Nr. 3, 409–415
- [18] Klassen, A.; Forster, V. E.; Juechter, V.; Körner, C.: *J. Mater. Process. Technol.* 247 (2017), 280–288, DOI: 10.1016/j.jmatprotec.2017.04.016
- [19] Schubert, H.: *Handbuch der Mechanischen Verfahrenstechnik*, Wiley-VCH, Weinheim, Deutschland, 2012
- [20] Gerling, R.; Leitgeb, R.; Schimansky, F.-P.: *Mater. Sci. Eng., A* 252 (1998), Nr. 2, 239–247
- [21] Chen, G.; Zhao, Y.; Tan, P.; Wang, J.; Xiang, C. S.; Tang, H. P.: *Powder Technol.* 333 (2018), 38–46, DOI: 10.1016/j.powtec.2018.04.013
- [22] Rafi, H. K.; Starr, T. L.; Stucker, B. E.: *Int. J. Adv. Manuf. Technol.* 69 (2013), 5–8, 1299–1309, DOI: 10.1007/s00170-013-5106-7
- [23] Couret, A.; Voisin, T.; Thomas, M.; Monchoux, J.-P.: *JOM* 69 (2017), Nr. 12, 2576–2582
- [24] Decker, S.; Lindemann, J.; Krüger, L.: *Mater. Sci. Eng., A* 674 (2016), 361–365, DOI: 10.1016/j.msea.2016.08.011
- [25] Yang, D.-Y.; Guo, S.; Peng, H.-X.; Cao, F.-Y.; Liu, N.; Sun, J.-F.: *Intermetallics* 61 (2015), 72–79, DOI: 10.1016/j.intermet.2015.02.017

Microstructural evolution and mechanical properties of an advanced γ -TiAl based alloy processed by spark plasma sintering

D. Wimler^{a*}, J. Lindemann^b, H. Clemens^a, S. Mayer^a

^a Department of Materials Science, Montanuniversität Leoben, 8700 Leoben, Austria

^b GfE Fremat GmbH, 09618 Brand-Erbisdorf, Germany

* Corresponding author

<https://doi.org/10.3390/ma12091523>

Materials 12 (2019) 1523

open access: CC BY 4.0



Keywords:

Spark plasma sintering; γ -TiAl based alloys; TNM alloy; heat treatment; mechanical properties

Abstract

Intermetallic γ -TiAl based alloys are innovative lightweight structural high-temperature materials used in aerospace and automotive applications due to already established industrial-scale processing routes, like casting and hot-working, i.e., forging. A promising alternative method of production, regarding manufacturing of near net-shape components, goes over the powder metallurgy route, more precisely by densification of TiAl powder via spark plasma sintering. In this study, gas atomized powder from the 4th generation TNM alloy, Ti-43.5Al-4Nb-1Mo-0.1B (in at.%), was densified and the microstructure was investigated by means of electron microscopy and X-ray diffraction. The sintered microstructure exhibits lamellar α_2 -Ti₃Al / γ -TiAl colonies surrounded by globular γ - and ordered β_o -TiAl phase. The coarse lamellar spacing stems from the low cooling rate after densification at sintering temperature. Against this background, subsequent heat treatments were designed to decrease the lamellar widths by a factor of ten. Accompanying, tensile tests and creep experiments at different temperatures revealed that the modified almost fully lamellar microstructure is enhanced in strength and creep resistance, where a small volume fraction of globular γ -phase provides ductility at ambient temperatures.

B.1 Introduction

The development of lightweight, high-temperature materials is still subject of worldwide research, because of the existing engine manufacturers' demands to design and manufacture more efficient and eco-friendly propulsion systems [1–4]. In addition to new and improved design concepts, previous works have been shown that the use of intermetallic titanium aluminides based on the ordered γ -TiAl phase plays a decisive role in replacing heavy Ni-based alloys as turbine blades or turbocharger turbine wheels. Particularly in the temperature range of 600 to 800 °C, intermetallic γ -TiAl based alloys exhibit high specific tensile strength levels. As an example, the β -solidifying γ -TiAl based TNM alloy, a process-adapted 4th generation alloy with a nominal composition of Ti-43.5Al-4Nb-1Mo-0.1B (in at.%), can be regarded as an appropriate benchmark. The addition of Nb improves the oxidation resistance and along with Mo the creep properties [1,2]. In contrast to other Ti-Al alloy systems, the TNM alloy family is distinguished by its excellent hot-workability, i.e., it can be forged under isothermal as well as near conventional conditions, demonstrating its universal applicability [5]. Within the last decades, mainly melt-metallurgical processes have been developed for the production of high-quality starting material, which has subsequently been processed into structural components by casting or hot-forming associated with advanced heat treatments [5]. However, the TNM alloy was already selected as an experimental alloy to prove the feasibility for powder metallurgical (PM) processing routes, like additive manufacturing (AM) or spark plasma sintering (SPS), which enable the production of complex near-net shape components. Although these techniques have not reached industrial readiness up to now, encouraging results have been achieved [6–8]. Therefore, in the framework of this study, SPS was chosen to densify TNM powder by mechanical pressure and high intensity pulsed direct electric current within a graphite die. The shape of the graphite die even allows the sintering of a turbine blade, as already demonstrated by Couret et al. [6]. Another advantage of SPS is the possibility of sintering at different temperatures and times, whereby various microstructures can be adjusted [8]. However, one disadvantage in this respect is the utilization of natural convection for cooling, i.e., the cooling rate is limited and further depends on the sample geometry [6].

In general, a PM approach generates a chemical homogeneous starting condition for further applications. While alloying elements determine the mechanical properties of TiAl alloys, a further decisive factor in this context is the arrangement of the constituting phases in the microstructure. In the case of the multi-phase TNM alloy, the adjustment of the strength and ductility is depended on the volume fraction and morphology of the ordered hexagonal α_2 -Ti₃Al phase (D0₁₉ structure), the ordered body-centered cubic (bcc) β_o -TiAl phase (B2 structure), as well as the ordered face-centered tetragonal γ -TiAl phase (L1₀ structure) [9]. The γ -phase, which appears both globular and lamellar within the heat-treated TNM microstructure, increases the ductility at room temperature (RT), because the predominant

deformation mechanisms are the glide of ordinary dislocation and mechanical twinning within the $L1_0$ structure [10,11]. In contrast, the brittle β_o -phase decreases the RT ductility, due to the lack of independent slip systems [11]. However, both α_2/γ -colony boundary phases, i.e., the globular γ - and the β_o -phase, suppress grain growth during thermal treatment, but affect the creep behavior negatively [10,12]. The creep and tensile strength can be further controlled by α_2/γ lamellar spacing. These lamellar colonies form during moderate cooling from the disordered hexagonal γ -phase, i.e., $\alpha \rightarrow \alpha_2/\gamma$, possessing the so-called Blackburn orientation relationship: $\langle 11\bar{2}0 \rangle_{\alpha_2} \parallel \langle 110 \rangle_{\gamma}$, $(0001)_{\alpha_2} \parallel \{111\}_{\gamma}$. Due to the fact that this transformation is diffusion-controlled the lamellar spacing depends on the cooling rate, meaning that high cooling rates generate fine lamellar widths, which improve creep resistance and strength [10,13,14]. At elevated cooling rates, however, supersaturated α_2 -phase can be obtained at RT, tendering the formation of fine γ -lamellae, i.e., $\alpha_2 \rightarrow \alpha_2/\gamma$, in a subsequent aging step [15]. As a result, nano-lamellar structures can be achieved [15,16].

Therefore, two-step heat treatments have been developed for TNM alloys, obtaining a thermally stable microstructure during long-term exposure at service temperature, which provides balanced mechanical properties. The first heat treatment step takes place within the $(\alpha + \beta + \gamma)$ phase field region followed by air-cooling (AC) [9,15]. The microstructure consists of small volume fraction of globular β_o - and γ -grains, as well as supersaturated α_2 -grains with a grain size well below 100 μm as described in ref. [17]. If the Al content of the TNM alloy is increased, an additional $(\alpha + \gamma)$ - and single α -phase field region arise [15], as shown in the quasi-binary phase diagram of the TNM alloy system reported in References [9,15,18]. Depending on the temperature and dwell time of the first heat treatment step and of the chemical composition, the adjustment of further types of lamellar microstructures, namely a nearly lamellar (NL) microstructure with traces of globular γ - (NL γ) and/or β_o -phase (NL β) or a fully lamellar (FL) microstructure, offering the highest creep resistance, as well as yield strength, can be accomplished [11,12]. The corresponding cooling and the subsequent second heat treatment step, which takes place in a temperature range above the service temperature and below the eutectoid temperature, followed by furnace cooling (FC), defines the average lamellar spacing. This so-called aging treatment must be selected in such a way that the optimum balance of mechanical properties is generated, in particular to obtain creep resistance at elevated temperature and to provide ductility below the brittle-to-ductile transition temperature [9].

In the case of SPS, current devices are able to consolidate, sinter and conduct a heat treatment step at the same time. However, unfortunately, the resulting coarse lamellar spacing, which is linked to the low feasible cooling rate in the course of natural convection, makes it impossible to optimally adjust the mechanical properties of the TNM alloy as described above. For this reason, the present study deals with the development of subsequent heat treatments on SPS manufactured samples in order to optimize their mechanical

properties, extending the scope of the SPS PM route towards improved high-temperature applications.

B.2 Experimental procedure

The TNM powder used in the present study was produced via electrode induction melting gas atomization (EIGA) [19] by Nanoval GmbH & Co. KG, Germany, applying a Laval nozzle, using argon inert gas [20]. The ingots needed for this process were produced according to refs. [21,22] by GfE Metalle und Materialien GmbH, Germany. A powder fraction smaller than 150 μm was utilized for the SPS experiment, which was carried out on a SPS device of the type HP D 25 by FCT Systems GmbH, Germany, at the Technische Universität Bergakademie Freiberg, Germany. This SPS device has a cylindrical graphite die with an inner diameter of 80 mm, which corresponds to the sample cross-section at a height of 14 mm. The densification of the powder is reached under vacuum condition by mechanical pressure and a pulsed electric current. For details regarding the SPS process, the reader is referred to References [6,23]. The chemical composition of the TNM alloy after SPS is shown in Table B.1. The concentrations of Ti, Al, Nb, and Mo were determined by means of X-ray fluorescence spectroscopy, while B was evaluated by inductively coupled plasma atomic emission spectroscopy. For analyzing the O content carrier gas hot extraction was used. The chemical analysis of the powder has shown the same results, with exception of the O content, which was 300 mass-ppm lower.

The TNM powder was sintered at 1300 °C for 3 min under an applied load of 50 MPa. This dwell temperature was reached by using a heating rate of 50 K/min between RT and 1000 °C and, beyond this, the heating rate was decreased to 40 K/min in order to prevent a temperature overshooting. After a dwell time of 3 min, the sintered disc of the diameter 80 mm was cooled to RT with around 90 K/min via natural convection cooling of the SPS device.

Thermal treatments were conducted under atmospheric conditions using a high-temperature furnace of the type RHF 1600 from Carbolite, Germany. Subsequently, AC was performed. The heat treatments were carried out on cylindrical samples with a diameter of 11 mm and a length of 70 mm, which were eroded by electrical discharge machining from the sintered discs. Also the samples in as-SPS or heat-treated condition for microstructural examination by scanning electron microscopy (SEM) were taken from the center of the disc.

Table B.1: Chemical composition of the investigated TNM alloy in at.% after SPS. The oxygen content is stated in mass-ppm.

Ti	Al	Nb	Mo	B	O
bal.	43.5	4.05	1.02	0.10	1300

The specimens were metallographically ground and electrolytically etched in accordance to Reference [24]. All SEM investigations were conducted on an EVO 50 by Zeiss, Germany, in back-scattered electron (BSE) mode at an acceleration voltage of 20 kV. Furthermore, the electrolytically etched samples, where the etching process reduced surface-near residual stresses, were investigated by X-ray diffraction (XRD) measurements using an AXS D8 Advanced diffractometer from Bruker, Germany. The Rietveld refinement [25] was used to quantify the fractions of the phases present, applying the Bruker software TOPAS 4.2, Germany.

Complementary, the SEM micrographs were analyzed via the image analysis software Stream Motion 1.9.3 from Olympus, Japan, to determine phase fractions and grain sizes. Thereby, the grain size corresponds to the equivalent circle diameter. For more details, the reader is referred to References [9,24].

The lamellar spacing of the α_2/γ -colonies was examined by means of transmission electron microscopy (TEM) employing a Philips CM12 microscope, Germany, operating at an acceleration voltage of 120 kV. For these investigations, specimens of 3 mm in diameter were electrolytically thinned to electron transparency using a Tenu Pol-5 using the electrolyte A3 by Struers, Germany. The TEM images were taken along the $\langle 110 \rangle$ zone axis of the γ -phase in “edge-on” condition of the α_2/γ -colonies. These TEM images were used to measure the width of α_2 and γ lamellae to determine the average lamellar spacing.

Hardness was measured according to Vickers HV10 using a universal testing machine M4C 025 G3M from EMCO, Austria. Each hardness value was calculated as arithmetic mean value from at least five indents.

Quasi-static tensile tests at RT, 300, 700 , and 800 °C were carried out on universal testing machines of the type Inspect 50-1 from Hegewald and Peschke, Germany, and AG-100 from Shimadzu, Japan, at the GfE Fremat GmbH, Germany. The tensile test specimens had a diameter of 5 mm and a gauge length of 25 mm. The initial strain rate of the tensile tests was always 10^{-4} s^{-1} . At each temperature, two specimens of the as-SPS condition and the heat-treated variants were tested.

Creep tests of the heat-treated samples were performed at a temperature of 750 °C, using an initial constant load of 150 MPa employing creep testing machines TC30 and TC50 from AET Technologies, France. The creep samples had an initial diameter of 6 mm and an initial gauge length of 30 mm. Extensometer bars were used to determine the creep strain. Stable thermal conditions along the specimen length were guaranteed through monitoring and controlling the temperature by three attached thermocouples.

B.3 Results

B.3.1 Microstructure

The TNM powder was spark plasma sintered at a dwell temperature of 1300 °C for 3 min under an applied pressure of 50 MPa, obtaining a dense specimen. The microstructure taken from the center of the as-SPS disc is shown in Fig. B.1a,b, exhibiting a NL $\gamma + \beta_o$ microstructure consisting of equiaxed lamellar α_2/γ -colonies surrounded by globular γ - (dark contrast) and β_o -phase (bright contrast). The SEM images of the as-SPS condition were evaluated via image analysis. As a result, the globular γ -phase was estimated to be around 4 vol.% and for the β_o -phase the value was below 1 vol.%. Additionally, XRD measurements (see Fig. B.1c) provide quantitative analysis regarding the crystallographic phase fraction, as listed in Table B.2. The γ -phase fraction of the as-SPS sample is around 60 vol.%, which stems from both the γ -lamellar and the globular γ -phase. The lamellar spacing is rather large and the individual lamellae are already visible in the SEM image. These coarse spacing distances stem from the low cooling rate of the SPS device.

Two-step heat treatments were carried out on as-SPS samples to optimize the mechanical properties by adjusting the microstructure, for example, minimizing the lamellar spacing. The first sample experienced a solution heat treatment at 1290 °C for 30 min. This heat treatment takes place within the ($\alpha + \beta$)-phase field region, approximately 35 °C above the γ solvus temperature ($T_{\gamma,solv}$), which is around 1255 °C in case of the TNM alloy [9]. After AC to RT, the samples were aged at 850 °C for 6 h followed by FC to stabilize the microstructure. A detailed record of the heat treatments as well as the quantitative evaluation of the microstructure is summarized in Table B.2. Figure B.2a shows the resulting microstructure. This microstructure is called NL β and consists mainly of fine lamellar α_2/γ -colonies and β_o -phase at colony boundaries and triple points. When compared to Fig. B.1a, the lamellar spacing cannot be resolved in this case due to the higher cooling, as achieved by AC. Furthermore, lenticular γ -phase (γ_{lens}) precipitates and coarsens within the β_o -phase during aging at 850 °C for 6 h in order to obtain a thermodynamic phase equilibrium [18]. The amount of γ_{lens} and β_o -phase was determined to be about 2 vol.%. In addition, so-called cellular reaction (CR) takes place along the colony boundaries. The CR is provoked by the fine lamellae causing a high amount of interface surfaces, thus decreasing the thermal stability of the α_2/γ -colonies. At aging or service temperature, this fine lamellar α_2/γ -colonies are prone to decompose in ($\alpha_2 + \beta_o + \gamma$)_{cellular}, starting from the colony boundaries that deteriorates the high temperature properties, as reported in References [5,17,26,27]. Furthermore, small pores are also visible inside the SEM micrograph as dark voids, located along the grain boundaries. It should be noted that these pores appear larger in the SEM image than they actually present in the material due to an enlarging effect during the electrolytically etching of the polished surface. Pores, along with the β_o -phase, which exists

Table B.2: Microstructural state in as-SPS and heat-treated condition (see text).

Type of microstructure	Heat treatment	Phase fractions measured via XRD*			Quantitative morphological analysis of SEM micrographs**				Lamellar spacing nm	Hardness HV10
		α_2 vol.%	γ vol.%	β_o vol.%	α_2/γ -colonies vol.%	μm	globular γ vol.%	$\beta_o + \gamma_{lens}$ vol.%		
as-SPS	-	35	61	4	94	19	5	<1	83±7	378±8
NL β	1290 °C/30 min/AC + 850 °C/6 h/FC	27	71	≤2	97	20	<1	2	8±9	466±4
FL	1265 °C/ 30 min/AC+ 850 °C/6 h/FC	30	68	≤2	98	29	<1	<1	10±6	461±7
NL γ	1290 °C/30 min/AC 1245 °C/30 min/AC+ 850 °C/6 h/FC	30	68	≤2	97	45	2	<1	9±8	445±5

* The estimated accuracy of the method is ± 2 vol.%.

** The estimated accuracy is ± 1 vol.%.

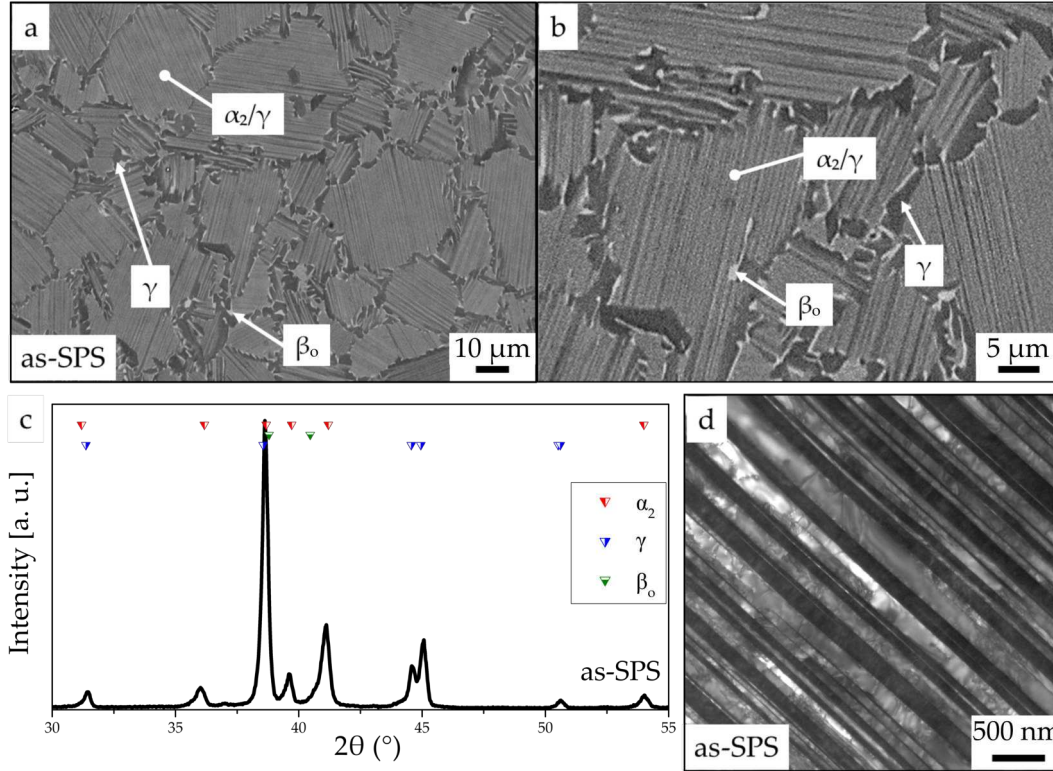


Figure B.1: a-b) NL $\gamma + \beta_o$ microstructure of the as-SPS TNM alloy consisting of equiaxed lamellar α_2/γ -colonies surrounded by globular γ - and β_o -phase. Owing to the low cooling rate from the dwell temperature (1300 °C), the lamellar spacing is rather large. The SEM images were taken in BSE mode, thus globular γ shows a dark contrast, whereas the β_o -phase appears in bright contrast. The α_2 -phase shows a contrast between those of γ and β_o . c) XRD spectrum of as-SPS sample. The phase fraction evaluated by applying Rietveld analysis is listed in Table B.2. d).TEM image of a lamellar α_2/γ -colony in an as-SPS specimen in "edge-on" condition

as disordered β -phase at 1290 °C, however, impede grain growth during the heat treatment within the $(\alpha + \beta)$ -phase field region. The mean size of the equiaxed α_2/γ -colonies was measured by image analysis to be around 20 μm, which corresponds to the as-SPS condition. The next heat treatment was carried out at 1265 °C for 30 min, followed by AC and an aging step at 850 °C for 6 h and FC. As a result, the globular γ - and β_o -phase fraction is decreased to a minimum and an almost FL microstructure could be achieved, which is depicted in Fig. B.2b. Pores and CR appear along the α_2/γ -colony boundaries almost in the same manner as they were detected in the previous heat-treated microstructure, see Fig. B.2a. The colony size of the FL microstructure increases slightly compared to the NL β one, see Table B.2. This is attributed to the low amount of a second phase, which is necessary to effectively inhibit grain coarsening during annealing at 1265 °C. Nevertheless, due to the short holding time of 30 min, the grain size is below 100 μm, which is postulated to be small enough to achieve moderate fracture elongation at RT [1].

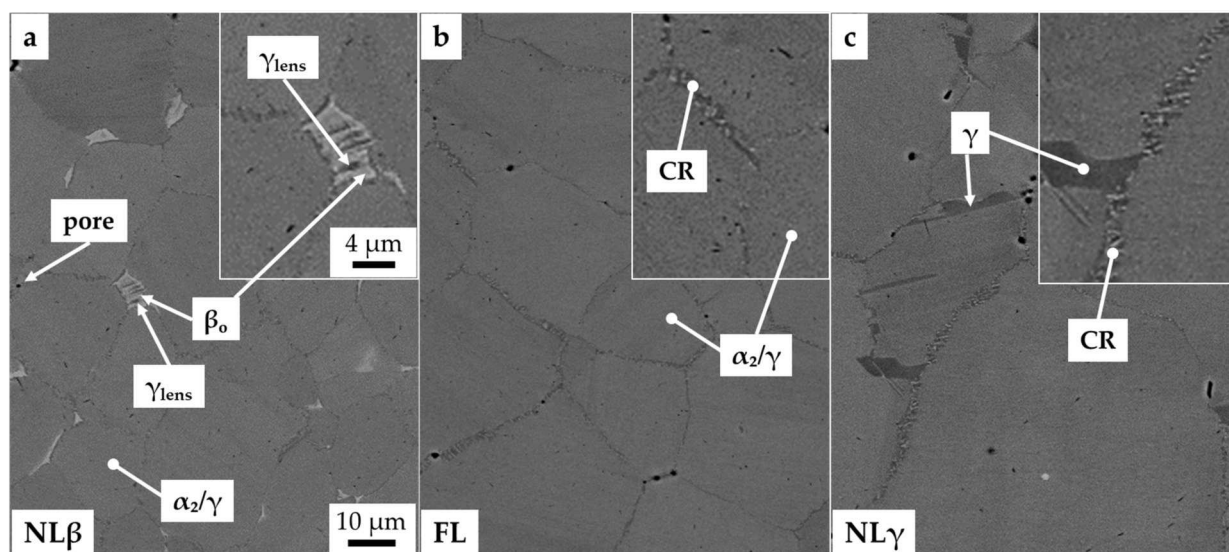


Figure B.2: SEM micrographs of microstructures after two-step heat treatment according to Table B.1: a) NL β ; b) FL; c) NL γ . The inserts in the upper right corner show microstructural details in higher magnification. At this point it should be noted that the pores show an enlarged size, caused by the electrolytically etching procedure (see text). SEM images were taken in BSE mode.

The third heat treatment started with an annealing step at 1290 °C for 30 min, as in the first heat treatment, providing a homogeneous ($\alpha + \beta$)-microstructure, but afterwards the samples were FC below $T_{\gamma, solv}$ to 1245 °C and held there for additional 30 min to precipitate globular γ -phase. The following AC and aging corresponds to the previous ones. The resulting microstructure, called NL γ , is shown in Fig. B.2c. Besides the globular γ -phase, α_2/γ -colonies, CR and pores are detectable. During the longer first heat treatment step, the former α -grains have grown resulting in a mean grain size of 45 μm . All phase fractions and grain sizes, which were determined via image analysis, are summarized in Table B.2. The quantitative image analysis is used to differ between the morphological characteristics of the phases. However, due to the limited resolution of this technique, fine lamellae within the α_2/γ -colonies cannot be evaluated. In contrast, XRD as a lattice-sensitive method leads to the overall phase fraction of α_2 , β_0 and γ , see Table B.2. The heat-treated samples show almost the same phase distribution with around 70 vol.% of γ -phase due to the stabilization annealing at 850 °C. Comparing the XRD measured γ -phase fraction with the globular γ -phase detected by image analysis, it is evident that the majority of the γ -phase is in the form of lamellae within the α_2/γ -colonies. These α_2/γ -lamellae are already visible in the as-SPS microstructure (Fig. B.1a). The lamellar spacing of the colonies can be investigated in more detail by means of TEM, as shown in Fig. B.1d. The lamellar spacing of the as-SPS sample was determined to be $83 \pm 7 \text{ nm}$, see chapter A.2. By the subsequent heat treatments, the average lamellar spacing could be reduced by a factor of ten. The average lamellar spacings are almost the same for the NL β , FL, and NL γ microstructures, see Table B.2, due to the

fact that the cooling rate as well as the following stabilization heat treatment, which defines the lamellar distance, were the same.

B.3.2 Mechanical testing

The obtained Vickers hardness of the different microstructures is also summarized in Table B.2. The hardness values reflect the microstructural aspects described in the previous chapter. The as-SPS condition shows the lowest hardness with around 378 HV10, due to the coarse lamellae and the highest volume fraction of globular γ -phase, see Table B.2. Decreasing the average lamellar spacing by subsequent heat treatments increases the hardness up to 450-470 HV10. For the heat-treated samples the same lamellar width was measured, but the NL γ microstructure shows the lowest hardness value (445 HV10), probably due to the larger colony size and the existence of globular γ -phase.

For a detailed investigation of the mechanical properties, tensile tests were carried out at 25, 300, 700, and 800 °C. If 0.2% plastic elongation is achieved, the $R_{p0.2}$ yield strength was evaluated (round icons inside Fig. B.3a). Otherwise, the ultimate tensile strength was determined (marked with a cross). The results are summarized in Fig. B.3a. The black dashed line represents the baseline provided by the as-SPS data, in order to establish the benefit of the heat treatment. In addition, Fig. B.3b shows the plastic strain to fracture. It becomes evident that the strength can be increased by heat treatments, due to reduced amount of globular phases and a finer lamellar spacing. However, the plastic strain to

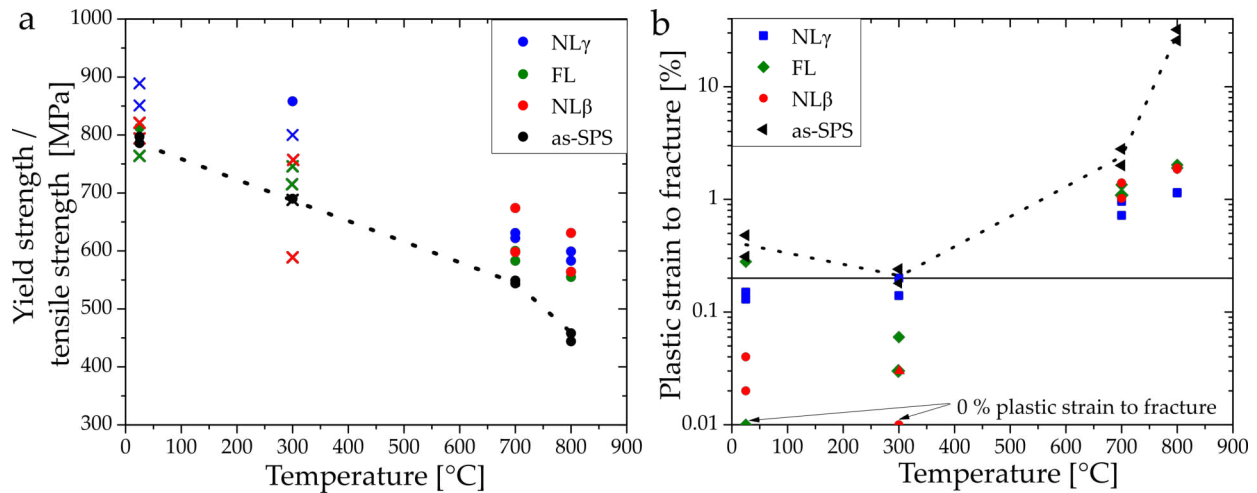


Figure B.3: Tensile properties of the investigated material conditions, see Table B.2: (a) the 0.2%-yield strength is marked with dots, whereas the ultimate tensile strength is denoted with crosses; (b) plastic strain to fracture. The 0.2% fracture elongation is indicated as a horizontal line. Two samples failed within the elastic regime. Their values are plotted at the bottom in the logarithmic diagram. The black dashed lines in (a) and (b) are the baseline provided by the as-SPS condition. For the interpretation of the references to color in this Fig. B. legend, the reader is referred to the online version of this article.

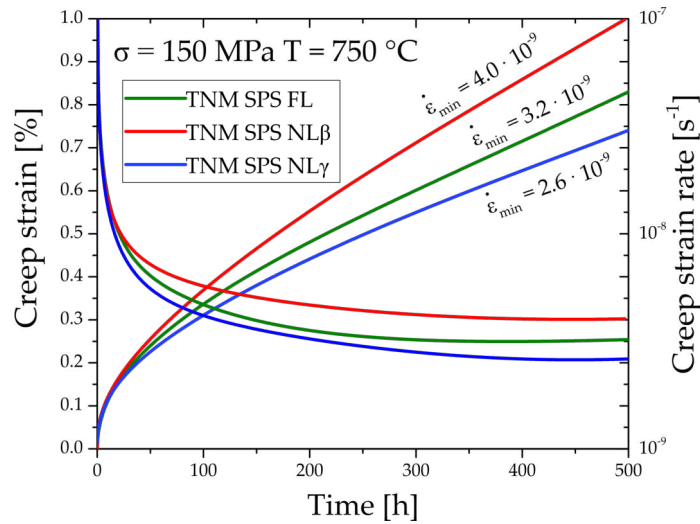


Figure B.4: Creep strain and creep strain rate as a function of time of the heat treated microstructures as a function of time at 750 °C and 150 MPa.

fracture decreases by the heat treatment as shown in Fig. B.3b. These values are always below the black dashed line provided by the as-SPS condition. In addition, in two cases, the plastic strain to fracture decreases to 0%, which is also indicated in the logarithmic diagram in Fig. B.3b. In summary, the results in Fig. B.3 show that the strength can be increased by additional heat treatment at 700 and 800 °C, while maintaining a certain ductility, too. Finally, creep tests were carried out at 750 °C using a load of 150 MPa. The creep tests provided the creep strain (ϵ) and the creep strain rate ($\dot{\epsilon}$) as a function of time. The corresponding graphs are plotted in Fig. B.4. The NL β microstructure results in a minimum creep rate ($\dot{\epsilon}_{min}$) of $4.0 \cdot 10^{-9} \text{ s}^{-1}$ after 400 h, the FL state reaches $\dot{\epsilon}_{min} = 3.2 \cdot 10^{-9} \text{ s}^{-1}$ after 350 h and the NL γ variant shows a $\dot{\epsilon}_{min}$ of $2.6 \cdot 10^{-9} \text{ s}^{-1}$ after 400 h. That means that all tested conditions exhibit a creep strain $\leq 1\%$ after 500 h at 750 °C.

B.4 Discussion

This study proved that it is possible to manufacture the engineering TNM alloy via SPS by sintering the powder at 1300 °C within the ($\alpha + \beta$)-phase field region. A similar fundamental study on the TNM alloy was conducted by Voisin et al. [8]. These authors showed that, at a dwell temperature of 1304 °C, the microstructure consists of α -phase surrounded by β -phase, which is also in agreement with the TNM phase diagram provided by Schwaighofer et al. [9]. During cooling from dwell temperature, a microstructure consisting of coarse lamellar α_2/γ -colonies, which are surrounded by globular γ - and β_o -phase was generated in the same way as in this investigation. But in this study, a subsequent heat treatment was designed for the SPS samples to exceed the mechanical results provided by Voisin et al. [8] and reach the full potential of the TNM PM route. The initial as-SPS condition exhibits

a $NL\gamma + \beta_o$ microstructure as shown in Fig. B.1a, which forms at a dwell temperature of 1300°C and during slow cooling, whereby globular γ -phase precipitates in the β/β_o -phase below the $T_{\gamma, solv}$ temperature. Another transformation, which takes place during cooling, is the formation of lamellar α_2/γ -colonies. As a consequence of the slow cooling rate, the average lamellar spacing is rather broad, which is associated with a negative influence on the tensile properties [10,13,14]. However, hardness values of 378 HV10 can be reached due to the fine-grained microstructure of the as-SPS condition and the elevated content of oxygen, see Table B.1, which acts as solid solution hardening element in γ -TiAl alloys [28,29]. As a consequence, the hardness is significantly higher than in a cast/HIP TNM alloy [9,18]. Comparing the tensile tests of this study with as-SPS results from literature [8], similar yield strengths are obtained, but a higher plastic strain to fracture have been reported for the TNM alloy. Obviously, the enhanced oxygen content embrittles the material [28,29], resulting in a deterioration of the fracture elongation. Due to the limited cooling rate of currently used SPS units [8], an optimized microstructure with balanced mechanical properties, i.e., sufficient ductility at RT and good creep resistance at elevated temperatures, as described in Reference [9], cannot be adjusted. Therefore, additional two-step heat treatments were carried out on SPS manufactured samples to remove the coarse lamellae with the adjustment of a $NL\gamma$, FL and $NL\beta$ microstructure. At this point, it should be noted that in a nominal TNM alloy, no FL microstructure can be adjusted [9]. However, due to the higher amount of oxygen, which stabilizes the α/α_2 -phase [28,30], the appearance of β_o - and γ -phase could almost be suppressed throughout the heat treatment. The heat treatments are summarized in Table B.2 and the resulting microstructures are shown in Fig. B.2. The hardness values, see Table B.2, reflect the arrangement of the constituting phases in these different microstructures. The $NL\gamma$ sample (Fig. B.2c) has the lowest hardness, due to its higher volume fraction of the “soft” globular γ -phase and its comparable large α_2/γ -colony size. In contrast, FL and $NL\beta$ exhibits no globular γ -phase, but show almost the same hardness values. Therefore, two opposite effects control the hardness: the high hardness of the β_o -phase at RT [10,18], whereas the slightly higher colony size of the $NL\beta$ microstructure believed to decreases it. Nevertheless, the hardness values of the three heat-treated microstructures show an increase of 70–90 HV10 when compared to the as-SPS microstructure. This behavior is mainly caused by the decreased average lamellar spacing (from 80 nm to 10 nm). The impact of the microstructure on the mechanical properties was also evaluated by tensile tests as summarized in Fig. B.3. Due to the increased strength of the heat-treated specimens, the ductility is decreased when compared to the as-SPS condition. Therefore, the evaluation of the yield strength at 0.2% plastic elongation was limited for testing temperatures below the ductile-to-brittle transition temperature and thus the ultimate tensile strength values were taken into account. The $NL\gamma$ microstructures shows the highest ultimate tensile strength (Fig. B.3a), together with a high fracture elongation (Fig. B.3b), due to the presence of the rather “soft” globular γ -phase. At 700°C and 800°C the strength is enhanced significantly

for all heat-treated specimens when compared to the as-SPS condition. The obtained values are in the same range as for a FL microstructure provided by conventional casting and subsequent heat treatment [9]. However, the fracture elongation is lower at RT. Therefore, it is tempting to speculate that the observed embrittlement is due to the increased oxygen content and the appearance of micropores, which are evidenced in Fig. B.2. In general, these spherical pores appear during the subsequent pressureless heat treatment around the sinter temperature. This effect is called thermally induced porosity (TIP) [31]. The Ar stems from entrapped atomization gas inside the powder, which gets more likely for large powder sizes [19,32] as also used in this study. From Fig. B.3b it seems that there is a weak minimum at 300 °C. Such a minimum might be attributed to strain aging, i.e., the dislocations are locked by mobile oxygen atoms. Such an embrittlement is also found in many metallic alloy systems. Therefore, in an ongoing project, this effect will be studied by in-situ TEM investigations. The different constituting phases in the heat-treated microstructures impact the creep properties as shown in Fig. B.4. The FL microstructure shows a better creep resistance than the NL β variant despite same average lamellar spacings. This is caused by the negative effect of the β_o -phase with B2 structure, which exhibits higher diffusion rates [10,17,33]. In addition, the distinctly smaller colony size of the NL β microstructure facilitates grain boundary sliding at the chosen creep testing conditions [10,34]. Therefore, as a result of their largest mean colony size, the NL γ microstructure shows the lowest $\dot{\epsilon}_{min}$, despite of the presence of the soft, globular γ -phase along the colony grain boundaries and same average lamellar spacing. In summary, all heat-treated microstructures shows a $\dot{\epsilon}_{min}$ within the same magnitude than observed for comparable microstructures produced via the conventional cast and heat treatment route [9], which again highlights the potential of SPS material when an additional heat treatment is performed.

B.5 Summary

In the framework of this study, spark plasma sintering, a technique which is capable of manufacturing complexly shaped components, was chosen to densify powders of an advanced intermetallic γ -TiAl based alloy, the so-called TNM alloy, with a chemical composition of Ti-43.5Al-4.1Nb-1.0Mo-0.1B. Therein, gas atomized powder was sintered at 1300 °C followed by cooling to RT with around 90 K/min. The as-SPS condition reveals a small-sized and homogenous NL γ + β_o microstructure. At RT the microstructure shows a hardness of 378 HV10 and an ultimate tensile strength of about 800 MPa due to small α_2/γ -colonies and an elevated oxygen content of 1300 ppm. The average lamellar spacing within the colonies was determined to be 83 \pm 7 nm. Subsequent two-step heat treatments shifted the amount of constituting phases during the adjustment of a NL γ , FL and NL β microstructure, also decreasing the average lamellar spacing to 10 \pm 3 nm in order to utilize the full potential

of the TNM alloy. As a consequence, the hardness could be increased to 466 ± 4 HV10 in case of the $NL\beta$ variant, however, tensile fracture elongation at RT decreased. At $800\text{ }^\circ\text{C}$ the $NL\beta$ microstructure attain a yield strength of around 600 MPa when compared to the 450 MPa of the initial as-SPS variant. Furthermore, a minimum creep rate of $4.0\cdot 10^{-9}\text{ s}^{-1}$ was achieved due to the fine lamellar $NL\beta$ microstructure. The FL and the $NL\gamma$ microstructure show lower $\dot{\epsilon}_{min}$ of $3.2\cdot 10^{-9}\text{ s}^{-1}$ and $2.6\cdot 10^{-9}\text{ s}^{-1}$, respectively, which was achieved by the larger mean colony size of 29 and 45 μm , when compared to 20 μm in the $NL\beta$ microstructure as well as the absence of the β_o -phase. Summarized, the strength and the creep performance at $750\text{ }^\circ\text{C}$ can keep up with the obtained levels of conventional cast and heat treatment processing routes [9]. Therefore, the study proves that SPS of the TNM alloy, along with a designed subsequent heat treatment, is a promising alternative manufacturing route besides the conventional processing of engineering γ -TiAl based alloys by means of investment casting.

Acknowledgments

The authors thank Sabine Decker from the Institute of Materials Engineering, TU Bergakademie Freiberg for conducting the SPS experiments.

B.6 References

- [1] Mayer, S.; Erdely, P.; Fischer, F. D.; Holec, D.; Kasthuber, M.; Klein, T.; Clemens, H.: *Advanced Engineering Materials* 19 (2017) 4, 1600735, DOI: 10.1002/adem.201600735.
- [2] Clemens, H.; Mayer, S.: *Advanced Engineering Materials* 15 (2013) 4, 191–215, DOI: 10.1002/adem.201200231.
- [3] Habel, U.; Heutling, F.; Kunze, C.; Smarsly, W.; Das, C.; Clemens, H.: in: *13th World Conf on Titanium*, V. Venkatesh, A. L. Pilchak, J. E. Allison; S. Ankern; R. Boyer; J. Christodoulou; H. L. Fraser; M. A. Imam; Y. Kosaka; H. J. Rack; A. Chatterjee; A. Woodfield (Eds.), 2016.
- [4] Bewlay, B. P.; Nag, S.; Suzuki, A.; Weimer, M. J.: *Materials at High Temperatures* 33 (2016) 4-5, 549–559, DOI: 10.1080/09603409.2016.1183068.
- [5] Clemens, H.; Wallgram, W.; Kremmer, S.; Güther, V.; Otto, A.; Bartels, A.: *Adv. Eng. Mater.* 10 (2008) 8, 707–713, DOI: 10.1002/adem.200800164.
- [6] Couret, A.; Voisin, T.; Thomas, M.; Monchoux, J.-P.: *JOM* 69 (2017), 2576–2582, DOI: 10.1007/s11837-017-2549-6.
- [7] Voisin, T.; Monchoux, J.-P.; Durand, L.; Karnatak, N.; Thomas, M.; Couret, A.: *Advanced Engineering Materials* 17 (2015) 10, 1408–1413, DOI: 10.1002/adem.201500019.
- [8] Voisin, T.; Monchoux, J.-P.; Hantcherli, M.; Mayer, S.; Clemens, H.; Couret, A.: *Acta Materialia* 73 (2014), 107–115, DOI: 10.1016/j.actamat.2014.03.058.
- [9] Schwaighofer, E.; Clemens, H.; Mayer, S.; Lindemann, J.; Klose, J.; Smarsly, W.; Güther, V.: *Intermetallics* 44 (2014), 128–140, DOI: 10.1016/j.intermet.2013.09.010.
- [10] Appel, F.; Paul, J.D.H.; Oehring, M.: *Gamma titanium aluminide alloys*, Wiley-VCH, Weinheim, Germany, 2012.

-
- [11] Kim, Y.-W.: *Acta Metallurgica et Materialia* 40 (1992), 1121–1134, DOI: 10.1016/0956-7151(92)90411-7.
- [12] Mayer, S.; Kastenhuber, M.; Clemens, H.: *Materials Science Forum* 941 (2018), 1484–1489, DOI: 10.4028/www.scientific.net/MSF.941.1484.
- [13] Takeyama, M.; Nakamura, M.; Kumagai, T.; Kikuchi, M.: in: *Proc First Int Symp Struct Intermet*. Publ by Minerals, Metals & Materials Soc (TMS), 1993, 167–176.
- [14] M. Beschliesser; A. Chatterjee; A. Lorich; W. Knabl; H. Kestler; G. Dehm; H. Clemens: *Materials Science and Engineering: A* 329 (2002), 124–129.
- [15] Wallgram, W.; Schmölder, T.; Cha, L.; Das, G.; Güther, V.; Clemens, H.: *International Journal of Materials Research* 100 (2009), 1021-1030, DOI: 10.3139/146.110154.
- [16] Klein, T.; Clemens, H.; Mayer, S.: *Materials (Basel, Switzerland)* 9 (2016) 9, 755, DOI: 10.3390/ma9090755.
- [17] Kastenhuber, M.; Klein, T.; Clemens, H.; Mayer, S.: *Intermetallics* 97 (2018), 27–33, DOI: 10.1016/j.intermet.2018.03.011.
- [18] Schloffer, M.; Iqbal, F.; Gabrisch, H.; Schwaighofer, E.; Schimansky, F.-P.; Mayer, S.; Stark, A.; Lippmann, T.; Göken, M.; Pyczak, F.; Clemens, H.: *Intermetallics* 22 (2012), 231–240, DOI: 10.1016/j.intermet.2011.11.015.
- [19] Gerling, R.; Clemens, H.; Schimansky, F. P.: *Advanced Engineering Materials* 6 (2004), 23–38, DOI: 10.1002/adem.200310559.
- [20] Werner Schatt, Klaus-Peter Wieters, Bernd Kieback: *Pulvermetallurgie*, Springer, Germany, 2002.
- [21] Achtermann, M.; Fürwitt, W.; Güther, V.; Nicolai, H.-P., EP2342365, 13. July.
- [22] Güther, V.; Allen, M.; Klose, J.; Clemens, H.: *Intermetallics* 103 (2018), 12–22, DOI: 10.1016/j.intermet.2018.09.006.
- [23] Voisin, T.; Durand, L.; Karnatak, N.; Le Gallet, S.; Thomas, M.; Le Berre, Y.; Castagné, J.-F.; Couret, A.: *Journal of Materials Processing Technology* 213 (2013) 2, 269–278, DOI: 10.1016/j.jmatprotec.2012.09.023.
- [24] M. Schloffer; T. Schmoelzer; S. Mayer; E. Schwaighofer; G. Hawranek; F.-P. Schimansky; F. Pyczak; H. Clemens: *Practical Metallography* 48 (2011), 594–604, DOI: 10.3139/147.110138.
- [25] McCusker, L. B.; Dreele, R. B. V.; Cox, D. E.; Louër, D.; Scardi, P.: *Journal of Applied Crystallography* 32 (1999), 36–50, DOI: 10.1107/S0021889898009856.
- [26] Cha, L.; Clemens, H.; Dehm, G.: *International Journal of Materials Research* (2011), 703–708.
- [27] Kastenhuber, M.; Klein, T.; Rashkova, B.; Weißensteiner, I.; Clemens, H.; Mayer, S.: *Intermetallics* 91 (2017), 100–109, DOI: 10.1016/j.intermet.2017.08.017.
- [28] Lamirand, M.; Bonnetien, J.-L.; Guérin, S.; Ferrière, G.; Chevalier, J.-P.: *Metall and Mat Trans A* 37 (2006) 8, 2369–2378, DOI: 10.1007/BF02586211.
- [29] Ding, H.; Nie, G.; Chen, R.; Guo, J.; Fu, H.: *Materials & Design* 41 (2012), 108–113, DOI: 10.1016/j.matdes.2012.04.050.
- [30] Lefebvre, W.; Menand, A.; Loiseau, A.: *Metall and Mat Trans A* 34 (2003) 10, 2067–2075, DOI: 10.1007/s11661-003-0271-1.
- [31] Wegmann, G.; Gerling, R.; Schimansky, F.-P.: *Acta Materialia* 51 (2003) 3, 741–752, DOI: 10.1016/S1359-6454(02)00465-2.
- [32] Wimler, D.; Kardos, S.; Lindemann, J.; Clemens, H.; Mayer, S.: *Practical Metallography* 55 (2018), 620–636, DOI: 10.3139/147.110547.
- [33] Dlouhý, A.; Kuchařová, K.: *Intermetallics* 12 (2004) 7-9, 705–711, DOI: 10.1016/j.intermet.2004.03.007.
- [34] Maruyama, K.; Yamamoto, R.; Nakakuki, H.; Fujitsuna, N.: *Materials Science and Engineering: A* 239-240 (1997), 419–428, DOI: 10.1016/S0921-5093(97)00612-6.

Novel intermetallic-reinforced near- α Ti alloys manufactured by spark plasma sintering

D. Wimler^{a*}, J. Lindemann^b, C. Gammer^c, P. Spoerk-Erdely^a, A. Stark^d, H. Clemens^a, S. Mayer^a

^a Department of Materials Science, Montanuniversität Leoben, 8700 Leoben, Austria

^b GfE Fremat GmbH, 09618 Brand-Erbisdorf, Germany

^c Erich Schmid Institute of Materials Science, Austrian Academy of Sciences, Jahnstr. 12, 8700 Leoben, Austria

^d Institute of Materials Research, Helmholtz-Zentrum Geesthacht, 21502 Geesthacht, Germany

* Corresponding author

<https://doi.org/10.1016/j.msea.2020.139798>

Materials Science and Engineering: A (2020) 139798

open access: CC BY-NC-ND 4.0



Keywords:

Spark plasma sintering; γ -TiAl based alloys; TNM alloy; heat treatment; mechanical properties

Abstract

Near- α Ti alloys are ideal candidates for high-temperature aerospace, automotive and nautical propulsion systems due to their high strength, low density and good corrosion resistance. However, the maximum service temperature of the well-known near- α alloy Ti6242S is limited to about 540 °C. By adding, for example, intermetallic γ -TiAl based alloy particles to Ti6242S powder a significant increase in yield strength up to 650 °C can be achieved by means of spark plasma sintering, along with sufficient room temperature ductility. In this study, investigations on the underlying strengthening mechanisms were carried out. For this purpose, mechanical tests and detailed microstructural characterization were performed.

Spark plasma sintering at 1150 °C of powder blends with 10 m.% spherical γ -TiAl based powder (<20 μm) leads to a homogeneous dissolution of the TiAl particles in the matrix material and a refinement of the lamellar microstructure. Due to the formation of ordered intermetallic α_2 -Ti₃Al precipitates, which are completely stable up to 670 °C in the newly evolved Ti-8.3Al-1.8Sn-3.7Zr-2.0Mo-0.9Nb-0.08Si alloy (m.%), the creep resistance at 600 °C has been increased significantly. In the B containing variant, it was found that finely distributed titanium borides TiB formed in the Ti6242 matrix and led to an even more pronounced refinement of the microstructure. For B additions of 1 m.%, however, the creep resistance at 600 °C is reduced compared to the other alloys, but the strength is increased up to 500 °C.

C.1 Introduction

The demand for light-weight structural components that endure high service temperatures has initiated a permanent development of new alloys as well as new processing routes. Presently, Ti-base alloys are used in structural high-temperature applications in the aerospace and automotive industries, as these alloys unite low density, high strength, and good corrosion and creep resistance at service temperature [1-5]. The common near- α Ti-base alloys (below 6 m.% Al) attain service temperatures below 600 °C, whereas intermetallic γ -TiAl-based alloys, which contain about 29–35 m.% Al (42–48 at.%), reach up to 800 °C with increasing creep, burn and oxidation resistance. TiAl alloys are already in use as turbine blades in advanced aircraft engines [6,7], valves in automotive engines [7,8] and turbocharger turbine wheels in automotive and nautical propulsion systems [5,8]. However, γ -TiAl alloys suffer from moderate ductility at room temperature (RT), which limits further applications [9,10].

Both, near- α Ti and γ -TiAl alloys are commonly produced by ingot metallurgy followed by hot deformation processes, e.g. forging or rolling, and subsequent multi-step heat treatments. However, powder-related processing routes provide the opportunity to manufacture complex near-net shapes, originating from pre-alloyed powder or powder blends. For example, the technique of spark plasma sintering (SPS) is quite a promising alternative to the conventional [1,4] and additive manufacturing (AM) technologies, e.g. see Ref. [11-14], of producing light-weight parts with high structural complexity like TiAl turbine blades [15]. Thereby, SPS employs pulsed electric current and a uniaxial load to densify powders [15,16]. The use of powder facilitates the blending of Ti-base powder with other alloys or compounds into so-called titanium metal matrix composites (Ti-MMC), which exhibit enhanced mechanical properties after densification because of elements dissolution, grain refinement and/or dispersion strengthening [17-23]. For that reason, Ti-MMC components have already been introduced in the automotive industry as engine components, e.g. intake valves and exhaust valves [24].

This study investigates various powders and powder blends based on near- α Ti-base alloys densified via SPS. On the one hand, the matrix alloy Ti6242 with a nominal composition of Ti-6Al-2Sn-4Zr-2Mo (in m.%) was reinforced with B, and on the other hand, the advanced Ti-6Al-2Sn-4Zr-2Mo-0.1Si (in m.%) (Ti6242S) alloy was strengthened with particles of an intermetallic γ -TiAl based alloy, the so-called TNM alloy, with a nominal composition of Ti-43.5Al-4Nb-1Mo-0.1B (in at.%) (Ti-28.6Al-9Nb-2.3Mo-0.03B in m.%). The densification of commonly available powder or powder blends in the SPS unit opens up a fast and independent way of processing Ti-base alloys with advanced mechanical properties.

In general, many Ti-base alloys utilize the occurrence of two phases: the body-centered cubic (bcc) β -Ti (A2 structure) and the hexagonal close-packed (hcp) α -Ti (A3 structure), whereby the α -Ti is not thermodynamically stable above the allotropic transformation temperature,

the so-called β transus temperature ($T_{\beta,trans}$). Below $T_{\beta,trans}$ both phases can appear, whereby the α/β ratio is determined by the chemical composition of the Ti-base alloy. For instance, Al and O are strong α stabilizers and therefore increase the amount of α phase in the microstructure, whereas Sn and Zr are considered to be weak α stabilizers. In contrast, Mo and Nb are β stabilizers, as they increase the β phase fraction, whereby Mo has an approximately four times stronger effect than Nb [4].

In this regard, Ti-base alloys are classified conventionally according to their equilibrium phase constitution, which consequently depends on the chemical composition [1-4]. The Ti6242 alloys belong to the near- α Ti alloys because the majority of the microstructure consists of the hcp α phase, which is appropriate for creep resistant high-temperature applications due to its low self-diffusion coefficient and its low number of dislocation slip systems when compared to the bcc β phase [1]. The addition of the β -eutectic element Si [1,4], which results in the so-called Ti6242S alloy, improves the mechanical properties at elevated temperatures by solution strengthening and the formation of stable intermetallic $(\text{Ti,Zr})_5\text{Si}_3$ precipitates (D8₈-structure) at the α/β lamellae boundaries and at grain boundaries [25-27], which retard dislocation movement in comparison to the Si-free Ti6242 variant [1,25]. Additional strengthening in Ti-base alloys can be reached, e.g. due to the addition of Sn, by increasing the volume fraction of the intermetallic, ordered hexagonal α_2 -Ti₃Al phase (D0₁₉ structure), since coherent precipitates are effective barriers for dislocation glide and climb [4]. The α_2 -Ti₃Al phase precipitates from its disordered counterpart α during a final annealing treatment, resulting in an age-hardening effect by these fine α_2 precipitates. This aging step has to take place below the α_2 solvus temperature ($T_{\alpha_2,solv}$). Aging or the application above $T_{\alpha_2,solv}$ will dissolve the α_2 precipitates and thus the age-hardening effect will be lost, while limiting the maximum service temperature of this type of Ti-base alloys. The occurrence of this ordering transformation depends on the chemical composition of the alloy. For Ti6242S, where the long-term service temperature is set at 540 °C [28], $T_{\alpha_2,solv}$ is about 650 °C according to literature [4,29]. The presence of O [29], Sn [4] or a further increase of the Al content [2,4,29] in Ti-base alloys promotes the formation of the intermetallic, ordered hexagonal α_2 phase, i.e. $T_{\alpha_2,solv}$ and hence the service temperature is increased.

Based on the size and arrangement of the two major phases, α and β , a variety of microstructures is adjustable, which is reflected in the material's mechanical properties. The highest service temperatures are reached when near- α Ti alloys exhibit a fully lamellar (FL) microstructure, which consists mainly of lamellar α separated by retained β phase [2,4]. Therefore, a heat treatment above $T_{\beta,trans}$, in the single β phase field region, is conducted followed by cooling to RT; here, β transforms to α , obeying the Burgers orientation relationship: $\langle 111 \rangle_{\beta} || \langle 11\bar{2}0 \rangle_{\alpha}$, $\{110\}_{\beta} || (0002)_{\alpha}$ [30]. The cooling rate from the β phase field region defines the extent of this first transformation reaction, which forms in the case of slow cooling a continuous α layer at the boundary of the parent β grain, the so-called α seam. The cooling rate also determines the width of the next transforming α lamellae and the size

of the α colonies.

During annealing above $T_{\beta,trans}$, the coarsening of the β grains can be inhibited by the presence of a second phase, such as TiB or TiC. Furthermore, adding borides and carbides into the metal matrix (e.g. as shown by Lu et al. [17] in the case of Ti6242S) results in a more fine-grained starting microstructure due to the fine particles which act as heterogeneous nucleation sites. As a consequence, the yield strength at room temperature is increased due to the combined strengthening effect of dispersoid and precipitate particles together with the finer grain size. Recent tensile tests of Ti-6Al-4V/(TiC+TiB)-MMCs up to 650 °C revealed a superior tensile strength at RT with a degradation around 600 °C [31]. However, tensile and creep test results at elevated temperatures for Ti6242/(TiB)-MMCs have not been published so far. The addition of intermetallic γ -TiAl alloy particles to a Ti-base alloy was reported first by Decker et al. [32,33]. These authors showed that the addition of 10–20 m.% of TNM powder increases the strength significantly at the expense of RT ductility, using Ti-6Al-4V [33] and Ti6242S [32] powder as matrix material densified via SPS. In case of the Ti6242S matrix, the addition of 10 m.% TNM particles smaller than 20 μm were considered to be an optimum in increasing strength but maintaining ductility as reported in Ref. [32] and was therefore chosen to be investigated in more detail. The present paper will clarify the strengthening mechanisms activated in Ti6242S reinforced with TNM powder particles and B at RT and elevated temperatures by using high-resolution electron microscopy along with ex situ and in situ X-ray diffraction. Finally, tensile and creep tests show the potential of the newly-designed Ti-MMCs and alloys for their use at 600 °C.

C.2 Materials and methods

All powders used were gas atomized employing argon inert gas and subsequently classified by sieving. The Ti6242S powder (10–106 μm) was atomized by LPW Technology Ltd, UK, and the TNM powder (<20 μm) by the Helmholtz-Zentrum Geesthacht, Germany. The pre-alloyed Ti6242 powder containing 1 m.% B (150–500 μm) was provided by Carpenter Technology (formerly Puris), USA. The Ti6242S + 10 m.% TNM powder blend was mixed under argon atmosphere via a shaker mixer Turbula T2 C from the WAB Group, Switzerland. The chemical compositions of the powders were determined by means of X-ray fluorescence (XRF) spectroscopy for Ti, Al, Nb, and Mo. Inductively coupled plasma-atomic emission spectroscopy (ICP-AES) was employed for B and Si. To analyze the interstitial O impurities, carrier gas hot extraction was employed. The composition of the powder blend after densification by SPS was determined with the same methods. The results are summarized in Table C.1.

The powders and their blends were compacted to cylindrical samples with a diameter of 80 mm and a height of 14 mm by an SPS device of the type HP D 25 from FCT Systems

Table C.1: Chemical composition of the powder alloys and their blends evaluated either at the initial state or after SPS. The composition of the blend was calculated from the ingredients as well.

Variant		Elements [m.%]								
		Ti	Al	Sn	Zr	Mo	Si	Nb	B	O
Ti6242S ^a	Powder	bal.	6.00	2.04	3.98	2.03	0.08	-	-	0.19
Ti6242 + 1 m.% B ^a	Powder	bal.	6.28	1.84	4.26	1.84	-	-	1.010	0.11
TNM ^a	Powder	bal.	28.6	-	-	2.30	-	9.1	0.025	0.15
Ti6242S + 10 m.% TNM ^a	SPS	bal.	8.26	1.81	3.72	2.04	0.08	0.9	0.005	0.19
Ti6242S + 10 m.% TNM ^b	Blend	bal.	8.26	1.80	3.60	2.03	0.07	0.9	0.003	0.18

^aChemical analysis. ^bCalculated.

GmbH, Germany, at the Technische Universität Bergakademie Freiberg, Germany. The densification of the powder was reached under vacuum by applying mechanical pressure and pulsed electric current. For more details regarding the SPS process, the reader is referred to Ref. [15,16,34]. The powders used in this study were sintered with different parameters, i.e. varying dwell temperature and dwell time, which are collectively shown for each condition in Table 2. All samples were cooled to RT at a rate of about 90 K/min, within the SPS unit via natural convection cooling. The dense samples in as-SPS condition were metallographically examined by light optical microscopy (LOM) and scanning electron microscopy (SEM). To this end, specimens were taken from the center of the SPS disc, embedded into the hot mounting resin PolyFast from Struers, Germany, ground and subsequently either polished for 10 min, using a colloidal silica solution (OP-S suspension) from Struers, Germany, or etched in Kroll's reagent [35] for 8 s. All LOM images were recorded employing a Zeiss Axio Imager M1m, Germany. The SEM investigations were conducted on an EVO 50 from Zeiss, Germany, in back-scattered electron (BSE) mode at a maximum acceleration voltage of 20 kV. Energy-dispersive X-ray spectroscopy (EDX) was performed at a Tescan SEM of the type CLARA, Czech Republic, with an acceleration voltage of 15 kV in combination with the X-Max system and the Aztec software from Oxford Instruments, United Kingdom. X-ray diffraction (XRD) measurements were conducted on OP-S polished samples using

Table C.2: SPS process parameters used for each investigated variant. All variants were heated to their dwell temperature with 50 K/min under an applied load of 50 MPa. After the dwell time, the samples were cooled via natural convection with about 90 K/min.

Variant	Spark plasma sintering	
	Dwell temperature	Dwell time
Ti6242S	1100 °C	0 min
Ti6242 + 1 m.% B	1200 °C	3 min
Ti6242S + 10 m.% TNM	1100 °C	0 min
Ti6242S + 10 m.% TNM	1150 °C	0 min

Cu-K α radiation in an AXS D8 Advanced diffractometer from Bruker, United States. The data obtained and the corresponding Rietveld refinement [36] were used to identify the appearing phases and evaluate the phase fractions with an accuracy of ± 3 m.%, applying the software program TOPAS from Bruker, United States. High-energy X-ray diffraction (HEXRD) experiments were conducted at the side station P07B of the high-energy materials science (HEMS) beamline operated by the Helmholtz-Zentrum Geesthacht at PETRA III at the Deutsches Elektronen-Synchrotron (DESY) in Hamburg, Germany [37]. During the experiments on cylindrical samples ($\varnothing 5 \times 10$ mm³), 2D diffraction patterns were continually collected in transmission geometry using a PerkinElmer XRD 1621 flat panel detector with a pixel matrix of 2048×2048 and a pixel size of 200×200 μm^2 . A mean photon energy of 87.1 keV was selected corresponding to a wavelength of 0.1424 Å. The experimental setup was calibrated with LaB6 powder. The recorded Debye-Scherrer rings were azimuthally integrated using the data reduction software program Fit2D [38]. Besides RT measurements, in situ HEXRD phase evolution experiments were conducted using a modified quenching and deformation dilatometer DIL805A/D from TA Instruments (formerly Bähr Thermoanalyse GmbH), Germany. Samples in as-SPS condition were heated up to 500 °C and held for 30 min. Afterwards, the temperature was increased to 1150 °C at a heating rate of 2 K/min. An exposure time of 2 s per image provided an adequate peak-to-background intensity ratio during the experiments. Phase fractions and their dependence on time and temperature were evaluated by the intensity ratio method [39,40]. Weighting factors were derived from the results of Rietveld analysis, which was performed for selected temperatures. The appearance of upper harmonics at P07B has been considered in the evaluation.

In order to analyze transformation sequences, differential scanning calorimetry (DSC) measurements were carried out on SPS samples, utilizing heating rates between 10 and 40 K/min in Ar-atmosphere. The measurements were executed on a LabSYS Evolution of Setaram Instrumentation, France, whereby the weight of the specimens was around 45 ± 5 mg, and the specimens were enclosed by a 100 μl alumina crucible. The samples tested were homogenized at 1150 °C for 4 h in a vacuum furnace ($5 \cdot 10^{-6}$ mbar) from HTM-Reetz, Germany, prior to the DSC experiments.

Quasi-static tensile tests were carried out at RT, 300 °C, 450 °C, 550 °C, 600 °C, and 650 °C at a strain rate of 10^{-4} s⁻¹ on universal testing machines of the type Inspect 50-1 from Hegewald and Peschke, Germany, and AG-100 from Shimadzu, Japan, according to DIN EN ISO 6892-1. At maximum two specimens were tested at each temperature. The tensile and creep test specimens were eroded from the sintered discs by electrical discharge machining. The final tensile test samples had a diameter of 5 mm and a gauge length of 25 mm. The creep samples had a diameter of 6 mm and a gauge length of 30 mm. The creep tests were performed at a temperature of 600 °C under an applied load of 210 MPa, employing AET Technologies', France, TC30 and TC50 creep testing machines. Extensometer bars were used to determine the creep strain. Stable thermal conditions along the gauge length were guaranteed through

three attached thermocouples, monitoring and controlling the temperature.

Transmission electron microscopy (TEM) investigations were carried out on a JEOL JEM-2200FS, Japan, operating at 200 kV. The samples (3 mm in diameter) were electrolytically thinned to electron transparency using a Temu Pol-5 and the electrolyte A3 from Struers, Germany.

C.3 Results

C.3.1 Microstructure

After spark plasma sintering of the different powders according to Table C.2, the etched as-SPS samples were investigated by means of LOM. Ti6242S powder was sintered above $T_{\beta,trans}$, which is about 1000 °C for this alloy according to Ref. [3]. Additionally, DSC measurements on the SPS sample determined $T_{\beta,trans}$ to be 1006 ± 5 °C. The adjusted microstructure is shown in Fig. C.1a. The employed dwell temperature of 1100 °C leads to coarse β grains, whose grain boundaries are still visible through the enclosing α seam. This α seam at the former grain boundaries of the parent β grains is generated firstly while cooling, followed by the formation of several differently oriented α colonies within each β grain. Due to the cooling rate of about 90 K/min, as achieved in the SPS unit for the present sample dimensions, the α seam, the α colonies and the single α lamellae are coarse and, therefore, visible in the LOM image.

As shown in Fig. C.1b, the addition of 1 m.% B drastically refines the microstructure due to the tendency of B to form intermetallic Ti borides which are already present in the powder. These borides act as heterogeneous nucleation sites for β in the melt, e.g. during gas atomization, and throughout the subsequent solid-state phase transformations, i.e. during the SPS process. Heterogeneous nucleation at Ti borides was already utilized for Ti-6Al-4V [17] and γ -TiAl alloys [41,42] and confirms the observed refined microstructure.

The powder blends containing 90 m.% Ti6242S and 10 m.% TNM are sintered at two different temperatures according to Table C.2. At 1100 °C the TNM powder particles are totally embedded in the Ti6242S matrix, but still visible in the LOM image of Fig. C.1c. The α colonies are significantly smaller than those of the Ti6242S microstructure in Fig. C.1a. The finer colonies are attributed to the pinning of the β grain boundaries by TNM particles during sintering above $T_{\beta,trans}$. Furthermore, no enclosing α seam is apparent. Thus, it can be concluded that the α formation starts rather at the TNM particles than at the β grain boundaries.

Increasing the sintering temperature to 1150 °C leads to the dissolution of the TNM particles, which is shown in Fig. C.1d and correlates with data from Decker et al. [32]. At this temperature the grain size could be kept small when compared to Ti6242S in Fig. C.1a, even though the TNM particles have dissolved. The observed effect is caused by the grain

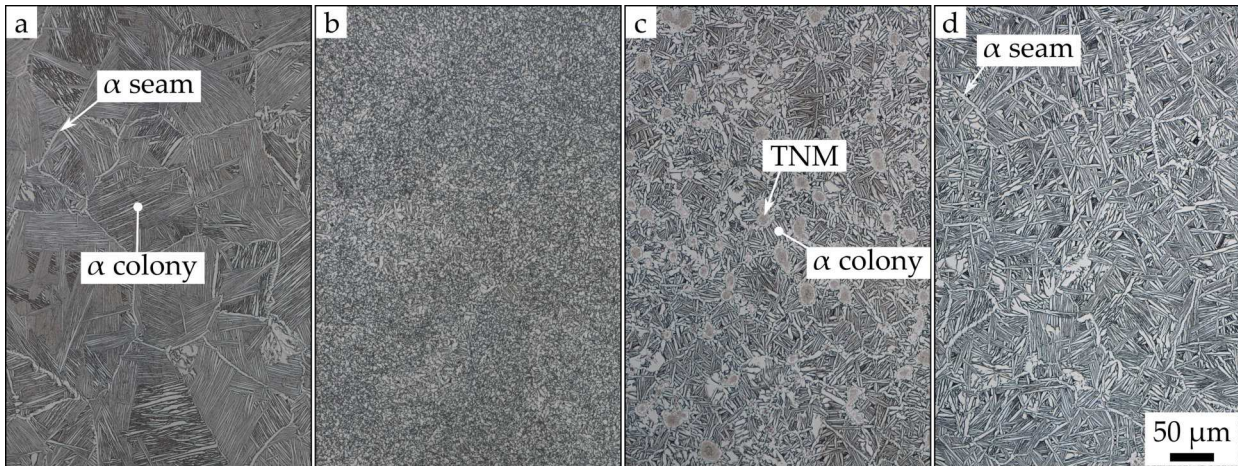


Figure C.1: LOM images of the Kroll etched specimens in as-SPS condition: a) Ti6242S; b) Ti6242 + 1 m.% B; c) Ti6242S + TNM, dwell temperature 1100 °C and d) Ti6242S + TNM, dwell temperature 1150 °C. a) The former β grains are apparent by the enclosing α seam. Parallel-oriented α -Ti lamellae are within the α colonies, which obviously nucleate at the α seam. b) A refined microstructure is visible when compared to a). c) The spherical TNM particles are recognizable between the refined colonies. d) All spherical TNM particles were dissolved into the Ti6242S matrix and the microstructure coarsened when compared to c) and a distinct α seam is again discernible (see text).

boundary pinning before the TNM particles have fully vanished. Afterwards, the short process time of SPS impedes grain coarsening. However, when compared to Fig. C.1c, the colony size is slightly larger and the α seam is again present at former β grain boundaries, facilitating the nucleation of colonies whose size is still refined when compared to the basic Ti6242S as-SPS microstructure, as shown in Fig. C.1a.

In the next section, a more detailed investigation of the as-SPS samples was conducted. Therefore, SEM images were taken in BSE mode. As shown in Fig. C.2a, the microstructure of the Ti6242S specimen contains the retained β phase (bright contrast) which either separates the parallel arranged α lamellae (gray) within a colony or in between these colonies. Spot EDX measurements on the α and β phase confirm the tendency of Al to accumulate in α , whereas Mo as well as Zr partition to the β phase, as does Sn, albeit to a lesser extent. The quantitative EDX results are presented in Table C.3. The Al and Mo distributions agree with Ref. [4], but in case of Zr and Sn the enrichment is contrary to literature, where enrichment in the α phase would be expected [4].

A comparable microstructure can be seen in Fig. C.2b for the Ti6242S alloy, where TNM particles were added and the blend was sintered at 1100 °C (see Table C.2). The TNM particles are still visible in the SEM image, appearing spherical and dark contrasted in BSE mode due to the higher Al content of the TNM alloy surrounded by gray α phase. EDX measurements on the α and β phase close to the TNM particle as well as on the TNM particle are summarized in Table C.3. The Al content in both phases, α and β , is increased

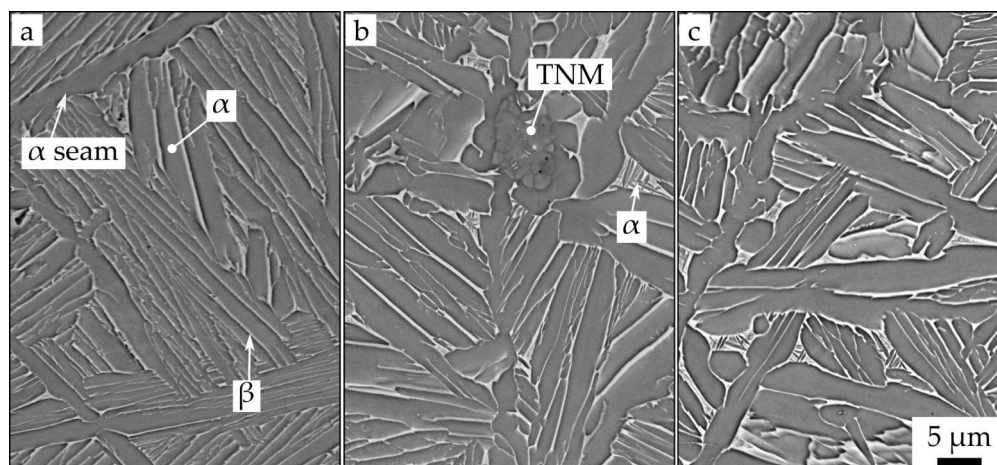


Figure C.2: SEM images of Kroll etched SPS samples taken in BSE mode: a) Ti6242S, b) Ti6242S + TNM, dwell temperature 1100 °C and c) Ti6242S + TNM, dwell temperature 1150 °C. a) The Ti6242S microstructure consists of gray contrasted α -Ti lamellae surrounded by the bright β phase. b) Inside the coarser β grains, fine α platelets are visible (as indicated). Similar α platelets can be seen in c), but without the presence of TNM particles.

Table C.3: Chemical composition of the phases and target areas determined by spot or area EDX measurements.

Variant	Phase or area	Elements [m.%]						
		Ti	Al	Sn	Zr	Mo	Si	Nb
Ti6242S	α	bal.	6.7	2.0	3.9	0.7	<0.2	-
	β	bal.	4.0	2.6	6.5	7.7	<0.2	-
Ti6242S + 10 m.% TNM 1100 °C	α	bal.	7.9	2.3	3.8	0.4	<0.2	0.0
	β	bal.	5.7	2.1	5.9	6.0	<0.2	1.5
	TNM particle	bal.	28.0	<0.2	<0.2	2.4	<0.2	9.1
Ti6242S + 10 m.% TNM 1150 °C	α	bal.	8.7	1.9	3.4	0.5	<0.2	0.5
	β	bal.	5.5	2.4	5.3	8.0	<0.2	1.4
	Area scan	bal.	8.0	2.0	4.1	2.2	<0.2	0.8

when compared to Ti6242S, confirming that the TNM particles already started to dissolve in the matrix. However, the center of the TNM particles still has its original composition (compare Table C.1, Table C.3). When comparing the microstructure of the pure Ti6242S in Fig. C.2a with the sintered blend in Fig. C.2b, expanded β phase areas, containing fine α phase, are visible. These α platelets harden the β phase, which results in an improvement of the mechanical properties as already reported for the Ti-6Al-4V alloy [29]. A similar α microstructure is adjusted in expanded β phase areas by sintering the Ti6242S + TNM blend at 1150 °C, see Fig. C.2c. All TNM powder particles have homogeneously dissolved into the matrix, whereby Al further accumulates in the α phase, whereas Nb and Mo are enriched in the β phase, as seen in Table C.3. An EDX area scan yielded a chemical composition of Ti-8.0Al-2.0Sn-4.1Zr-2.2Mo-0.8Nb, which is in agreement with the values in Table C.1,

demonstrating the accuracy of the EDX quantification for these elements.

The pre-alloyed Ti6242 + 1 m.% B powder was sintered at 1200 °C for 3 min, resulting in the microstructure shown in Fig. C.3. The microstructure consists of black Ti borides and gray α phase surrounded by bright β phase. The α phase appears globular and no longer attains the shape of lamellar colonies. The α grain size is significantly smaller when compared to the pure Ti6242S alloy shown in Fig. C.1a. During the sintering at 1200 °C, the borides prevent an extensive growth of the β grains above $T_{\beta,trans}$ and act as heterogeneous nucleation sites during heating and cooling. Therefore, the B-containing microstructure represents the finest one of all the investigated microstructures. Qualitative spot EDX measurements on the acicular, black-appearing phase confirmed the presence of finely dispersed Ti borides. A quantitative determination of the light element B was not possible.

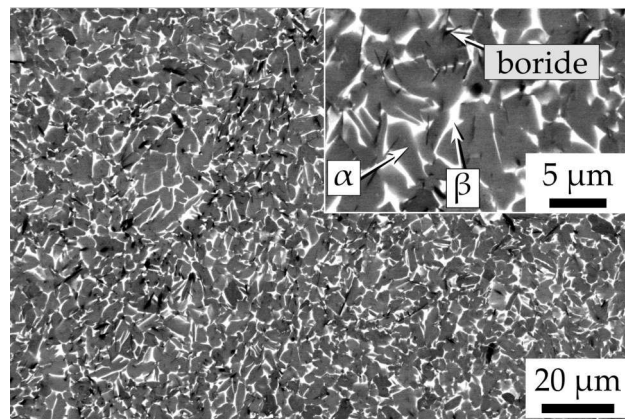


Figure C.3: SEM images of OP-S polished specimens in BSE mode: Ti6242 + 1 m.% B, whereby the insert shows microstructural details at a higher magnification. The acicular phase is identified as TiB, which appears dark in the BSE contrast. The SEM image shows finely dispersed borides in a fine globular microstructure.

C.3.2 X-ray diffraction

The samples in as-SPS condition were investigated by means of XRD to identify the phases appearing in the microstructure as well as to determine their phase fraction at RT. In Fig. C.4 diffraction patterns are shown where the intensity is plotted logarithmically as a function of the 2θ angle along with the peak positions of α , α_2 , β , and TiB. The top graph (red color) shows the spectrum of Ti6242S serving as a reference, where α and β peaks are identified. The application of Rietveld refinement resulted in 90 m.% α phase and 10 m.% β phase. The weak peaks at 41.5° and 54.0° occur in any XRD pattern in Fig. C.4 and could not be assigned to any mentioned phase. However, the HEXRD measurement discussed below does not show such peaks, which is why they are neglected in the following discussion.

The next graph (blue) was obtained for a Ti6242 sample containing 1 m.% B. Rietveld refinement resulted in 89 m.% α phase and 11 m.% β phase by taking only these two phases

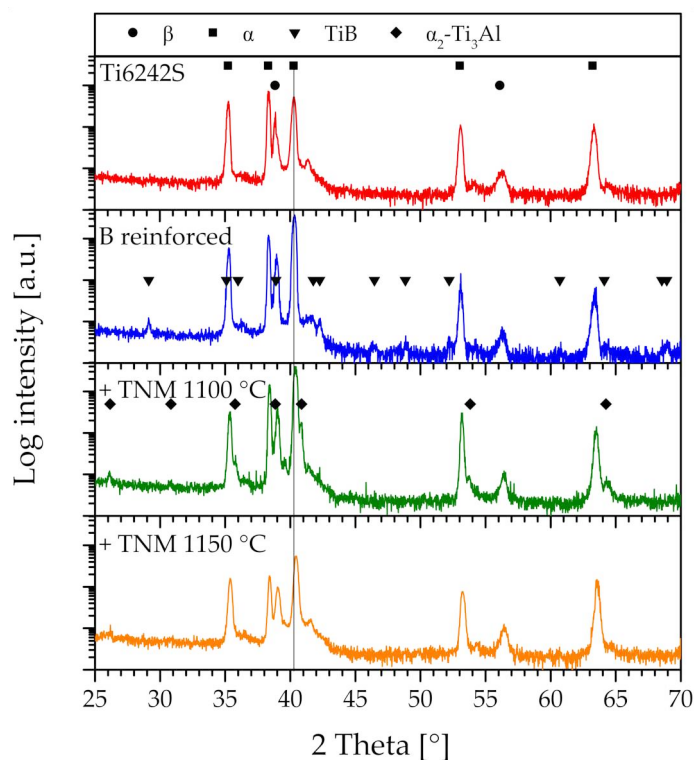


Figure C.4: XRD intensity spectrum (logarithmic intensity scale) of four samples in as-SPS condition. Due to different powder blends and sinter temperatures in use, different phases can be identified (see text).

into account. However, the XRD intensity spectrum also exhibits peaks that belong to orthorhombic TiB (B27 structure [9]), e.g. at 29.2° or 46.5° . These peaks confirm the presence of Ti borides, also detected in the SEM micrograph (Fig. C.3) and associated EDX measurement. Due to their low phase fraction and orthorhombic structure, their peak-to-background ratio is too weak for quantitative Rietveld analysis. The peak positions, however, fit the indicated orthorhombic B27 structure, rather than the hexagonal TiB_2 structure, which could be taken next into consideration [9,19]. Supposing that each B atom in the alloy forms a monoboride together with one Ti atom, while Ti has 4.4 times the molar mass of B, 1 m.% boron in our alloy should result in 5.4 m.% TiB.

The third graph from the top (green) in Fig. C.4 shows the intensity spectrum of Ti6242S which contains 10 m.% TNM powder particles and was sintered at 1100°C , i.e. the blend for which a complete dissolution of the TNM particles has not yet been achieved. The spectrum reveals additional peaks, e.g. at 26.1° , 35.8° , 40.9° , 53.7° and 64.1° , belonging to the α_2 phase. Since both α and its ordered counterpart α_2 show a hexagonal crystal structure, superlattice peaks, such as at 26.1° , are a clear indication of the existence of the α_2 phase [43]. The other α_2 -peaks can be found on the right side of the corresponding α peaks, which is due to a slightly different hexagonal lattice when compared to the disordered α phase, including the chemical heterogeneity of undissolved TNM particles. The α peaks are also shifted to higher

2θ angles, e.g. from 40.38° in Ti6242S (marked with a vertical line in Fig. C.4) to 40.42° in the Ti6242S + TNM 1100°C variant. In the TNM-containing sample this is caused by elements stemming from already dissolved TNM powder particles which in turn change the lattice parameters. The β phase fraction is 8 m.%. An exact differentiation between the α and α_2 phase fraction cannot be made and therefore their fraction adds up to 92 m.%. The bottom graph in Fig. C.4 shows the same Ti6242S + TNM blend sintered at 1150°C , leading to a total dissolution of the TNM particles. In the spectrum, the superlattice of α_2 peak is barely detectable at 26.1° . When compared to the specimen sintered at 1100°C , no additional α_2 peaks can be found on the right side of the α peaks. It is concluded that both α and α_2 exhibit a hexagonal lattice with similar lattice parameters, due to a homogeneous distribution of the elements. A separation into α and α_2 phase fractions is also not possible. Their collective phase fraction was therefore summed up to 91 m.%. The remaining phase fraction is attributed to the β phase. Again, a peak shift to higher 2θ angle can be identified when comparing with the α peaks of the Ti6242S variant (marked with a vertical line). The shift is a consequence of the change in the lattice parameter by additional elements. The corresponding lattice volume of the hexagonal α phase was evaluated, and this resulted in a reduction of the unit-cell volume by 1% owing to the dissolution of the TNM particles. Yet at the same time, the α/α_2 and β phase fractions stay at 90 ± 3 and 10 ± 3 m.%, respectively, for all variants.

C.3.3 High-energy X-ray diffraction

First, for the sake of comparison, HEXRD experiments were conducted on Ti6242S and Ti6242S + TNM 1150°C samples in the as-SPS condition at RT. Rietveld analyses of both samples resulted in $\alpha/\alpha_2 = 90 \pm 2$ and $\beta = 10 \pm 2$ m.%, and the unit cell volume of α was found to decrease by roughly 1% in the course of dissolving the TNM particles. The α_2 phase could be detected in the as-SPS condition of Ti6242S + TNM 1150°C , but not in the Ti6242S variant. These results confirm those provided in chapter C.3.2. However, despite the high brilliance of the synchrotron beam and the good peak-to-background ratio, the respective contribution of α and α_2 could not be measured quantitatively.

Secondly, besides RT experiments, in situ heating HEXRD experiments were also conducted. Therefore, a Ti6242S + TNM 1150°C sample in as-SPS condition was heated to 1150°C . The intensity plot in Fig. C.5a confirms the presence of α , α_2 and β at 500°C , whereby the α/α_2 fraction is 90 ± 2 m.% and the remaining 10 ± 2 m.% phase is β . When increasing the temperature, first the α_2 peaks vanish. This behavior can be observed most distinctly by tracing the α_2 superlattice reflections at small 2θ angles. Upon further heating, also the α reflections vanish for the benefit of β . To quantitatively determine the α solvus temperature $T_{\alpha_2, \text{solv}}$ as well as the β transus transformation temperature $T_{\beta, \text{trans}}$, Fig. C.5b shows the summed intensity of selected α_2 superlattice reflections ($10\bar{1}1$ and $11\bar{2}0$, black curve) and

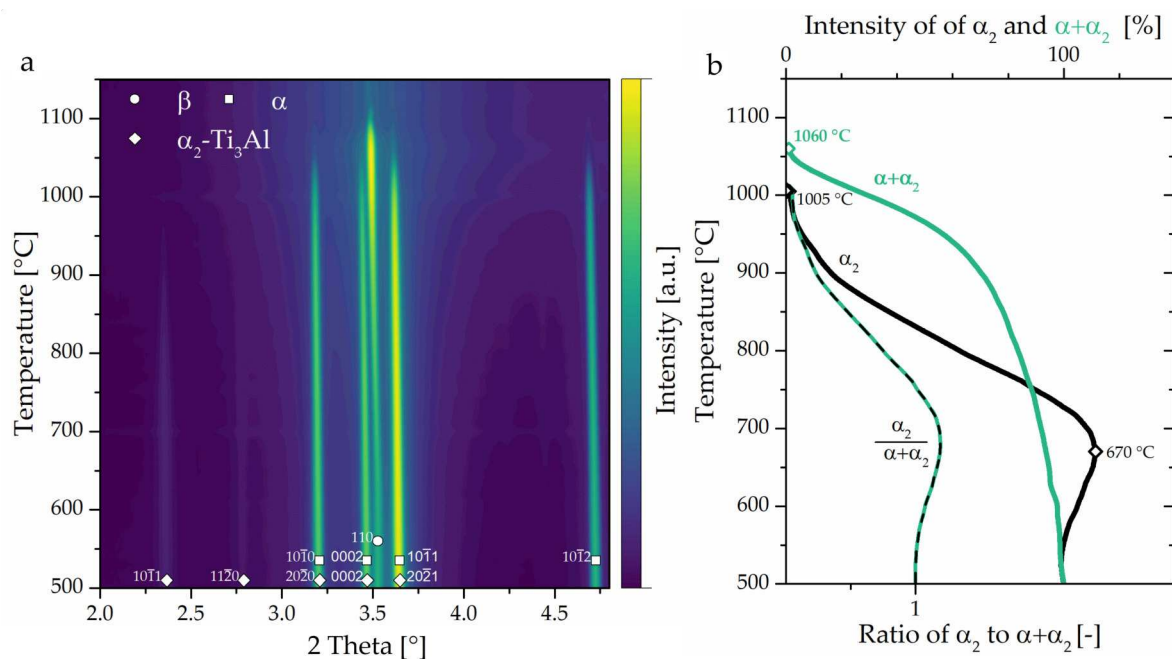


Figure C.5: In situ HEXRD measurement on the Ti6242S + TNM 1150 °C sample in as-SPS condition. a) The measured intensity is plotted logarithmically, showing α , α_2 and β at 500 °C. b) The intensity of α_2 superlattice reflections and $\alpha+\alpha_2$ fundamental reflections as well as their ratio as a function of the temperature, where intensity values are normalized to the intensity observed at 500 °C. The solvus temperatures of α_2 and α were determined to be 1005 and 1060 °C, respectively, where the intensity decreased to 1 % of its maximum value.

fundamental peaks (α : $10\bar{1}0$, $10\bar{1}1$ and $10\bar{1}2$, green curve). The intensity of α_2 starts to increase at roughly 600 °C, reaching a maximum at 670 °C ($T_{\alpha_2,max}$). Consequently, the α_2 phase was not precipitated entirely from α in the as-SPS condition, and further ordering was promoted by an increase in temperature during the HEXRD experiment. Above 670 °C, the α_2 intensity and, thus, its phase fraction decreases. It drops below 1% of the intensity maximum at 1005 °C, which is set as $T_{\alpha_2,solv}$. The α solvus temperature, which equals $T_{\beta,trans}$, was determined as 1060 °C. This result is in accordance with the DSC measurements, which found $T_{\beta,trans}$ to be 1054 ± 7 °C. Note, when $T_{\beta,trans}$ is exceeded, a single phase field region is reached, and thus grain growth occurs during further heating, which can also be recognized by the decreasing intensity of the β peaks in Fig. C.5a. Finally, the ratio between the α_2 and $\alpha + \alpha_2$ intensities is also shown in Fig. C.5b. As discussed above, the change in the ratio points out that both α_2 and α are present side by side and their respective phase fraction increases or decreases at the expense of the other in the course of ordering or disordering transformations. Otherwise the ratio would be constant. Based on the HEXRD intensities of the Ti6242S + TNM 1150 °C sample, the phase fractions of α/α_2 (collective amount) and β were evaluated as a function of the temperature and plotted in Fig. C.6. In addition, the transformation temperature, mentioned above were marked for further discussions.

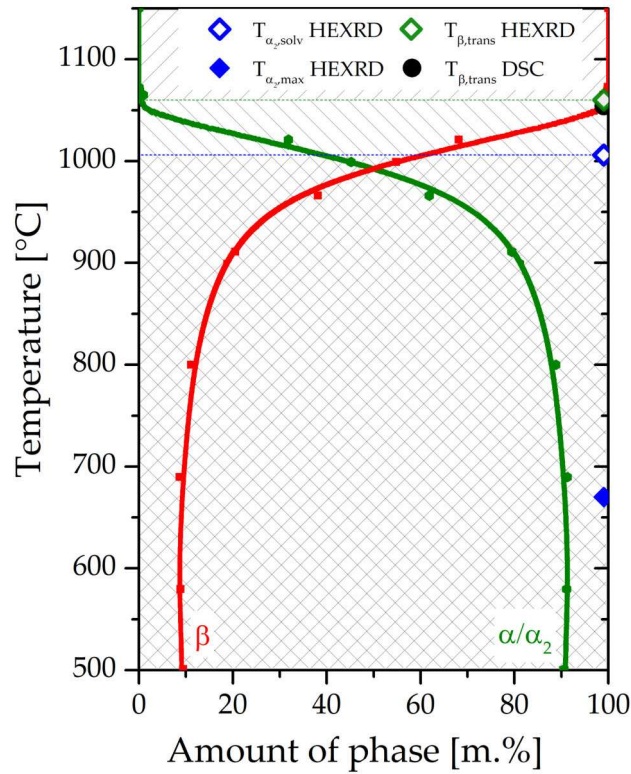


Figure C.6: Phase fraction diagram of the Ti6242S + TNM 1150 °C sample with the chemical composition of Ti-8.3Al-1.8Sn-3.7Zr-2.0Mo-0.9Nb-0.08Si (m.%), including relevant temperatures (see text).

C.3.4 Transmission electron microscopy

In order to examine the appearance of the ordered α_2 -Ti₃Al phase in the microstructure, TEM investigations were conducted on a Ti6242S and a Ti6242S + 10 m.% TNM 1150 °C specimen in as-SPS condition. Diffraction patterns (DP) can disclose the presence of the ordered α_2 due to superlattice reflections, which would be missing in the case of a completely disordered hexagonal α phase [44,45]. Figure C.7a and b show DP of a Ti6242S and a Ti6242S + TNM 1150 °C sample, respectively, in as-SPS condition tilted in the same [0001] zone axis. This comparison clarifies that in the Ti6242S sample, the α -phase is completely disordered due to missing superlattice reflections. Conversely, in Ti6242S + 10 m.% TNM 1150 °C in as-SPS condition, where the superlattice reflections are located between the regular hexagonal reflections, the α_2 phase is present. Therefore, a detailed microstructural investigation was conducted on this specimen, as shown in Fig. C.8. Figure. C.8a shows a high angle annular dark field (HAADF) scanning transmission electron microscopy (STEM) image of an α/β colony. The HAADF STEM provides an atomic number (Z) contrast, i.e. the heavier the elements in the phase, the brighter the phase appears in the image [46]. As a result, the β phase, which is enriched in heavy elements such as Mo and Nb, appears in bright contrast, whereas the Al-enriched α phase appears in dark contrast. Inside the bright β phase, no

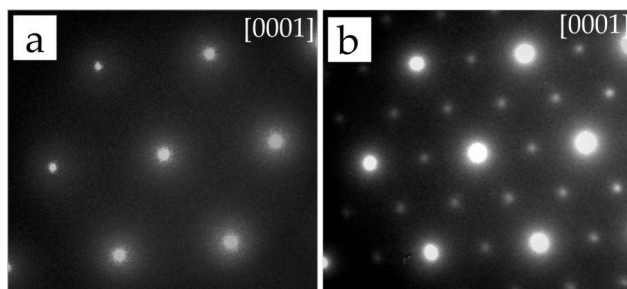


Figure C.7: DP of the $[0001]$ zone axis of the α phase: a) Ti6242S and b) Ti6242S + TNM 1150 °C, to show that superlattice reflections, that belong to the α_2 phase, are only present in the Ti6242S + TNM 1150 °C variant.

contrast differences are detectable, so no additional α phase has formed in the fine, retained β lamellae. This is in contrast to extended β phase areas, as analyzed in Fig. C.2c. Selective area diffraction (SAD) was conducted on the α phase. The corresponding DP again discloses the presence of the ordered α_2 due to superlattice reflections. The insert in Fig. C.8b shows the DP of a selected area taken in $[1\bar{2}1\bar{3}]$ zone axis. By using the $10\bar{1}1_{\alpha_2}$ superlattice reflection, a dark field (DF) image was taken, shown in Fig. C.8b. The illuminated areas are ordered domains (OD) of α_2 phase, whereas the disordered areas remain dark. The size of the OD is below 10 nm and they occupy almost the entire grain, occasionally only separated by anti-phase boundaries (APB), appearing as dark contrasted lines in the DF image.

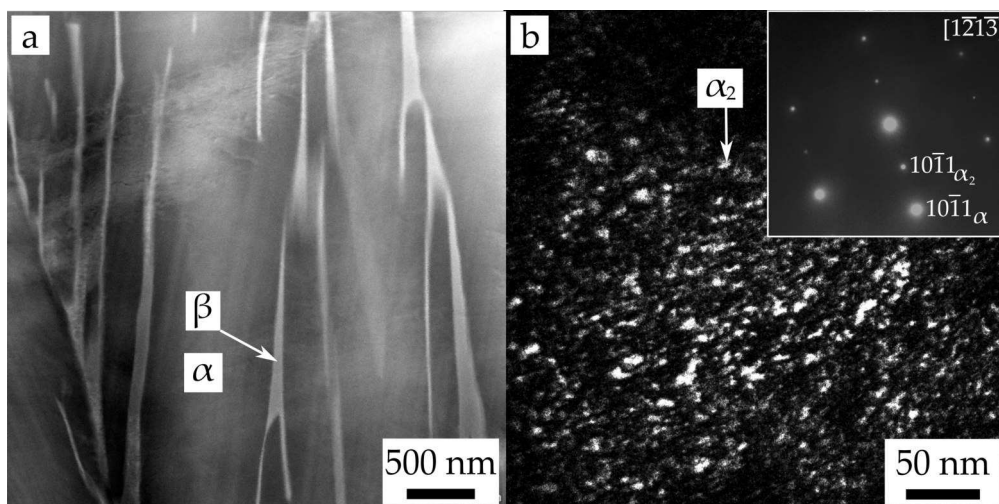


Figure C.8: a) TEM investigation of the Ti6242S + TNM 1150 °C sample in as-SPS condition. DF STEM image of α/β colonies, where the dark α lamellae are separated by bright, retained β phase. b) DF image of an α lamella. The insert shows the corresponding $[1\bar{2}1\bar{3}]$ diffraction pattern of the selected area, which reveals a hexagonal structure as well as superlattice reflections. The $10\bar{1}1_{\alpha_2}$ superlattice reflection was used for the DF image. This $10\bar{1}1_{\alpha_2}$ DF image illuminates nanometer sized ordered α_2 domains separated by disordered α phase or anti-phase boundaries, which appears in dark contrast.

C.3.5 Mechanical testing

The samples in as-SPS condition were further investigated by evaluating their mechanical properties. At first, tensile tests were carried out at different temperatures. As a result, the yield strength at an offset of 0.2% plastic strain and the plastic strain to fracture were evaluated for each tensile test specimen shown in Fig. C.9a and Fig. C.9b, respectively. Decker et al. [32] already reported that the addition of 10 m.% of TNM powder particles to the Ti6242S matrix leads to enhancement of the yield strength throughout the entire tested temperature range when compared to pure Ti6242S, see Fig. C.9a. Comparing the yield strength of Ti6242S + TNM blends with partially and completely dissolved particles, no difference can be seen. The addition of 1 m.% B shows an increase in yield strength of almost 100 MPa when compared to the Ti6242S + TNM variants. This can be seen up to 550 °C. Above, grain boundary sliding becomes dominant in the fine-grained microstructure of the B-containing variant (Fig. C.1b) and the curve drops sharply. Concurrently, the plastic strain to fracture increases from 2% at RT to above 40% at 650 °C because of the just mentioned grain boundary sliding. The sudden drop in the yield strength of the B reinforced variant above 550 °C, however, cannot be seen in the TNM containing variants.

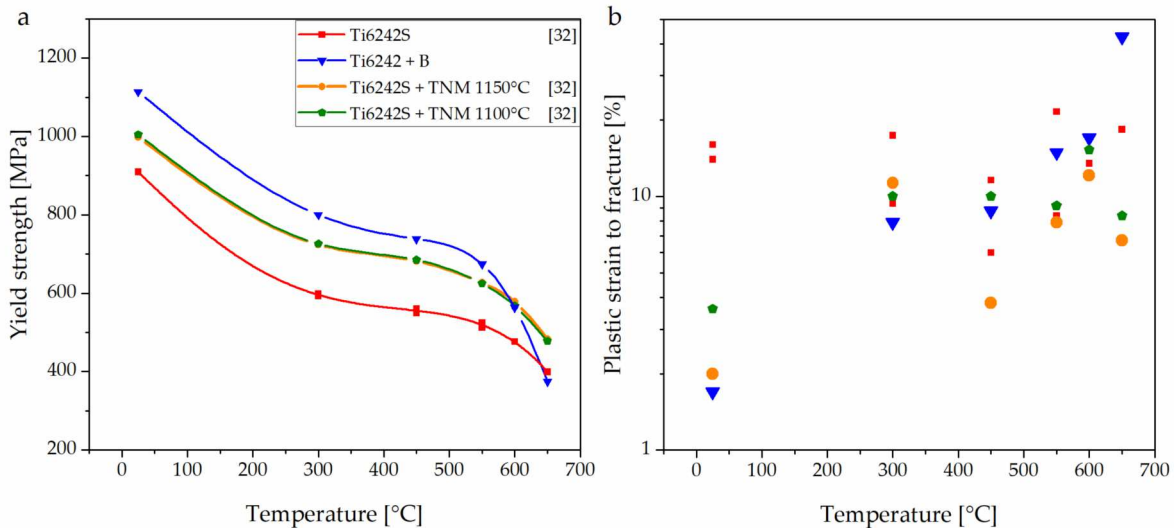


Figure C.9: The tensile test results show an enhanced yield strength for the B reinforced alloy variant up to 550 °C when compared to the values provided by Decker et al. [32]. At elevated temperatures, grain boundary sliding becomes dominant in the fine-grained B-containing variant, leading to a deteriorating yield strength but increasing fracture elongation, as shown in b).

In addition, in the present study creep tests were conducted at 600 °C under an applied load of 210 MPa on all variants in as-SPS condition. The resulting creep strain (ϵ) as a function of time is shown in Fig. C.10. Crosses mark the position of the minimum creep rate ($\dot{\epsilon}_{min}$) for each curve, and the value of $\dot{\epsilon}_{min}$ is given next to the corresponding curve. The benchmark

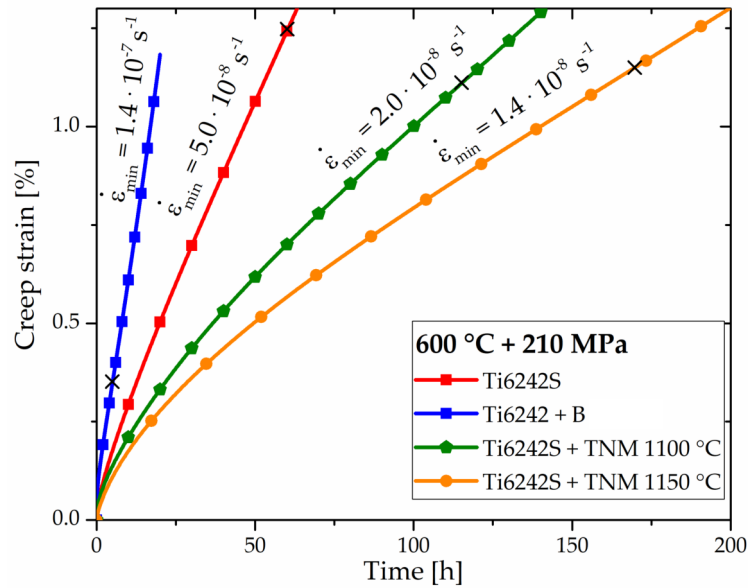


Figure C.10: Creep experiments are conducted at 600 °C under an applied load of 210 MPa for four different variants. Besides the creep curves, crosses on each curve mark the minimum creep strain rate, whose value is also given.

forms the Ti6242S in as-SPS condition reaching an $\dot{\epsilon}_{min}$ of $5.0 \cdot 10^{-8} \text{ s}^{-1}$ after 60 h. On the one hand, the fine-grained B containing variant, which shows the best tensile properties up to 550 °C because of the small grain size, has the highest $\dot{\epsilon}_{min}$ and thus reaches $\epsilon > 1\%$ creep strain already after 20 h under the applied load. On the other hand, the addition of TNM powder particles into the Ti6242S matrix improves the creep performance. In case of Ti6242S + TNM 1100 °C, $\dot{\epsilon}_{min}$ is significantly decreased to $2.0 \cdot 10^{-8} \text{ s}^{-1}$ after 115 h, resulting in a creep strain below 1% after 100 h under the applied load. The highest creep resistance is achieved for the Ti6242S + TNM 1150 °C variant with dissolved TNM where $\dot{\epsilon}_{min}$ of $1.4 \cdot 10^{-8} \text{ s}^{-1}$ is reached after 170 h.

C.4 Discussion

The technique of SPS is capable of producing dense near- α Ti-base alloys and their composites. All samples investigated in this study are in as-SPS condition (the process parameters are shown in Table C.2), which is a suitable state to allow the comparison of the different samples, due to equal cooling rates. The Ti6242S sample with a lamellar α/β microstructure in as-SPS condition, as shown in Fig. C.1a, contains coarse α colonies. This microstructure forms during moderate cooling from the β single phase field region ($T_{\beta,trans} = 1006 \pm 5 \text{ °C}$) and exhibits excellent mechanical properties which we consider to be the benchmark. This is confirmed by the tensile tests provided by Decker et al. [32] for Ti6242S in as-SPS condition, which show similar yield strength and elongation values similar to other

published data for Ti6242S [29], Ti6242 [2,47] or IMI834 (Ti-5.8Al-4Sn-3.5Zr-0.5Mo-0.7Nb-0.35Si-0.06C, m.%) [29]. Furthermore, the creep performance of Ti6242S in as-SPS condition as provided by the present study (Fig. C.10), is in the same range as that derived for Ti6242S, produced via the casting route [2], demonstrating the potential of the SPS technique.

The addition of 1 m.% B to a Ti6242 alloy in this study yields high-melting titanium monoborides TiB, as identified by means of SEM, EDX and XRD. These needle-shaped borides are finely distributed in the matrix. The presence of borides leads to a drastic decrease in grain size (see Fig. C.1b) due to heterogeneous nucleation. Furthermore, the microstructure changes to a non-lamellar one, which contains globular α phase surrounded by retained β phase, see Fig. C.3. Grain boundary strengthening strongly affects the tensile properties. The TiB particles seem to provide only a minor strengthening contribution in the form of dispersoid strengthening according to Ref. [18,48-51], which can be split into two parts: Orowan strengthening and load transfer mechanism. The former is negligible due to the large size and inter-particle spacing of TiB, but the latter provides significant strengthening due to the amount of TiB with a high aspect ratio. As shown in Fig. C.9, the yield strength could be increased to about 1100 MPa at RT for the TiB composite. This value exceeds the Ti6242S + TNM variants by about 100 MPa. An elongation to fracture of 1.7% could be maintained, despite the high amount of acicular brittle TiB. However, the strengthening effect of the fine α grain size gets lost at 600 °C due to grain boundary sliding [49], which appears at high temperatures for fine-grained microstructures and results in a drop of the yield strength and an increase in ductility. As a consequence, the creep resistance at 600 °C deteriorates, caused by diffusion-controlled creep, which is pronounced for small grain sizes. Additionally, the B-reinforced variant contains no Si to form silicides, that would further improve the high-temperature properties [1].

Decker et al. [32] started mixing different amounts of TNM powder with Ti6242S, achieving an increase in yield strength. The Ti6242S variants with 10 m.% TNM particles (<20 μm particle size) and spark plasma sintering at 1100 °C or 1150 °C show an increase in yield strength of about 100 MPa compared to the benchmark Ti6242S sample and simultaneously maintain a fracture elongation above 2%, see Fig. C.9. In the present study, creep experiments were conducted on these Ti6242S + TNM variants, which reveal the improvement of the creep resistance, i.e. a decrease in $\dot{\epsilon}_{min}$ by half a magnitude. Consequently, 1% creep strain is still not reached after 100 h at 600 °C under the applied load of 210 MPa, as shown in Fig. C.10. Regarding the tensile and creep results, the activated strengthening mechanisms have an effect up to 600 °C, no matter whether the TNM particles are dissolved in the Ti6242S matrix (SPS at 1150 °C) or not (SPS at 1100 °C). Therefore, it is concluded that there is no composite effect, but rather one that is traceable to the refinement of the microstructure and a change in the chemical composition. The refinement of the α colonies, and hence the reduction in the effective length for dislocation slip, is controlled by heterogeneous nucleation at the TNM particles during cooling, e.g. during transformation of

β into α . Partial heterogeneous nucleation at the TNM particles is suggested by the absence of an α seam in Fig. C.1c. Note, that the cooling rate, which is responsible for this α seam, stays roughly the same for all samples. As soon as the TNM particles are dissolved, grain growth of the β phase takes place, attributed to the lack of particles that effectively pin the β grain boundaries. Furthermore, the nucleation starts again exclusively at the parent β grain boundaries, confirmed by the α seam, as indicated in Fig. C.1d. Consequently, slightly coarser grain structures are present in the Ti6242S + TNM 1150 °C variant when compared to the variant sintered at 1100 °C. Next to the α colonies, extended β grains appear at triple junctions of the TNM containing variants (see Fig. C.2b and c). In general the large β grains would decrease the high-temperature strength [4], but the precipitation of α phase according to the Burgers orientation relationship again hardens it [4,52]. However, these small crossed α platelets could not be found in the retained β phase between the α lamellae of the α colonies (see Fig. C.8a) as reported in Ref. [29,52]. Note that the adjustment of the lamellar spacing, which is almost equal for the three Ti6242S variants (see Fig. C.2), is not crucial as the retained β phase in-between the parallel-oriented α lamellae easily enables the transfer of slip across the phase boundaries [4]. Therefore, it is concluded that the colony size is the major factor, which increases the strength of the TNM-containing variants by decreasing the effective length for dislocation slip.

An increase of 50 °C in the dwell temperature is enough to dissolve the TNM particles, which can still be identified at 1100 °C dwell temperature by employing SEM (see Fig. C.2b). At a dwell temperature of 1150 °C, the TNM particles are dissolved homogeneously in the β matrix of the Ti6242S alloy. As a consequence of the change in the overall chemical composition, $T_{\beta,trans}$ increases to about 1060 °C, which is 60 °C above $T_{\beta,trans}$ of Ti6242S. Concurrently, the phase fractions at RT stay the same, i.e. 10 ± 2 m. % β and 90 ± 2 m. % α/α_2 . However, due to the change in the chemical composition of the phases, additional strengthening mechanisms take place. The β phase exhibits an enrichment in Nb, shown in Table C.3, leading to solid solution strengthening [4]. The majority phase α shows enrichment in Al, which leads to precipitation hardening by the formation of the intermetallic α_2 -Ti₃Al phase smaller than 10 nm inside the α phase. Although the absolute amount of the α_2 phase could not be determined, its presence was confirmed by XRD (Fig. C.4), HEXRD (Fig. C.5) and TEM (Fig. C.8). Furthermore, the in situ HEXRD experiment showed the α_2 -maximum at 670 °C and $T_{\alpha_2,solv}$ at 1005 °C, thus about 355 °C above $T_{\alpha_2,solv}$ of the Ti6242S alloy [4,29]. The α_2 phase strengthens the Ti6242S + TNM variants at the expense of ductility. This behavior can be seen for the new Ti6242S + TNM alloy in the tensile results, presented in Fig. C.9. Furthermore, the strengthening effect endures across the entire temperature range tested, seen by the parallel shift in the yield strength compared to the benchmark Ti6242S sample. The existence of α_2 benefits the creep resistance, as seen in Fig. C.10. This proves the potential of the Ti6242S + TNM alloy for use at service temperatures up to 600 °C, which already exceed the maximum service temperature of 500 °C of Ti6242 [4], 540 °C of

Ti6242S [28] and 550 °C of IMI834 [4].

The Ti6242S + 10 m.% TNM 1150 °C variant, where the TNM particles are completely dissolved and a chemical homogenization has taken place, represents a new alloy whose chemical composition can be determined by adding the mass fractions of the blend's components, as shown in Table C.1. This newly manufactured alloy, Ti-8.3Al-1.8Sn-3.7Zr-2.0Mo-0.9Nb-0.08Si (m.%), represents a more ductile Ti-14Al-20Nb-3.2V-2Mo (m.%) variant at RT, which is called the Super Alpha2 alloy with excellent high-temperature properties [53]. Moreover, the maximum service temperature of Ti-6Al-based alloys of around 550 °C is already surpassed by the newly developed alloy in as-SPS condition. Nevertheless, an adjustment of the microstructure by a subsequent heat treatment or thermomechanical treatment, based on the phase fraction diagram in Fig. C.6, will further improve the mechanical properties of the new alloy, which is currently under investigation.

C.5 Summary

Spark plasma sintering was applied to generate new Ti-base alloys or composites with advanced mechanical properties up to 600 °C and is a straightforward tool to design new alloys or composites in a fast and independent manner on the basis of pre-alloyed powder. The addition of B to the Ti6242 alloy improves the strength of the material by about 200 MPa at RT, when compared to the Ti6242S alloy, traceable mainly to the fine-grained globular α microstructure and, to a lesser extent, to a load transfer mechanism on the needle-shaped TiB. Here, the borides act as heterogeneous nucleation sites for the α transformation. The strength values of the Ti6242/TiB-MMC are always the highest compared to the other alloys investigated up to 550 °C. However, at higher temperatures the fine-grained structure deteriorates, which is also reflected in the creep results.

The Ti6242S + TNM blend sintered at 1100 °C forms a composite, where the TNM particles still appear in the microstructure, whereas when sintering at 1150 °C the TNM particles got entirely dissolved into the matrix and a new alloy was generated: Ti-8.3Al-1.8Sn-3.7Zr-2.0Mo-0.9Nb-0.08Si (m.%). The microstructures are lamellar and formed during cooling from the β single phase field region. The β grain size could be kept small in the Ti6242S + TNM variants due to grain boundary pinning by the TNM particles. When compared to the Ti6242S microstructure, the α colony size was refined due to the nucleation at the boundaries of the small β parent grains, confirmed by an α seam in the 1150 °C variant. The new Ti-8.3Al-1.8Sn-3.7Zr-2.0Mo-0.9Nb-0.08Si (m.%) alloy manufactured at 1150 °C from the Ti6242S + TNM blend enables the strengthening of the Al-enriched α phase by intermetallic α_2 -Ti₃Al precipitates, which were identified by their superlattice reflections by means of (HE)XRD and TEM. Their domain size is estimated to be around 10 nm and they are completely stable up to 670 °C, which is essential for application. The Ti6242S +

TNM variants show an equally improved tensile yield strength across the tested temperature range, but the newly developed Ti alloy exhibits a better performance during creep at 600 °C and 210 MPa. The outcomes prove that the strengthening is due to the refinement of the colonies as well as the alloying of additional elements rather than the presence of a metal matrix composite. Therefore, the high Al- and Nb-containing alloy further exceeds the service temperature limit of 550 °C established by Ti-6Al base alloys.

C.6 References

- [1] C. Leyens, M. Peters, *Titanium and Titanium Alloys: Fundamentals and Applications*, Wiley-VCH, Weinheim, Chichester, 2003, 3527305343.
- [2] D. Eylon, S. Fujishiro, F.H. Froes, Titanium alloys for high temperature applications — a review, *High Temp. Mater. Process.* 6 (1984) 1685, DOI: 10.1515/ HTMP.1984.6.1-2.81 .
- [3] W. Sha, S. Malinov, *Titanium Alloys: Modelling of Microstructure, Properties and Applications*, Woodhead Pub, Cambridge, 2009, 9781439801482.
- [4] G. Lütjering, J.C. Williams, *Titanium*, Springer, Berlin Heidelberg, 2013, 9783540713982.
- [5] F.H. Froes, H. Friedrich, J. Kiese, D. Bergoint, Titanium in the family automobile: the cost challenge, *J. Occup. Med.* 56 (2004) 40–44, DOI: 10.1007/ s11837-004-0144-0.
- [6] B.P. Bewlay, S. Nag, A. Suzuki, M.J. Weimer, TiAl alloys in commercial aircraft engines, *Mater. A. T. High. Temp.* 33 (2016) 549–559, DOI: 10.1080/ 09603409.2016.1183068.
- [7] S. Mayer, P. Erdely, F.D. Fischer, D. Holec, M. Kasthuber, T. Klein, H. Clemens, Intermetallic β -Solidifying γ -TiAl based alloys from fundamental research to application, *Adv. Eng. Mater.* 19 (2017), 1600735, DOI: 10.1002/ adem.201600735.
- [8] P. McQuay, Cast gamma TiAl alloys: are we there yet? in: K.J. Hemker (Ed.), *Structural Intermetallics 2001: Proceedings of the Third International Symposium on Structural Intermetallic Minerals Metals & Materials Society*, 2001, pp. 83–90. Warrendale, Pa. 0873395115.
- [9] F. Appel, J.D.H. Paul, M. Oehring, *Gamma Titanium Aluminide Alloys: Science and Technology*, Wiley-VCH, Germany, 2012, 9783527315253.
- [10] S. Mayer, M. Kasthuber, H. Clemens, Advanced Titanium Aluminides - how to improve the creep resistance via compositional and microstructural optimization, *Mater. Sci. Forum* 941 (2018) 1484–1489. DOI: 10.4028/www.scientif ic.net/MSF.941.1484.
- [11] S. Dadbakhsh, R. Mertens, L. Hao, J. van Humbeeck, J.-P. Kruth, Selective laser melting to manufacture “in situ” metal matrix composites: a review, *Adv. Eng. Mater.* 21 (2019), 1801244, DOI: 10.1002/adem.201801244.
- [12] W.H. Yu, S.L. Sing, C.K. Chua, C.N. Kuo, X.L. Tian, Particle-reinforced metal matrix nanocomposites fabricated by selective laser melting: a state of the art review, *Prog. Mater. Sci.* 104 (2019) 330–379, DOI: 10.1016/j. pmatsci.2019.04.006.
- [13] T. DebRoy, H.L. Wei, J.S. Zuback, T. Mukherjee, J.W. Elmer, J.O. Milewski, A. M. Beese, A.

- Wilson-Heid, A. De, W. Zhang, Additive manufacturing of metallic components – process, structure and properties, *Prog. Mater. Sci.* 92 (2018) 112–224, DOI: 10.1016/j.pmatsci.2017.10.001.
- [14] S. Liu, Y.C. Shin, Additive manufacturing of Ti6Al4V alloy: a review, *Mater. Des.* 164 (2019), 107552, DOI: 10.1016/j.matdes.2018.107552.
- [15] T. Voisin, J.-P. Monchoux, L. Durand, N. Karnatak, M. Thomas, A. Couret, An innovative way to produce γ -TiAl blades: spark Plasma Sintering, *Adv. Eng. Mater.* 17 (2015) 1408–1413, DOI: 10.1002/adem.201500019.
- [16] P. Cavaliere, *Spark Plasma Sintering of Materials: Advances in Processing and Applications*, Springer International Publishing, 2019, 9783030053277.
- [17] W. Lu, Di Zhang, X. Zhang, Y. Bian, R. Wu, T. Sakata, H. Mori, Microstructure and tensile properties of in situ synthesized (TiBw + TiCp)/Ti6242 composites, *J. Mater. Sci.* 36 (2001) 3707–3714, DOI: 10.1023/A:1017917631855.
- [18] X. Guo, L. Wang, M. Wang, J. Qin, Di Zhang, W. Lu, Effects of degree of deformation on the microstructure, mechanical properties and texture of hybridreinforced titanium matrix composites, *Acta Mater.* 60 (2012) 2656–2667, <https://doi.org/10.1016/j.actamat.2012.01.032>.
- [19] X. Tao, Z. Yao, S. Zhang, Reconstruction and refinement of TiB whiskers in titanium matrix composite after electron beam remelting, *Mater. Lett.* 225 (2018) 13–16, DOI: 10.1016/j.matlet.2018.04.099.
- [20] A. Popov, N. Rossina, M. Popova, The effect of alloying on the ordering processes in near-alpha titanium alloys, *Mater. Sci. Eng., A* 564 (2013) 284–287, <https://doi.org/10.1016/j.msea.2012.11.043>.
- [21] H.T. Tsang, C.G. Chao, C.Y. Ma, Effects of volume fraction of reinforcement on tensile and creep properties of in-situ MMC, *Scripta Mater.* 37 (1997) 1359–1365, DOI: 10.1016/S1359-6462(97)00251-0.
- [22] T. Wang, B. Li, Z. Wang, Z. Nie, A microstructure with improved thermal stability and creep resistance in a novel near-alpha titanium alloy, *Mater. Sci. Eng., A* 731 (2018) 12–20, DOI: 10.1016/j.msea.2018.06.034.
- [23] M. Ozerov, M. Klimova, A. Kolesnikov, N. Stepanov, S. Zhrebtsov, Deformation behavior and microstructure evolution of a Ti/TiB metal-matrix composite during high-temperature compression tests, *Mater. Des.* 112 (2016) 17–26, <https://doi.org/10.1016/j.matdes.2016.09.051>.
- [24] T. Saito, The automotive application of discontinuously reinforced TiB-Ti composites, *J. Occup. Med.* 56 (2004) 33–36, DOI: 10.1007/s11837-004-0125-3.
- [25] H.M. Flower, P.R. Swann, D.R.F. West, Silicide precipitation in the Ti Zr Al Si system, *Metall. Mater. Trans. B* 2 (1971) 3289–3297, DOI: 10.1007/BF02811609. [26] S. Syngellakis, J.J. Connor (Eds.), *Advanced Methods and Technologies in Metallurgy in Russia*, Springer International Publishing, Cham, 2018, 9783319663531.
- [27] W. Jia, W. Zeng, H. Yu, Effect of aging on the tensile properties and microstructures of a near-alpha titanium alloy, *Mater. Des.* 58 (2014) 108–115, DOI: 10.1016/j.matdes.2014.01.063.
- [28] Titanium Metals Corporation, Timet - Datasheets, 2020. <https://www.timet.com/assets/local/documents/datasheets/alphaalloys/6242.pdf>. (Accessed 17 March 2020).
- [29] G. Lütjering, Influence of processing on microstructure and mechanical properties of (α + β) titanium alloys, *Mater. Sci. Eng., A* 243 (1998) 32–45, DOI: 10.1016/S0921-5093(97)00778-8.
- [30] W.G. Burgers, On the process of transition of the cubic-body-centered modification into the hexagonal-

- close-packed modification of zirconium, *Physica* 1 (1934) 561–586, DOI: 10.1016/S0031-8914(34)80244-3.
- [31] C. Wei, X. Ma, X. Yang, M. Zhou, C. Wang, Y. Zheng, W. Zhang, Z. Li, Microstructural and property evolution of Ti6Al4V powders with the number of usage in additive manufacturing by electron beam melting, *Mater. Lett.* 221 (2018) 111–114, DOI: 10.1016/j.matlet.2018.03.124.
- [32] S. Decker, J. Lindemann, L. Krüger, Metal matrix composites based on Ti-6242 synthesized by spark plasma sintering, *Mater. Sci. Eng., A* 732 (2018) 35–40, DOI: 10.1016/j.msea.2018.06.103.
- [33] S. Decker, J. Lindemann, L. Krüger, Synthesis and mechanical properties of TiAl particle reinforced Ti-6Al-4V, *Mater. Sci. Eng., A* 674 (2016) 361–365, <https://doi.org/10.1016/j.msea.2016.08.011>.
- [34] T. Voisin, L. Durand, N. Karnatak, S. Le Gallet, M. Thomas, Y. Le Berre, J.-F. Castagne, A. Couret, Temperature control during spark plasma sintering and application to up-scaling and complex shaping, *J. Mater. Process. Technol.* 213 (2013) 269–278, DOI: 10.1016/j.jmatprotec.2012.09.023.
- [35] G. Petzow, *Metallographisches, Keramographisches, Plastographisches Atzen*, sixth ed., Borntraeger-Verlag, Berlin, 1994, 9783443230142.
- [36] L.B. McCusker, R.B.V. Dreele, D.E. Cox, D. Louer, P. Scardi, Rietveld refinement guidelines, *J. Appl. Crystallogr.* 32 (1999) 36–50, DOI: 10.1107/S0021889898009856.
- [37] N. Schell, R.V. Martins, F. Beckmann, H.U. Ruhnau, R. Kiehn, A. Schreyer, The high energy materials science beamline at PETRA III, in: *Stress Evaluation in Materials Using Neutrons and Synchrotron Radiation*, Trans Tech, Stafa-Zurich, United Kingdom, 2008, pp. 261–266. DOI: 10.4028/www.scientific.net/MSF.571-572.261.
- [38] A.P. Hammersley, S.O. Svensson, M. Hanfland, A.N. Fitch, D. Hausermann, Twodimensional detector software: from real detector to idealised image or two-theta scan, *High Pres. Res.* 14 (1996) 235–248, DOI: 10.1080/08957959608201408.
- [39] T. Schmoelzer, K.-D. Liss, P. Staron, S. Mayer, H. Clemens, The contribution of high-energy X-rays and neutrons to characterization and development of intermetallic titanium Aluminides, *Adv. Eng. Mater.* 13 (2011) 685–699, <https://doi.org/10.1002/adem.201000296>.
- [40] L. Spieß, G. Teichert, R. Schwarzer, H. Behnken, C. Genzel, *Moderne Röntgenbeugung: Röntgendiffraktometrie für Materialwissenschaftler, Physiker und Chemiker*, second., überarbeitete und erweiterte Auflage, Vieweg+Teubner Verlag/GWV Fachverlage GmbH Wiesbaden, Wiesbaden, 2009, 9783835101661.
- [41] R.M. Imayev, V.M. Imayev, M. Oehring, F. Appel, Alloy design concepts for refined gamma titanium aluminide based alloys, *Intermetallics* 15 (2007) 451–460, DOI: 10.1016/j.intermet.2006.05.003.
- [42] W. Wallgram, T. Schmolzer, L. Cha, G. Das, V. Güther, H. Clemens, Technology and mechanical properties of advanced γ -TiAl based alloys, *Int. J. Mater. Res.* 100 (2009) 1021–1030, DOI: 10.3139/146.110154.
- [43] M. Kastenhuber, T. Klein, B. Rashkova, I. Weißensteiner, H. Clemens, S. Mayer, Phase transformations in a β -solidifying γ -TiAl based alloy during rapid solidification, *Intermetallics* 91 (2017) 100–109, DOI: 10.1016/j.intermet.2017.08.017.
- [44] S. Cao, C.V.S. Lim, B. Hinton, X. Wu, Effects of microtexture and Ti₃Al (α 2) precipitates on stress-corrosion cracking properties of a Ti-8Al-1Mo-1V alloy, *Corrosion Sci.* 116 (2017) 22–33, DOI:

10.1016/j.corsci.2016.12.012.

- [45] P. Samimi, I. Ghamarian, D. Brice, M.J. Kaufman, P.C. Collins, On the influence of compositional variations on the oxidation performance and oxygen-induced phase transformations in Ti-based systems, in: V. Venkatesh, A.L. Pilchak, J.E. Allison, S. Ankem, R. Boyer, J. Christodoulou, H.L. Fraser, M.A. Imam, Y. Kosaka, H. J. Rack, A. Chatterjee, A. Woodfield (Eds.), Proceedings of the 13th World Conference on Titanium: Sponsored by Titanium Committee of the Structural Materials Division of the Minerals, Metals & Materials Society (TMS), Held August 16-20, 2015, Wiley, Hoboken, New Jersey, 2016, pp. 1521–1526, DOI: 10.1002/9781119296126.ch255. Manchester Grand Hyatt, San Diego, California, USA.
- [46] P.D. Nellist, S.J. Pennycook, The principles and interpretation of annular dark-field Z-contrast imaging, in: P.W. Hawkes (Ed.), Advances in Imaging and Electron Physics, Academic Press, San Diego, San Francisco, 2000, pp. 147–203, [https://doi.org/10.1016/S1076-5670\(00\)80013-0](https://doi.org/10.1016/S1076-5670(00)80013-0).
- [47] J.R. Davis, Properties and Selection: Nonferrous Alloys and Special-Purpose Materials, [tenth. ed.], Sixth, ASM International, Materials Park, Ohio, 2000, 0871703785 print.
- [48] S. Wei, L. Huang, X. Li, Y. Jiao, W. Ren, L. Geng, Network-strengthened Ti-6Al-4V/ (TiC+TiB) composites: powder metallurgy processing and enhanced tensile properties at elevated temperatures, Metall. Mater. Trans. 50 (2019) 3629–3645, DOI: 10.1007/s11661-019-05244-7.
- [49] R.W. Cahn, P. Haasen, Physical Metallurgy, Fourthth, Rev. And Enhanced, ed., North-Holland, Amsterdam, New York, 2010, 9780444898753.
- [50] F. Saba, F. Zhang, S. Liu, T. Liu, Reinforcement size dependence of mechanical properties and strengthening mechanisms in diamond reinforced titanium metal matrix composites, Compos. B Eng. 167 (2019) 7–19, DOI: 10.1016/j.compositesb.2018.12.014.
- [51] T.W. Clyne, P.J. Withers, An Introduction to Metal Matrix Composites, first. paperback ed., Cambridge Univ. Press, Cambridge, 1995, 0521418089.
- [52] Y. Chong, N. Tsuji, T. Bhattacharjee, Investigation on the Bi-lamellar microstructure in Ti-6Al-4V, in: V. Venkatesh, A.L. Pilchak, J.E. Allison, S. Ankem, R. Boyer, J. Christodoulou, H.L. Fraser, M.A. Imam, Y. Kosaka, H.J. Rack, A. Chatterjee, A. Woodfield (Eds.), Proceedings of the 13th World Conference on Titanium: Sponsored by Titanium Committee of the Structural Materials Division of the Minerals, Metals & Materials Society (TMS), Held August 16-20, 2015, Wiley, Manchester Grand Hyatt, San Diego, California, USA, 2016, pp. 663–667, DOI: 10.1002/9781119296126.ch110. Hoboken, New Jersey.
- [53] G. Proske, G. Lütjering, J. Albrecht, D. Helm, M. Daeubler, The microstructure and mechanical properties of the intermetallic compound Super Alpha 2, in: C.T. Liu, D. P. Pope, S.-H. Whang (Eds.), High Temperature Aluminides and Intermetallics: Proceedings of the Second International ASM Conference on High Temperature Aluminides and Intermetallics, September 16-19, 1991, Elsevier, San Diego, CA, USA, 1992, pp. 310–316, DOI: 10.1016/B978-1-85166-822-9.50051-0 London.

Designing advanced intermetallic titanium aluminide alloys for additive manufacturing

D. Wimler^{a*}, J. Lindemann^b, M. Reith^c, A. Kirchner^d, M. Allen^e, W. Garcia Vargas^f, M. Franke^c, B. Klöden^d, T. Weißgärber^d, V. Güther^e, M. Schloffer^f, H. Clemens^a, S. Mayer^a

^a Department of Materials Science, Montanuniversität Leoben, 8700 Leoben, Austria

^b GfE Fremat GmbH, 09618 Brand-Erbisdorf, Germany

^c Neue Materialien Fürth GmbH, 90762 Fürth, Germany

^d Fraunhofer Institute for Manufacturing Technology and Advanced Materials IFAM, 01277 Dresden, Germany

^e GfE Metalle und Materialien GmbH, 90431 Nuremberg, Germany

^f MTU Aero Engines AG, 80995 Munich, Germany

* Corresponding author

<https://doi.org/10.1016/j.intermet.2021.107109>

Intermetallics (2021)

open access: CC BY-NC-ND 4.0



Keywords:

Titanium aluminides; alloy development; microstructure; mechanical properties, electron beam melting; heat treatment

Abstract

Lightweight intermetallic γ -TiAl based alloys are innovative high-temperature structural materials. So far, these alloys are in use as turbine blades or turbocharger turbine wheels in advanced aerospace and automotive engines, where they are produced by means of investment casting as well as wrought processing, e.g. hot-forging. Through the development of powder-based additive manufacturing processes within the last decade, a real paradigm shift for future component production as well as their design and materials properties was created. While so-called proven alloy systems are presently used worldwide for additive manufacturing, the approach of this work is the development of novel process-adapted γ -TiAl based alloys, which on the one hand fulfill the specific requirements of additive manufacturing and on the other hand provide excellent high-temperature properties after a suitable heat treatment. Based on the concept of an engineering γ -TiAl based alloy, i.e. the so-called TNM alloy, two alloys are presented. Due to the chemical reactivity of titanium aluminide alloys, electron beam melting processes come into consideration as production methods using optimized manufacturing parameters, providing dense components with only small variations in the Al content between the individual powder layers, which is a decisive factor for the subsequent heat treatment above the γ solvus temperature. The additively produced samples show a fine equiaxed microstructure, whereas the heat-treated samples exhibit a fully lamellar α_2/γ microstructure with an excellent creep resistance. In summary, the adaptation of the additive manufacturing parameters in combination with innovative alloys and subsequent heat treatments are the basis for producing reliable high-performance TiAl components in the near future.

D.1 Introduction

Advanced lightweight materials that resist high temperatures are of major interest for both the aerospace and automotive industry, especially if they show the potential to replace heavy Ni-base superalloys. Intermetallic titanium aluminides based on the ordered γ -TiAl phase represent such a materials class in use as turbine blades or turbocharger turbine wheels in the present and next generation of aircraft and automotive engines. Their alloy development was driven by increasing both, the processability, e.g. forgeability, and the mechanical properties, such as creep resistance and high-temperature strength [1,2]. As a consequence, complex multi-phase alloys, such as the TNM alloy which has a nominal composition of Ti-43.5Al-4Nb-1Mo-0.1B (in atomic percent unless stated otherwise), were developed reaching a service temperature up to 750 °C [3]. In addition, the TNM alloy can be non-isothermally forged under near conventional conditions, while maintaining well balanced mechanical properties after a subsequent heat treatment [1]. A circumstance that allowed the TNM alloy to be part of the 4th generation of γ -TiAl based alloys, which represent process-adapted alloys.

The focus on processability in the course of alloy development continuous to exist as additive manufacturing (AM) provides new opportunities for the extended processing technology of high-quality powders to the production of complex near-net-shape components [4-7]. However, γ -TiAl based alloys are currently used in many AM studies, which originally were developed for investment casting or hot working. This results in several severe issues concerning texture in building direction (z-direction) and Al loss, which affects the mechanical properties significantly due to a locally different microstructure [7-11]. As a consequence, the aim of this study is to develop tailor-made TiAl alloys that are especially adapted to the AM process and its characteristics and establishing the full potential of these alloys considering the interplay of chemical composition and microstructure.

D.1.1 Alloy design considerations for intermetallic titanium aluminides suitable for AM

In order to determine a suitable alloy composition, years of experience of theoretical and experimental alloy design and development are used, based on the TNM alloy concept as reported in Refs. [1,12-14]. At room temperature (RT), the complex multi-phase TNM alloy consists of three ordered phases, the face-centered tetragonal γ -phase, the hexagonal α_2 -phase and the body-centered cubic (bcc) β_o -phase. Despite the brittle behavior of the β_o -phase [1,12,15], its disordered counterpart at elevated temperatures, the bcc β -phase, provides a sufficient number of independent slip systems and thus is essential for hot-forging [13,16]. In the present case of AM no hot-working is required, whereby the brittle β_o -phase is omitted in the process-adapted γ -TiAl based alloy, in the following termed as TNM^{AM}.

This can be achieved by adjusting the chemical composition, e.g. the Al content. As a guidance, Fig. D.1 shows a quasi-binary phase diagram through the TNM alloy system as a function of the Al content according to Ref. [16]. The content of 4 at.% Nb, 1 at.% Mo and 0.1 at.% B is kept constant. A red and blue arrow on top of Fig. D.1 marks the Al content of the two alloys investigated in this work, which will be discussed in detail later. The black arrow on top of Fig. D.1 marks the TNM alloy specification with an Al content of 43.5 at.%. This alloy solidifies completely through the β -phase according

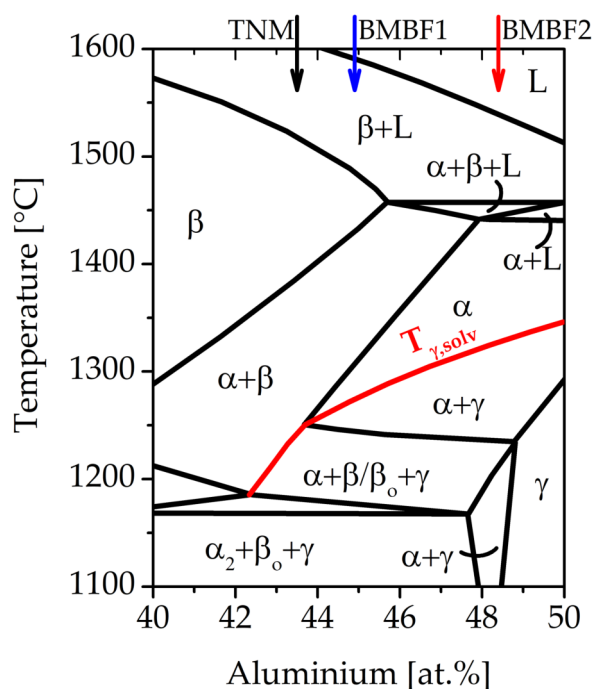


Figure D.1: Experimental quasi-binary phase diagram of the Ti-xAl-4Nb-1Mo-0.1B [at.%] alloy system according to Ref. [16]. Three arrows at the top of the diagram mark the Al content of the TNM and the BMBF alloys. Note that the BMBF alloys contain additional alloying elements when compared to the TNM alloy, which are shifting the respective phase boundaries (see Table D.1).

to $L \rightarrow L + \beta \rightarrow \beta \rightarrow \alpha + \beta \rightarrow \dots$, which possess a refined equiaxed microstructure and no significant casting texture as reported in Refs. [1,13,14]. In contrast, for AM a solidification via the single β -phase field region results in a (100) fiber texture and columnar growth of the original β -grains in building direction, due to the high temperature gradient during EBM processing [17,18]. In particular, a high energy input and low pre-heating temperature encourage the formation of a strongly textured component, as also shown for other alloying systems in Refs. [19-21]. Besides optimizing these processing parameters, the chemical composition of a tailor-made γ -TiAl based alloy for AM can also be adopted to minimize texture effects. For example, an increasing Al content constricts the single β -phase field region, as depicted in Fig. D.1, until, as in case of the TNM alloy system, this

phase field region vanishes at an Al content of around 45.5 at.%. At higher Al contents the solidification takes place peritectically via $L \rightarrow L + \beta \rightarrow L + \beta + \alpha \rightarrow \alpha \rightarrow \alpha \dots$ as reported in Refs. [13,22]. In-situ synchrotron solidification experiments by Kenel et al. [23] conducted on the binary peritectic Ti-48Al alloy, applying high cooling rates, have shown that the formation of the α -phase takes place directly from the melt without the presence of the β -phase. Furthermore, Barriobero-Vila et al. [24] pointed out that rapid solidification of a peritectic Ti-based alloy leads to an independent simultaneous nucleation of β - and α -phase from the melt, which are not in crystallographic orientation relation with each other, thus minimizing anisotropy [23,24]. Therefore, a peritectic transformation may prevent the formation of a pronounced grain texture towards the building axis in AM components [18]. Besides the peritectic solidification path, a higher Al content increases the fraction of the γ -phase, which forms in many different orientations via solid state transformation. This process contributes to the minimization of the columnar microstructure and thus prevents anisotropic mechanical behavior as the γ -phase mainly carries the plastic deformation [2]. In addition, a high Al content in γ -TiAl based alloys opens up a single α -phase field region above the γ solvus temperature ($T_{\gamma,solv}$), see red line in Fig.D.1, where no γ -phase is thermodynamically stable. Obviously, the size of this single phase field region and $T_{\gamma,solv}$ increase with increasing Al content [16]. A fact that is also of great interest in the design of the subsequent heat treatments where the first step usually takes place around $T_{\gamma,solv}$ [1,12]. Coming back to the process of AM, where the Al content varies locally inside the layers due to process-related Al evaporation on top of the “short-lived” melt pool, which is leading to an inhomogeneous microstructure with varying mechanical properties within the AM component. More precisely, the top area of the melt pool is depleted in Al [9,25], i.e. considering the phase diagram in Fig. D.1, will show a higher amount of the brittle β_o -phase, whereas the areas with a higher Al content show a higher amount of the γ -phase, which is the “softest” phase among the constituent phases [2,16]. Nevertheless, the mechanical properties of the individual phases can be enhanced by solid solution strengthening through alloying with other elements, which distort the crystal lattice of the respective phase by foreign atoms. In case of the TNM alloy these are Nb and Mo atoms. Because of their solubility preference, both elements thermodynamically stabilize the β/β_o -phase; Mo even four times stronger than Nb [1]. At this point, it should be mentioned that also W stabilizes the β/β_o -phase, thermodynamically slightly stronger than Mo by possessing a comparable atomic radius [17,26], leading to the successful introduction of W in engineering γ -TiAl based alloys, such as the IRIS alloy [27,28] and the ABB alloy [29,30]. Thus, all three elements (Nb, Mo, W) act as β -stabilizing solid solution hardening elements and also lower the solid state diffusion rate associated with an enhancement of the high-temperature strength as well as the creep resistance due to deceleration of thermally activated dislocation climb [1,2,31-33]. The small amount of B is added to γ -TiAl based alloys forming acicular borides, which serve as heterogeneous nucleation sites of the β - and α -phase, thus refining the microstructure

during solidification and subsequent solid-state phase transformations [34].

Intermetallic titanium aluminides represent a dynamic field of materials research, particularly as the current alloy design concepts aim to further improve the high-temperature capability of the TNM alloy, especially with respect to yield strength and creep resistance at elevated temperatures. Micro-alloying with Si and C results in enhanced tensile strength and creep resistance at elevated temperature when compared to the TNM alloy causing the operating temperature to rise to 800 °C. By an appropriate adaption of the thermomechanical processing, i.e. fine fully lamellar microstructure can be obtained, which leads to balanced mechanical properties, i.e. sufficient ductility and fracture toughness at room temperature and good creep strength at application temperature [12,15,35]. This modified alloy system, constituting the so-called TNM⁺ alloy, benefits from a significantly decreased dislocation mobility and shows a drastically enhanced microstructure stability at elevated temperatures. More precisely, Si and C act either as solid solution strengthener or as strong precipitate-forming elements, such as silicides (ζ -Ti₅Si₃) and carbides (p-type, Ti₃AlC). Furthermore, the fine distributed silicides additionally prevent grain coarsening during a heat treatment within the single α -phase field region due to grain boundary-pinning, thus opening the processibility to adjust a so-called designed fully lamellar (FL) microstructure. This “silicide effect” inhibits grain boundary motion according to the Zener-drag mechanism, keeping the α -grain size small during the heat treatment [15]. The occurrence of a single α -phase field region in case of the TNM⁺ alloy is due to the presence of C, which acts as an about 6 times stronger α -stabilizer than Al [36].

Designing a β_o -free high strength FL γ -TiAl based alloy for additive manufacturing, Zr should also be taken into account as it is a potential solid solution hardening element for the γ -phase, due to its partitioning preference for the γ -phase [26,37,38], unlike Nb, Mo or W, which tend to stabilize the β/β_o -phase. In addition, ζ -Ti₅Si₃ will be stabilized by Zr, where Zr substitutes Ti [38]. This is of particular interest in case of heat treatment which takes place within the single α -phase field region, followed by cooling and a subsequent annealing treatment. The obtained small α_2/γ -colony size, which leads to a sufficient ductility at RT, is caused by the presence of stable silicides, which hinder grain boundary motion as mentioned before.

Based on this knowledge, the study presents two γ -TiAl based alloys which are designed according to the TNM alloying concept [14]. However, these new alloys are adapted to the EBM process against the background of high creep resistance after a proper heat treatment.

D.2 Materials and methods

Two TNM^{AM} alloys, hereafter called BMBF1 and BMBF2, were produced via a powder metallurgical approach with chemical compositions, determined according to Ref. [39], which

mainly differ in the Al and Zr content as summarized in Table D.1. Note, that at that time these complex γ -TiAl based alloys cannot be thermodynamically calculated with sufficient accuracy [1,14,40].

The powders were produced via an electrode induction melting gas atomization (EIGA) process using Ar as processing gas as reported in Ref. [41]. The required ingots were produced as described in Refs. [42,43]. The nomenclature of the alloys refers to an ongoing project (NextTiAl 03XP0088A) on tailor-made TiAl alloys for additive manufacturing by electron beam melting funded by the German Federal Ministry of Education and Research (BMBF) from which these two alloys emerged. For the EBM process, powder particle sizes in the range of 50–125 μm were used. Within this study, two EBM machines of the type A2X from Arcam AB, Sweden, were used, one for each alloy, to build up cuboids, $15 \times 15 \times 12 \text{ mm}^3$, and cylindrical samples with a diameter of 11 mm and a height of 80 mm with a maximum focused electron beam. The layer thickness for all experiments was 100 μm and the hatching distance was also kept constant at 100 μm using a snake-like hatching strategy, which was rotated by 90° every layer, i.e., a so-called cross-snake hatching was used. In case of the BMBF1 alloy this hatching was performed on one cube before moving over to the next one and is referred to as model-wise melting, as shown in Fig. D.2a, whereas for the BMBF2 alloy, this hatching strategy was done cube across, as shown in Fig. D.2b. These two different strategies were also used for manufacturing cylindrical samples in 0, 45 and 90° in building direction (z) of the respective BMBF alloys. Besides the different scanning strategies, the cylindrical samples also differ in their position in x-y direction resulting in different scanline lengths, see Fig. D.2a and b, which means that an unequal absolute energy input on these two alloys has to be discussed. One energy input can be quantified by the following equation:

$$E_L = \frac{U \cdot I}{v}, \quad (\text{D.1})$$

where E_L is the line energy, U is the acceleration voltage, I is the beam current, and v is the scan speed. The voltage was kept constant at 60 kV, in contrast to I and v , which varied from 3 to 26 mA and from 500 to 4000 mm/s, respectively. Each cubic sample was built with one constant parameter set of I and v . On the contrary, the cylindrical samples were made with an Arcam automatic function, i.e. holding E_L constant over the different scanline lengths (Fig. D.2). BMBF1 cylinders were built using an E_L of 120 J/m, whereas for the BMBF2 alloy E_L was adjusted to be about 300 J/m. During all building processes, the pre-heating temperature of the top layers was kept in the range of 1000–1050 $^\circ\text{C}$ by fast scanning with a defocused electron beam, thus preventing thermal cracking. It should be noted at this point that the ductile-to-brittle transition temperature of intermetallic γ -TiAl based alloys is in the range of 700–900 $^\circ\text{C}$ [2], depending on alloy composition, microstructure and the test conditions (e.g. strain rate). Below this temperature the plastic fracture elongation is only a few percent, making the material crack sensitive. For more detailed information regarding the setup of EBM machines and the EBM process itself, the reader is referred to Refs. [6,44].

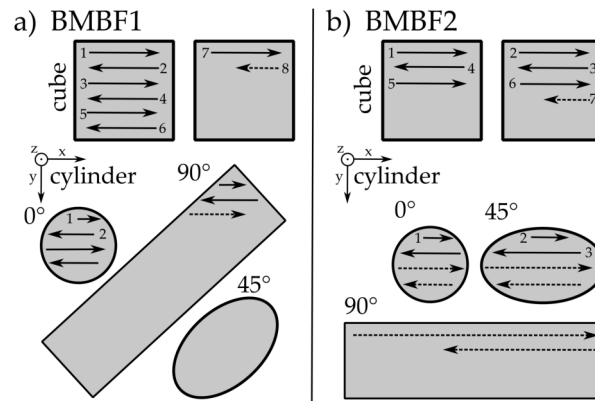


Figure D.2: Schematically illustration of the two different electron beam hatching strategies for building up cube (top) or cylindrical (bottom) samples layer by layer: a) model-wise melting each cube one layer over the other before moving on to the next (used for BMBF1) and b) hatching across several cubes (used for BMBF2). The cylindrical samples of the BMBF alloys in 0, 45 and 90° to the building direction z also differ in their position in x - y -direction, resulting in different scanline lengths.

For metallographic preparation, all samples were cut out along the building direction (xz -plane) from the center of the as-built cubic specimen in order to prevent edge effects. The samples were ground, polished and electrolytically etched according to Ref. [45] and subsequently investigated by means of scanning electron microscopy (SEM) using an EVO 50 from Zeiss, Germany, operated at 20 kV in back-scattered electron (BSE) mode. In the SEM images, the building direction z is always aligned vertically.

In order to identify phase transformation sequences within the two alloys and to adjust heat treatment parameters, differential scanning calorimetry (DSC) measurements were carried out on the powders and as-EBM specimens, which were manufactured with different E_L , utilizing heating rates between 10 and 40 K/min in Ar-atmosphere. The measurements were executed on a LabSYS Evolution of Setaram Instrumentation, France. The weight of the samples was around 60 ± 5 mg always enclosed by a 100 μ l alumina crucible.

Heat treatments were firstly conducted in a Carbolite, Great Britain, RHF 1600 high-temperature chamber furnace under atmosphere followed by water quenching (WQ) to maintain the microstructure, which exists at annealing temperature. Secondly, the FL microstructure was adjusted within a hot isostatic pressing (HIP) facility of the type QIH-9 URQ by Quintus Technologies, Sweden, at the Ruhr Universität Bochum, Germany, which combines HIP and heat treatment, applying different temperatures, pressures as well as cooling rates.

For determining the lamellar spacing of the α_2/γ -colonies transmission electron microscopy (TEM) was conducted using a Philips CM12, Germany, operating at an acceleration voltage of 120 kV as described in Ref. [15]. The TEM images were taken along the $\langle 110 \rangle$ zone axis

of the γ phase in “edge-on” condition of the α_2/γ -colonies. Based on these TEM images, the average interface lamellar spacing, including α_2/γ and γ/γ interface, was determined. Additionally, hardness tests corresponding to Vickers HV10 were performed on electrolytically polished specimens using a universal hardness testing machine M4C 025 G3M from EMCO, Austria, by pushing the tip in the xz-plane. In this study, all HV10 values are given by the arithmetic average and the corresponding standard deviation of at least five individual hardness measurements.

Finally, creep tests were carried out at 850 °C and 150 MPa using creep testing machines of the type TC30 and TC50 from AET Technologies, France. The samples were manufactured from the cylindrical EBM samples in heat-treated condition and had an initial diameter and gauge length of 6 mm and 30 mm, respectively. During the creep experiments, the creep strain was measured by extensometer bars and the temperature was controlled by three thermocouples which were positioned along the measuring length.

D.3 Results

D.3.1 Alloy design strategy for additive manufacturing

One aim of the alloy design concept is to develop a TNM^{AM} alloy, which shows no pronounced columnar microstructure in building direction by inhibiting the solidification via the single β -phase field region [18]. As a first step in this direction, a higher amount of Al must be added to obtain a peritectic solidification reaction. The BMBF1 alloy with an Al content of 44.9 at.% is marked with a blue arrow in Fig. D.1. According to the quasi-binary phase diagram from Ref. [16], the BMBF1 alloy should solidify entirely through the single β -phase field region, i.e. no peritectic reaction should take place. Nevertheless, at this point, it should be mentioned that the phase diagram shown was determined for the nominal composition of the TNM alloy, i.e. Ti-43.5Al-4Nb-1Mo-0.1B (at.%), and therefore Fig. D.1 should only act as guidance. Further, both BMBF alloys contain additional alloying elements, such as W, Zr, Si and C (see Table D.1), when compared to the TNM alloy, which stabilize, for example, the α -phase (e.g. C) or the γ -phase (e.g. Zr), while constricting the single β -phase field region. The amount of the β -stabilizing element W was chosen to be 0.7 at.%. As a result of the BMBF1 alloy design, DSC measurements of the powder revealed that no single β -phase field region is present, which would be expressed by the lack of specific DSC signals. Therefore, a solidification along the peritectic reaction has to take place.

The BMBF2 alloy, exhibiting an Al content of 48.4 at.% (marked with a red arrow in Fig. D.1), shows a peritectic solidification according to the quasi-binary phase diagram. Accompanying DSC measurements on this powder confirmed that no single β -phase field region exists.

As a second step, the appearance of a single α -phase field region within the chemical

Table D.1: Chemical composition of the investigated BMBF alloy powder in at.%. The oxygen content is stated in mass-ppm.

TNM ^{AM}	Ti	Al	Nb	W	B	Zr	Si	C	O
BMBF1	bal.	44.9	4.1	0.7	0.08	1.1	0.38	0.52	1000
BMBF2	bal.	48.4	4.1	0.7	0.08	-	0.36	0.55	800

composition of an EBM manufactured TNM^{AM} alloy is necessary for adjusting a FL microstructure during a subsequent heat treatment. The nomenclature ΔT_α corresponds to the width of the single α -phase field region above $T_{\gamma,solv}$, which was determined by DSC measurements at the powder. The BMBF1 alloy exhibits a $T_{\gamma,solv}$ of $1325 \pm 5^\circ\text{C}$ and ΔT_α is about 90°C . Due to the higher Al content of the BMBF2 alloy, $T_{\gamma,solv}$ increases to $1390 \pm 5^\circ\text{C}$, but ΔT_α drops to around 50°C . Furthermore, the solidus temperature was determined to be at $1461 \pm 1^\circ\text{C}$ for BMBF1 and $1469 \pm 2^\circ\text{C}$ for BMBF2. The higher solidus temperature for higher Al contents does not match with the phase diagram in Fig. D.1 due to the already discussed differences in the chemical composition. In case of the first alloy, there is the fact that Zr is added, which generally decreases the solidus temperature in γ -TiAl based alloys [46].

D.3.2 Processing window for electron beam melting

Cubes were built up with varying v and I in order to evaluate the optimal process parameters for titanium aluminides using the EBM process. Figure D.3 depicts the parameter set (colored areas), which on the one hand produces compact specimens and on the other hand does not lead to the swelling phenomena. Swelling describes a material displacement, resulting in an uneven melt flow. This phenomenon can even lead to an abort of the EBM build-job, if the material displacement extends beyond the layer thickness. Swelling can be caused by a high E_L and an incorrect choice of the scanning strategy as reported in Refs. [47,48]. However, a low E_L , according to Eq. (D.1), results in an insufficient layer connection, so-called bonding faults. These faults decrease the relative density of the EBM produced specimens. For that reason, each found processing window shown in Fig. D.3 is limited in the upper area by swelling and in the lower range by lack of fusion defects. In addition to these defects, randomly distributed, spherical gas pores were detected. However, a heat treatment under pressure as described in chapter D.3.3 reduce their size to a negligible minimum.

Selected cubes were investigated in detail with regard to the Al loss (ΔAl). For this purpose, the chemical composition of the powder (shown in Table D.1) was compared with the EBM cubes and ΔAl determined, as summarized in Fig. D.4a. Evidently, the deviation in the Al content to the EBM manufactured sample is obvious, which is a result of the global Al evaporation. The total Al content of the samples decreases with increasing E_L , resulting in

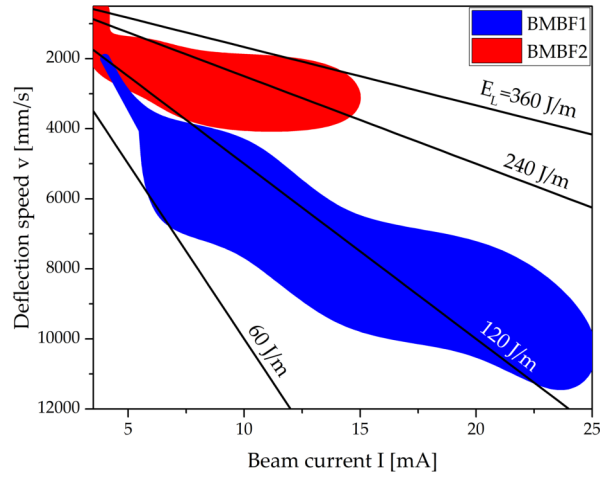


Figure D.3: The colored areas represent the EBM process parameters for both titanium aluminide alloys for the production of dense cube specimens, see text. Below the lower limit of the colored areas, fusion defects appear, whereas above the upper limit, swelling takes place. The plotted isolines describe a constant line energy calculated according to Eq. (D.1).

an increase of ΔAl . Moreover, from these results it emerges that the BMBF2 alloy exhibits a varying ΔAl with varying I at a constant E_L of 240 J/m, more precisely the Al loss is 1.1 at.% for 4 mA and 1.6 at.% for 8 and 12 mA, respectively (Fig. D.4a), whereby an influence of the beam current is given. As a consequence of the Al loss, $T_{\gamma,\text{solv}}$ decreases according to

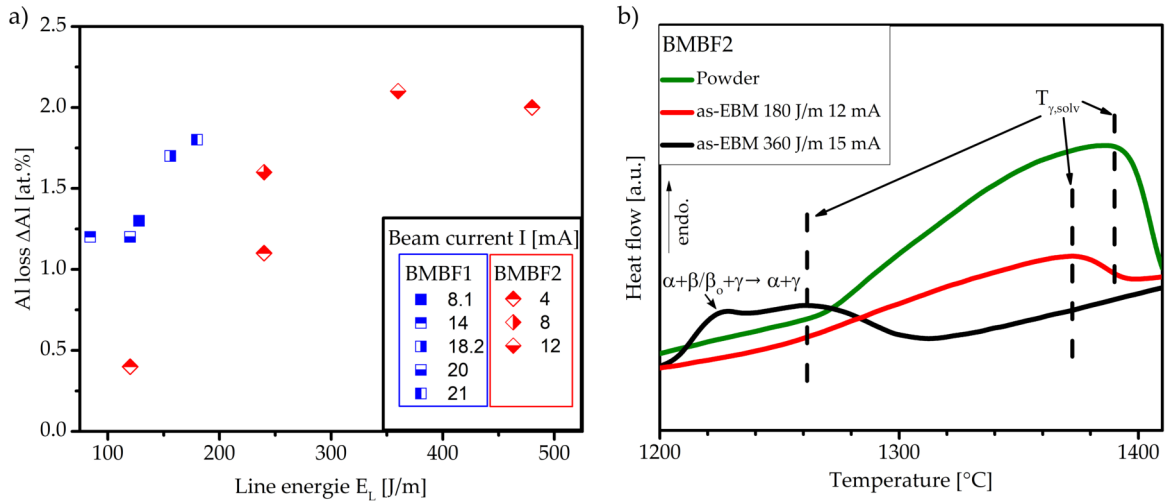


Figure D.4: a) Difference in Al content when comparing the initial powder with the EBM manufactured samples for different line energies (E_L) and beam currents (I). ΔAl increases with increasing E_L and I . Note, that the results of 8 and 12 mA overlap at 240 J/m; b) DSC measurements conducted on BMBF2 powder and two EBM as-built samples, manufactured with different parameters (as indicated in the insert). $T_{\gamma,\text{solv}}$ decreases with increasing E_L and I because of the Al loss, which will also allow the determination of the $\alpha + \beta/\beta_0 + \gamma \rightarrow \alpha + \gamma$ solid state transformation temperature for 360 J/m and 15 mA (see text).

the phase diagram in Fig. D.1 and this is verified by DSC measurements conducted on the BMBF2 powder and similar EBM as-built samples, as shown in Fig. D.4b. This diagram compares three DSC curves measured during heating with 20 K/min. The powder (Al = 48.4 at.%) exhibits the highest $T_{\gamma,solv}$, i.e. 1390 °C, indicated by dashed vertical lines. As a consequence of the Al evaporation during the EBM process, $T_{\gamma,solv}$ of the first as-built sample, with $E_L = 180$ J/m and $I = 12$ mA, decreases by 20 K to around 1370 °C. Doubling E_L and increasing the current to 15 mA further decreases $T_{\gamma,solv}$ to around 1260 °C. In addition, a second peak at a lower temperature was detected in the heating curve, stemming from the decomposition of the higher amount of β/β_o -phase at the transition from $\alpha + \beta/\beta_o + \gamma$ to $\alpha + \gamma$, also due to Al loss.

The occurring phases in the as-EBM microstructure were identified by SEM in BSE mode. Figure D.5 presents three SEM images of the BMBF1 alloy manufactured with different process parameters, whereby E_L decreases from Fig. D.5a–c. The insert shows a higher magnification of the microstructure, consisting of dark γ - and gray α_2 -phase within lamellar α_2/γ -colonies, showing a broad lamellar spacing. The wide lamellar spacing is attributed to the heat-affected zone (HAZ) caused by multiple thermal cycling effects during the layer-by-layer fabrication, which enhances the coarsening effect. Besides, bright globular β_o -phase and small, bright spherical ζ -Ti₅Si₃ precipitations are apparent in the SEM micrographs. Figure D.5a exhibits a banded structure, indicated by white dotted lines. The bright β_o -phase

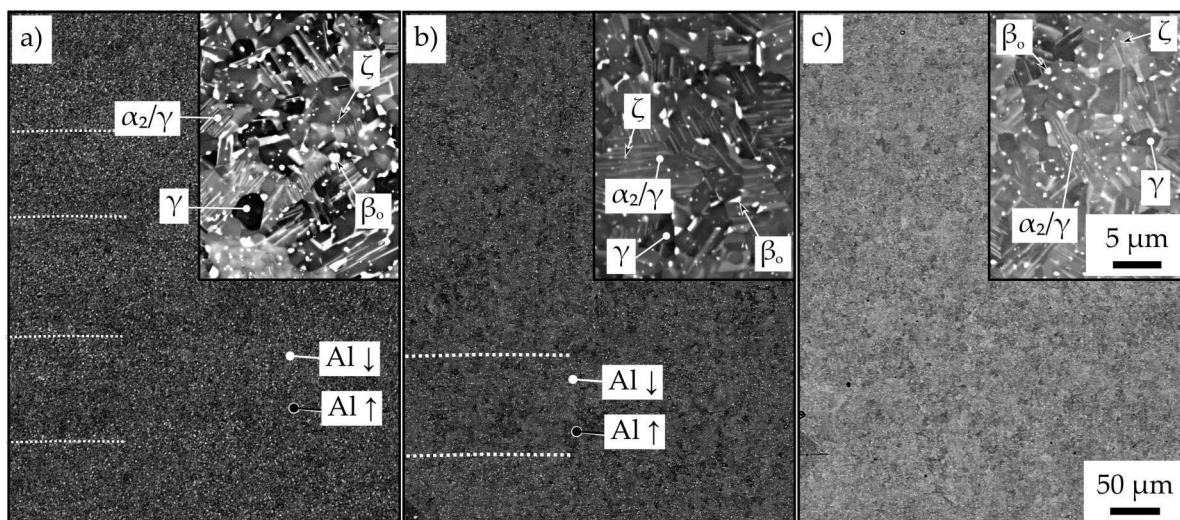


Figure D.5: SEM micrographs showing the microstructure of the BMBF1 alloy in as-EBM condition taken along the xz -plane. The cube-shaped specimens were manufactured with different process parameters: a) $E_L = 128$ J/m, $I = 8.1$ mA; b) $E_L = 120$ J/m, $I = 14$ mA; c) $E_L = 84$ J/m, $I = 14$ mA. The inserts show the microstructural details in higher magnification. Dotted guide lines indicate the appearance of a layered structure. All images are taken in BSE mode. Consequently, the γ -phase shows a dark contrast and the α_2 -phase appears gray, whereas the β_o -phase and the ζ -silicides are exhibiting the brightest contrast [35], see text for details. For high-quality images, the reader is referred to the online version.

in the SEM image, whose volume fraction increases with decreasing Al content, contributes to the formation of this banded structure due to the periodically varying Al content in EBM as-built samples especially when manufactured with high E_L . This layered microstructure nearly vanishes in the microstructure of Fig. D.5b, which was manufactured with a higher current, but using a lower E_L , which impacts the Al loss in EBM samples as shown in Fig. D.4a for the BMBF1 alloy. The microstructure in Fig. D.5c was manufactured with the lowest E_L , using the same current as before. Here, although β_o phase is present, no repeating layered structure was identified. Therein, the majority of the bright phase are small, spherical ζ -Ti₅Si₃ precipitations, whose amount is rather constant in the microstructure.

The microstructure of three as-EBM BMBF2 cube shaped samples are shown in Fig. D.6. The specimen in Fig. D.6a was built using a high E_L of 360 J/m. The microstructure consists of α_2/γ -colonies, ζ -silicides and β_o -phase. The amount of the bright β_o -phase together with the gray lamellar α_2 -phase is slightly higher in the top section of the micrograph, which indicating a lower Al content which is in accordance with the phase diagram in Fig. D.1. Decreasing E_L to 240 J/m results in the microstructure of Fig. D.6b, which exhibits also a different phase composition between top and bottom layer. In the SEM-BSE image, the top layer appears darker due to a higher Al concentration, i.e. leading to more γ -phase. In addition, a low porosity is observed, implying a not completely dense specimen. At $E_L = 120$ J/m, as shown in Fig. D.6c, the microstructure is homogenous of mainly γ -phase and ζ as well as minor α_2 -phase, reflecting the minor Al loss, but connection defects appear on a macroscopic scale, which are not shown in the micrograph.

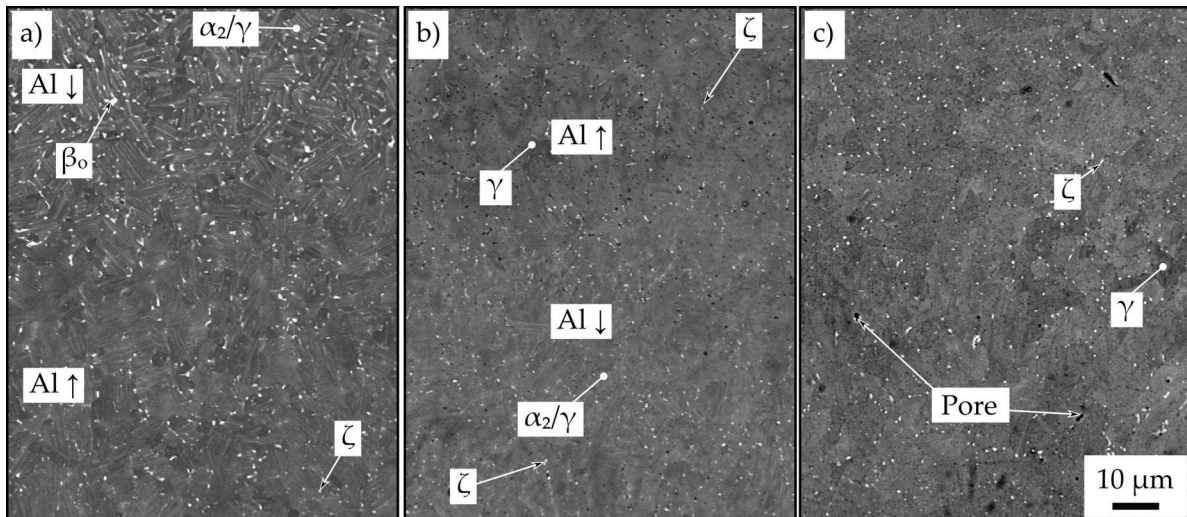


Figure D.6: SEM micrographs showing the microstructure of the BMBF2 alloy in as-EBM condition along the xz -plane, manufactured with different process parameters: a) $E_L = 360$ J/m, $I = 12$ mA; b) $E_L = 240$ J/m, $I = 8$ mA, c) $E_L = 120$ J/m, $I = 4$ mA. SEM images are taken in BSE mode. See text for details.

D.3.3 Post-processing heat treatments

The heat treatments were conducted on the cylindrical samples manufactured with an automatic mode, holding E_L roughly constant over different scanline lengths in order to build cylinders in different orientations. The BMBF1 alloy was built up using an E_L of 120 J/m and the BMBF2 alloy applying 300 J/m. The total ΔAl was determined to be 1 at.% for BMBF1 and 0.5 at.% for BMBF2. In order to adjust the desired FL microstructure by annealing in the single α -phase field region, $T_{\gamma,\text{solv}}$ measured by DSC at the powder was additionally confirmed on the bulk material by heat treatment studies for 30 min around $T_{\gamma,\text{solv}}$ followed by water quenching (WQ). Figure D.7a shows the microstructure of a BMBF1 sample heat-treated at 1310 °C, i.e. 15 °C below $T_{\gamma,\text{solv}}$ of the powder. A horizontal band consisting of gray α_2 - and dark γ -phase is present in the center of the micrograph. At the bottom of this band the volume fraction of γ -phase is higher, indicating a higher Al content, see Fig. D.1. Within this banded structure the fraction of γ -phase decreases in building direction until only residues of broad γ lamellae are apparent. At a certain point the γ -phase vanishes due to the local crossing of $T_{\gamma,\text{solv}}$ and the heat treatment is performed in the single α -phase field region. As a result equiaxed fine-grained α_2 -bands form, which transforms to α_2 during cooling. The spherical bright ζ -silicides are homogeneous distributed, which indicates that their stability is rather independent of the occurring Al variations. The same applies to rod-shaped borides, which are also evident in the SEM image.

The heat treatment conducted at 1330 °C for 30 min followed by WQ was carried out throughout the single α -phase field region in case of the BMBF1 alloy. In contrast, the BMBF2 alloy with the higher Al content is in the single α -phase field region at 1400 °C. Consequently, the heat treatments have to take place above the $T_{\gamma,\text{solv}}$ of the powder, e.g. 1325 ± 5 °C for BMBF1 and 1390 ± 5 °C for BMBF2, in order to ensure that also high Al-containing bands transform into α . Based on these findings, the heat treatment parameters were defined for adjusting a FL microstructure in both BMBF alloy variants. The entire heat treatment was carried out using a Quintus HIP device combining HIP and heat treatment and, most importantly, to prevent thermally induced porosity (TIP) that would occur under a pressureless heat treatment above the HIP temperature. For more details regarding TIP, the reader is referred to Ref. [49]. In the present study, the employed heat treatment consists of a conventional HIP step at 1225 °C for 4 h using a pressure of 170 MPa, followed by an annealing step for 30 min under pressure (170 MPa) within the single α -phase field region, i.e. 1330 °C for BMBF1 and 1400 °C for BMBF2. Then, the specimens were cooled to 600 °C. The cooling rate was around 300 K/min for BMBF1 and about 80 K/min for BMBF2 in order to precipitate γ -lamellae within the α/α_2 -phase instead of forming massive γ , which can appear in case of high Al containing γ -TiAl based alloys during fast cooling [50,51]. Finally, a stabilization heat treatment was carried out within the HIP unit at 900 °C for 4 h with a reduced pressure of 100 MPa. The resulting FL microstructure for the BMBF1

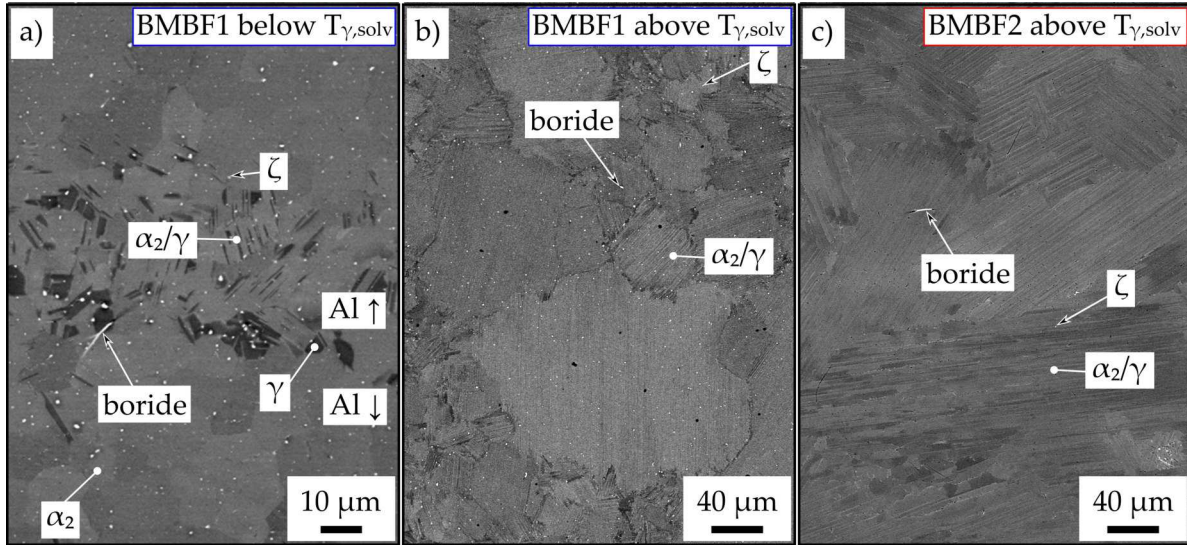


Figure D.7: a) SEM micrographs showing the microstructure of the BMBF1 alloy along the xz -plane after a heat treatment at 1310 °C for 30 min, followed by WQ. There are two areas: one consisting of a mixture of lamellar α_2/γ -colonies and globular γ grains. In this banded area the Al loss was lowest. The other area exhibits α_2 grains only, because of the local loss of Al which results in a decrease of $T_{\gamma,solv}$ and consequently leads to a heat treatment within the single α -phase field region. FL microstructures of the BMBF alloys along the xz -plane: b) BMBF1, c) BMBF2. For both alloys the heat treatment was conducted in the single α -phase field region, i.e. 1330 °C for b) and 1400 °C for c). The exact heat treatment sequence and the microstructures are described in detail in the text. All SEM images are taken in BSE mode.

alloy is shown in Fig. D.7b and for the BMBF2 alloy in Fig. D.7c. After the homogenization heat treatment in the single α -phase field region both FL microstructures show no banded structure due to Al inhomogeneities, as it was the case in the as-EBM (Fig. D.5a) or the heat-treated condition (Fig. D.7a). Besides the lamellar α_2/γ -colonies, spherical ζ -silicides are present. The colony size has coarsened during the heat treatment and, due to low cooling rates, the γ lamellae are already visible within the α_2/γ -colonies. As a result of different cooling rates, the BMBF1 alloy (Fig. D.7b) exhibits a finer lamellar spacing than the BMBF2 alloy (Fig. D.7c). For an accurate determination of the average lamellar spacing, TEM was conducted. The mean lamellar spacing of the BMBF1 alloy was determined to be 60 ± 20 nm and in case of the BMBF2 alloy a value of 410 ± 240 nm was obtained. In addition, the hardness was determined for both FL microstructures, resulting in 439 ± 10 HV10 for the BMBF1 alloy and 300 ± 10 HV10 for the BMBF2 alloy. The size of the indents in the xz -plane is around $200 \mu\text{m} \times 200 \mu\text{m}$, therefore, at least two layers were penetrated.

Finally, creep tests were carried out at 850 °C and 150 MPa on FL samples built in horizontal, vertical and 45° orientation, as shown in Fig. D.2. The results are summarized in a Larson-Miller plot displayed in Fig. D.8. The Larson-Miller-parameter (LMP) was calculated using the time until 1% creep strain is reached for each sample orientation and summarized in

one data point together with the standard deviation. The BMBF2, which contains a higher Al content exceeds the BMBF1 alloy. On the other hand, the BMBF1 alloy shows roughly no deviation. After the creep experiments (in case of BMBF1 and BMBF2 after 150 h and 200 h, respectively), the finer lamellar spacing in the colonies of FL BMBF1 exhibits a slightly higher decomposition by cellular reaction at the colony boundaries than the BMBF2 FL microstructure. However, as the minimization of the surface energy is one of the driving forces of the cellular reaction [52], it occurs only in a few μm thin area around the coarse lamellar colonies. For further information on the cellular reaction during creep of TNM alloys, the reader is referred to Ref. [52].

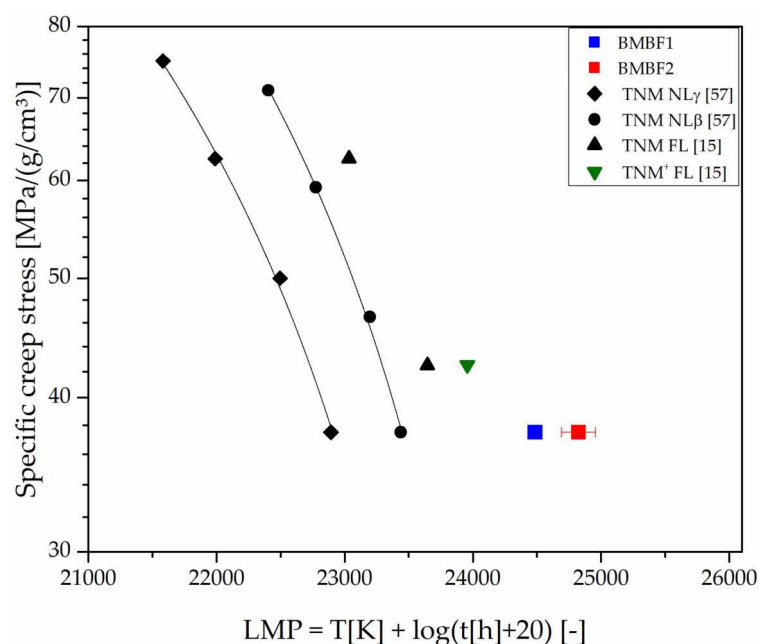


Figure D.8: Results of creep tests of the FL BMBF samples represented in a Larson-Miller plot in a temperature range of 750–850 °C, whereby the time at 1 % creep strain was used for calculating the Larson-Miller parameter (LMP). For comparison, data of the precursor alloys, e.g. TNM and TNM⁺, are included.

D.4 Discussion

D.4.1 EBM manufacturing of dense and isotropic specimens using the designed TNM^{AM} alloys

The TNM^{AM} alloy variants, here marked as BMBF1 and BMBF2 alloy, represent a further development of the intermetallic engineering TNM alloy, which originally represents a high-strength 4th generation TiAl alloy suitable for hot-working. In order to adapt this alloy for EBM processing some considerable changes in the alloy design concept are needed. First of

all, derived from own results [18], the solidification of the TNM alloy via a single β phase field region, resulting in a $\{001\}_{\beta_o}$ fiber texture parallel to the building direction, must be changed into a peritectic solidification. This can be realized by increasing the amount of Al, Si and C as well as by decreasing the amount of β -stabilizing elements, like Nb or W, see Table D.1. Indeed, the DSC measurements conducted on both BMBF alloys confirmed the absence of a single β -phase field region, whereby these alloys are processible by means of EBM within the process window shown in Fig. D.3. Both alloys exhibit no obvious columnar solidification texture in building direction, when compared to other β -solidifying Ti-alloys [20] or the TNM alloy [18] fabricated by means of AM. In the framework of this study, a wide range of process parameters were tested and no columnar structures are apparent in the micrographs along the building direction (z-direction). Obviously, the selected chemical compositions suppress the formation of a pronounced β -texture in both alloys due to the occurrence of a peritectic solidification, whereby both α - and β -phase nucleate independently from the melt pool during the fast cooling in the course of the EBM process, as shown in Refs. [23,24] and in chapter D.1. The following solid state transformations, according to well-known transformation pathways, into the majority γ -phase, which mainly carries the plastic deformation of these multi-phase alloys, further prevent anisotropic mechanical behavior [2]. However, at this point, due to the complexity of the alloy system, the effects responsible for the obtained isotropic microstructure cannot be separated.

The BMBF2 alloy, red area in Fig. D.3, requires a higher energy input than the BMBF1 alloy, blue area. The approximately 10 °C higher solidus temperature of the BMBF2 alloy affects the EBM process parameters, but the main impact on the as-built microstructure is the scanning strategy [25,53], which differs between the BMBF alloys, see chapter D.3. Therefore, the employed process parameters can be compared and ranked only for one alloy variant, but not between them.

Contrast differences between areas with different compositions are visible in the banded structures which are arranged in a distance of about 100 μm , see Fig. D.5a and b. This is caused by the repeated Al evaporation on top of the melt pool, which lead to alternating local minima in the Al content of the specimen. This effect increases with increasing energy input and is well-known for EBM processed TiAl alloys, see Refs. [4,25,55]. In the case of the BMBF1 alloy (Fig. D.5a), the minimum of the Al content is manifested in the presence of the β_o -phase, which is stable at low Al contents according to the phase diagram shown in Fig. D.1. Similar contrast differences occur within the BMBF2 alloy (Fig. D.6a). The amount of the α_2 -lamellae varies significantly over the layer, where the highest fraction of α_2 -lamellae appears in the Al-lean areas. However, the formation of bands consisting of coarse γ -grains, as detected in the as-EBM microstructure of the well-known Ti-48Al-2Cr-2Nb alloy [8] could not be observed in case of both BMBF alloys. In brief, the contrast variation in the SEM images due to the different phase fractions develops in particular when a high E_L is used. This behavior matches the trend observed in Fig. D.4a, where the Al loss increases with

increasing E_L , due to higher maximum temperatures on top of the short-lived melt pool, which leads to enhanced local Al evaporation [25]. Furthermore, DSC measurements on the BMBF2 alloy confirmed the Al loss by its impact on phase transformation temperatures, such as $T_{\gamma, solv}$, see Fig. D.4b. Here, $T_{\gamma, solv}$ drops by around 15 °C using the process parameters $E_L = 180 \text{ J/m}$ and $I = 12 \text{ mA}$. According to the dependence of $T_{\gamma, solv}$ on the Al content as displayed in the phase diagram shown in Fig. D.1, an Al loss of approximately 1.3 at.% can be estimated. This is also in good agreement with the measured values of Fig. D.4a as well as published results for γ -TiAl based alloys [10,25]. An E_L of 360 J/m with $I = 15 \text{ mA}$ results in a further decrease of $T_{\gamma, solv}$ of around 130 °C to 1260 °C, which is a similar value of a nominal TNM alloy [16]. In addition, a characteristic $(\alpha + \beta/\beta_o + \gamma \rightarrow \alpha + \gamma)$ -peak is identified in the heating curve of the DSC measurement shown in Fig. D.4b, attributable to the stabilization of the β_o -phase in the Al lean bands of the as-EBM sample manufactured with a high E_L . Such a DSC peak has also been observed in the TNM alloy as reported in Ref. [12]. However, according to the chemical analysis given in Fig. D.4a, for BMBF2 a ΔAl of only 2–3 at.% is estimated for $E_L = 360 \text{ J/m}$ and $I = 15 \text{ mA}$. As a consequence, especially in the case of a high energy input, due to a lack of reliable and confirmed data for beam currents above 12 mA, an extrapolation of chemical composition may underestimate the Al loss. However, at this point it should be further stated that the results of chemical analysis and DSC represent an average Al loss throughout several layers. Hence, local variations of the Al content cannot be determined by those methods. However, these are decisive in the evolution of the as-built EBM microstructure and subsequently in the resulting heat-treated microstructure.

D.4.2 Adjusting a subsequent heat treatment for high-temperature application

The local Al content varies across the layer-by-layer manufactured samples, which influences and thus limits the parameter field of the subsequent heat treatment. Consequently, the adjustment of a so-called nearly lamellar γ (NL γ) microstructure, which consists of lamellar α_2/γ -colonies and a small volume fraction of homogeneously distributed globular γ -grains at the colony boundaries is in an EBM component with an inhomogeneous Al distribution not possible. Such a NL γ microstructure, for example, was adjusted in cast and/or forged TNM material, providing balanced mechanical properties, i.e. sufficient ductility at RT and good creep strength at elevated temperatures, as described in Refs. [1,12,13]. However, the adjustment of a NL γ microstructure with isotropic mechanical properties requires a homogeneous as-built EBM microstructure, which implies a homogeneous distribution of the constituting chemical elements, e.g. Al. A heat treatment for adjusting a NL γ microstructure, in the investigated BMBF alloys, will lead to a banded structure, consisting of globular γ -grains and α_2/γ -colonies arranged in the same way as shown in Fig. D.7a.

However, at this point it should be mentioned that the microstructure in Fig. D.7a was WQ after annealing at 1310 °C for 30 min. Therefore, the high-temperature α -phase was “frozen-in” and only an $\alpha \rightarrow \alpha_2$ ordering to α_2 -phase took place. Nevertheless, a layered NL γ microstructure in EBM components would result in an anisotropy of the mechanical properties, strongly depending on the building direction [8]. As a consequence for BMBF alloys the heat treatment was conducted above $T_{\gamma, solv}$, i.e. inside the single α -phase field region, where a homogenization of the Al distribution and subsequently a minimization of the microstructural anisotropy can take place. This heat treatment is possible due to the chemical composition, which generates a large single α -phase field region for both BMBF alloys and, as described in chapter D.3, leads to FL microstructures as displayed in Fig. D.7b and c. Obviously, the appearance of β_o -phase in the former Al lean bands is prevented and only bright ζ are present. Most importantly, these precipitations of ζ inhibit grain growth due to the mentioned Si effect [15] during annealing in the single α -phase field region. The grains coarsened, but are still finer when compared to other FL microstructures of high Al containing γ -TiAl based alloys which contain no Si in sufficient concentrations [5,15,56]. From the FL microstructures shown in Fig. D.7b and c no pronounced anisotropic mechanical behavior is expected. A first evaluation of the mechanical properties was performed by hardness testing. Despite the high Al content and an average lamellar spacing of 60 ± 20 nm of the FL BMBF1 alloy, its hardness (439 HV10) is comparable to that of a cast, hot-forged and heat-treated FL TNM alloy (427 HV10) [16]. Furthermore, the comparably large lamellar spacing of the BMBF1 alloy improves the thermal stability of the FL microstructure at elevated temperatures. As seen in Fig. D.7b, no break-up of the lamellar colonies via a so-called cellular reaction, as observed for TNM alloys [15,52] takes place during the stabilization heat treatment conducted at 900 °C for 4 h. The same behavior was analyzed for the BMBF2 alloy, which was cooled more slowly in the course of the heat treatment, resulting in an even wider lamellar spacing (Fig. D.7c) leading to a hardness of around 300 HV10.

Finally, creep tests reveal the high-temperature potential of the developed alloys, see Larson-Miller plot in Fig. D.8. The BMBF1 alloy shows almost no deviation, demonstrating the isotropic behavior in respect to the building direction. On the other hand, the creep results of BMBF2 deviates slightly, but exceeds the creep resistance of BMBF1, proving the thermal stability of the coarser lamellar microstructure. In addition, both BMBF alloys exhibit a better creep resistance than their predecessors, e.g. the TNM [15,57] and the TNM⁺ alloy [15], which were manufactured conventionally via a melt [57] or powder metallurgical route [15] including a subsequent heat treatment. In summary, this study proceeds the development of an intermetallic γ -TiAl based alloy, which on the one hand satisfies the demands of AM and on the other hand raises the potential application temperature up to 850 °C by increasing the creep resistance considerably.

D.5 Summary

In the present work new process-adapted 4th generation intermetallic γ -TiAl based alloys were developed for EBM. The so-called BMBF alloys have been designed to provide isotropic mechanical properties after a subsequent heat treatment. Especially to prevent the formation of a columnar texture a careful selection of the alloy's composition and the EBM process parameter was necessary:

- The amount of β_o -phase, which produces a solidification texture is reduced to a minimum due to an enhanced Al, Si and C content and a decreased amount of β -stabilizing elements. Therefore, both BMBF alloys solidify along the peritectic path allowing a parallel nucleation of the α -phase and the β -phase directly from the liquid melt during the EBM process. The further solid-state transformations lead to randomly distributed γ grain orientations and no elongated parent β -grains are present as reported for the basic TNM alloy in as-EBM condition.

Furthermore, in this study, the formation of a band-like phase distribution in the final microstructure has been reduced:

- A lower E_L decreases the Al loss on top of the melt pool, which prevents a local shift of $T_{\gamma,solv}$. However, a specific input of energy is necessary to guarantee a dense component. Therefore, a complete homogeneous Al distribution cannot be reached.
- Due to the selected chemical composition of both BMBF alloys, a large single α -phase field region was obtained. Therein, the heat treatment resulted in a homogeneous FL microstructure. Although the lamellar spacings are wide, hardness values up to 439 HV10 can be reached by the addition of solid solution hardening elements, such as C, Zr, W, and Nb.
- The FL microstructures of the developed EBM-TiAl alloys are thermodynamically stable and show excellent creep resistance up to 850 °C, thus exceeding other engineering TiAl alloys.

Acknowledgements

The research work was conducted within the framework of the BMBF project 03XP0088C, Germany. The support of the Ruhr Universität Bochum, Lehrstuhl Werkstofftechnik, performing the advanced heat treatments within a Quintus HIP unit, is gratefully acknowledged.

D.6 References

- [1] H. Clemens, S. Mayer, Design, processing, microstructure, properties, and applications of advanced intermetallic TiAl alloys, *Adv. Eng. Mater.* 15 (2013) 191–215, DOI:10.1002/adem.201200231.
- [2] F. Appel, J.D.H. Paul, M. Oehring, *Gamma Titanium Aluminide Alloys: Science and Technology*, Wiley-VCH, Germany, 2012.
- [3] R. Pflumm, A. Donchev, S. Mayer, H. Clemens, M. Schütze, High-temperature oxidation behavior of multi-phase Mo-containing γ -TiAl-based alloys, *Intermetallics* 53 (2014) 45–55, DOI:10.1016/j.intermet.2014.04.010.
- [4] G. Baudana, S. Biamino, B. Klöden, A. Kirchner, T. Weißgärber, B. Kieback, M. Pavese, D. Ugues, P. Fino, C. Badini, Electron beam melting of Ti-48Al-2Nb- 0.7Cr-0.3Si: feasibility investigation, *Intermetallics* 73 (2016) 43–49, <https://doi.org/10.1016/j.intermet.2016.03.001>.
- [5] V. Juechter, M.M. Franke, T. Merenda, A. Stich, C. Körner, R.F. Singer, Additive manufacturing of Ti-45Al-4Nb-C by selective electron beam melting for automotive applications, *Additive Manufacturing* 22 (2018) 118–126, DOI 10.1016/j.addma.2018.05.008.
- [6] M. Galati, L. Iuliano, A literature review of powder-based electron beam melting focusing on numerical simulations, *Additive Manufacturing* 19 (2018) 1–20, DOI: 10.1016/j.addma.2017.11.001.
- [7] M. Seifi, A.A. Salem, D.P. Satko, U. Ackelid, S.L. Semiatin, J.J. Lewandowski, Effects of HIP on microstructural heterogeneity, defect distribution and mechanical properties of additively manufactured EBM Ti-48Al-2Cr-2Nb, *J. Alloys Compd.* 729 (2017) 1118–1135, DOI: 10.1016/j.jallcom.2017.09.163.
- [8] M. Todai, T. Nakano, T. Liu, H.Y. Yasuda, K. Hagihara, K. Cho, M. Ueda, M. Takeyama, Effect of building direction on the microstructure and tensile properties of Ti-48Al-2Cr-2Nb alloy additively manufactured by electron beam melting, *Additive Manufacturing* 13 (2017) 61–70, DOI: 10.1016/j.addma.2016.11.001.
- [9] K. Cho, R. Kobayashi, J.Y. Oh, H.Y. Yasuda, M. Todai, T. Nakano, A. Ikeda, M. Ueda, M. Takeyama, Influence of unique layered microstructure on fatigue properties of Ti-48Al-2Cr-2Nb alloys fabricated by electron beam melting, *Intermetallics* 95 (2018) 1–10, DOI: 10.1016/j.intermet.2018.01.009.
- [10] H. Yue, Y. Chen, X. Wang, F. Kong, Effect of beam current on microstructure, phase, grain characteristic and mechanical properties of Ti-47Al-2Cr-2Nb alloy fabricated by selective electron beam melting, *J. Alloys Compd.* 750 (2018) 617–625, DOI: 10.1016/j.jallcom.2018.03.343.
- [11] M. Jop, R. Wartbichler, P. Staron, E. Maawad, S. Mayer, H. Clemens, Microstructural and phase analysis of an additively manufactured Intermetallic TiAl alloy using Metallographic Techniques and High-Energy X-Rays, *Pract. Metallogr.* 57 (2020) 84–95, DOI: 10.3139/147.110611.
- [12] S. Mayer, P. Erdely, F.D. Fischer, D. Holec, M. Kastnerhuber, T. Klein, H. Clemens, Intermetallic β -Solidifying γ -TiAl based alloys - from fundamental research to application, *Adv. Eng. Mater.*, 19 (2017), DOI: 1600735, 10.1002/adem.201600735.
- [13] W. Wallgram, T. Schmörlzer, L. Cha, G. Das, V. Güther, H. Clemens, Technology and mechanical properties of advanced γ -TiAl based alloys, *Int. J. Mater. Res.* 100 (2009) 1021–1030, DOI: 10.3139/146.110154.
- [14] H. Clemens, W. Wallgram, S. Kremmer, V. Güther, A. Otto, A. Bartels, Design of novel β -solidifying TiAl alloys with adjustable β /B2-phase fraction and excellent hot-workability, *Adv. Eng. Mater.* 10 (2008) 707–713, DOI: 10.1002/adem.200800164.
- [15] M. Kastnerhuber, T. Klein, H. Clemens, S. Mayer, Tailoring microstructure and chemical composition of advanced γ -TiAl based alloys for improved creep resistance, *Intermetallics* 97 (2018) 27–33, DOI: 10.1016/j.intermet.2018.03.011.
- [16] E. Schwaighofer, H. Clemens, S. Mayer, J. Lindemann, J. Klose, W. Smarsly, V. Güther, Microstructural design and mechanical properties of a cast and heat-treated intermetallic multi-phase γ -TiAl based alloy,

- Intermetallics 44 (2014) 128–140, DOI: 10.1016/j.intermet.2013.09.010.
- [17] I.S. Jung, H.S. Jang, M.H. Oh, J.H. Lee, D.M. Wee, Microstructure control of TiAl alloys containing β stabilizers by directional solidification, *Mater. Sci. Eng., A* 329–331 (2002) 13–18, DOI: 10.1016/S0921-5093(01)01494-0.
- [18] R. Wartbichler, H. Clemens, S. Mayer, Electron beam melting of a β -solidifying intermetallic titanium aluminide alloy, *Adv. Eng. Mater.* (2019), DOI: 10.1002/adem.201900800.
- [19] E. Chauvet, C. Tassin, J.-J. Blandin, R. Dendievel, G. Martin, Producing Ni-base superalloys single crystal by selective electron beam melting, *Scripta Mater.* 152 (2018) 15–19, DOI: 10.1016/j.scriptamat.2018.03.041.
- [20] S.S. Al-Bermani, M.L. Blackmore, W. Zhang, I. Todd, The origin of microstructural diversity, texture, and mechanical properties in electron beam melted Ti-6Al-4V, *Metall. Mater. Trans.* 41 (2010) 3422–3434, DOI: 10.1007/s11661-010-0397-x.
- [21] W. Kan, B. Chen, C. Jin, H. Peng, J. Lin, Microstructure and mechanical properties of a high Nb-TiAl alloy fabricated by electron beam melting, *Mater. Des.* 160 (2018) 611–623, DOI: 10.1016/j.matdes.2018.09.044.
- [22] F. Appel, M. Oehring, J.D.H. Paul, C. Klinkenberg, T. Carneiro, Physical aspects of hot-working gamma-based titanium aluminides, *Intermetallics* 12 (2004) 791–802, DOI: 10.1016/j.intermet.2004.02.042.
- [23] C. Kenel, D. Grolimund, J.L. Fife, V.A. Samson, S. van Petegem, H. van Swygenhoven, C. Leinenbach, Combined in situ synchrotron micro X-ray diffraction and high-speed imaging on rapidly heated and solidified Ti-48Al under additive manufacturing conditions, *Scripta Mater.* 114 (2016) 117–120, <https://doi.org/10.1016/j.scriptamat.2015.12.009>.
- [24] P. Barriobero-Vila, J. Gussone, A. Stark, N. Schell, J. Haubrich, G. Requena, Peritectic titanium alloys for 3D printing, *Nat. Commun.* 9 (2018) 3426, <https://doi.org/10.1038/s41467-018-05819-9>.
- [25] A. Klassen, V.E. Forster, V. Juechter, C. Körner, Numerical simulation of multi-component evaporation during selective electron beam melting of TiAl, *J. Mater. Process. Technol.* 247 (2017) 280–288, DOI: 10.1016/j.jmatprotec.2017.04.016.
- [26] R. Kainuma, Y. Fujita, H. Mitsui, I. Ohnuma, K. Ishida, Phase equilibria among α (hcp), β (bcc) and γ (L10) phases in Ti–Al base ternary alloys, *Intermetallics* 8 (2000) 855–867, DOI: 10.1016/S0966-9795(00)00015-7.
- [27] A. Couret, D. Reyes, M. Thomas, N. Ratel-Ramond, C. Deshayes, J.-P. Monchoux, Effect of ageing on the properties of the W-containing IRIS-TiAl alloy, *Acta Mater.* 199 (2020) 169–180, DOI: 10.1016/j.actamat.2020.07.061.
- [28] T. Voisin, J.-P. Monchoux, M. Hantcherli, S. Mayer, H. Clemens, A. Couret, Microstructures and mechanical properties of a multi-phase β -solidifying TiAl alloy densified by spark plasma sintering, *Acta Mater.* 73 (2014) 107–115, <https://doi.org/10.1016/j.actamat.2014.03.058>.
- [29] J. Lapin, Creep behaviour of a cast TiAl-based alloy for industrial applications, *Intermetallics* 14 (2006) 115–122, DOI: 10.1016/j.intermet.2005.03.008.
- [30] A. Dlouhý, K. Kucharova, Creep and microstructure of near-gamma TiAl alloys, *Intermetallics* 12 (2004) 705–711, DOI: 10.1016/j.intermet.2004.03.007.
- [31] K. Maruyama, R. Yamamoto, H. Nakakuki, N. Fujitsuna, Effects of lamellar spacing, volume fraction and grain size on creep strength of fully lamellar TiAl alloys, *Mater. Sci. Eng., A* 239–240 (1997) 419–428, DOI: 10.1016/S0921-5093(97)00612-6.
- [32] G. Dehm, C. Motz, C. Scheu, H. Clemens, P.H. Mayrhofer, C. Mitterer, Mechanical size-effects in miniaturized and bulk materials, *Adv. Eng. Mater.* 8 (2006) 1033–1045, DOI: 10.1002/adem.200600153.
- [33] S. Nishikiori, S. Takahashi, S. Satou, T. Tanaka, T. Matsuo, Microstructure and creep strength of fully-lamellar TiAl alloys containing beta-phase, *Mater. Sci. Eng., A* 329–331 (2002) 802–809, DOI:

10.1016/S0921-5093(01)01638-0.

- [34] R.M. Imayev, V.M. Imayev, M. Oehring, F. Appel, Alloy design concepts for refined gamma titanium aluminide based alloys, *Intermetallics* 15 (2007) 451–460, DOI: 10.1016/j.intermet.2006.05.003.
- [35] T. Klein, B. Rashkova, D. Holec, H. Clemens, S. Mayer, Silicon distribution and silicide precipitation during annealing in an advanced multi-phase γ -TiAl based alloy, *Acta Mater.* 110 (2016) 236–245, DOI: 10.1016/j.actamat.2016.03.050.
- [36] E. Schwaighofer, B. Rashkova, H. Clemens, A. Stark, S. Mayer, Effect of carbon addition on solidification behavior, phase evolution and creep properties of an intermetallic β -stabilized γ -TiAl based alloy, *Intermetallics* 46 (2014) 173–184, DOI: 10.1016/j.intermet.2013.11.011.
- [37] J. Bresler, S. Neumeier, M. Ziener, F. Pyczak, M. Göken, The influence of niobium, tantalum and zirconium on the microstructure and creep strength of fully lamellar γ/α_2 titanium aluminides, *Mater. Sci. Eng., A* 744 (2019) 46–53, DOI: 10.1016/j.msea.2018.11.152.
- [38] Z.W. Huang, Thermal stability of Ti–44Al–4Nb–4Zr–0.2Si–1B alloy, *Intermetallics* 42 (2013) 170–179, DOI: 10.1016/j.intermet.2013.06.007.
- [39] D. Wimler, S. Kardos, J. Lindemann, H. Clemens, S. Mayer, Aspects of powder characterization for additive manufacturing, *Pract. Metallogr.* 55 (2018) 620–636, DOI: 10.3139/147.110547.
- [40] R. Werner, M. Schloffer, E. Schwaighofer, H. Clemens, S. Mayer, Thermodynamic calculations of phase equilibria and phase fractions of a β -solidifying TiAl alloy using the CALPHAD approach, *MRS Proc* 1516 (2012) 59–64, DOI: 10.1557/opl.2012.1680.
- [41] R. Gerling, H. Clemens, F.P. Schimansky, Powder metallurgical processing of intermetallic gamma titanium aluminides, *Adv. Eng. Mater.* 6 (2004) 23–38, DOI: 10.1002/adem.200310559.
- [42] M. Achtermann, W. Fürwitt, V. Güther, H.P. Nicolai EP2342365, 2011.
- [43] V. Güther, M. Allen, J. Klose, H. Clemens, Metallurgical processing of titanium aluminides on industrial scale, *Intermetallics* 103 (2018) 12–22, DOI: 10.1016/j.intermet.2018.09.006.
- [44] J. Schwerdtfeger, C. Körner, Selective electron beam melting of Ti–48Al–2Nb–2Cr: microstructure and aluminium loss, *Intermetallics* 49 (2014) 29–35, <https://doi.org/10.1016/j.intermet.2014.01.004>.
- [45] M. Schloffer, T. Schmoelzer, S. Mayer, E. Schwaighofer, G. Hawranek, F.-P. Schimansky, F. Pyczak, H. Clemens, The characterisation of a powder metallurgically manufactured TNM Titanium Aluminide alloy using complimentary quantitative methods, *Pract. Metallogr.* 48 (2011) 594–604, DOI: 10.3139/147.110138.
- [46] J. Soyama, M. Oehring, W. Limberg, T. Ebel, K.U. Kainer, F. Pyczak, The effect of zirconium addition on sintering behaviour, microstructure and creep resistance of the powder metallurgy processed alloy Ti–45Al–5Nb–0.2B–0.2C, *Mater. Des.* 84 (2015) 87–94, DOI: 10.1016/j.matdes.2015.06.095.
- [47] C. Körner, Additive manufacturing of metallic components by selective electron beam melting - a review, *Int. Mater. Rev.* 61 (2016) 361–377, DOI: 10.1080/09506608.2016.1176289.
- [48] A.M. Rausch, M. Markl, C. Körner, Predictive simulation of process windows for powder bed fusion additive manufacturing: influence of the powder size distribution, *Comput. Math. Appl.* 78 (2018) 2351–2359, DOI: 10.1016/j.camwa.2018.06.029.
- [49] G. Wegmann, R. Gerling, F.-P. Schimansky, Temperature induced porosity in hot isostatically pressed gamma titanium aluminide alloy powders, *Acta Mater.* 51 (2003) 741–752, DOI: 10.1016/S1359-6454(02)00465-2.
- [50] M. Takeyama, M. Nakamura, T. Kumagai, M. Kikuchi, Cooling rate dependence of the α/γ phase transformation in titanium aluminides and its application to alloy development, in: *Proc First Int Symp Struct Intermet*, Publ by Minerals, Metals & Materials Soc (TMS), 1993, pp. 167–176.
- [51] S.R. Dey, A. Hazotte, E. Bouzy, S. Naka, Development of Widmanstätten laths in a near- γ TiAl alloy, *Acta Mater.* 53 (2005) 3783–3794, DOI: 10.1016/j.actamat.2005.04.007.
- [52] M. Kastenhuber, B. Rashkova, H. Clemens, S. Mayer, Enhancement of creep properties and

- microstructural stability of intermetallic β -solidifying γ -TiAl based alloys, *Intermetallics* 63 (2015) 19–26, DOI: 10.1016/j.intermet.2015.03.017.
- [53] N. Raghavan, R. Dehoff, S. Pannala, S. Simunovic, M. Kirka, J. Turner, N. Carlson, S.S. Babu, Numerical modeling of heat-transfer and the influence of process parameters on tailoring the grain morphology of IN718 in electron beam additive manufacturing, *Acta Mater.* 112 (2016) 303–314, DOI: 10.1016/j.actamat.2016.03.063.
- [54] Jie Liu, Staron Peter, Stefan Riekehr, Andreas Stark, Norbert Schell, Norbert Huber, Andreas Schreyer, Martin Müller, Nikolai Kashaev, Phase transformation and residual stress in a laser beam spot-welded TiAl-based alloy, *Metall. Mater. Trans.* 47 (2016) 5750–5760, DOI: 10.1007/s11661-016-3745-7.
- [55] V. Juechter, T. Scharowsky, R.F. Singer, C. Körner, Processing window and evaporation phenomena for Ti–6Al–4V produced by selective electron beam melting, *Acta Mater.* 76 (2014) 252–258, DOI: 10.1016/j.actamat.2014.05.037.
- [56] T. Voisin, J.-P. Monchoux, M. Perrut, A. Couret, Obtaining of a fine near-lamellar microstructure in TiAl alloys by spark plasma sintering, *Intermetallics* 71 (2016) 88–97, DOI: 10.1016/j.intermet.2016.01.003.
- [57] M. Schloffer, *Gefüge und Eigenschaften der intermetallischen TNM-Legierung*, Dissertation, Leoben, 2013.

How electron beam melting tailors the Al-sensitive microstructure and mechanical response of a novel γ -TiAl based alloy

D. Wimler^{a*}, K. Kásznar^a, M. Musi^a, C. Breuning^b, M. Markl^b, J. Keckes^a, H. Clemens^a, C. Körner^b, S. Mayer^a

^a Department of Materials Science, Montanuniversität Leoben, 8700 Leoben, Austria

^b Chair of Materials Science and Engineering for Metals, Friedrich-Alexander-Universität Erlangen-Nürnberg, Erlangen, Germany

* Corresponding author

SCI Journal (2021)

under review

Keywords:

Additive manufacturing; titanium aluminides; microstructure; crystal orientation; heat treatment

Abstract

Additive manufacturing of lightweight intermetallic γ -TiAl based alloys combines process-related freedom of design with material-specific excellent high-temperature properties. Nevertheless, where locally melting the powder by an electron beam, there is a risk that Al evaporates due to its high vapor pressure, causing compositional and microstructural variations. This work investigates the impact of different process parameters on the total and local Al-content as well as the resulting as-built and heat-treated microstructure in a complex multiphase Ti-44.8Al-4.1Nb-0.7W-1.1Zr-0.4Si-0.5C-0.1B (at.%) alloy. The examinations applied are complementary, employing electron microscopy, X-ray spectroscopy and diffraction experiments with synchrotron X-ray radiation, supported by numerical simulations. The mechanical anisotropy of the heat-treated microstructure was analyzed by micro-hardness measurements. The results demonstrate that the amount of γ -TiAl phase decreases with increasing energy input of the electron beam in the as-built and heat-treated microstructure owing to the total and local loss of Al. Besides, the investigations of the crystal orientations within the multiphase alloy reveal a preferred orientation of the γ phase at high energy inputs. This follows from the fact that the preferred γ orientation is inherited through directional solidification of the β phase.

In summary, the obtained results show that tailor-made material properties of additively manufactured γ -TiAl components are achievable through the use of adopted and optimized process parameters.

E.1 Introduction

For decades, the need for lightweight components, such as turbine blades, to design more efficient propulsion systems, has driven the research in γ -TiAl based alloys as well as the progress in additive manufacturing (AM). In principle, both, γ -TiAl alloys and AM, have their respective advantages. On the one hand, γ -TiAl based alloys are an alternative material to the twice as heavy Ni-base alloys for temperatures up to 800 °C, proven by the so-called TNM alloy, which represents the first process-adapted γ -TiAl based alloy of the 4th generation [1-7]. On the other hand, the AM technology provides design freedom to add shape or functional complexity in components [8-11] and in this context decreases the buy-to-fly ratio, important in the aviation industry, due to better material efficiency [12, 13]. In combination, the processing of γ -TiAl based alloys via electron beam melting (EBM), the commercially available AM method for structural TiAl aerospace parts, indicates a great potential [14-20]. However, for the production of γ -TiAl AM parts on an industrial scale, specific challenges have to be overcome, ideally through the understanding of the interaction between EBM parameters and the material properties of the γ -TiAl alloys.

In general, three ordered phases can appear in the microstructure of 4th generation γ -TiAl based alloys at service temperature: the face-centered tetragonal γ -TiAl phase (L1₀ structure), the hexagonal α_2 -Ti₃Al phase (D0₁₉ structure) as well as the body-centered cubic (bcc) β_o -TiAl phase (B2 structure). Besides, α (A3 structure) and β phase (A2 structure) exist as disordered high-temperature counterpart of α_2 and β_o , respectively. The fractions of the ordered phases as well as their morphologies define the designation of the microstructure and the material properties. As an example, the so-called nearly lamellar γ (NL γ) microstructure is considered mechanically balanced between room temperature (RT) ductility and high-temperature creep strength. In this microstructure, the "soft" γ phase forms in two manners: globular γ (γ_g) grains develop during an isothermal heat treatment in the $\alpha + \gamma$ phase field region, while γ laths precipitate during subsequent cooling or stabilization annealing with the formation of lamellar α_2/γ colonies [4, 21-23]. Such a heat treatment is often carried out to optimize the as-manufactured microstructure, e.g. as-cast [2, 21, 24, 25] or as-forged [2, 3], and to tailor the mechanical properties according to the application of the envisaged γ -TiAl component.

In the last decade, attempts have been made to substitute the conventional investment casting production of γ -TiAl alloys with AM, owing to the advantages already mentioned. During the EBM process, the powder is melted with a focused electron beam in a layer-wise manner under vacuum. More precisely, each powder layer has to be melted, solidified, and remelted to generate a dense part. The electron beam can be defocused and, thus, used to heat the powder bed as well as the built-up component to prevent thermal cracking. For more details regarding the EBM process the reader is referred to Refs. [10, 11, 26-28]. The arising as-EBM microstructure in γ -TiAl alloys differs from as-cast, as-forged [2, 3, 6, 24, 25, 29]

and other powder metallurgical approaches [30-36] by its phase distribution, morphology and orientation as well as in the course of the local Al content [19, 20, 37-43]. These differences rest upon the physical metallurgy aspects of the Ti-Al system and the process itself controlled by the selected process parameters. The aim of this work is to gain knowledge about the just mentioned interactions by investigating a novel engineering γ -TiAl based alloy manufactured with different EBM parameters. In this respect, a characterization of the samples from top to bottom was performed with electron microscopy, electron backscatter diffraction, as well as high-energy X-ray diffraction and, additionally, was supported by means of numeric simulation. Finally, application-relevant heat treatments point out the impact of the selected EBM process parameter on the adjusted microstructure and mechanical response.

E.2 Material and methods

Alloy powder with a composition of Ti-44.8Al-4.1Nb-0.7W-1.1Zr-0.4Si-0.5C-0.1B (in at.%, unless stated otherwise) and 1000 m.ppm O in the particle diameter range of 50-125 μm was used as starting material. The investigated alloy is also known as BMBF1 alloy, see Ref. [19]. This nomenclature refers to the project "NextTiAl" (03XP0088A) on tailor-made γ -TiAl based alloys for AM by means of EBM funded by the German Federal Ministry of Education and Research (BMBF). The concentrations of the elements Ti, Al, Nb, W, and Zr were determined by X-ray fluorescence spectroscopy (XRF) while Si, C and B were evaluated by inductively coupled plasma-atomic emission spectroscopy (ICP-AES). For analyzing the O content, carrier gas hot extraction was used [44]. The powder was produced via electrode induction melting gas atomization (EIGA) [45] by TLS Technik GmbH & Co. Spezialpulver KG, Germany. The ingots for the EIGA process were produced according to Refs. [46, 47] by GfE Metalle und Materialien GmbH, Germany. To manufacture the cuboid test samples layer-by-layer from powder material, an EBM machine of the type A2X from Arcam AB, Sweden, was used at Neue Materialien Fürth GmbH, Germany. Four different scanning parameter sets (P1, P2, P3, and P4) were used to build up cuboid EBM samples ($15 \times 15 \times 80 \text{ mm}^3$) against the background of determining the influence of a constant beam current (I), deflection speed (v) as well as line energy (E_L), as illustrated in Fig. E.1, on the formation of the microstructure. E_L was calculated according to $E_L = \frac{U \cdot I}{v}$, where U is the acceleration voltage of 60 kV. For all experiments, a layer thickness of 100 μm was set. The focused electron beam was operated to melt the layers using a cross-snake hatching strategy with a hatching distance (HD) of 100 μm . The preheating temperature was reached via defocused electron beam and was around 1020 °C.

The specimens were sectioned along the x-z midplane then metallographically ground, polished and electrolytically etched in accordance with Ref. [48]. To avoid edge effects, always the center regions of the cross-sections in respect of the x direction were investigated.

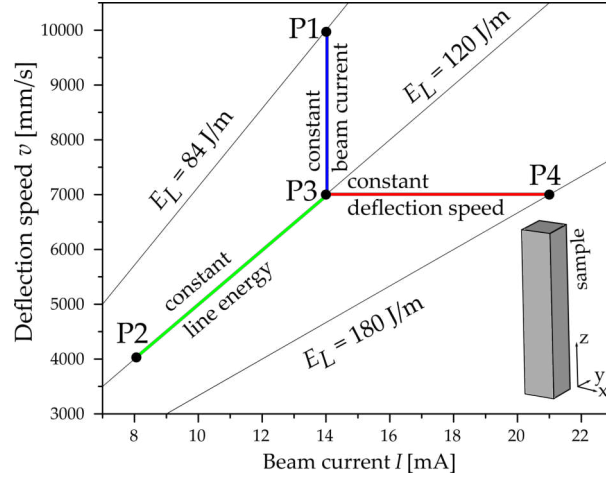


Figure E.1: EBM parameters used for building up the four cuboid TiAl samples (P1-P4) with a dimension of $15 \times 15 \times 80 \text{ mm}^3$, whereby the layer thickness, HD, U, and the preheating temperature are kept constant at $100 \mu\text{m}$, $100 \mu\text{m}$, 60 kV , and 1020°C , respectively. Note that z denotes the building direction during the EBM process.

The samples were examined using a Tescan scanning electron microscope (SEM) of the type CLARA, Czech Republic, in backscattered electron (BSE) mode, in combination with an energy-dispersive X-ray spectroscopy (EDX) system of the type X-Max and the corresponding Aztec software, both from Oxford Instruments, United Kingdom. A SEM of the type Versa 3D DualBeam equipped with an EDAX Hikari XP camera from Thermo Fisher (formerly FEI), United States of America, was applied for electron backscatter diffraction (EBSD) measurements. The corresponding data evaluation was carried out using OIM Analysis 7. For example, the colony sizes were determined by the equivalent circle diameter (ECD) taking colonies larger than $2 \mu\text{m}$ into account. The orientation analysis was carried out by using the generalized spherical harmonic series expansion method [49].

High-energy X-ray diffraction (HEXRD) experiments were performed at the high-energy materials science (HEMS) beamline P07B of PETRA III at DESY, Germany, operated by the Helmholtz Zentrum Geesthacht [50]. The characterization was performed using a mean photon energy of 87.1 keV and a beam cross-section of about $20 \times 500 \mu\text{m}^2$ in x and z direction with regard to the sample geometry. For the cross-sectional micro X-ray diffraction (CSmicroXRD) experiments, $100 \mu\text{m}$ thick samples (y direction) were moved along the building direction z with increments of $20 \mu\text{m}$ for about $5000 \mu\text{m}$, thus a total material volume of $250 \cdot 10^6 \mu\text{m}^3$ was investigated. For more details regarding the CSmicroXRD setup, the reader is referred to Ref. [51]. During these experiments, 2D diffraction patterns, i.e. Debye-Scherrer rings, were continually collected in transmission geometry using a Perkin Elmer XRD 1621 flat panel detector with a pixel matrix of 2048×2048 and a pixel size of $200 \times 200 \mu\text{m}^2$. The recorded Debye-Scherrer rings were summed up and integrated using the data reduction software program Fit2D [52]. The Rietveld refinement [53] was used

to quantify the fractions of the phases present, applying the software MAUD [54] with an accuracy of 2 vol.%.

Heat treatments were conducted under atmospheric conditions using a high-temperature furnace of the type RHF 1600 from Carbolite, Germany. For evaluating the mechanical response of the material, Vickers hardness measurements HV10 and HV0.05 were performed at the polished xz cross-sections.

Numerical simulations were used to analyze the alloy composition during EBM as a function of the process parameters. These simulations were conducted by means of the software tool *SAMPLE^{2D}* (simulation of additive manufacturing on the powder scale using a laser or electron beam), which is described in detail in Ref. [55]. It is based on a Lattice Boltzmann framework that solves full hydrodynamics in the melt pool, thermodynamics in the entire domain and supports multi-component evaporation [56]. The setup used in the current study consists of a rectangle simulation domain with a length of 1.8 mm, whereby 1.5 mm were used for melting. The simulation plane is placed in the center of the scan lines. For each of the 15 scanlines with 100 μm HD, the beam moves out of the simulation plane between -7.5 and 7.5 mm with defined v and beam power. A 100 μm powder layer with a relative density of 0.5 was applied for each of the ten simulated layers on top of an ideal substrate with a thickness of 300 μm . The hatch direction was rotated by 180° between each layer. The initial temperature of the simulation domain was set to 1200 °C, to resemble the conditions in the stationary state of the hatch. The material properties of both powder particles and the substrate were taken from the well-known Ti-48Al-2Cr-2Nb γ -TiAl based alloy [56]. Multi-component evaporation was considered. The initial concentrations for the two main constituents of the simulation were $x^{\text{Ti}}=55.2$ at.% and $x^{\text{Al}}=44.8$ at.%, neglecting all other constituents. The calculations were performed using a uniform grid with $\Delta x=3$ μm and a time step size of $\Delta t=5 \cdot 10^{-8}$ s. The final alloy composition was determined from molten cells only, excluding unmelted powder particles at the edge of the simulation domain.

E.3 Results

E.3.1 as-EBM condition of the four sample states P1-P4

Al content

The samples were built with four different process parameter sets as illustrated in Fig. E.1, i.e. v , I and E_L varied systematically. A subsequent chemical analysis via XRF provides the Al content, which is summarized in Table E.1 together with the Al content of the starting powder. Based on these results, the Al evaporation (ΔAl) was calculated as difference between the Al content of the powder and the built specimens. The lowest ΔAl shows the sample manufactured with the lowest E_L (P1): $\Delta Al=1.20$ at.%, while the highest ΔAl

of 1.80 at.% was measured for the sample P4, i.e. using the highest E_L . In between are P2 and P3 with a $\Delta Al=1.27$ and 1.25 at.%, respectively. Therefore, it is evident that the higher E_L , the higher is the Al loss. The marginal difference between P2 and P3 may stem from different beam currents and deflection speeds. However, it should be noted that this difference is within the measurement error of about 0.025 at.% for Al in γ -TiAl based alloys [46].

Table E.1: The table indicates E_L used to build up the four TiAl samples shown in Fig. E.1 and compares the material's properties which are discussed in detail in the text. ΔAl was calculated from the chemical analysis via XRF of the powder and the samples. Based on the numerical simulations of the spatial Al distribution, ΔAl was evaluated too. The numerical simulation of P4 leads to inaccurate hydrodynamics and evaporation in the two-dimensional representation as a result of the high E_L , thus a significantly higher ΔAl is expected. The HEXRD experiments at the samples in as-EBM condition result in the phase fractions of γ , α_2 and β_o . The globular γ_g phase fraction was evaluated from SEM-BSE images of the heat-treated condition, i.e. after 1290 °C for 30 min followed by water quenching. The hardness according to Vickers was determined within the xz-cross-section of the heat-treated samples at 1290 °C/ 30 min followed by air cooling and a stabilization treatment at 900 °C for 4 h (furnace cooled), i.e. with equal γ_g fractions.

Sample		XRF		Simulation	HEXRD			γ_g	Hardness
Name	E_L [J/m]	Al [at.%]	ΔAl [at.%]	ΔAl [at.%]	γ [vol.%]	α_2 [vol.%]	β_o [vol.%]	[vol.%]	HV10
Powder		44.80							
P1	84	43.60	1.20	0.41	80	17	3	24	413±5
P2	120	43.53	1.27	0.62	78	19	3	13	427±10
P3	120	43.55	1.25	0.60	78	19	3	16	439±7
P4	180	43.00	1.80	$\Delta Al \gg 0.63$	77	20	3	5	477±10

The numerical simulation of the Al loss in the xz cross-section implementing the parameter P3 reveals an Al distribution as shown in Fig. E.2. Obviously, the Al content is spatially inhomogeneously distributed with an Al loss between 1.5 at.% Al in the bright yellow bands and 0 at.% Al in the powder and the underneath bulk, which acts as starting plate for the simulation setup. In addition to the alloy composition, bonding faults arise during the simulation. As expected, connection faults can be identified at the edges, which form due to insufficient melt pool depth at the start of the hatch. Further, a bonding fault with remaining unmolten powder particles can be identified in the center of the simulation. Above this bonding fault, the Al content is high due to the locally insufficient energy input to remelt the layer below. As a consequence, a sharp transition between the two layers can be seen. Otherwise, the Al distribution appears wavy due to the melting of differently sized powder particles and remelting of uneven layers. The mean Al loss of the molten material for the parameter set P3 yields to a ΔAl of 0.6 at.%. The simulation results obtained for all parameter combinations regarding ΔAl are stated in Table E.1, which shows an increasing

ΔAl with higher E_L . Although P2 and P3 share the same E_L , sample P2, which was built with a lower beam current, shows a higher loss in Al, like the experimental values. Note that the simulation result of parameter set P4 with $E_L=180$ J/m shows a ΔAl of 0.63 at.%, which does not vary compared to the values obtained for process parameters P2 and P3. This is caused by the high E_L , which leads to inaccurate hydrodynamics and evaporation in the two-dimensional simulation, thus higher ΔAl than 0.63 at.% are expected, which will be discussed in section E.4.1.

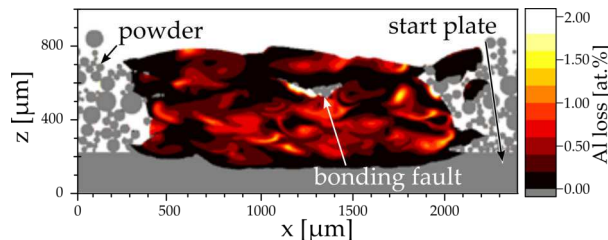


Figure E.2: Simulation of the Al distribution of parameter set P3 (see Fig. E.1) across the xz midplane. The Al evaporation varies between areas with almost 0 at.% and areas with up to 2 at.% Al loss. The calculation across the molten area reveals a mean ΔAl of 0.60 at.%.

Microstructural characterization of the as-built sample

Figure E.3a shows the microstructure of the sample center P3 in the z direction. The microstructure consists of several phases, which can be distinguished in the SEM BSE image by their contrast and morphology: the gray lamellar α_2 , the dark gray γ , the bright white β_o phase, and small spherical white particles, which are ζ -silicides. Complementary, an EDX mapping was conducted on the same area, displayed in Fig E.3b. The corresponding results are shown for Si, W and Al. Si is enriched in the small spherical white contrasted ζ particles, whereas the bright white β_o phase contains W. Both phases, i.e. ζ and β_o , as well as the lamellar α_2 phase are depleted in Al when compared to the γ phase. An additional overview SEM image in BSE mode reveals contrast differences in the as-EBM microstructure alternating about every layer thickness, i.e. $100 \mu m$, as shown in Fig. E.3c for the sample P3. Therein, bright bands are Al lean due to their enrichment in β_o and, on the contrary, the Al rich areas contain a lot of γ . This just discussed microstructure (Fig. E.3), i.e. the morphology of the phases and the banded structure, appears in all four samples and forms during preheating at $1020^\circ C$. Note that despite different Al contents, the composition of the individual phases does not change, because the missing Al is compensated by a change of the phase fractions. The overall phase fractions of the four samples were determined from Debye-Scherrer rings, which are recorded during HEXRD experiments. The resultant intensities integrated over the azimuthal angle are shown in Fig. E.4 along the 2θ angle and the determined phase fractions of the three ordered phases, i.e. α_2 , β_o , and γ , are listed in Table E.1. Besides these phases, a weak Ti_5Si_3 peak (D8₈ structure) was identifiable in all

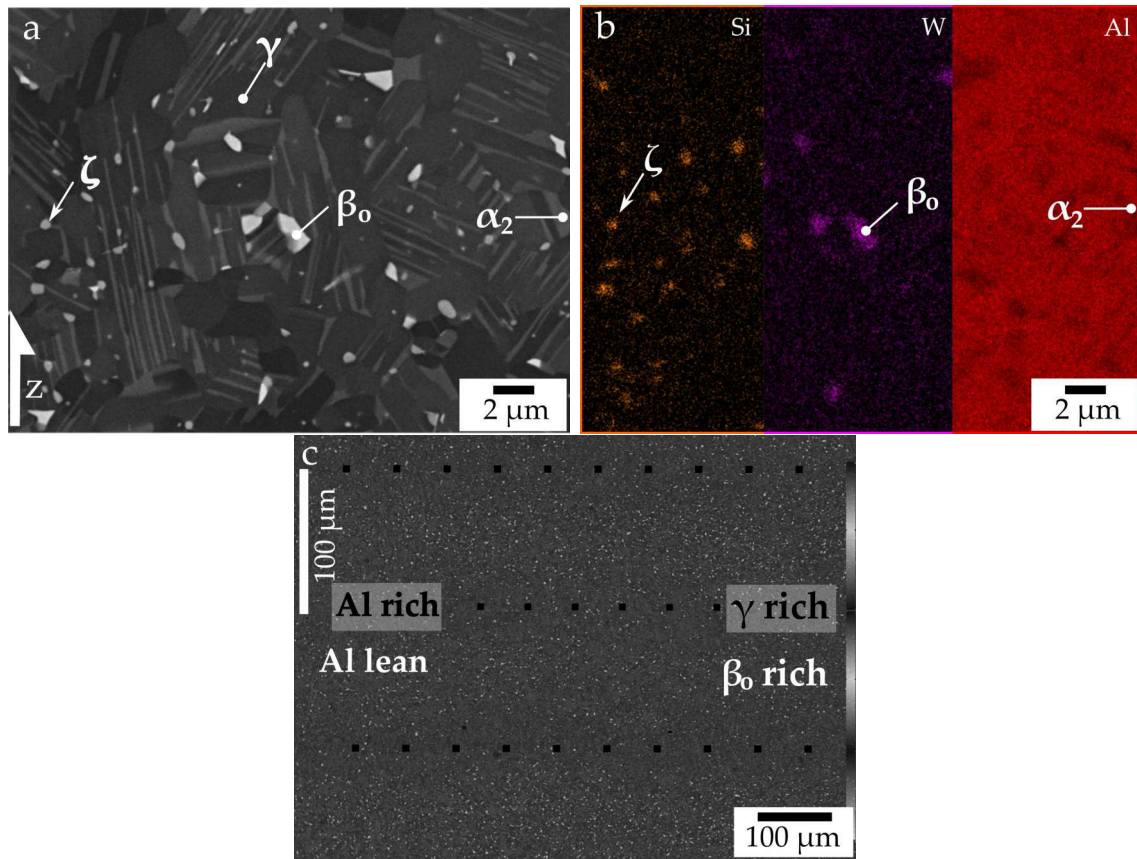


Figure E.3: a) SEM BSE image of the P3 sample taken from the center. The microstructure has been formed during preheating, where the elements Si, W and Al partitioning according to b); c) SEM BSE image over several layers of P3, revealing an alternating phase distribution caused by the varying Al content each layer, see text. Note that in all images the z direction is always orientated vertically.

spectra in Fig. E.4, confirming the presence of silicides. However, their amount is too low to be quantified. The results for the phase fractions (see Table E.1) show an increase of the α_2 phase at the expense of γ when E_L is increased, whereas the minor content of 3 vol.% β_0 remains constant. Considered in total, the differences in the phase fractions are present, but small. This behavior is due to the fact that the phase fractions are less impacted by the Al content at the preheating temperature of 1020 °C, where the final as-EBM phase distribution is adjusted. Nevertheless, the overall phase distribution in the as-built condition depends on the process parameter as follows: The higher E_L , the higher is the phase fraction of the α_2 phase. A significant difference between P2 and P3 (same E_L) could not be determined. Besides the evaluation of the Debye-Scherrer rings along the 2θ angle, the rings were also analyzed along the azimuthal angle ϕ to determine preferential orientations of the phases. The results for the closest packed planes, i.e. $\{111\}$ for γ and $\{110\}$ for β_0 are shown in Figs. E.4b and c, respectively. The close-packed plane of the α_2 phase, i.e. (0001), overlaps with $\{111\}$ of γ . Note that at an angle $\phi = 90^\circ$ the reflection of the particular plane is in

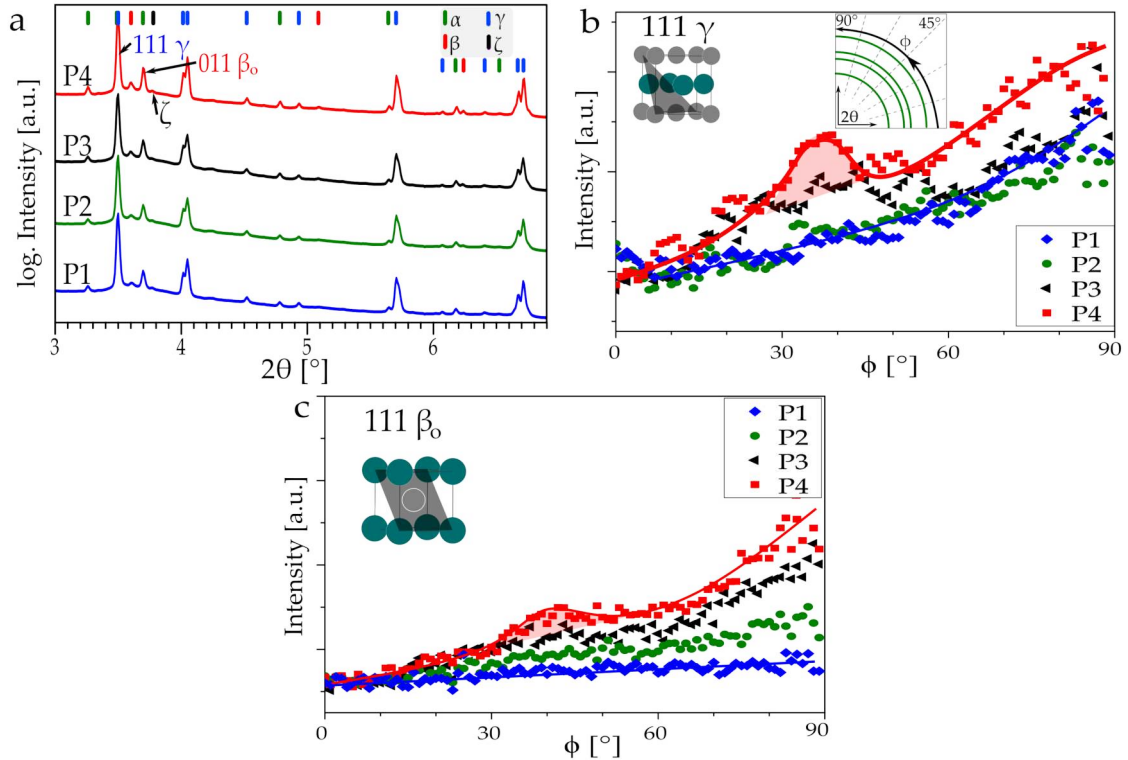


Figure E.4: a) HEXRD spectra obtained for the as-built samples P1-P4 (see Fig. E.1). The quantitative results are summarized in Table E.1. The HEXRD signals were also analyzed along the azimuthal angle ϕ . The results are shown for the closest packed planes of γ -TiAl and β_o -TiAl, i.e. the $\{111\}\gamma$ in b) and the $\{011\}\beta_o$ in c), which are also marked in their stoichiometric crystal lattice. Note that the intensity signal of the planes normal to the building direction z reflects at $\phi = 90^\circ$, whereas parallel ones at $\phi = 0^\circ$, as illustrated in the insert in b) by the quarter of the Debye-Scherrer rings. The significant deviation from a continuous slope, such as in case of P4, indicates a preferred orientation, see text.

building direction z , as shown in the schematic insert in Figs. E.4b and c. At first glance, all graphs show a continuous increase from 0 to 90° . This stems from the experimental setup and can be found for any peak, even for the LaB_6 powder used for calibration, and can therefore be neglected. The evaluation of the 111γ peak in Fig. E.4b shows in case of sample P4 a pronounced deviation from the continuous slope between 30 and 50° . These deviations can be addressed as a preferred orientation of $\{111\}\gamma$ in the sample built with the highest E_L . However, sample P3 also shows such deviations from the continuous slope, but much weaker. Sample P1 and P2 show no deviation. Concurrently, in Fig. E.4c the β_o phase along the $\{011\}$ plane exhibits also a minor deviation between 30 and 50° , which is solely pronounced in P4. Thus both, $\{011\}\beta_o$ as well as $\{111\}\gamma$, exhibit a preferred orientation between 30 and 50° . The γ phase transformed along its close-packed planes from α_2 according to the Blackburn crystal orientation relationship (BBOR): $\langle 11\bar{2}0 \rangle_{\alpha_2} || \langle 110 \rangle_\gamma, (0001)_{\alpha_2} || \{111\}_\gamma$ [57], whereby the high-temperature α phase is formed from β via the Burgers crystal orientation

relationship (BOR): $\langle 111 \rangle_{\beta} || \langle 11\bar{2}0 \rangle_{\alpha}$, $\{110\}_{\beta} || (0001)_{\alpha}$ [58]. Therefore, it can be assumed that the preferred orientation of the γ is related to the preferred orientation of the parental β phase, whose origin is discussed in section E.4.2.

E.3.2 Basic characterization of the top layers

In order to thoroughly investigate the solidification and thermal history of the EBM manufactured samples, SEM and EBSD images were taken at the topmost layers of the cuboids. It must be emphasized that the top layer was not remelted or affected by the focused electron beam, only preheated at 1020 °C. Therefore, all samples have a changing microstructure at the top, which is most pronounced in sample P4 as shown in Figs. E.5a-c. In the top area of the SEM image of P4 (Fig. E.5a), the microstructure consists of equiaxed α_2/γ colonies from whose boundaries the cellular reaction (CR) emanates. In general, CR is a discontinuous precipitation reaction according to $\alpha_2/\gamma \rightarrow (\alpha_2 + \gamma + \beta_o)$ to achieve the thermodynamic phase equilibrium. It is provoked by a high amount of interface surface to minimize the interface energy by coarsening and spheroidization of fine lamellae in α_2/γ colonies as described in [59-62]. Here, the CR indicates that the as-built microstructure is thermally unstable at the preheating temperature, i.e. around 1020 °C, as the α_2/γ colonies are fine-lamellar due to the high cooling rates [63] which are achieved in the EBM process [39, 56]. At the bottom of Fig. E.5a, approximately 600 μm below the topmost layer, the microstructural condition is approaching the microstructure of the center, which is shown in Fig E.3a, i.e. fine-grained, coarse-lamellar α_2/γ colonies decorated with ζ and β_o . The transition that occurs is easier to see in the corresponding inverse pole figure (IPF) map derived by EBSD, shown in Fig. E.5b, wherein each color represents a different γ orientation. From this it follows that the colonies consist of two kinds of γ lamellae: γ and γ_{twin} [4, 64]. As EBSD can not resolve the small tetragonality of the γ cell, it is not possible to differentiate between all six γ variants in a colony. Note that the fine α_2 lamellae between the γ laths could also not be resolved by EBSD. In the scan, the γ and γ_{twin} are separated by twin boundaries which are rotated 60° around $\{111\}_{\gamma}$. To identify the colony boundaries, the other high angle grain boundaries are marked as thin black lines in the IPF map. Obviously, the amount and size of colonies decrease from top to the analyzed depth of 600 μm . This indicates that the microstructure in the center of the specimens transforms from coarse-grained, fine-lamellar α_2/γ colonies to fine-grained, coarse-lamellar ones through thermal cycling due to the heat-affected zone of above-deposited layers, which is discussed in detail in section E.4. The IPF maps of the topmost layers of the other samples are plotted in Figs. E.5d-f. Sample P1 (Fig. E.5d) exhibits only one layer of colonies, whereas in Fig. E.5e for P2 the colonies are rather large and exist up to a depth of about 200 μm . Based on these IPF maps, an evaluation of the colony size in the first 200 μm from top reveals the following d_{50} values: P1=17.5 μm , P2=32.0 μm , P3=21.1 μm , and P4=47.6 μm . Besides the

trend that the colony size in the topmost layers increases with increasing E_L , the colony size between P2 and P3 let us assume that a lower deflection speed also promotes coarser colonies.

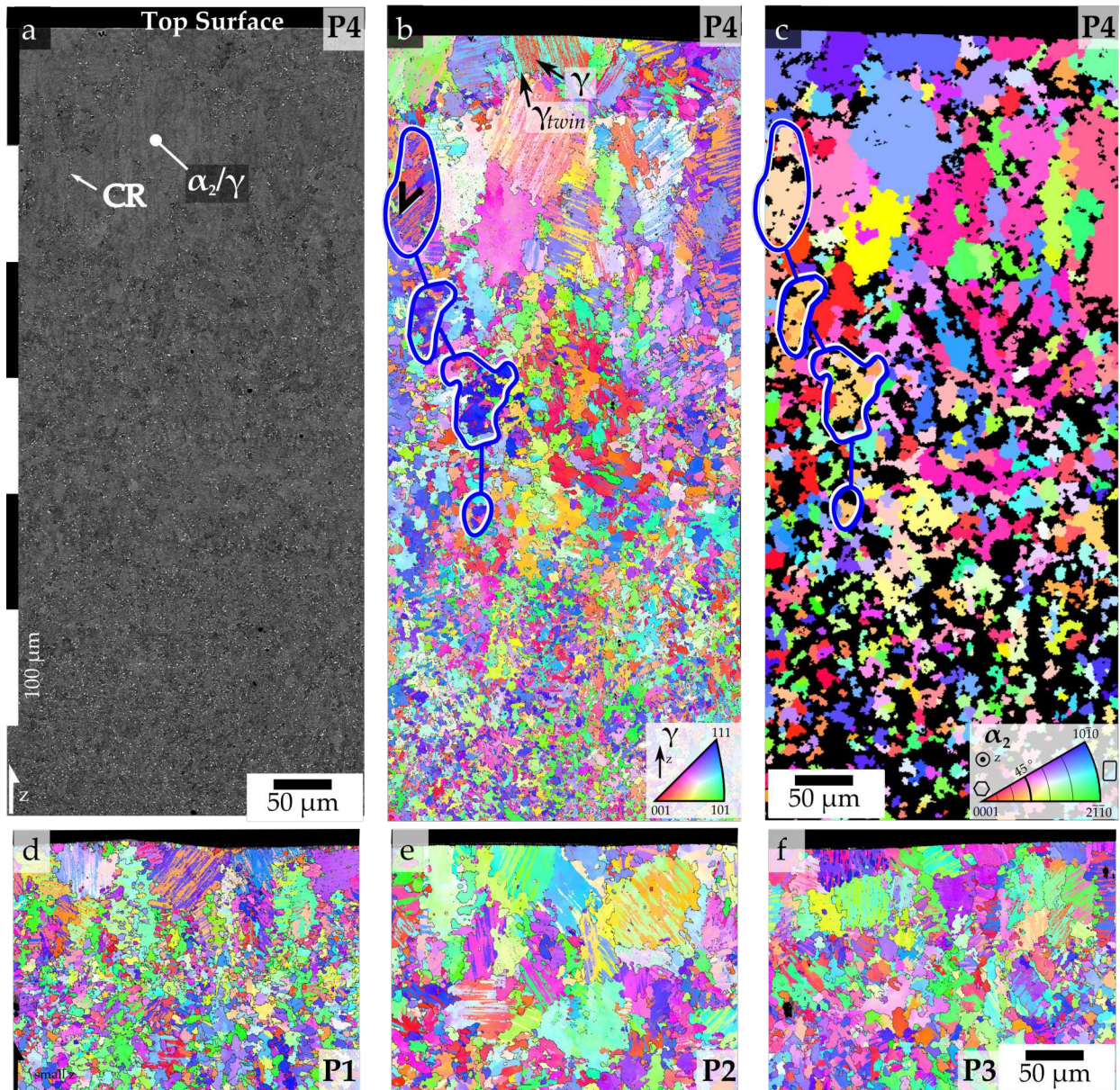


Figure E.5: a) SEM micrograph in BSE mode of the top layers of sample P4. The topmost layer was only preheated and not remelted in contrast to all other layers below; b) corresponding IPF map, wherein the grain and colony boundaries are marked by black lines. Note that each colony consists of two colors, representing γ and γ_{twin} lamellae, which is explained in detail in the text. c) Recalculated parent α_2 grains shown in the IPF map which was rotated according to the insert. For orientation, a split colony of blue and red γ laths was circled in b) and the corresponding α_2 grains in c). Images d), e) and f) are the IPF maps which corresponds to the top layer of P1, P2 and P3, respectively. For comparison, every image has the same scale.

Note that some colonies in Fig. E.5b appear slightly columnar. Besides, colonies with the same grain orientation, as those encircled in blue, can be traced down to a depth of about $400\ \mu\text{m}$, stemming from equal γ (blue) and γ_{twin} (red). The lamellae in these colonies enclose an angle of about 45° to the z direction, as illustrated by the angle sign in Fig. E.5b. Since the γ phase develops from the BBOR, i.e. $\langle 11\bar{2}0 \rangle_{\alpha_2} || \langle 110 \rangle_{\gamma}$, $(0001)_{\alpha_2} || \{111\}_{\gamma}$ [57], it is considered that the $(0001)_{\alpha_2}$ plane also inclines 45° to the z direction. This is confirmed by recalculating the α_2 phase on the basis of such large colonies. Here, the γ phase in the colonies of the EBSD scan is used to recalculate the parent α_2 phase by implementing the BBOR in the software tool ARPGE (automatic reconstruction of parent grains from EBSD) [65]. Thereby, superimposed $\{111\}$ positions of the γ phase present in each colony get replaced by their $(0001)_{\alpha_2}$ parent phase. These calculation results are shown in Fig. E.5c for P4 in an IPF map which is rotated in z direction, as indicated in the insert. The black areas, however, could not be recalculated. The pink and orange α_2 grains are located at an angle of about 45° relative to z. This calculation confirms the former assumption that the 45° lamellae (encircled in Fig. E.5b) stem from a $(0001)_{\alpha_2}$ plane rotated 45° in z direction (also encircled in Fig. E.5c). It is worth noting that in Fig. E.5c the pink and orange color, i.e. representing an orientation of around 45° , is dominant and mostly columnar aligned. Furthermore, there are minor fractions of colored red (0°) as well as blue and green (90°) α_2 grains, whose origin is discussed in section E.4.2.

Apart from the size of the α_2 grains, no further differences were quantified in the top layer, because any rating of a preferred orientation reflects the colony size. Therefore, $360 \times 275\ \mu\text{m}^2$ EBSD scans about $2000\ \mu\text{m}$ below the top layer, i.e. in the fine-grained area of the samples were performed. These scans are used for an evaluation of the 111 pole figure from the crystallographically adopted cubic-face centered γ phase. The results exhibit in the case of the sample P4 a 3.8 maximum multiples of random distribution (MRD) [49, 66] of $\{111\}_{\gamma}$. This value is twice as high when compared to MRD of P1=1.6, P2=2.1, and P3=1.7 confirming a strong preference orientation within the microstructure inherited from the α phase.

In summary, the EBSD results show that P4, i.e. the sample with the highest E_L , indicates an anisotropic orientation of the γ phase. This behavior may stem from the coarse colonies, that appear columnar and obviously reach deep into the microstructure. Although statistical reliability is always an issue regarding EBSD, the other samples show a MRD and a colony size of only half, which indicates a significant effect of the energy input on the crystal orientation within the as-EBM microstructure.

E.3.3 Effect of a subsequent heat treatment

The former sections revealed the influence of the EBM process parameter on the microstructure of the as-EBM condition. However, an as-manufactured TiAl microstructure,

regardless of the production process, will rarely go directly into high-performance applications. Therefore, a wide range of subsequent heat treatments can be applied, e.g. hot isostatic pressing and/or multi-step heat treatments around the solvus temperature of the γ phase ($T_{\gamma,solv}$). According to previous work [19], $T_{\gamma,solv}$ of the powder is 1325 ± 5 °C. Aiming for a NL γ microstructure, i.e. α_2/γ colonies combined with globular γ_g [4, 21-23], the heat treatment was conducted below $T_{\gamma,solv}$ at 1290 °C for 30 min, followed by water quenching (WQ) to "freeze-in" the high-temperature microstructure. However, it must be considered that the $\alpha \rightarrow \alpha_2$ ordering transformation cannot be suppressed by WQ [67]. Figure E.6a shows a SEM image in BSE mode of the heat-treated sample P3, wherein the γ phase appears dark, the α_2 phase gray, and the homogeneously dispersed ζ particles bright. The presence of ζ -Ti₅Si₃ is independent of the Al content, which is why they are neglected in the further discussion. During this heat treatment, γ_g has only begun to spheroidize, concurrently to the coarsening of the α_2/γ lamellae. The microstructure shows a locally varying phase distribution of α_2 and γ_g . This reflects the local Al content: in Al lean areas, the α_2 phase is dominating, whereas in Al rich areas, the microstructure consists of α_2 and γ_g . This structure is illustrated in the schematic insert in Fig. E.6a. Therein, the intersections between the red curve and the black vertical line show the Al content where the dissolution of the γ phase takes place, i.e. at $T_{\gamma,solv} = 1290$ °C. The sharp transition between the α_2 and $\alpha_2 + \gamma_g$ regions at the white dashed line represents a former melt pool top, whereupon a new layer was deposited. The melt pool top is Al lean due to an easy Al evaporation, while the bottom of the melt pool, remains Al rich. Inside one layer, i.e. one melt pool, no homogenization of the Al content is possible, because the liquid phase exists only for less than 30 ms as reported in [68]. This results in a smooth gradient in the phase distribution from the layer bottom (Al rich) to the top (Al lean).

For a macroscopic evaluation, several SEM images were compiled along the z direction and γ_g was colored in red, as shown in Figs. E.6b-e. From a theoretical point of view, one would assume a periodicity every 100 μm , i.e. every powder layer. However, this is not always the case due to a turbulent melt pool dynamics [56, 69]. Nevertheless, the amount of γ_g phase decreases from left (Figs. E.6b e.g. low E_L) to right (Figs. E.6e.g. high E_L), which was also confirmed quantitatively by the evaluated volume fraction of γ_g , inserted at the bottom of the SEM images. In Fig. E.6e the γ_g phase fraction decreases down to 5 ± 2 vol.% by using $E_L=180$ J/m (sample P4). In addition, large α_2 grains can be detected. These grains grow during the heat treatment, due to the absence of the γ phase, which consequently represents an Al lean area. Concurrently, for the Al rich areas, the heat treatment is still conducted in the $\alpha + \gamma$ two-phase field region, where grain growth is hindered by the presence of the two phases. Note, that the bright ζ precipitates are few and relatively large and thus provide no effective drag for the α grain boundaries during annealing in the α single phase field region [70-72].

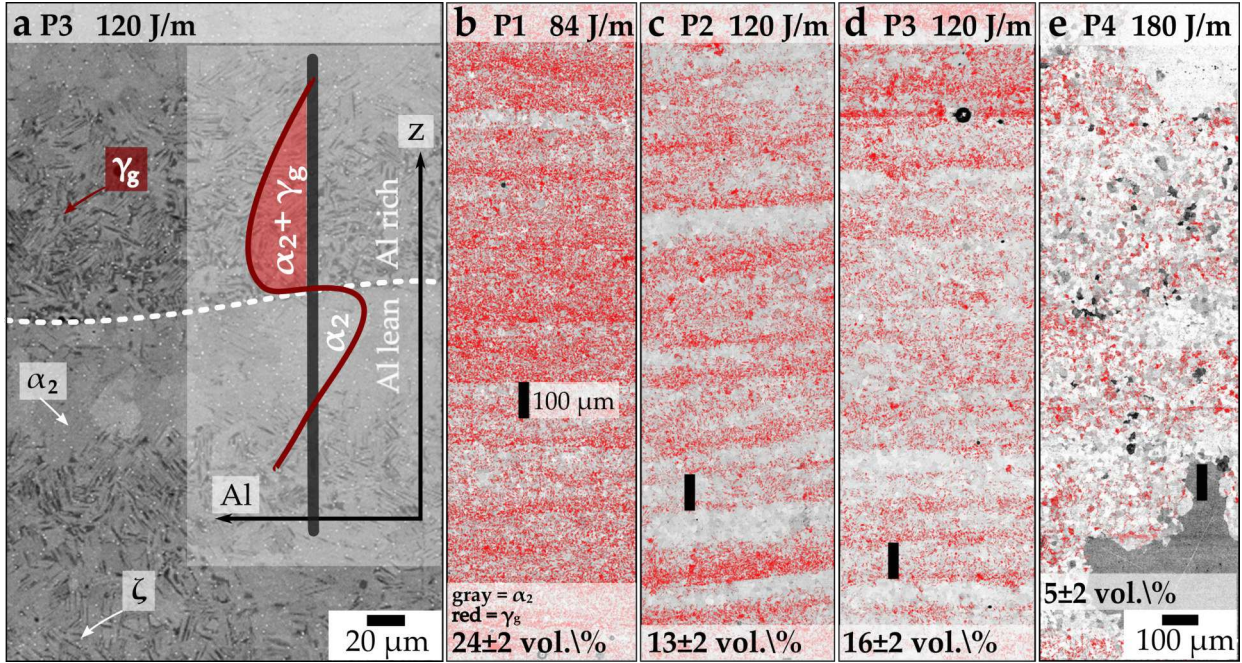


Figure E.6: Microstructure of the EBM samples after a subsequent heat treatment at 1290°C, 30 min, followed by WQ; a) a BSE SEM image in a higher magnification of the layered phase distribution, which appears due to an inhomogeneous Al distribution, as illustrated by the schematic diagram. Therein, the vertical line represents the Al content at $T_{\gamma, solv}$. Thus a local transition between $\alpha_2 + \gamma_g$ and α_2 microstructure occurs. Note that homogeneously distributed ζ -Ti₅Si₃ particles are always present; b)-e) are SEM images taken in BSE mode, where γ_g is colored red and its volume fraction is stated on the bottom of the respective image. Spherical pores are present in every sample introduced by the powder [45], which appear enlarged due to the former polishing procedure.

The mechanical evaluation was conducted by hardness measurements at samples two-step heat-treated at 1290°C for 30 min followed by AC and at 900°C for 4 h followed by furnace cooling (FC), to adjust a NL γ microstructure how it is actually used in industry [1, 3]. The resulting microstructures are similar to those shown in Figs. E.6b-e with the same γ_g fraction. However, no complete homogenization of the Al content took place, only a local approximation to the thermodynamic equilibrium through the formation of γ -lamellae in the supersaturated α_2 phase, i.e. α_2/γ colonies are generated in the course of the stabilization annealing. The mean values from HV10 measurements are shown in Table E.1. The HV10 hardness increases from the lowest energy input, e.g. P1 = 413 \pm 5 HV10, to the highest E_L , e.g. P4 = 477 \pm 10 HV10, which is an increase of 14%. Thereby, the hardness increases as the volume fraction of α_2 increases at the expense of γ phase. Note, that the HV10 indentations are larger than 200 μm in diameter, thus at least two 100 μm thick layers are penetrated. Therefore, HV10 represents a macroscopic hardness value of the NL γ microstructure. For an evaluation of the microstructural inhomogeneity, HV0.05 measurements, whose indentation diameter is below 15 μm , were carried out at the polished xz cross-section of all samples.

Because of the small indents, the HV0.05 measurements, as a micro-hardness procedure, suits to determine the layer response. The results are shown in Fig. E.7. The HV0.05 values scatter strongly within one sample due to the spatial phase distribution, e.g. there are soft areas in P1 exhibiting a hardness of about 440 HV0.05, whereas hard areas reach 520 HV0.05, which represents an increase of 15 %. The individual areas with this high hardness are Al lean layers, i.e. at 1290 °C only α is present, which then transforms into α_2/γ colonies during cooling and the subsequent stabilization heat treatment. The soft areas are Al rich, thus consisting of α and γ phase at 1290 °C (see Fig. E.6), creating a microstructure with α_2/γ colonies and γ_g , after the multi-step heat treatment.

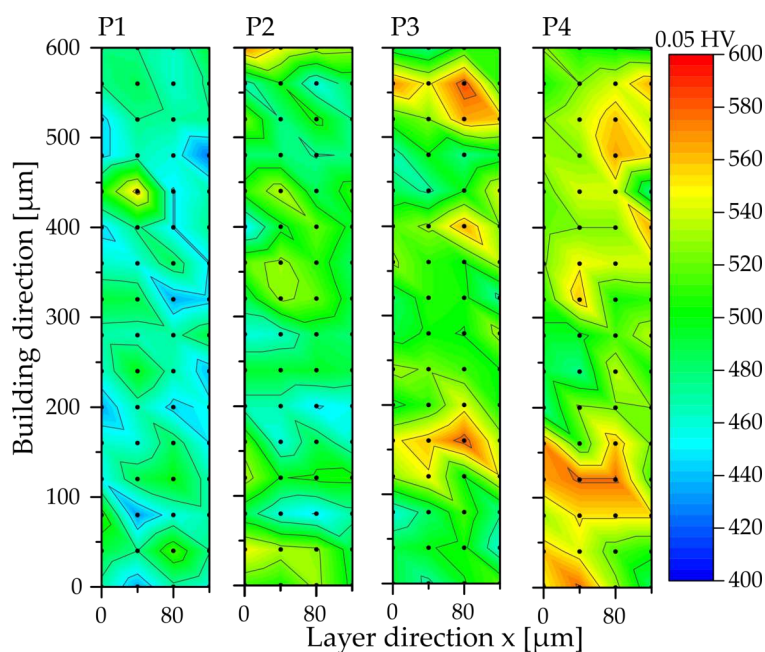


Figure E.7: HV0.05 measurements on heat-treated TiAl samples with a NL γ microstructure, built with the process parameters P1-P4; for the explanation of the hardness differences see text.

E.4 Discussion

E.4.1 Total and local Al content and its impact on the microstructure and mechanical response

Cuboid samples were additively manufactured from Ti-44.8Al-4.1Nb-0.7W-1.1Zr-0.4Si-0.5C-0.1B (in at.%) powder with four different process parameters, as illustrated in Fig. E.1. In general, the manufacturing of each layer via EBM starts with the formation of a melt pool, existing only for less than 30 ms [68]. Despite this short lifetime of the melt pool, Al evaporation takes place. The XRF results in Table E.1 show that up to 1.8 at.% Al is lost in the specimen with the highest E_L (i.e. 180 J/m for sample P4). The comparison of

P1 (i.e. $E_L=84\text{ J/m}$, $\Delta\text{Al}=1.2\text{ at.}\%$) to P4 (i.e. $E_L=180\text{ J/m}$, $\Delta\text{Al}=1.8\text{ at.}\%$) shows that a 96 J/m higher E_L results in a $0.6\text{ at.}\%$ higher ΔAl in the EBM manufactured specimen. This $E_L \uparrow \rightarrow \Delta\text{Al} \uparrow$ tendency is also reflected by the conducted process simulation for parameter P1-P3, see Table E.1. However, the calculated Al evaporation values are lower compared to the experimental values. The emerging hydrodynamics of the melt pool below the electron beam and the resulting material loss are significantly different in two-dimensional simulation when compared to the real three-dimensional case. Under the action of the recoil pressure, the melt is pushed away from the center of the melt pool and the electron beam interacts with new material that has a higher Al content. This effect is limited in two dimensions. As a result, the calculated ΔAl is lower compared to the experimental values. This effect is even more pronounced in the case of the parameter set P4 with the highest E_L , where the higher peak temperature of the melt pool leads to higher evaporation rates and recoil pressures. In this case, the two-dimensional representation is not able to accurately calculate the emerging hydrodynamics and thus underestimate the resulting Al loss. Such a ΔAl trend as determined in this work is also reported in Refs. [39, 40, 56, 73] for other TiAl alloys. Therein it is argued that the superheated melt pool with temperatures of up to $3500\text{ }^\circ\text{C}$ results in Al evaporation on top due to its high vapor pressure, in combination with the prevailing vacuum in the building chamber, which is schematically shown in Fig. E.8a. Despite the numerous papers describing the Al content variation in EBM manufactured TiAl specimens, only a few deal with the consequences on the microstructure and mechanical properties. In this study, the influence on the phase fractions was measured by HEXRD (Table E.1 and Fig. E.4a). These results reveal minor differences in the phase contents of the as-EBM conditions, whose microstructure is set by the applied preheating temperature in the $\alpha_2 + \gamma + \beta_o$ phase field region. For better understanding, the phase diagram based on Ref. [21], shown in Fig. E.8b, should act as guidance. The HEXRD results imply that the α_2 phase fraction increases at the expense of the γ phase by increasing E_L due to the Al evaporation, as the volume fraction of the γ phase decreases with decreasing Al content [4, 30]. However, these small differences in as-EBM microstructure develop in drastic changes in the microstructure during a subsequent heat treatment at $1290\text{ }^\circ\text{C}$, i.e. near $T_{\gamma,\text{solv}}$ to adjust an application-relevant microstructure (see Fig. E.6). For example, the γ_g phase fraction decreases by about $20\text{ vol.}\%$ due to an increase in E_L of 96 J/m between P1 and P4. Concurrently, the hardness increases by about 50 HV_{10} . This relationship between the process parameters and the phase distribution can be summarized as follows:

$$E_L \uparrow \Rightarrow \Delta\text{Al} \uparrow \Rightarrow \text{Al} \downarrow \Rightarrow \gamma \downarrow \Rightarrow \alpha_2(+\beta_o) \uparrow \Rightarrow \text{HV} \uparrow.$$

So far, only the influence of the total Al content on the material has been discussed, not the local changes. Actually, a limited number of papers on EBM of TiAl investigated the local Al differences in detail [74] and its impact on the microstructure [37-40]. In this study, the influence of the local Al content on the microstructure formation of the as-EBM state

was detected (Fig. E.3c) and, more obviously, after a subsequent heat treatment near $T_{\gamma, solv}$ (Fig. E.6). In both cases, the microstructure adapts spatially to the local Al content. On the one hand, in the as-EBM condition, as already mentioned, the microstructure is formed at the preheating temperature of 1020 °C. Thereby Al lean areas are β_o rich and thus brightly contrasted in the SEM BSE images, due to enrichment of heavy elements, like W, and a simultaneous depletion of light elements, e.g. Al (see Fig. E.3b). On the other hand, in the heat-treated condition, i.e. 1290 °C, Al lean areas already entered the single α phase field region, as schematically pictured in Fig. E.8a and the phase diagram in Fig. E.8b. Note that the inhomogeneous phase distribution is often layered and repeats every 100 μm (see Fig. E.3c and Fig. E.6), i.e. in the same scale as the specified layer thickness. However, sometimes this repetition is interrupted, also evident by the Al content simulation (Fig. E.2). This is caused by the raked powder layers which are randomly packed due to the real powder size distribution, as described in detail in Refs. [56, 69, 75]. Finally, as a consequence of the layered phase distribution in the heat-treated condition, the mechanical response, i.e. hardness, shows a variation across the specimen, too. The HV0.05 measurement grids (Fig. E.7) exhibit variations of about 60-80 HV0.05 within one grid. More precisely, hardness maxima are observed in areas which are Al lean, thus rich in α_2 phase, whereas hardness minima occur in the Al rich areas due to the presence of the "soft" γ phase. This relationship can be summarized as

$$\text{local Al } \uparrow \text{ (Al rich)} \Rightarrow \gamma \uparrow \Rightarrow HV \downarrow.$$

As a consequence, the heat-treated microstructure of the samples can be presumed as a layered composite of two individual microstructures rather than an almost NL γ one. The composite consists of a hard and fully lamellar α_2/γ colony band in the Al lean areas, which show excellent creep properties [19, 22, 23, 61] and a soft, so-called near gamma microstructure in the Al rich areas resulting in a good deformability at elevated temperatures [21-23, 34]. Such layered phase distribution also impacts the isotropy of the mechanical properties, which is shown by the tensile test results conducted by Todai et al. [17], who investigated the Ti-48Al-2Cr-2Nb alloy manufactured via EBM. Thereby, the as-built microstructure shows strongly developed γ bands perpendicular to the building direction. As a consequence, the tensile elongation changes with the direction in which the tensile sample was built, i.e. 0° results in about 0.5%, 45° in about 3%, and at 90° the elongation was 2%. Although these results cannot be applied directly to the BMBF alloy and its microstructures, it points out that a composite on a μm -level, provoked by Al evaporation and controlled by the process parameters, enables the manufacturing of γ -TiAl alloys with

target-oriented microstructures.

E.4.2 Change of the grain orientation evoked by the EBM process parameters

The evaluation of the Debye-Scherrer rings along ϕ (Figs. E.4b and c) as well as the EBSD results (Figs. E.5b and c) reveals preferred orientations of γ , α_2 and β_o in the P4 microstructure. These preferred orientations originate from the solidification of the melt pool, which determines the further solid-state phase transformations. In principle, the melt pool formed by the electron beam solidifies by experiencing high thermal gradients, i.e. 10^5 K/m [68], as well as high cooling rates, i.e. 10^6 K/s [39, 56]. This rapid solidification can be examined by investigating the α_2/γ colonies of the most top layer, done in Fig. E.5. Although these α_2/γ colonies are not present during the liquid/solid transformation, they form basically via $L \rightarrow L + \beta \rightarrow \beta \rightarrow \beta + \alpha \rightarrow \alpha \rightarrow \alpha_2 \rightarrow \alpha_2/\gamma$ at high cooling rates and the subsequent preheating [4]. The colonies on the top surface are fine-lamellar, which confirms the high cooling rates present [63]. In general, the β to α transformation satisfies the BOR [58]. Therefore, 3×2 unique α crystal orientations can form based on one β grain. Thereby the α crystals inherit an angle of 45° or 90° , between $[001]_\beta$ and $[0001]_\alpha$, as schematically shown in Fig. E.8c. Note that $[0001]_\alpha$ is perpendicular to the close-packed plane of α , $(0001)_\alpha$ and that the cubic β crystal solidifies along $\langle 001 \rangle_\beta$ as reported in [76-80]. Further, the γ lamellae form along the close-packed plane of α_2 according to the BBOR [57]. This provokes additional six possible orientations of the γ crystals [4] within one α_2/γ colony. The γ -laths are always orientated parallel to the close-packed (0001) planes of the α_2 crystal. As a geometrical consequence following BOR and BBOR, in case of a directional solidification of $[001]_\beta$ towards a thermal gradient (∇T), the orientation of the $[0001]_\alpha$ directions and thus of the lamellae packages have to be tilted by an angle of 45° or be perpendicular (90°) with respect to ∇T , as shown in Fig. E.8c and can be summarized as followed:

$$\nabla T \parallel [001]_\beta \Rightarrow \nabla T \angle [0001]_{\alpha_2} = 45^\circ \text{ or } 90^\circ.$$

This transformation behavior was also obtained experimentally by Jung et al. [76, 77], Johnson et al. [78, 79] and Yamaguchi et al. [80], who investigated the directional solidification of Ti-Al-W, Ti-Al-Si, Ti-Al-Mo and Ti-Al-Mo-B alloys. In our work, in the topmost layers of the as-EBM material columnar grain structures were identified, see Fig. E.5, by the deep-reaching pink and orange areas, i.e. tilted 45° to the building direction z as well as larger blue areas, representing a 90° tilt to z . Therefore, it is concluded that the majority of the melt pool solidifies via β , aligning its $\langle 001 \rangle$ direction in z , enforced by a thermal gradient directed towards the building direction:

$$\nabla T \parallel z \parallel \langle 001 \rangle_\beta.$$

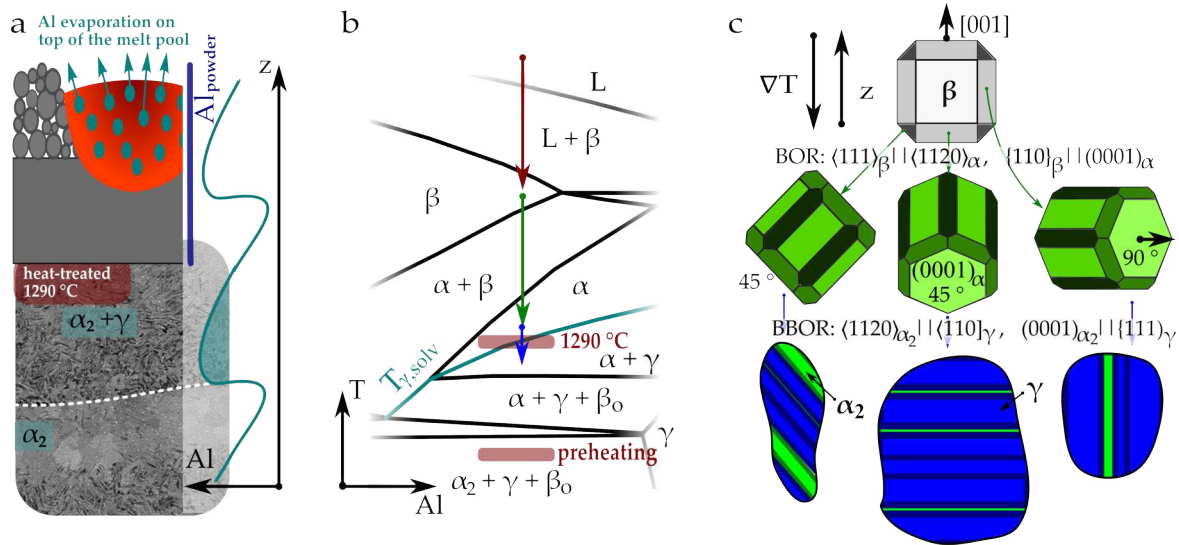


Figure E.8: a) Schematic illustration of the melt pool and its impact on the local Al content and consequently on the heat-treated microstructure, as described in detail in the text; b) phase diagram according to Ref. [21]. Therein a solidification path and the essential heat treatment temperatures are included; c) schematic illustration of the BOR: $\beta \rightarrow \alpha$ and the BBOR: $\alpha_2 \rightarrow \gamma$ in case of a $\langle 001 \rangle_\beta$ solidification texture in building direction z towards a temperature gradient, ∇T , see text.

Further, this selected orientation gets inherited into the material, where P4 shows a significant preferred orientation of the γ phase as determined complementarily by EBSD and HEXRD. In addition, the remaining β_o phase shows the same preferred orientation of $\{011\}_{\beta_o}$, thus follows $\{011\}_{\beta_o} \parallel \{111\}_\gamma$, which corresponds to the combination of BOR and BBOR. However, it can not be stated whether the β_o phase remains from the solidification or forms during the preheating along close-packed planes. Nevertheless, the preferred orientation exists in the sample built with parameter P4, the highest E_L , whereas they are minor or not significant in the others. Such columnar grain structures and preferred orientations in EBM materials were well documented in Ni- [68, 81, 82] and Ti-base [74, 82-86] alloys. These authors found that columnar grain structures and, thus, preferred orientations are enhanced by a higher E_L during EBM, due to a higher ∇T and larger melt pools. Besides, at higher E_L , higher ΔAl were determined, causing a shift of the solidification path into the β single-phase field region, i.e. to the left in Fig. E.8b, which may additionally benefit a $\langle 001 \rangle_\beta$ solidification texture [19, 37]. With reference to the minor preferred orientation of the γ phase in P3 (see Fig. E.4b), when compared to P2, manufactured with the same E_L but a higher v , the reader is referred to the simulations of Raghavan et al. [68]. Those authors showed that with a constant E_L and a shorter beam-on time on the material, which means a higher v , ∇T and the size of the melt pool increase.

To summarize, the following relationship can be established by the evaluation of the crystal orientations in our engineering γ -TiAl based alloy:

$$E_L \uparrow \Rightarrow \nabla T \uparrow \Rightarrow \langle 001 \rangle_\beta \uparrow \Rightarrow \gamma\text{-anisotropy} \uparrow.$$

Such crystalline anisotropy of the γ phase may further result in anisotropic mechanical behavior, which is detrimental for applications involving multidirectional stresses, whether with globular or lamellar morphology, as described in Refs. [4, 76, 78].

E.5 Summary

An intermetallic multiphase γ -TiAl based alloy (Ti-44.8Al-4.1Nb-0.7W-1.1Zr-0.4Si-0.5C-0.1B in at.%) was additively manufactured by means of electron beam melting using four different process parameter sets. The influence of these EBM parameters was investigated with complementary characterization methods regarding both, the total and local Al content, and its impact on the microstructure as well as the arising crystalline anisotropy. The obtained results and conclusions can be summarized as follows:

- The total Al loss within the samples due to Al evaporation was investigated via XRF and numerical simulation. The effects of the decreasing Al content on the microstructure in the as-built and heat-treated condition reveal the following relationship: $E_L \uparrow \Rightarrow \Delta Al \uparrow \Rightarrow Al \downarrow \Rightarrow \gamma \downarrow \Rightarrow \alpha_2(+\beta_o) \uparrow \Rightarrow HV \uparrow$. Thereby, the macroscopic hardness (HV10) increases as the volume fraction of α_2 and β_o increases at the expense of γ phase.
- The local Al distribution was predicted by numerical simulation. Further, the spatial varying Al content was determined via a detailed microstructural characterization in the as-EBM condition of the samples and after a technically relevant heat treatment near $T_{\gamma, solv}$. Therein, a layered NL γ composite consisting of two microstructures, i.e. a soft, near gamma and a hard, fully lamellar one, was detected and further locally measured by micro-hardness test. This led to the following assertion: local Al \uparrow (Al rich) $\Rightarrow \gamma \uparrow \Rightarrow HV \downarrow$.
- Sample P4, manufactured with the highest E_L , exhibits a preferred orientation of the γ phase as evidenced by EBSD and HEXRD measurements. The investigation of the topmost layers via EBSD points out that due to a thermal gradient in building direction a coarse columnar microstructure emerges, stemming from a favored $\langle 001 \rangle_\beta$ solidification. Therefore, an inheritance of the initial coarse columnar microstructure into the material is concluded, i.e.: $E_L \uparrow \Rightarrow \nabla T \uparrow \Rightarrow \langle 001 \rangle_\beta \uparrow \Rightarrow \gamma\text{-anisotropy} \uparrow$.

The gained knowledge points out that by using a complex multiphase γ -TiAl based alloy, a broad spectrum of material properties can be adjusted solely by changing the process parameter E_L . Therefore, complementary experimental investigations form the basis for the additive manufacturing of forthcoming structural TiAl components with locally tailor-made microstructures.

Acknowledgment

This research work was conducted within the framework of the BMBF project "NextTiAl" 03XP0088C, Germany, funded by the Federal Ministry of Education and Research. The support of the project partners is gratefully acknowledged.

E.6 References

- [1] S. Mayer, P. Erdely, F. D. Fischer, D. Holec, M. Kasthuber, T. Klein, H. Clemens, Intermetallic β -solidifying γ -TiAl based alloys – From fundamental research to application, *Advanced Engineering Materials* 19 (4) (2017) 1600735. doi:10.1002/adem.201600735.
- [2] Y.-W. Kim, S.-L. Kim, Advances in gammalloy materials–processes–application technology: successes, dilemmas, and future, *JOM* 70 (4) (2018) 553–560. doi:10.1007/s11837-018-2747-x.
- [3] W. Wallgram, T. Schmöler, L. Cha, G. Das, V. Güther, H. Clemens, Technology and mechanical properties of advanced γ -TiAl based alloys, *International Journal of Materials Research* 100 (2009) 1021–1030. doi:10.3139/146.110154.
- [4] F. Appel, J. Paul, M. Oehring, *Gamma titanium aluminide alloys: science and technology*, Wiley-VCH, Weinheim, Germany, 2012.
- [5] P. A. Bartolotta, D. L. Krause, *Titanium aluminide applications in the high speed civil transport*, NASA/TM 209071 (1999).
- [6] P. Janschek, Wrought TiAl blades, *Materials Today: Proceedings* 2 (2015) S92–S97. doi:10.1016/j.matpr.2015.05.024.
- [7] B. P. Bewlay, S. Nag, A. Suzuki, M. J. Weimer, TiAl alloys in commercial aircraft engines, *Materials at High Temperatures* 33 (4-5) (2016) 549–559. doi:10.1080/09603409.2016.1183068.
- [8] M. Süß, C. Schöne, R. Stelzer, B. Klöden, A. Kirchner, T. Weißgärber, B. Kieback, Aerospace case study on topology optimization for additive manufacturing, in: *DDMC 2016*, Fraunhofer Verlag, Stuttgart, Germany, 2016, pp. 37–41.
- [9] L. E. Murr, S. M. Gaytan, F. Medina, H. Lopez, E. Martinez, B. I. Machado, D. H. Hernandez, L. Martinez, M. I. Lopez, R. B. Wicker, J. Bracke, Next-generation biomedical implants using additive manufacturing of complex, cellular and functional mesh arrays, *Philosophical transactions. Series A, Mathematical, physical, and engineering sciences* 368 (2010) 1999–2032. doi:10.1098/rsta.2010.0010.
- [10] A. Gisario, M. Kazarian, F. Martina, M. Mehrpouya, Metal additive manufacturing in the commercial aviation industry: A review, *Journal of Manufacturing Systems* 53 (2019) 124–149. doi:10.1016/j.jmsy.2019.08.005.
- [11] C. Körner, Additive manufacturing of metallic components by selective electron beam melting — a review, *International Materials Reviews* 61 (5) (2016) 361–377. doi:10.1080/09506608.2016.1176289.
- [12] R. Huang, M. Riddle, D. Graziano, J. Warren, S. Das, S. Nimbalkar, J. Cresko, E. Masanet, Energy and emissions saving potential of additive manufacturing: the case of lightweight aircraft components, *Journal of Cleaner Production* 135 (2016) 1559–1570. doi:10.1016/j.jclepro.2015.04.109.

- [13] A. Timmis, A. Hodzic, L. Koh, M. Bonner, C. Soutis, A. W. Schäfer, L. Dray, Environmental impact assessment of aviation emission reduction through the implementation of composite materials, *The International Journal of Life Cycle Assessment* 20 (2) (2015) 233–243. doi:10.1007/s11367-014-0824-0.
- [14] V. Juechter, M. M. Franke, T. Merenda, A. Stich, C. Körner, R. F. Singer, Additive manufacturing of Ti-45Al-4Nb-C by selective electron beam melting for automotive applications, *Additive Manufacturing* 22 (2018) 118–126. doi:10.1016/j.addma.2018.05.008.
- [15] G. Baudana, S. Biamino, B. Klöden, A. Kirchner, T. Weißgärber, B. Kieback, M. Pavese, D. Ugues, P. Fino, C. Badini, Electron beam melting of Ti-48Al-2Nb-0.7Cr-0.3Si: Feasibility investigation, *Intermetallics* 73 (2016) 43–49. doi:10.1016/j.intermet.2016.03.001.
- [16] G. Baudana, S. Biamino, D. Ugues, M. Lombardi, P. Fino, M. Pavese, C. Badini, Titanium aluminides for aerospace and automotive applications processed by Electron Beam Melting: Contribution of Politecnico di Torino, *Metal Powder Report* 71 (3) (2016) 193–199. doi:10.1016/j.mprp.2016.02.058.
- [17] M. Todai, T. Nakano, T. Liu, H. Y. Yasuda, K. Hagihara, K. Cho, M. Ueda, M. Takeyama, Effect of building direction on the microstructure and tensile properties of Ti-48Al-2Cr-2Nb alloy additively manufactured by electron beam melting, *Additive Manufacturing* 13 (2017) 61–70. doi:10.1016/j.addma.2016.11.001.
- [18] H. Yue, Y. Chen, X. Wang, S. Xiao, F. Kong, Microstructure, texture and tensile properties of Ti-47Al-2Cr-2Nb alloy produced by selective electron beam melting, *Journal of Alloys and Compounds* 766 (2018) 450–459. doi:10.1016/j.jallcom.2018.07.025.
- [19] D. Wimler, J. Lindemann, M. Reith, A. Kirchner, M. Allen, W. G. Vargas, M. Franke, B. Klöden, T. Weißgärber, V. Güther, M. Schloffer, H. Clemens, S. Mayer, Designing advanced intermetallic titanium aluminide alloys for additive manufacturing, *Intermetallics* 131 (2021) 107109. doi:10.1016/j.intermet.2021.107109.
- [20] M. Reith, M. Franke, M. Schloffer, C. Körner, Processing 4th generation titanium aluminides via electron beam based additive manufacturing – characterization of microstructure and mechanical properties, *Materialia* 14 (2020) 100902. doi:10.1016/j.mtla.2020.100902.
- [21] E. Schwaighofer, H. Clemens, S. Mayer, J. Lindemann, J. Klose, W. Smarsly, V. Güther, Microstructural design and mechanical properties of a cast and heat-treated intermetallic multi-phase γ -TiAl based alloy, *Intermetallics* 44 (2014) 128–140. doi:10.1016/j.intermet.2013.09.010.
- [22] Y.-W. Kim, Microstructural evolution and mechanical properties of a forged gamma titanium aluminide alloy, *Acta Metallurgica et Materialia* 40 (1992) 1121–1134. doi:10.1016/0956-7151(92)90411-7.
- [23] Y.-W. Kim, Strength and ductility in TiAl alloys, *Intermetallics* 6 (1998) 623–628. doi:10.1016/S0966-9795(98)00037-5.
- [24] Y.-W. Kim, D. M. Dimiduk, Progress in the understanding of gamma titanium aluminides, *JOM* 43 (1991) 40–47. doi:10.1007/BF03221103.
- [25] P. McQuay, Cast gamma TiAl alloys: Are we there yet?, in: K. J. Hemker (Ed.), *Structural intermetallics 2001*, Minerals Metals & Materials Society, Warrendale, Pa., 2001, pp. 83–90.
- [26] M. Galati, L. Iuliano, A literature review of powder-based electron beam melting focusing on numerical simulations, *Additive Manufacturing* 19 (2018) 1–20. doi:10.1016/j.addma.2017.11.001.

-
- [27] L. Yang, K. Hsu, B. Baughman, D. Godfrey, F. Medina, M. Menon, S. Wiener, Additive manufacturing of metals: The technology, materials, design and production, Springer Series in Advanced Manufacturing, Springer International Publishing, Cham and s.l., 2017. doi:10.1007/978-3-319-55128-9.
- [28] D. Herzog, V. Seyda, E. Wycisk, C. Emmelmann, Additive manufacturing of metals, *Acta Materialia* 117 (2016) 371–392. doi:10.1016/j.actamat.2016.07.019.
- [29] U. Habel, F. Heutling, C. Kunze, W. Smarsly, C. Das, H. Clemens, Forged intermetallic γ -TiAl based alloy low pressure turbine blade in the geared turbofan, in: V. Venkatesh, A. L. Pilchak, J. E. Allison, S. Ankern, R. Boyer, J. Christodoulou, H. L. Fraser, M. A. Imam, Y. Kosaka, H. J. Rack, A. Chatterjee, A. Woodfield (Eds.), 13th World Conf on Titanium, 2016. doi:10.1002/9781119296126.ch208.
- [30] S. Mayer, D. Schimbäck, R. Wartbichler, D. Wimler, H. Clemens, Metallography of Intermetallic Titanium Aluminides – the (Additive) Manufacturing Makes the Difference, *Practical Metallography* 56 (9) (2019) 567–584. doi:10.3139/147.110622.
- [31] D. Wang, H. Yuan, J. Qiang, The microstructure evolution, mechanical properties and densification mechanism of TiAl-based alloys prepared by spark plasma sintering, *Metals* 7 (2017) 201. doi:10.3390/met7060201.
- [32] J. Bieske, M. Franke, M. Schloffer, C. Körner, Microstructure and properties of TiAl processed via an electron beam powder bed fusion capsule technology, *Intermetallics* 126 (2020) 106929. doi:10.1016/j.intermet.2020.106929.
- [33] A. Couret, T. Voisin, M. Thomas, J.-P. Monchoux, Development of a TiAl alloy by spark plasma sintering, *JOM* 69 (2017) 2576–2582. doi:10.1007/s11837-017-2549-6.
- [34] M. Schloffer, F. Iqbal, H. Gabrisch, E. Schwaighofer, F.-P. Schimansky, S. Mayer, A. Stark, T. Lippmann, M. Göken, F. Pyczak, H. Clemens, Microstructure development and hardness of a powder metallurgical multi phase γ -TiAl based alloy, *Intermetallics* 22 (2012) 231–240. doi:10.1016/j.intermet.2011.11.015.
- [35] T. Voisin, J.-P. Monchoux, M. Hantcherli, S. Mayer, H. Clemens, A. Couret, Microstructures and mechanical properties of a multi-phase β -solidifying TiAl alloy densified by spark plasma sintering, *Acta Materialia* 73 (2014) 107–115. doi:10.1016/j.actamat.2014.03.058.
- [36] D. Wimler, J. Lindemann, H. Clemens, S. Mayer, Microstructural Evolution and Mechanical Properties of an Advanced γ -TiAl Based Alloy Processed by Spark Plasma Sintering, *Materials* 12 (2019) 1523. doi:10.3390/ma12091523.
- [37] R. Wartbichler, H. Clemens, S. Mayer, Electron beam melting of a β -solidifying intermetallic titanium aluminide alloy, *Advanced Engineering Materials* (2019). doi:10.1002/adem.201900800.
- [38] W. Kan, Y. Liang, H. Peng, B. Chen, H. Guo, J. Lin, Microstructural degradation of Ti-45Al-8Nb alloy during the fabrication process by electron beam melting, *JOM* 69 (2017) 2596–2601. doi:10.1007/s11837-017-2592-3.
- [39] W. Kan, B. Chen, C. Jin, H. Peng, J. Lin, Microstructure and mechanical properties of a high Nb-TiAl alloy fabricated by electron beam melting, *Materials & Design* 160 (2018) 611–623. doi:10.1016/j.matdes.2018.09.044.
- [40] W. Kan, B. Chen, H. Peng, Y. Liang, J. Lin, Formation of columnar lamellar colony grain structure

in a high Nb-TiAl alloy by electron beam melting, *Journal of Alloys and Compounds* 809 (2019) 151673. doi:10.1016/j.jallcom.2019.151673.

[41] S. Biamino, A. Penna, U. Ackelid, S. Sabbadini, O. Tassa, P. Fino, M. Pavese, P. Gennaro, C. Badini, Electron beam melting of Ti–48Al–2Cr–2Nb alloy: Microstructure and mechanical properties investigation, *Intermetallics* 19 (2011) 776–781. doi:10.1016/j.intermet.2010.11.017.

[42] D. Cormier, O. Harrysson, T. Mahale, H. West, Freeform fabrication of titanium aluminide via electron beam melting using prealloyed and blended powders, *Research Letters in Materials Science* 2007 (2008). doi:10.1155/2007/34737.

[43] L. E. Murr, S. M. Gaytan, A. Ceylan, E. Martinez, J. L. Martinez, D. H. Hernandez, B. I. Machado, D. A. Ramirez, F. Medina, S. Collins, Characterization of titanium aluminide alloy components fabricated by additive manufacturing using electron beam melting, *Acta Materialia* 58 (5) (2010) 1887–1894. doi:10.1016/j.actamat.2009.11.032.

[44] D. Wimler, S. Kardos, J. Lindemann, H. Clemens, S. Mayer, Aspects of powder characterization for additive manufacturing, *Practical Metallography* 55 (2018) 620–636. doi:10.3139/147.110547.

[45] R. Gerling, H. Clemens, F. P. Schimansky, Powder metallurgical processing of intermetallic gamma titanium aluminides, *Advanced Engineering Materials* 6 (2004) 23–38. doi:10.1002/adem.200310559.

[46] V. Güther, M. Allen, J. Klose, H. Clemens, Metallurgical processing of titanium aluminides on industrial scale, *Intermetallics* 103 (2018) 12–22. doi:10.1016/j.intermet.2018.09.006.

[47] M. Achtermann, W. Fürwitt, V. Güther, H.-P. Nicolai, Method for producing of γ -TiAl base alloy (2011).

[48] C. Fleißner-Rieger, T. Pogriely, D. Obersteiner, T. Pfeifer, H. Clemens, S. Mayer, An additively manufactured titanium alloy in the focus of metallography, *Practical Metallography* (2021). doi:10.1515/pm-2020-0001.

[49] H.-J. Bunge, *Texture analysis in materials science: mathematical methods*, Elsevier, 2013.

[50] N. Schell, R. V. Martins, F. Beckmann, H. U. Ruhnau, R. Kiehn, A. Schreyer, The high energy materials science beamline at PETRA III, in: A. R. Pyzalla, A. Borbély, H.-P. Degischer (Eds.), *Stress evaluation in materials using neutrons and synchrotron radiation*, Materials science forum, Trans Tech, Stafa-Zurich and United Kingdom, 2008, pp. 261–266. doi:10.4028/www.scientific.net/MSF.571-572.261.

[51] S. C. Bodner, L. van de Vorst, J. Zalesak, J. Todt, J. F. Keckes, V. Maier-Kiener, B. Sartory, N. Schell, J. W. Hooijmans, J. J. Saurwalt, J. Keckes, Inconel-steel multilayers by liquid dispersed metal powder bed fusion: Microstructure, residual stress and property gradients, *Additive Manufacturing* 32 (2020) 101027. doi:10.1016/j.addma.2019.101027.

[52] A. P. Hammersley, S. O. Svensson, M. Hanfland, A. N. Fitch, D. Hausermann, Two-dimensional detector software: From real detector to idealised image or two-theta scan, *High Pressure Research* 14 (1996) 235–248. doi:10.1080/08957959608201408.

[53] L. B. McCusker, R. B. V. Dreele, D. E. Cox, D. Louër, P. Scardi, Rietveld refinement guidelines, *Journal of Applied Crystallography* 32 (1999) 36–50. doi:10.1107/S0021889898009856.

[54] L. Lutterotti, Total pattern fitting for the combined size–strain–stress–texture determination in thin film diffraction, *Nuclear Instruments and Methods in Physics Research Section B: Beam Interactions with*

- Materials and Atoms 268 (3-4) (2010) 334–340. doi:10.1016/j.nimb.2009.09.053.
- [55] M. Markl, A. M. Rausch, V. E. Kueng, C. Koerner, SAMPLE: A software suite to predict consolidation and microstructure for powder bed fusion additive manufacturing, *Advanced Engineering Materials* 22 (2020). doi:10.1002/adem.201901270.
- [56] A. Klassen, V. E. Forster, V. Juechter, C. Körner, Numerical simulation of multi-component evaporation during selective electron beam melting of TiAl, *Journal of Materials Processing Technology* 247 (2017) 280–288. doi:10.1016/j.jmatprotec.2017.04.016.
- [57] S. Banerjee, P. Mukhopadhyay, Phase transformations: Examples from titanium and zirconium alloys, Vol. 12 of Pergamon materials series, Elsevier, Amsterdam and Oxford, 2007.
- [58] W. G. Burgers, On the process of transition of the cubic-body-centered modification into the hexagonal-close-packed modification of zirconium, *Physica* 1 (7) (1934) 561–586. doi:10.1016/S0031-8914(34)80244-3.
- [59] S. Mitao, L. A. Bendersky, Morphology and growth kinetics of discontinuous coarsening in fully lamellar Ti 44 Al (at.%) alloy, *Acta Materialia* 45 (11) (1997) 4475–4489. doi:10.1016/S1359-6454(97)00139-0.
- [60] M. Kastenhuber, T. Klein, B. Rashkova, I. Weißensteiner, H. Clemens, S. Mayer, Phase transformations in a β -solidifying γ -TiAl based alloy during rapid solidification, *Intermetallics* 91 (2017) 100–109. doi:10.1016/j.intermet.2017.08.017.
- [61] M. Kastenhuber, T. Klein, H. Clemens, S. Mayer, Tailoring microstructure and chemical composition of advanced γ -TiAl based alloys for improved creep resistance, *Intermetallics* 97 (2018) 27–33. doi:10.1016/j.intermet.2018.03.011.
- [62] L. Cha, H. Clemens, G. Dehm, Microstructure evolution and mechanical properties of an intermetallic Ti-43.5Al-4Nb-1Mo-0.1B alloy after ageing below the eutectoid temperature, *International Journal of Materials Research* (2011) 703–708.
- [63] M. Takeyama, M. Nakamura, T. Kumagai, M. Kikuchi, Cooling rate dependence of the α/γ phase transformation in titanium aluminides and its application to alloy development, in: *Proc First Int Symp Struct Intermet*, Publ by Minerals, Metals & Materials Soc (TMS), 1993, pp. 167–176.
- [64] S. R. Dey, A. Hazotte, E. Bouzy, Crystallography and phase transformation mechanisms in TiAl-based alloys – A synthesis, *Intermetallics* 17 (2009) 1052–1064. doi:10.1016/j.intermet.2009.05.013.
- [65] C. Cayron, ARPGE: a computer program to automatically reconstruct the parent grains from electron backscatter diffraction data, *Journal of Applied Crystallography* 40 (Pt 6) (2007) 1183–1188. doi:10.1107/S0021889807048777.
- [66] O. Engler, V. Randle, *Introduction to Texture Analysis*, CRC Press, 2009. doi:10.1201/9781420063660.
- [67] K.-D. Liss, A. Bartels, H. Clemens, S. Bystrzanowski, A. Stark, T. Buslaps, F.-P. Schimansky, R. Gerling, C. Scheu, A. Schreyer, Recrystallization and phase transitions in a γ -TiAl-based alloy as observed by ex situ and in situ high-energy X-ray diffraction, *Acta Materialia* 54 (2006) 3721–3735. doi:10.1016/j.actamat.2006.04.004.
- [68] N. Raghavan, R. Dehoff, S. Pannala, S. Simunovic, M. Kirka, J. Turner, N. Carlson, S. S. Babu, Numerical modeling of heat-transfer and the influence of process parameters on tailoring the grain morphology of IN718 in electron beam additive manufacturing, *Acta Materialia* 112 (2016) 303–314. doi:10.1016/j.actamat.2016.03.063.

- [69] M. Markl, C. Körner, Multiscale modeling of powder bed-based additive manufacturing, *Annual Review of Materials Research* 46 (2016) 93–123. doi:10.1146/annurev-matsci-070115-032158.
- [70] C. S. Smith, Grains, phases, and interphases: an interpretation of microstructure, *TrMS* 175 (1948) 15–51.
- [71] I. Andersen, Ø. Grong, Analytical modelling of grain growth in metals and alloys in the presence of growing and dissolving precipitates—I. Normal grain growth, *Acta Metallurgica et Materialia* 43 (1995) 2673–2688. doi:10.1016/0956-7151(94)00488-4.
- [72] I. Andersen, Ø. Grong, N. Ryum, Analytical modelling of grain growth in metals and alloys in the presence of growing and dissolving precipitates—II. Abnormal grain growth, *Acta Metallurgica et Materialia* 43 (1995) 2689–2700. doi:10.1016/0956-7151(94)00489-5.
- [73] J. Schwerdtfeger, C. Körner, Selective electron beam melting of Ti–48Al–2Nb–2Cr: Microstructure and aluminium loss, *Intermetallics* 49 (2014) 29–35. doi:10.1016/j.intermet.2014.01.004.
- [74] V. Juechter, T. Scharowsky, R. F. Singer, C. Körner, Processing window and evaporation phenomena for Ti–6Al–4V produced by selective electron beam melting, *Acta Materialia* 76 (2014) 252–258. doi:10.1016/j.actamat.2014.05.037.
- [75] A. M. Rausch, M. Markl, C. Körner, Predictive simulation of process windows for powder bed fusion additive manufacturing: Influence of the powder size distribution, *Computers & Mathematics with Applications* 78 (2018) 2351–2359. doi:10.1016/j.camwa.2018.06.029.
- [76] I.-S. Jung, M.-C. Kim, J.-H. Lee, M.-H. Oh, D.-M. Wee, High temperature phase equilibria near Ti–50 at% Al composition in Ti–Al system studied by directional solidification, *Intermetallics* 7 (1999) 1247–1253. doi:10.1016/S0966-9795(99)00031-X.
- [77] I. S. Jung, H. S. Jang, M. H. Oh, J. H. Lee, D. M. Wee, Microstructure control of TiAl alloys containing β stabilizers by directional solidification, *Materials Science and Engineering: A* 329–331 (2002) 13–18. doi:10.1016/S0921-5093(01)01494-0.
- [78] D. R. Johnson, H. Inui, M. Yamaguchi, Directional solidification and microstructural control of the TiAl/Ti3Al lamellar microstructure in TiAl–Si Alloys, *Acta Materialia* 44 (1996) 2523–2535. doi:10.1016/1359-6454(95)00338-X.
- [79] D. R. Johnson, K. Chihara, H. Inui, M. Yamaguchi, Microstructural control of TiAl–Mo–B alloys by directional solidification, *Acta Materialia* 46 (1998) 6529–6540. doi:10.1016/S1359-6454(98)00310-3.
- [80] M. Yamaguchi, D. Johnson, H. Lee, H. Inui, Directional solidification of TiAl–base alloys, *Intermetallics* 8 (2000) 511–517. doi:10.1016/S0966-9795(99)00157-0.
- [81] J. A. Koepf, M. R. Gotterbarm, M. Markl, C. Körner, 3D multi-layer grain structure simulation of powder bed fusion additive manufacturing, *Acta Materialia* 152 (2018) 119–126. doi:10.1016/j.actamat.2018.04.030.
- [82] T. DebRoy, H. L. Wei, J. S. Zuback, T. Mukherjee, J. W. Elmer, J. O. Milewski, A. M. Beese, A. Wilson-Heid, A. De, W. Zhang, Additive manufacturing of metallic components – Process, structure and properties, *Progress in Materials Science* 92 (2018) 112–224. doi:10.1016/j.pmatsci.2017.10.001.
- [83] M. M. Kirka, P. Nandwana, Y. Lee, R. R. Dehoff, Solidification and solid-state transformation sciences in metals additive manufacturing, *Scripta Materialia* 135 (2017) 130–134. doi:10.1016/j.scriptamat.2017.01.005.

- [84] P. Barriobero-Vila, J. Gussone, A. Stark, N. Schell, J. Haubrich, G. Requena, Peritectic titanium alloys for 3D printing, *Nature communications* 9 (2018) 3426. doi:10.1038/s41467-018-05819-9.
- [85] S. P. Narra, R. Cunningham, J. Beuth, A. D. Rollett, Location specific solidification microstructure control in electron beam melting of Ti-6Al-4V, *Additive Manufacturing* 19 (2018) 160–166. doi:10.1016/j.addma.2017.10.003.
- [86] S. S. Al-Bermani, M. L. Blackmore, W. Zhang, I. Todd, The origin of microstructural diversity, texture, and mechanical properties in electron beam melted Ti-6Al-4V, *Metallurgical and Materials Transactions A* 41 (2010) 3422–3434. doi:10.1007/s11661-010-0397-x.

Microstructure and mechanical properties of novel TiAl alloys tailored via phase and precipitate morphology

D. Wimler^{a*}, J. Lindemann^b, T. Kremmer^c, H. Clemens^a, S. Mayer^a

^a Department of Materials Science, Montanuniversität Leoben, 8700 Leoben, Austria

^b GfE Fremat GmbH, Brand-Erbisdorf, Germany

^c Chair of Nonferrous Metallurgy, Montanuniversität Leoben, Leoben, Austria

* Corresponding author

SCI Journal (2021)

under review

Keywords: Spark plasma sintering; intermetallics; titanium aluminides; mechanical properties; microstructure; heat treatment; precipitation

Abstract

Research and development of alloys based on the intermetallic γ -TiAl phase is experiencing a renewed interest since powder metallurgical approaches provide new near-net-shape processing options. In this work, the manufacturing via spark plasma sintering was facilitated, a straightforward manufacturing technique to consolidate gas atomized pre-alloyed TiAl powder for microstructural and mechanical evaluation. Two alloys, the so-called BMBF3 alloy (Ti-47.4Al-5.6Nb-0.4W, in at.%) and the BMBF2 alloy (Ti-48.6Al-4.1Nb-0.7W-0.4Si-0.5C-0.1B, in at.%) were microstructurally designed via a heat treatment into a mechanically balanced nearly lamellar γ microstructure, i.e. γ appears in globular and lamellar morphology, as well as a creep resistant fully lamellar one. The latter exhibits high creep strength up to 850 °C, especially due to the formation of p-Ti₃AlC carbides. A heat treatment study upon this fully lamellar microstructure of the C-containing alloy links carbide formation and growth kinetics to the mechanical response of the microstructure. Thus, a stabilization heat treatment at 800 °C leads to the formation of finest carbides which are homogeneously distributed, whereas an annealing at higher temperatures results in coarsening of the carbides and the lamellar structure, which decrease the strength of the microstructure due to higher dislocation mobility. At even higher annealing temperatures, i.e. 1000 °C, the carbides dissolve.

The two investigated alloys can be addressed as either a ductile TiAl alloy employable up to 750 °C (BMBF3), while the BMBF2 alloy is considered useable up to 850 °C.

F.1 Introduction

Extensive research and development of advanced intermetallic titanium aluminides (TiAl) have been driven by the desire for lightweight high-temperature structural materials for applications in the aerospace and automotive industry. As a result of these intensive research activities, well-known alloys, such as the well-known Ti-48-2-2 alloy (Ti-48Al-2Nb-2Cr in at.%, unless stated otherwise) or the TNM alloy (Ti-43.5Al-4Nb-1Mo-0.1B) were introduced successfully as, for example, turbine blade material in advanced jet engines [1-3]. Thereby, the engineering TNM alloy of the 4th generation reaches application temperatures in the range of 600 to 800 °C [4]. At higher temperatures, the high-temperature strength and/or thermal stability of intermetallic TiAl alloys generally decreases [1, 5-8]. However, further alloy development based on the TNM alloy by adding 0.3 at.% C and 0.3 at.% Si, forming the so-called TNM⁺ alloy, enhances the high-temperature capabilities, but at the expense of the already moderate ductility of TiAl alloys at ambient temperature [9]. To improve the capability of plastic deformation at room temperature (RT) while maintaining creep and tensile strength, a continued alloy design together with a detailed microstructural and mechanical characterization have to be performed. Thus in the course of this work, two tailor-made TiAl alloys, namely the Ti-47.4Al-5.6Nb-0.4W alloy and the Ti-48.6Al-4.1Nb-0.7W-0.4Si-0.5C-0.1B alloy, were manufactured via spark plasma sintering (SPS) and subsequently subjected to a detailed analysis. Note, that these alloys are developed for the powder metallurgical approach, e.g. electron beam melting (EBM) [10, 11] and SPS, to establish novel process-adapted 4th generation TiAl alloys.

For optimizing the mechanical properties via alloy and microstructure design, the effects of the individual alloy elements have to be known. At first, the Al content controls the phase constitution present at service temperature: The higher the Al content, the higher the amount of the ordered, tetragonal face-centered γ -TiAl phase (L1₀ structure), which carries the majority of plastic deformation by motion of dislocations and mechanical twinning [12-18]. At lower Al contents, the amount of the ordered hexagonal α_2 -Ti₃Al phase (D0₁₉ structure) increases [19], whereby in binary TiAl alloys the highest ductilities can be reached around 48 at% Al [20]. The addition of Nb and W stabilizes the brittle, ordered body-centered cubic (bcc) β_o phase (B2 structure) at service temperature. Here, Mo and W are four times stronger β -stabilizers than Nb, and, concurrently, also expand the single phase field region of the high-temperature disordered bcc β phase (A2 structure) [21-24]. Nb and W also reduce diffusion processes which benefit creep resistance [7, 25]. Furthermore, the strength properties of TiAl alloys are increased by the addition of Si and C. Responsible for this is solid solution strengthening as well as precipitation hardening when the solubility limit is exceeded and finest carbides and silicides form, more precisely ζ -Ti₅Si₃ silicides (D8₈ structure) and p-Ti₃AlC carbides (E2₁ structure) [12, 26]. Although B also forms precipitates, those borides emerge from the melt and, thus, are coarse and rather act as

grain refining agent than as precipitation hardener [27].

Besides the modification of the chemical composition of intermetallic titanium aluminides based on the γ -TiAl phase, a broad spectrum of mechanical properties for application can be adjusted by the microstructure evolution during processing and subsequent heat treatments [5, 28, 29]. For example, a fully lamellar (FL) microstructure, which is adjusted by heat treatment above the solvus temperature of the γ phase ($T_{\gamma,\text{solv}}$), i.e. within the single α phase field region, shows the best creep properties as durable α_2/γ colonies forms from the α phase during cooling [30, 31]. Concurrently, however, the grain size is increased due to rapid grain coarsening evoked by the absence of a second phase during the heat treatment [32], which deteriorates the RT ductility [33]. An alternative designed microstructure is the so-called nearly lamellar γ (NL γ) microstructure, consisting of lamellar α_2/γ colonies surrounded by "soft" globular γ phase (γ_g), hence showing increased ductile behavior as reported in [5, 28].

In this work, both microstructures, i.e. FL and NL γ , are adjusted for the two new TiAl alloys and mechanically evaluated regarding their service maximum temperature. Furthermore, the thermal stability of the 0.5 at.% C-containing TiAl alloy variant in FL condition is evaluated up to 1000 °C. The conducted investigations show the potential of these novel TiAl alloys with tailor-made microstructures, when compared to established engineering γ -TiAl based alloy. Further, the results gain knowledge for TiAl alloys regarding the precipitation kinetics of p-Ti₃AlC carbides, which act as effective dislocation barrier as long as they are finely and homogeneously precipitated by applying an optimized annealing treatment.

F.2 Materials and methods

Two TiAl alloys, the so-called BMBF3 and BMBF2 alloy, were manufactured via SPS. The alloy nomenclature refers to the project "NextTiAl" (03XP0088A) funded by the German Federal Ministry of Education and Research (BMBF). The chemical compositions of the starting powders are Ti-47.4Al-5.6Nb-0.4W and 800 m. ppm O for BMBF3 as well as Ti-48.6Al-4.1Nb-0.7W-0.4Si-0.5C-0.1B and 800 m. ppm O for BMBF2. The concentrations of the elements Ti, Al, Nb, and W were determined by means of X-ray fluorescence (XRF) spectroscopy while Si, C, and B were measured by inductively coupled plasma-atomic emission spectroscopy (ICP-AES). For analyzing the O content, carrier gas hot extraction (CGHE) was used [34]. The powders were produced via electrode induction melting gas atomization (EIGA) [35] by TLS Technik GmbH & Co. Spezialpulver KG, Germany. The ingots for the EIGA process were produced according to Refs. [36, 37] by GfE Metalle und Materialien GmbH, Germany. The powders < 150 μm were consolidated in a graphite die to cylindrical discs with a diameter of either 20 or 80 mm and a height of 14 mm with a SPS unit of the type HP D 25 from FCT Systems GmbH, Germany, at the Technische Universität

Bergakademie Freiberg, Germany. The heating of the SPS device is done by pulsed electric current, whereas the cooling is achieved by natural convection (NC) [38]. Therefore, the cooling rate is dependent on the geometry and the size of the sintered part. An evaluation of the cooling rate for the 20 and 80 mm diameter revealed a rate of 300-450 K/min and around 90 K/min, respectively, between 1200 and 1000 °C as measured by a thermocouple in the center of the graphite die. The applied pressure was 50 MPa.

Heat treatments were conducted either on cut samples of the dimension 10×10×10 mm³ or cylindrical blanks for tensile and creep specimens with a diameter of 11 mm and a length of 70 mm under atmosphere by employing a high-temperature furnace of the type RHF 1600 from Carbolite Gero GmbH & Co. KG, Germany, with a furnace cooling (FC) rate of < 30 K/min. The stabilization heat treatments up to 1000 °C were performed in a chamber oven from Nabertherm GmbH, Germany, with a subsequent FC rate of < 2 K/min.

The as-SPS or heat-treated samples were metallographically prepared according to Ref. [39] and examined by employing a scanning electron microscope (SEM) from TESCAN GmbH, Czech Republic, of the type CLARA in back-scattered electron (BSE) mode.

Further, the polished samples were investigated by X-ray diffraction (XRD) measurements using an AXS D8 ADVANCE diffractometer from Bruker AXS GmbH, Germany. Thereby, a 2θ range between 30 and 46° was recorded using a step size of 0.02° and an exposure time of 10 s/°. Corresponding Rietveld refinement [40] was used to quantify the fractions of the present phases, applying the Bruker software TOPAS 4.2, Germany. For transmission electron microscopy (TEM) specimens with 3 mm in diameter were electrolytically thinned to electron transparency employing a Tenu Pol-5 with the associated electrolyte A3 by Struers, Germany. To determine the average lamellar spacing within the α_2/γ colonies, a Philips CM12 microscope, Germany, operating at an acceleration voltage of 120 kV was employed, whereby the images were taken along the $\langle 110 \rangle$ zone axis of the γ -phase, i.e. in so-called “edge-on” condition of the colonies. High angle annular dark field (HAADF), bright field (BF) and energy dispersive X-ray (EDX) studies were carried out using a TEM of the type Thermo Scientific Talos F200X from Thermo Fisher Scientific, United States.

The mechanical properties were determined via hardness measurements according to Vickers (HV5) upon polished samples using a Q60A+ testing device from ATM Qness GmbH, Austria, whereby each value was determined as the arithmetic mean value from at least ten indents. Quasi-static tensile tests were conducted at 25, 300, 700, and 850 °C on machines of the type Inspect 501 from Hegewald and Peschke GmbH, Germany, and AG-100 from Shimadzu, Japan, according to DIN EN ISO 6892-1. The initial strain rate of the tensile tests was 10⁻⁴ s⁻¹, whereby the tensile test specimens had a diameter of 5 mm and a gauge length of 25 mm machined from the former mentioned cylindrical blanks. For creep experiments, the samples had a diameter of 6 mm and a gauge length of 30 mm. The creep tests were conducted at 750 and 850 °C under an applied load of 150 MPa using equipment from AET Technologies, France, of the type TC30 and TC50.

F.3 Results and discussion

F.3.1 Microstructure adjustment

3.1.1. BMBF3 alloy - Ti-47.4Al-5.6Nb-0.4W

The so-called BMBF3 powder was sintered at 1370 °C for 3 min into a 20 mm sample. Figure F.1a shows the resulting FL microstructure, consisting solely of α_2/γ colonies. Despite the short dwell time of 3 min, their size exceeds 200 μm , due to unhindered and, thus, fast grain coarsening within the single α phase field region present at 1370 °C. Although coarse grains are beneficial for the creep resistance in principle [25, 41, 42], Maruyama et al. [41] showed that the creep rate of TiAl alloys is independent when the grain size is $> 100 \mu\text{m}$. Besides, the large grain size deteriorates the RT ductility [28, 33, 43, 44]. Therefore, the additional 80 mm samples were sintered within the $\alpha + \gamma$ phase field region at 1350 °C for 3 min. However, due to the low cooling rate of approximately 90 K/min of the SPS unit by NC, a subsequent heat treatment at 1350 °C for 60 min followed by air cooling (AC) was conducted to minimize the average lamellar spacing within the colonies [30]. The resulting microstructure consists of small, lamellar α_2/γ colonies surrounded by dark contrasted γ_g , i.e. a NL γ microstructure, as shown in the SEM image in Fig. F.1b recorded in BSE mode. The amount of γ_g was determined to be 10 vol.%, as shown in the insert of Fig. F.1b, where all other conducted heat treatment temperatures between 1290 and 1350 °C for adjusting a NL γ microstructure are summarized. The NL γ microstructure with 10 vol.% γ_g , thus called NL10 γ (shown in Fig. F.1b), was chosen for the further mechanical evaluation, as literature suggests balanced mechanical properties between tensile strength, ductility as well as creep resistance [28]. For the purpose of tensile and creep tests up to 850 °C, a common stabilization heat treatment step was finally performed on the NL10 γ microstructure, i.e. at 900 °C for 4 h followed by FC [10, 45]. The 900 °C annealing temperature was selected to be above the highest testing temperature to prevent microstructural changes during the mechanical tests. The stabilized microstructure does not differ from Fig. F.1b, neither in morphology nor appears so-called cellular reaction [9, 46] at the colony boundaries, which is a form of discontinuous coarsening (DC) [56]. The lamellar colonies were further investigated by TEM to determine the average lamellar spacing, resulting in $30 \pm 20 \text{ nm}$. This value is essential for the interpretation of mechanical properties [25, 30, 41], see section F.3.2.

3.1.2. BMBF2 alloy - Ti-48.6Al-4.1Nb-0.7W-0.4Si-0.5C-0.1B

The BMBF2 alloy, sintered at 1325 °C for 3 min and subsequent NC in cylindrical discs with 80 mm in diameter, exhibits a microstructure mainly composed of dark fine-grained γ_g , as shown in Fig. F.2a, which is called a near gamma (NG) microstructure [28]. Only a few small lamellar α_2/γ colonies are observable in the SEM image. In a higher magnification

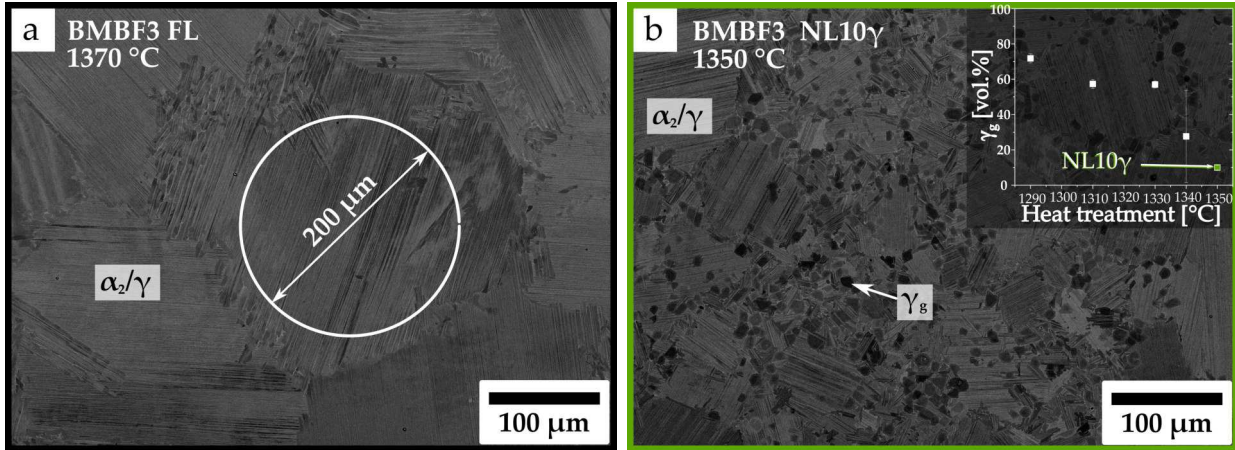


Figure F.1: SEM images in BSE mode of the BMBF3 alloy with a chemical composition of Ti-47.4Al-5.6Nb-0.4W exhibiting a) a FL microstructure adjusted within the SPS unit at 1370 °C for 3 min, whose lamellar α_2/γ colony size exceeds 200 μm , and b) a NL γ microstructure adjusted during sintering at 1350 °C for 3 min and a subsequent heat treatment at 1350 °C for 60 min followed by AC. The amount of dark appearing γ_g was determined via quantitative analysis of SEM micrographs to be 10 vol.%, see insert and text for details.

in the insert, bright phases are detectable as well as the gray contrasted α_2 phase. These white appearing precipitates are either bright-white β_o phase, as it is enriched in W, or, slightly darker, ζ silicides, which can be found within the grains or larger at their boundaries [10]. As they are difficult to differentiate in the SEM, they were analyzed in the TEM and will be discussed in detail in section F.3.3.3. This NG microstructure was subsequently heat-treated at 1400 °C to adjust a FL microstructure as shown in Fig. F.2b. The holding time was set at 30 min to prevent extensive grain coarsening. Therefore and due to the optimized chemical composition, when compared to the BMBF3 alloy. Additional Si and B are forming high-temperature stable precipitates, inhibiting grain boundary migration [9, 47, 48]. As a consequence, the colony size was kept at around 100 μm in the FL BMBF2 microstructure. The silicides, ζ , are indicated in the insert in Fig. F.2b as small spherical bright precipitates, whereas the borides are present as white, large, needle-shaped precipitates in small quantities. After the heat treatment at 1400 °C in the α single phase field region, the sample was cooled down with a medium cooling rate of about 100-150 K/min, whereby β_o can precipitate bright-white at lamellar interfaces via $\alpha_2 \rightarrow \beta_o + \gamma$ in an ellipsoid morphology as reported in Refs. [49-52] for Ti-(47-48)Al+(W/Mo) alloys. Faster cooling would prevent the β_o -formation and lead to a smaller lamellar spacing and, thus better strength and creep resistance [25, 30, 41]. However, higher cooling rates can lead to the formation of massive γ via short-range diffusion, i.e. $\alpha \rightarrow \gamma_m$ [53-55], which is undesired in the FL microstructure.

The adjusted FL microstructure in the BMBF2 alloy is shown in Fig. F.2b. Therein, the

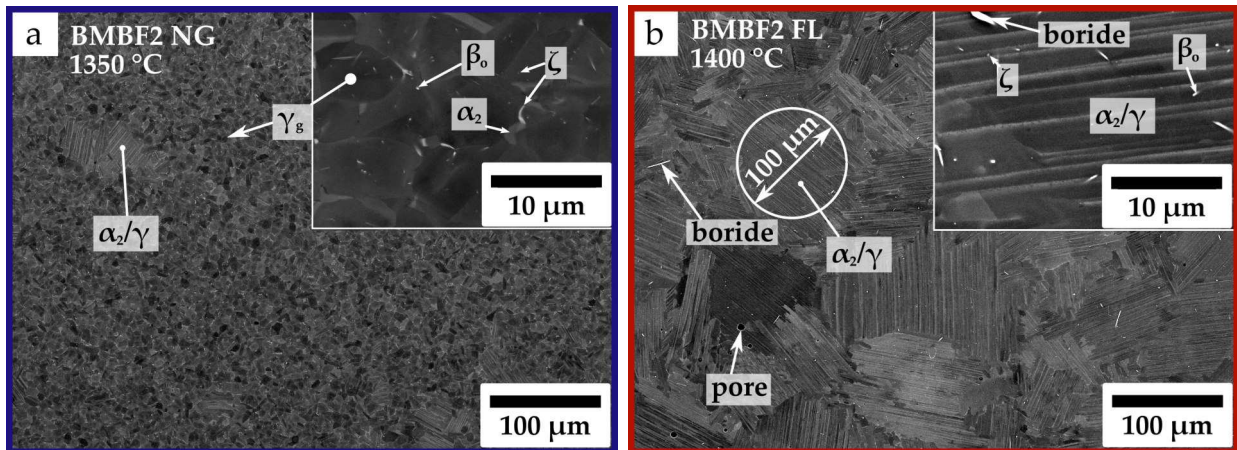


Figure F.2: a) BMBF2 alloy (Ti-48.6Al-4.1Nb-0.7W-0.4Si-0.5C-0.1B) densified via SPS at 1325 °C, 3 min dwell time and subsequent NC, which results in a NG microstructure, i.e. dark-contrasted γ_g and traces of lamellar α_2/γ colonies in the SEM BSE image. The insert shows bright-contrasted ζ silicides and bright-white β_o phase along with the gray α_2 phase at γ_g boundaries; b) FL microstructure adjusted via a subsequent heat treatment at 1400 °C for 30 min exhibit a colony size of about 100 μm . The small white precipitates are ζ and β_o , whereas the large, needle-shaped ones are borides. A detailed evaluation is given in section F.3.3.3. Pores, enlarged by etching, are also present as a consequence of TIP, see text.

colonies appear irregular serrated, as in Fig. F.1a, stemming from the onset of discontinuous coarsening, common in slowly cooled FL microstructures of high Al containing TiAl alloys according to Denquin et al. [56], as discussed in detail in section F.3.3.

The last features of the FL microstructure in Fig. F.2b are spherical pores, which appear enlarged due to prior etching. These pores stem from the internal porosity of the gas atomized powder in use [34, 35], which are filled with trapped Ar inert gas. Those pores are compressed during the SPS processing by applying pressure and temperature. However, through the pressureless heat treatment at 1400 °C, they expand again due to the high pressure of the indissoluble Ar gas within the compressed pores. This phenomenon is called thermally induced porosity (TIP) [57, 58] and can impact the mechanical properties negatively. However, the pores are spherical and μm -sized, therefore, two orders of magnitude smaller than the largest microstructural feature, namely the α_2/γ colonies.

Upon the adjusted FL microstructure, the same additional stabilization heat treatment as for the NL10 γ microstructure of BMBF3 was conducted, i.e. 900 °C for 4 h, FC. Again, the stabilization treatment did not lead to any alteration of the microstructure. No cellular reaction takes place, starting from the α_2/γ boundaries. The average spacing between the lamellar interfaces was determined by TEM to be 121 ± 130 nm. A more detailed analysis, regarding the stability of those lamellar structures, is presented in section F.3.3.

F.3.2 Tensile and creep tests up to 850 °C

Three microstructural conditions were mechanically evaluated: i) the NL10 γ condition of BMBF3 (Fig. F.1b), ii) the NG (Fig. F.2a) and iii) the FL (Fig. F.2b) condition of BMBF2, whereby the respective heat treatment route and the resulting microstructures are described in the previous chapter.

3.2.1. NL10 γ microstructure of BMBF3

The tensile results of the NL10 γ microstructure of the BMBF3 alloy (green color coding in Fig. F.3) exhibit a yield strength, determined at an offset of 0.2% plastic strain ($R_{p0.2}$), of about 490 MPa and an ultimate tensile strength (UTS) of about 610 MPa. Concurrently, a plastic strain at fracture (A_5) [59] of 0.9% is maintained. An increase of the test temperature provokes a slight decrease of the strength values, while the ductility, i.e. A_5 , increases. Between the tensile test at 700 and 850 °C, a pronounced reduction of the strength can be observed, while a strong increase of the elongation values to more than 10% appears. Such a mechanical response as a function of the temperature is common for engineering TiAl alloys, i.e. maintaining strength levels up to a specific temperature, above which a drop takes place [6, 7, 12, 45, 60, 61], i.e. at the so-called brittle-to-ductile-transition temperature (BDTT). The BDTT in TiAl alloys is in the range between 700 and 900 °C, whereby the exact temperature depends on the chemical composition of the alloy, its microstructure and the testing condition, e.g. used strain rate [12, 13, 62]. For comparison, Figs. F.3a-c contain literature values, in gray, from SPS manufactured engineering TiAl alloys, namely the TNM alloy in FL condition as a representative high-strength γ -TiAl based alloy [60] as well as the Ti-48Al-2Nb-2Cr (Ti-48-2-2) alloy with a duplex microstructure [63] (i.e. about 50% γ_g and 50% α_2/γ [64]) characterized by a satisfactory RT ductility. The comparison of the tensile test results with the literature shows that the BMBF3 NL10 γ is close to the Ti-48-2-2 alloy, but slightly stronger. Nevertheless, the creep tests conducted at 750 °C (see Fig. F.3d) reveal that the creep resistance of BMBF3 NL10 γ is enhanced, when compared to the TNM alloy [60] inserted in Fig. F.3d. However, creep tests at 850 °C of the BMBF3 samples show that 1% creep strain is reached after 20 h, which is not acceptable for application at this temperature. Nevertheless, in summary, the BMBF3 alloy in NL10 γ condition is more ductile than the high-strength FL TNM alloy [60] and stronger when compared to the ductile duplex Ti-48-2-2 alloy [63], thus representing balanced mechanical properties in the course of the tensile tests. In addition, its creep resistance exceeds the value of the FL TNM alloy, making it a potential alloy for application up to 750 °C.

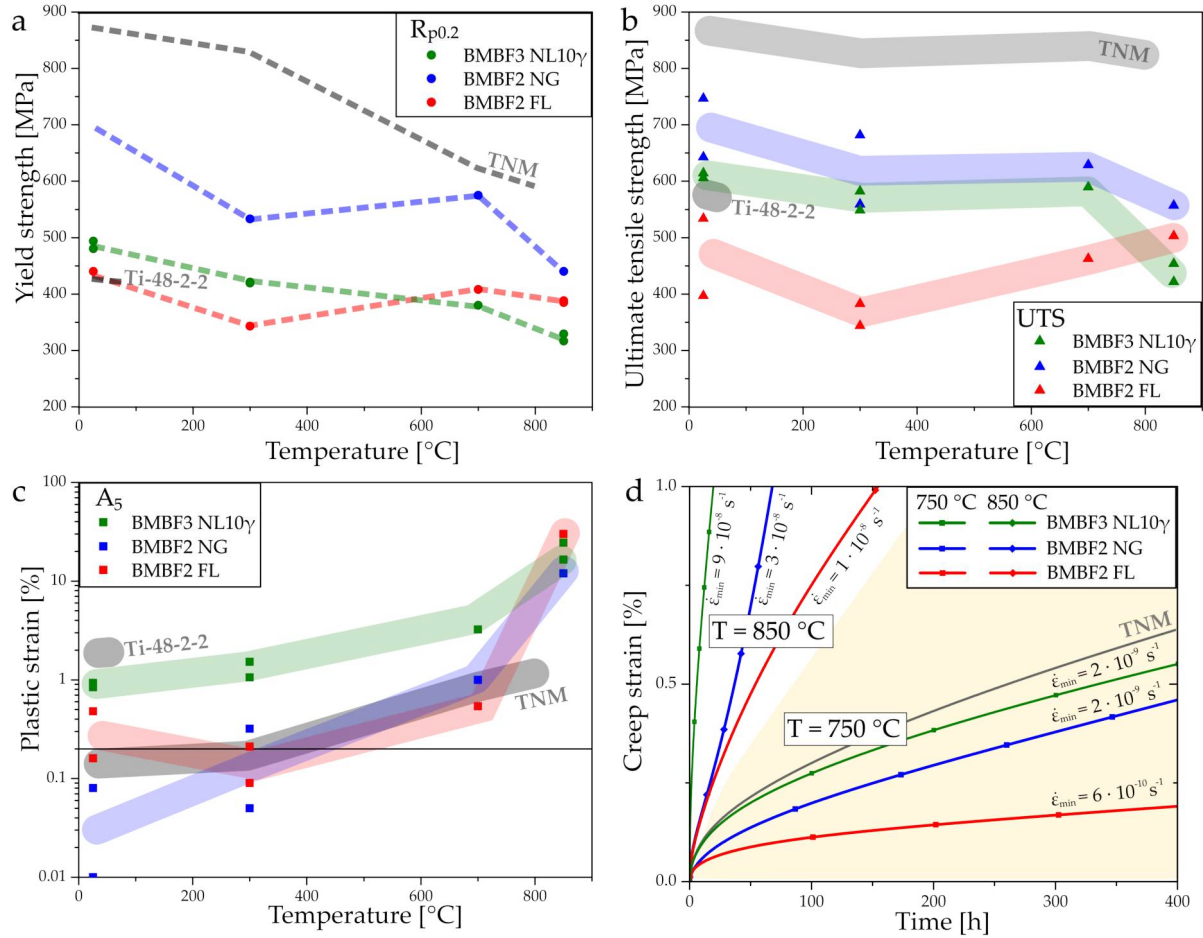


Figure F.3: Results of the tensile and creep tests of the selected microstructures: NL10 γ BMBF3 (green), NG BMBF2 (blue) and FL BMBF2 (red): a) yield strength, $R_{p0.2}$, b) ultimate tensile strength, UTS, and c) plastic strain at fracture, A_5 , as a function of temperature. d) Creep strain as a function of time determined at 750 and 850 °C and 150 MPa. a)-d) includes also data from literature for comparison with i) a high-strength and ii) a ductile TiAl alloy, more precisely i) the TNM alloy manufactured via SPS with a FL microstructure [60] and ii) the Ti-48-2-2 alloy with a duplex microstructure also processed via SPS [63] in a)-c).

3.2.2. NG microstructure of BMBF2

Aiming for higher service temperature, the BMBF2 alloy was designed with a chemical composition of Ti-48.6Al-4.1Nb-0.7W-0.4Si-0.5C-0.1B, against the background of solid solution strengthening by Nb and W, precipitation hardening through Si and C, forming fine ζ -Ti₅Si₃ and p-Ti₃AlC particles, as well as B, generating borides for heterogeneous nucleation [12, 21, 25-27]. First, the tensile test results of the NG microstructure (blue color coding in Fig. F.3) show the highest strength at RT with about 700 MPa, but with $A_5 < 0.1\%$ also the lowest plasticity. Note that at this temperature $R_{p0.2}$ could not be determined, which means that no data points are marked in Fig. F.3a and, therefore, the course of the line

originates from the UTS values. Despite the above-mentioned strengthening mechanisms, the tensile test results are surpassed by the FL TNM alloy with a colony size of about 45 μm [60]. This may be caused by the lower Al content of the TNM alloy, i.e. a lower γ content along with a higher α_2 and β_o phase fraction, as well as oversized precipitates, e.g. ζ , which surround and/or penetrate the γ_g phase as shown in Fig. F.2a. The coarse precipitates may also explain the low ductility of the NG microstructure, which is otherwise known as the most ductile TiAl microstructure showing a poor creep resistance [28, 29]. However, the creep resistance (see Fig. F.3d) of the fine-grained BMBF2 NG microstructure could be enhanced when compared to the TNM alloy as well as to the BMBF3 NL10 γ variant at 750 and 850 °C. At 850 °C, 1 % creep strain is reached after around 70 h under applied load and temperature, i.e. significantly before 100 h, which represents a benchmark time for aerospace application [12]. In addition, the low ductility restricts the application of this microstructure due to a low damage tolerance [1, 2]. Thus, a further microstructural adjustment was conducted which is discussed in the next section.

3.2.3. FL microstructure of BMBF2

In contrast to the NG microstructure, the FL microstructure (Fig. F.2b) with a subsequent stabilization heat treatment at 900 °C is about 250 MPa softer at RT, i.e. the strength level in Fig. F.3a is around 450 MPa, which is comparable to the Ti-48-2-2 alloy [63]. A plastic strain at fracture of about 0.2 % was measured (Fig. F.3c), similar to the TNM alloy (likewise manufactured via SPS), whereas the Ti-48-2-2 alloy is significantly more ductile. The UTS values as well as $R_{p0.2}$ remain almost at the same level up to 850 °C. However, note a slight drop in strength and ductility at 300 °C. This sign of embrittlement stems from the occurrence of a thermally activated antisite mechanism locking dislocations, as it was observed in the temperature range of 200-500 °C in Refs [65, 66] and theoretically treated in Ref [67].

The creep results of the FL BMBF2 microstructure exceed all examined material conditions at both temperatures, see Fig. F.2d. At 850 °C the 1 % creep strain benchmark is reached after 150 h, due to the low minimum creep rate of $1 \cdot 10^{-8} \text{ s}^{-1}$, whereby at 750 °C $\dot{\epsilon}_{min}$ was $6 \cdot 10^{-10} \text{ s}^{-1}$. The microstructural investigations via SEM after the creep experiments revealed no obvious difference in the FL microstructure, as shown in Fig. F.4 taken on a sample crept for 360 h at 850 °C beyond the occurrence of the minimum strain rate. Therefore, the BMBF2 FL microstructure is well suited and stable for an application at 850 °C, expanding the field of application of TiAl alloys. Furthermore, its excellent creep properties were also confirmed by additive manufacturing of samples and their testing in FL condition [10].

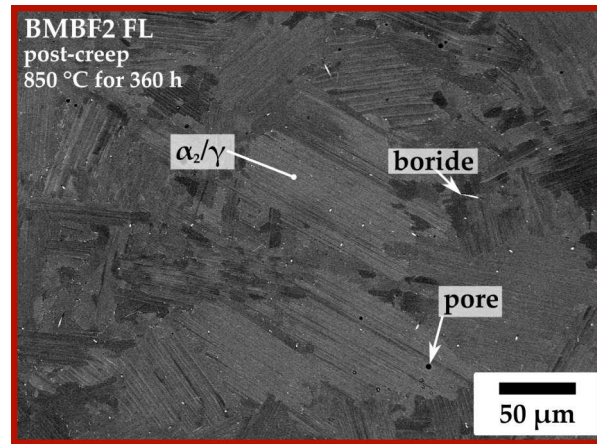


Figure F.4: SEM image in BSE mode of the FL microstructure of the BMBF2 alloy crept for 360 h at 850 °C. The creep strain was 2%. The microstructure reveals the same microstructural features when compared to the initial microstructure, see Fig. F.2b, and no obvious differences have occurred.

F.3.3 Microstructural stability of the C-containing fully lamellar condition of the BMBF2 alloy

The stability of the microstructure under thermal exposure plays an important role for TiAl alloys, as it influences the mechanical properties at high temperatures. Therefore, stabilization heat treatments slightly above the service temperature are implemented to prevent microstructural changes during application, as it was done in section F.3.2, i.e. stabilization annealing at 900 °C and subsequent testing up to 850 °C. Thereby, no microstructural degradation was found in the SEM images, when comparing Fig. F.2b with Fig. F.4.

3.3.1. Hardness response with regard to heat treatment parameters

The initial condition was a SPS sample of the BMBF2 alloy with a diameter of 20 mm sintered at 1400 °C followed by NC cooling. The resulting FL microstructure, as shown in Fig. F.5a, reveals lamellar α_2/γ colonies as well as bright contrasted phases, like borides, ζ and β_o . As mentioned before, the colony boundaries appear rather serrated than straight. This is caused by the onset of DC during the moderate cooling from the single α phase field region, as it was described by Denquin et al. [56]. Thereby the γ nuclei grow across the former α boundary in the adjacent grain. The adjusted FL microstructure of the BMBF2 alloy, in the following called as-SPS condition, exhibits a hardness of 324 ± 4 HV₅. Subsequent different stabilization heat treatments were then conducted on the as-SPS microstructure, i.e. for different times: 10, 100 and 240 min as well as at different temperatures: 800, 900 and 1000 °C followed by FC. Although no difference could be detected in the SEM images, when compared to the as-SPS microstructure in Fig. F.5a, the hardness differs significantly, see

Fig. F.5b. Therein, annealing at 1000 °C shows an immediate drop in hardness. In the case of annealing at 900 °C, after an initial increase at 10 min, the hardness decreases continuously to the level observed at 1000 °C. On the contrary, holding the as-SPS microstructure at 800 °C for 100 min and beyond, an increase of the hardness to about 375 HV5 could be observed, corresponding to a rise of 15 %. As mentioned, no difference could be found in the SEM images, i.e. no CR [9, 46, 68], which could explain a hardness drop or increase. Consequently, further XRD and TEM experiments were conducted.

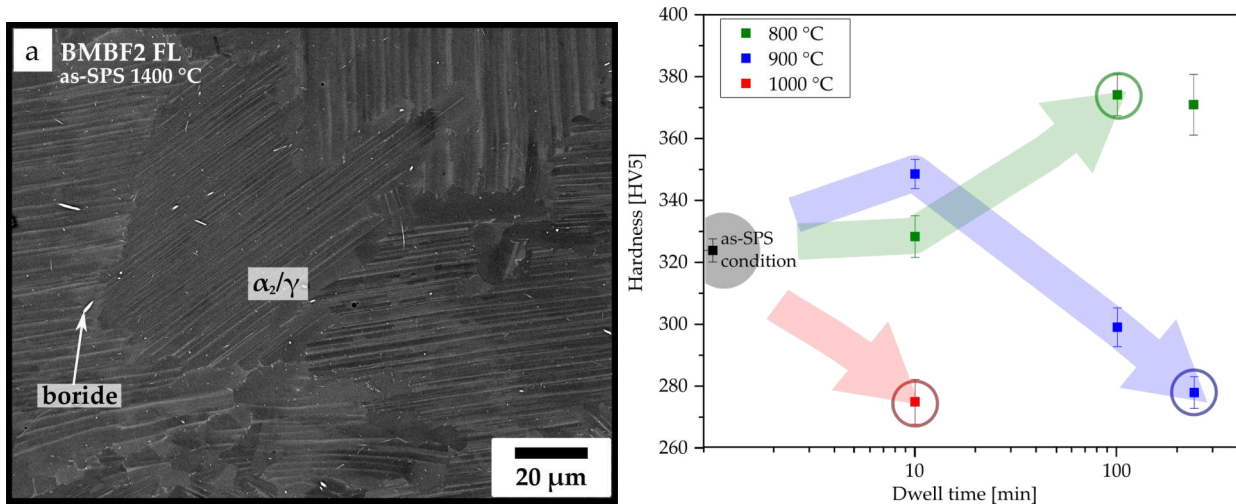


Figure F.5: a) SEM image in BSE mode of sintered BMBF2 powder at 1400 °C with a FL microstructure, in the following called as-SPS condition. b) Hardness of the as-SPS condition and SPS microstructures, which were stabilized at different temperatures and times. The encircled conditions were further investigated, see text.

3.3.2. Occurring phases according to X-ray diffraction

XRD experiments were conducted at specific samples, i.e. as-SPS and stabilization annealed, and the results are compiled in Fig F.6. According to the corresponding Rietveld refinement [40] all microstructures consist mainly of γ phase, i.e. $94 \pm 3 \text{ vol.}\%$, whereby individual peaks indicate the occurrence of additional phases ($< 6 \pm 3 \text{ vol.}\%$). The β_o phase is present in all conditions, slightly more distinctive after a dwell temperature of 900 and 1000 °C. The as-SPS condition (black line) reveals a pronounced α_2 peak which almost vanishes in annealed condition. Moreover, a significant peak at 43.3° arises corresponding to the perovskitic p-Ti₃AlC in the 900 °C/ 240 min condition. Note that no ζ -Ti₅Si₃ silicides could be determined in any XRD spectra. This may be caused by their small amount and complex D8₈ structure [12], which means that only peaks of low intensity occur, thus sinking into the background of the diffractograms. Besides, no peaks for the hexagonal h-carbides (Ti₂AlC) could be detected, however, those should only occur for C contents higher than 0.7 at.% [69,70].

Based on those results it can be concluded that the initial as-SPS condition consists of thermodynamically unstable α_2 phase, which dissolves mainly during the stabilization heat treatment. As well-known in literature, α_2 solves up to 1.5 at.% C [71], which have to be dissolved or precipitated in the remaining phases as soon as the α_2 volume fraction is decreased. The remaining microstructure, however, consists mainly of the γ phase, whose solubility limit is ~ 0.25 at.% at RT [71, 72]. At 900 °C, it appears that the p-carbides form to an extent that XRD can resolve them. However, they are not present at 1000 and 800 °C. At the former temperature, the C may still be solved in the remaining microstructure, because the temperature lays above their solvus temperature as proposed by Refs. [6, 71] who also found no carbides at 1050 °C by TEM, atom probe tomography (APT) and small-angle neutron scattering (SANS) in a Ti-45Al-5Nb-0.5C alloy. Wang et al. [73] were determined the p-carbide solvus temperature between 900 and 1000 °C via extensive TEM and high-energy X-ray diffraction (HEXRD) investigations on the solution annealed and aged Ti-45Al-5Nb-0.5C samples. However, the remaining of the C after stabilization at 800 °C could not be detected via XRD. Since it is unlikely that the C content is dissolved entirely in the remaining microstructure at 800 °C, finely dispersed p-carbides are more probable, but they are not resolved by XRD due to their size-related peak broadening and, thus, vanish into the background [73, 74].

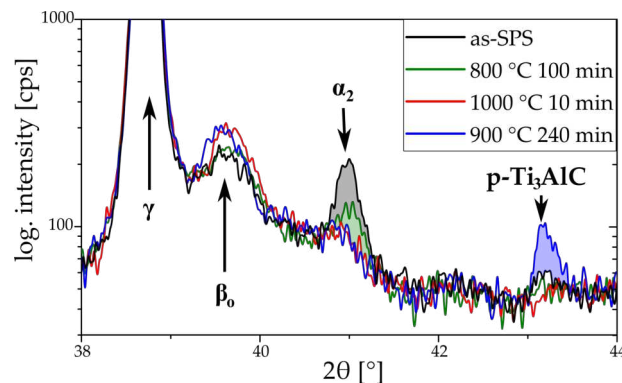


Figure F.6: Section of the XRD spectra, revealing the presence of up to four phases, depending on the thermal history, see text.

3.3.3. Transmission electron microscopy on the FL microstructure

TEM investigations were conducted on the as-SPS samples with FL microstructure as well as on two stabilized conditions, i.e. 900 °C/240 min and 800 °C/100 min, as shown in Fig. F.7. Thereby, the techniques of scanning transmission electron microscopy (STEM) in BF or HAADF imaging mode were employed. The latter mode provides information about the composition of the observed phases, i.e. via Z-contrast, whereby phases enriched on heavy elements appear in bright contrast [75]. For more details regarding the chemical composition, EDX mappings were performed in STEM mode. The average lamellar spacing

of the FL microstructure in as-SPS condition was determined to be 310 ± 300 nm. This broad distribution stems from fine lamellar α_2 phase, which is enriched in Ti, and broad Al-rich γ lamellae, as shown by the STEM image of a α_2/γ colony in Fig. F.7a and the corresponding EDX mappings in Fig. F.7b. The α_2/γ colonies form during cooling via the Blackburn orientation relationship, i.e. $\langle 11\bar{2}0 \rangle_{\alpha_2} \parallel \langle 110 \rangle_{\gamma}$, $(0001)_{\alpha_2} \parallel \{111\}_{\gamma}$ [76]. Thereby, the γ lamellae nucleate in six different variants and grow continuously at the expense of α_2 , which results in γ/γ (Fig. F.7a) as well as α_2/γ interfaces [12]. The α_2 lamellae in the close-up of Fig. F.7a are occasionally interrupted due to another form of DC, i.e. the discontinuous growth of the thermodynamically stable γ phase via atomic-sized ledges [25, 77, 78]. Furthermore, DC takes place across several γ laths, leaving behind one γ grain inside the α_2/γ colony as indicated in Fig. F.7a. This DC took place during the slow cooling, but after the formation of the α_2/γ colonies. This phenomenon, although inhibited by broad lamellae and alloying with W and B, is well-known in FL TiAl alloys containing a high Al content [56, 77, 78], deteriorating the strength of the microstructure as dislocation mobility increases. As a consequence of the high γ phase fraction (94 vol.%), which has a lower solubility for Ti, W, Si and C than the α_2 phase [21, 71, 79], these elements became either supersaturated in the γ laths or tended to precipitate. The EDX measurements reveal Ti, W, Nb rich precipitates. Those are up to 500 nm in length and are identified as β_o . In addition, ζ silicide particles form, but finer shaped as β_o . Both, the fine ζ as well as the larger β_o precipitates form during cooling as the amount of α_2 phase decreases. Finally, no evidence of C-containing precipitates could be detected in the TEM, which confirms the XRD analyses of this condition. Only minor C accumulations could be found in the EDX mapping, where the α_2 phase decomposes either into β_o , γ or ζ , which have a lower solubility for C than the α_2 phase [80].

Exposing the FL microstructure to a temperature of 900 °C for 240 min results in further decomposition of the α_2 laths, as recognizable in the upper left colony of Fig. F.7c. Therein, the former α_2 laths leave behind a trace of fine white ζ and β_o precipitates, which were identified as either Si or W rich, due to the low solubility limit of these elements in γ [79]. Besides, in the bottom grain of Fig. F.7c, fine precipitates were found uniformly aligned in the γ phase, as pointed out in the image with higher magnification. Next to these precipitates, coarse and non-uniformly arranged particles were detected, which are Ti and C rich, as well as lean in Al, see Fig. F.7d. Therefore, it is concluded that those are p-Ti₃AlC carbides formed by heterogeneous nucleation at dislocations as similarly reported in Refs. [69, 73]. Although the EDX mapping does not detect a C enrichment in the case of the aforementioned uniformly arranged precipitates, it is concluded that these are fine p-carbides, as occurring in TiAl+0.5C alloys [69, 73, 81]. These precipitates are always arranged in specific distances around other carbides, boundaries as well as former α_2 lamellae. Thus, forming precipitation free zones (PFZ) as described in Refs. [73, 81] and indicated in Fig. F.7c. Beyond, the γ grains are enriched in C, which leads to the homogeneous precipitation of the p-carbides according to $(001)_{\gamma} \parallel (001)_p$ and $(010)_{\gamma} \parallel (010)_p$ [81] in a needle-shaped manner along their

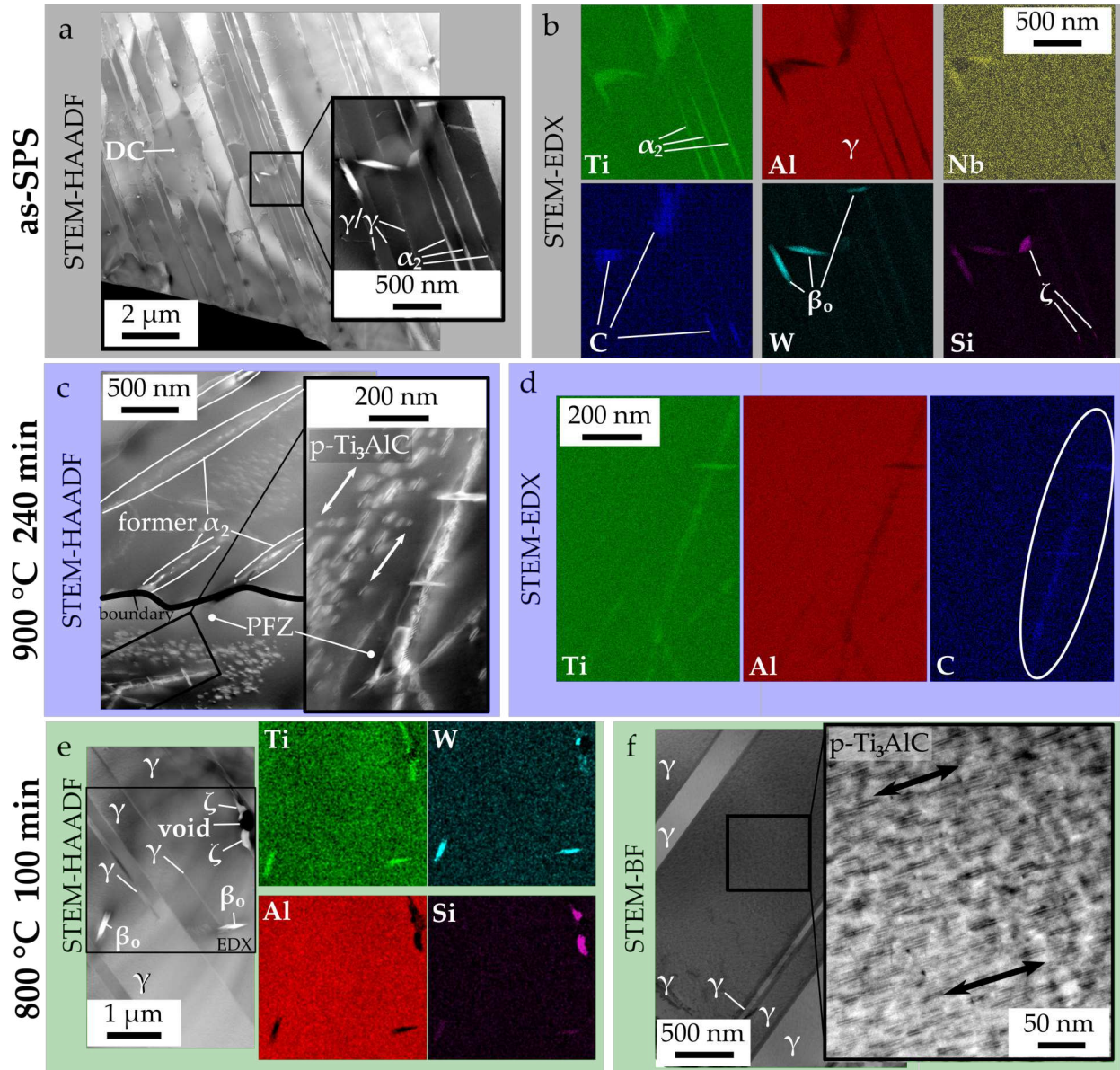


Figure F.7: Various TEM investigations, described in detail in the text, of a)-b) the initial FL as-SPS condition, revealing element partitioning and the formation of precipitates; c)-d) FL microstructure after 240 min at 900 °C showing C-containing precipitates located in the remaining γ phase; e) STEM-HAADF and f) STEM BF images reveal fine homogeneous distributed carbides within the γ lamellae of the FL microstructure stabilized at 800 °C for 100 min, whereby the carbides could be identified as p-Ti₃AlC precipitates.

[001] direction [81, 82]. These precipitates form in a significant amount and are about a few tens of nanometer thick, thus identifiable via XRD see Fig. F.6b. Although p-carbides are considered as an effective dislocation barrier, it seems that the coarse p-carbides, the PFZ [81] as well as the decomposition of the lamellar structure by the observed coarsening of the γ phase [56] lead to a drastic drop in hardness.

After 100 min at 800 °C the colonies are still exhibit a lamellar feature, as shown in Fig. F.7e. However, the EDX mappings show no lamellae enriched in Ti and depleted in Al, concluding that mainly γ laths are present after the stabilization treatment at 800 °C. In addition, there are coarse β_o and coarse ζ precipitates present in Fig. F.7e as discussed before (see Fig. F.7a), but no traces of Si and W rich fine precipitates located at former α_2 laths as seen at 900 °C in Fig. F.7c. In BF mode, Fig. F.7f, the γ laths show the appearance of very fine precipitates homogeneously distributed and there are no PFZs at the interface boundaries. Note, that the precipitate visibility in Fig. F.7f is orientation dependant, i.e. better visibility in specific zone axes, thus the bright γ laths do not show them, even though they might be present. The higher magnification of a γ lath confirms again the presence of needle-shaped p-carbides equally arranged. However, they are thinner and more frequent, when compared to the p-carbides in Fig. F.7c, thus explaining their absence in the corresponding XRD spectrum (Fig. F.6), as fine particles broaden the XRD peaks. Note that the majority of the TEM contrast stems from the misfit strain evoked by the p-carbides .

Wang et al. [73] showed that the size of the PFZs can be minimized by heat treatments, but they could not be eliminated. At 800 °C, the p-carbides in the γ laths precipitated fine and in a uniform manner, without PFZ at the interfaces. Those precipitates effectively impede the motion of dislocations within the γ laths [25, 82], thus increasing the hardness of the FL microstructure (see Fig. F.5). This strengthening mechanism is counteracted by the dissolution of the α_2 lamellae due to continuous and discontinuous coarsening of the γ phase [83]. This coarsening is accelerated at a higher stabilization temperature [56, 77, 78], i.e. more progressed in the sample annealed at 900 °C (Fig. F.7c). The α_2 laths are effective dislocation barriers, while γ interfaces are weaker ones [83], thus the lower α_2 phase fraction and the broader γ phase within the colonies decrease the hardness in the 900 °C condition. Note, that in the sample annealed at 900 °C, the carbides (as well as the β_o and ζ phase) are few and coarse and, therefore, less effective in strengthening the FL microstructure. In addition, there is a more pronounced and faster decomposition, which reduces the hardness.

F.4 Summary

In this work, two new 4th generation γ -TiAl based alloys were investigated regarding their microstructure and mechanical properties, i.e. the BMBF3 alloy with a nominal composition of Ti-47.4Al-5.6Nb-0.4W and the BMBF2 alloy consisting of Ti-48.6Al-4.1Nb-0.7W-0.4Si-

0.5C-0.1B. Both alloys were gas atomized and the powders were used for the densification via SPS, which forms the starting condition for the subsequent heat treatments to extend the field of application for TiAl alloys.

- The BMBF3 alloy was heat-treated to adjust a NL γ microstructure containing 10 vol.% γ_g . Since the resulting mechanical properties are UTS=610 MPa and $A_5=0.9\%$, the comparison with the literature shows that this microstructural condition can be addressed as a more ductile TNM alloy as well as a harder Ti-48-2-2 alloy. Concurrently, its creep resistance exceeds these two engineering reference alloys at 750 °C under an applied load of 150 MPa.
- For the BMBF2 alloy, two microstructures were adjusted and tested. A fine-grained NG microstructure, which showed the highest tensile strength level within this work, but it lacks on RT ductility. The adjustment of a FL microstructure reveals low strength values but higher RT ductility, when compared to the NG microstructure. Furthermore, the FL condition shows an excellent creep resistance up to 850 °C, i.e. 1 % creep strain was withstood up to 150 h under 150 MPa under an applied load of 150 MPa.

The FL BMBF2 alloy contains 0.5 at.% C and is subjected to a so-called stabilization heat treatment to improve the mechanical properties. Although not visible in the SEM images, effects of carbide precipitation could be confirmed by hardness, XRD as well as TEM experiments:

- A stabilization heat treatment at 800 °C reveals an increase in hardness from the initial 324 HV5 to 375 HV5. This is caused by the fine and homogeneous precipitation of p-Ti₃AlC carbides within the γ lamellae, whereby no PFZs are detectable at the lamellar interfaces.
- After dwelling at 900 °C, p-carbides are big enough to be detectable by XRD, thus representing less efficient barriers for dislocations. Concurrently, significant discontinuous coarsening of the γ laths leaves behind traces of β_o (W rich) and ζ silicide precipitates, which deteriorates the lamellar structure of the colonies. As a consequence, the hardness drops below 300 HV5.
- At 1000 °C, besides discontinuous coarsening, whose formation is accelerated at higher temperatures, it is argued that C is mainly present in a dissolved state, as proposed by literature and confirmed by missing XRD peaks. Since C is a weak solid solution strengthener in TiAl alloys, the hardness drops immediately at this temperature.

The BMBF2 FL microstructure stabilized at 900 °C shows excellent high-temperature strength and creep resistance up to 850 °C, thus 100 °C higher than obtained by already introduced engineering TiAl alloys.

Acknowledgement

The research work was conducted within the framework of the BMBF project 03XP0088C, Germany. The multi-annual BMBF project is focusing on alloy development of γ -TiAl based alloys. The support of the project partners is gratefully acknowledged. Furthermore, the work received support from the Austrian Research Promotion Agency (FFG) in the project 3DnanoAnalytics (FFG-no. 858040).

F.5 References

- [1] B. P. Bewlay, S. Nag, A. Suzuki, M. J. Weimer, TiAl alloys in commercial aircraft engines, *Materials at High Temperatures* 33 (2016) 549–559. doi:10.1080/09603409.2016.1183068.
- [2] U. Habel, F. Heutling, C. Kunze, W. Smarsly, C. Das, H. Clemens, Forged intermetallic γ -TiAl based alloy low pressure turbine blade in the geared turbofan, in: V. Venkatesh, A. L. Pilchak, J. E. Allison, S. Ankern, R. Boyer, J. Christodoulou, H. L. Fraser, M. A. Imam, Y. Kosaka, H. J. Rack, A. Chatterjee, A. Woodfield (Eds.), 13th World Conf on Titanium, 2016. doi:10.1002/9781119296126.ch208.
- [3] M. Burtscher, T. Klein, J. Lindemann, O. Lehmann, H. Fellmann, V. Güther, H. Clemens, S. Mayer, An Advanced TiAl Alloy for High-Performance Racing Applications, *Materials* 13 (2020). doi:10.3390/ma13214720.
- [4] S. Mayer, P. Erdely, F. D. Fischer, D. Holec, M. Kasthuber, T. Klein, H. Clemens, Intermetallic β -solidifying γ -TiAl based alloys – From fundamental research to application, *Advanced Engineering Materials* 19 (2017) 1600735. doi:10.1002/adem.201600735.
- [5] Y.-W. Kim, S.-L. Kim, Advances in gammalloy materials–processes–application technology: successes, dilemmas, and future, *Journal of Materials* 70 (2018) 553–560. doi:10.1007/s11837-018-2747-x.
- [6] R. Gerling, F. P. Schimansky, A. Stark, A. Bartels, H. Kestler, L. Cha, C. Scheu, H. Clemens, Microstructure and mechanical properties of Ti 45Al 5Nb+(0–0.5C) sheets, *Intermetallics* 16 (2008) 689–697. doi:10.1016/j.intermet.2008.02.004.
- [7] T. Voisin, J.-P. Monchoux, M. Thomas, C. Deshayes, A. Couret, Mechanical Properties of the TiAl IRIS Alloy, *Metallurgical and Materials Transactions A* 47 (2016) 6097–6108. doi:10.1007/s11661-016-3801-3.
- [8] A. Couret, D. Reyes, M. Thomas, N. Ratel-Ramond, C. Deshayes, J.-P. Monchoux, Effect of ageing on the properties of the W-containing IRIS-TiAl alloy, *Acta Materialia* 199 (2020) 169–180. doi:10.1016/j.actamat.2020.07.061.
- [9] M. Kasthuber, T. Klein, H. Clemens, S. Mayer, Tailoring microstructure and chemical composition of advanced γ -TiAl based alloys for improved creep resistance, *Intermetallics* 97 (2018)

- 27–33. doi:10.1016/j.intermet.2018.03.011.
- [10] D. Wimler, J. Lindemann, M. Reith, A. Kirchner, M. Allen, W. G. Vargas, M. Franke, B. Klöden, T. Weißgärber, V. Güther, M. Schloffer, H. Clemens, S. Mayer, Designing advanced intermetallic titanium aluminide alloys for additive manufacturing, *Intermetallics* 131 (2021) 107109. doi:10.1016/j.intermet.2021.107109.
- [11] M. Reith, M. Franke, M. Schloffer, C. Körner, Processing 4th generation titanium aluminides via electron beam based additive manufacturing – characterization of microstructure and mechanical properties, *Materialia* 14 (2020) 100902. doi:10.1016/j.mtla.2020.100902.
- [12] F. Appel, J. Paul, M. Oehring, *Gamma titanium aluminide alloys: science and technology*, Wiley-VCH, Weinheim, Germany, 2012.
- [13] F. Appel, U. Lorenz, M. Oehring, U. Sparka, R. Wagner, Thermally activated deformation mechanisms in micro-alloyed two-phase titanium aluminide alloys, *Materials Science and Engineering: A* 233 (1997) 1–14. doi:10.1016/S0921-5093(97)00043-9.
- [14] Z.-W. Ji, S. Lu, Q.-m. Hu, D. Kim, R. Yang, L. Vitos, Mapping deformation mechanisms in lamellar titanium aluminide, *Acta Materialia* 144 (2018) 835–843. doi:10.1016/j.actamat.2017.11.028.
- [15] U. Fröbel, F. Appel, Strain ageing in γ (TiAl)-based titanium aluminides due to antisite atoms, *Acta Materialia* 50 (2002) 3693–3707. doi:10.1016/S1359-6454(02)00182-9.
- [16] H. Inui, M. H. Oh, A. Nakamura, M. Yamaguchi, Room-temperature tensile deformation of polysynthetically twinned (PST) crystals of TiAl, *Acta Metallurgica et Materialia* 40 (1992) 3095–3104. doi:10.1016/0956-7151(92)90472-Q.
- [17] M. A. Morris, Dislocation mobility, ductility and anomalous strengthening of two-phase TiAl alloys: effects of oxygen and composition, *Intermetallics* 4 (1996) 417–426. doi:10.1016/0966-9795(95)00060-7.
- [18] P. Erdely, P. Staron, E. Maawad, N. Schell, H. Clemens, S. Mayer, Lattice and phase strain evolution during tensile loading of an intermetallic, multi-phase γ -TiAl based alloy, *Acta Materialia* 158 (2018) 193–205. doi:10.1016/j.actamat.2018.07.062.
- [19] J. C. Schuster, M. Palm, Reassessment of the binary Aluminum-Titanium phase diagram, *Journal of Phase Equilibria and Diffusion* 27 (2006) 255–277. doi:10.1361/154770306X109809.
- [20] S.-C. Huang, E. L. Hall, Plastic deformation and fracture of binary TiAl-base alloys, *Metallurgical Transactions A* 22 (1991) 427–439. doi:10.1007/BF02656810.
- [21] R. Kainuma, Y. Fujita, H. Mitsui, I. Ohnuma, K. Ishida, Phase equilibria among α (hcp), β (bcc) and γ (L10) phases in Ti–Al base ternary alloys, *Intermetallics* 8 (2000) 855–867. doi:10.1016/S0966-9795(00)00015-7.
- [22] I. S. Jung, H. S. Jang, M. H. Oh, J. H. Lee, D. M. Wee, Microstructure control of TiAl alloys containing β stabilizers by directional solidification, *Materials Science and Engineering: A* 329–331 (2002) 13–18. doi:10.1016/S0921-5093(01)01494-0.
- [23] H. F. Chladil, H. Clemens, G. A. Zickler, M. Takeyama, E. Kozeschnik, A. Bartels, T. Buslaps, R. Gerling, S. Kremmer, L. Yeoh, K.-D. Liss, Experimental studies and thermodynamic simulation of phase transformations in high Nb containing γ -TiAl based alloys, *International Journal of Materials Research* 98 (2007) 1131–1137. doi:10.3139/146.101569.

- [24] B. Rashkova, K. Spiradek-Hahn, M. Brabetz, Z. Zhang, T. Schöberl, H. Clemens, S. Mayer, Microstructural evolution and grain refinement in an intermetallic titanium aluminide alloy with a high molybdenum content, *International Journal of Materials Research* 106 (2015) 725–731. doi:10.3139/146.111235.
- [25] F. Appel, J. D. H. Paul, M. Oehring, U. Fröbel, U. Lorenz, Creep behavior of TiAl alloys with enhanced high-temperature capability, *Metallurgical and Materials Transactions A* 34 (2003) 2149–2164. doi:10.1007/s11661-003-0279-6.
- [26] Y.-W. Kim, S.-L. Kim, Effects of microstructure and C and Si additions on elevated temperature creep and fatigue of gamma TiAl alloys, *Intermetallics* 53 (2014) 92–101. doi:10.1016/j.intermet.2014.04.006.
- [27] R. M. Imayev, V. M. Imayev, M. Oehring, F. Appel, Alloy design concepts for refined gamma titanium aluminide based alloys, *Intermetallics* 15 (2007) 451–460. doi:10.1016/j.intermet.2006.05.003.
- [28] Y.-W. Kim, D. M. Dimiduk, Progress in the understanding of gamma titanium aluminides, *Journal of Materials* 43 (1991) 40–47. doi: 10.1007/BF03221103.
- [29] H. Clemens, S. Mayer, Design, processing, microstructure, properties, and applications of advanced intermetallic TiAl alloys, *Advanced Engineering Materials* 15 (2013) 191–215. doi:10.1002/adem.201200231.
- [30] M. Takeyama, M. Nakamura, T. Kumagai, M. Kikuchi, Cooling rate dependence of the α/γ phase transformation in titanium aluminides and its application to alloy development, in: *Proc First Int Symp Struct Intermet, Minerals, Metals & Materials Soc (TMS)*, 1993, pp. 167–176.
- [31] J. Lapin, K. Kamyshnykova, T. Pelachova, S. Nagy, Effect of carbon addition and cooling rate on lamellar structure of peritectic TiAl-based alloy, *Intermetallics* 128 (2021) 107007. doi:10.1016/j.intermet.2020.107007.
- [32] W. Li, K. Xia, Kinetics of the α grain growth in a binary Ti–44Al alloy and a ternary Ti–44Al–0.15Gd alloy, *Materials Science and Engineering: A* 329–331 (2002) 430–434. doi:10.1016/S0921-5093(01)01617-3.
- [33] Y.-W. Kim, Strength and ductility in TiAl alloys, *Intermetallics* 6 (1998) 623–628. doi:10.1016/S0966-9795(98)00037-5.
- [34] D. Wimler, S. Kardos, J. Lindemann, H. Clemens, S. Mayer, Aspects of powder characterization for additive manufacturing, *Practical Metallography* 55 (2018) 620–636. doi:10.3139/147.110547.
- [35] R. Gerling, H. Clemens, F. P. Schimansky, Powder metallurgical processing of intermetallic gamma titanium aluminides, *Advanced Engineering Materials* 6 (2004) 23–38. doi:10.1002/adem.200310559.
- [36] V. Güther, M. Allen, J. Klose, H. Clemens, Metallurgical processing of titanium aluminides on industrial scale, *Intermetallics* 103 (2018) 12–22. doi:10.1016/j.intermet.2018.09.006.
- [37] M. Achtermann, W. Fürwitt, V. Güther, H.-P. Nicolai, Method for producing of gamma-TiAl base alloy, EP2342365 (2011).
- [38] P. Cavaliere, *Spark plasma sintering of materials: advances in processing and applications*, Springer International Publishing, 2019.
- [39] C. Fleißner-Rieger, T. Pogrietz, D. Obersteiner, T. Pfeifer, H. Clemens, S. Mayer, An additively manufactured titanium alloy in the focus of metallography, *Practical Metallography* (2021). doi:10.1515/pm-2020-0001.
- [40] L. B. McCusker, R. B. V. Dreele, D. E. Cox, D. Louër, P. Scardi, Rietveld refinement guidelines,

- Journal of Applied Crystallography 32 (1999) 36–50. doi:10.1107/S0021889898009856.
- [41] K. Maruyama, R. Yamamoto, H. Nakakuki, N. Fujitsuna, Effects of lamellar spacing, volume fraction and grain size on creep strength of fully lamellar TiAl alloys, *Materials Science and Engineering: A* 239-240 (1997) 419–428. doi:10.1016/S0921-5093(97)00612-6.
- [42] S. Nishikiori, S. Takahashi, S. Satou, T. Tanaka, T. Matsuo, Microstructure and creep strength of fully-lamellar TiAl alloys containing beta-phase, *Materials Science and Engineering: A* 329-331 (2002) 802–809. doi:10.1016/S0921-5093(01)01638-0.
- [43] H. Saage, A. J. Huang, D. Hu, M. H. Loretto, X. Wu, Microstructures and tensile properties of massively transformed and aged Ti46Al8Nb and Ti46Al8Ta alloys, *Intermetallics* 17 (2009) 32–38. doi:10.1016/j.intermet.2008.09.006.
- [44] V. Imayev, T. Oleneva, R. Imayev, H.-J. Christ, H.-J. Fecht, Microstructure and mechanical properties of low and heavy alloyed γ -TiAl + α 2-Ti3Al based alloys subjected to different treatments, *Intermetallics* 26 (2012) 91–97. doi:10.1016/j.intermet.2012.03.010.
- [45] E. Schwaighofer, H. Clemens, S. Mayer, J. Lindemann, J. Klose, W. Smarsly, V. Güther, Microstructural design and mechanical properties of a cast and heat-treated intermetallic multi-phase γ -TiAl based alloy, *Intermetallics* 44 (2014) 128–140. doi:10.1016/j.intermet.2013.09.010.
- [46] L. Cha, H. Clemens, G. Dehm, Microstructure evolution and mechanical properties of an intermetallic Ti-43.5Al-4Nb-1Mo-0.1B alloy after ageing below the eutectoid temperature, *International Journal of Materials Research* (2011) 703–708 doi:10.3139/146.110526.
- [47] C. S. Smith, Grains, phases, and interphases: an interpretation of microstructure, *Transactions of the American Institute of Mining and Metallurgical Engineers* 175 (1948) 15–51.
- [48] I. Andersen, Ø. Grong, Analytical modelling of grain growth in metals and alloys in the presence of growing and dissolving precipitates—I. Normal grain growth, *Acta Metallurgica et Materialia* 43 (1995) 2673–2688. doi:10.1016/0956-7151(94)00488-4.
- [49] M. Takeyama, S. Kobayashi, Physical metallurgy for wrought gamma titanium aluminides: Microstructure control through phase transformations, *Intermetallics* 13 (2005) 993–999. doi:10.1016/j.intermet.2004.12.014
- [50] J. Beddoes, W. R. Chen, L. Zhao, Precipitation of β particles in a fully lamellar Ti-47Al-2Nb-1Mn-0.5W-0.5Mo-0.2Si (at.[51] D. Seo, J. Beddoes, L. Zhao, G. Botton, The influence of aging on the microstructure and creep behaviour of a γ -Ti-48[52] H. Zhu, D. Y. Seo, K. Maruyama, Strengthening of lamellar TiAl alloys by precipitation bands of β_0 particles, *Materials Science and Engineering: A* 510-511 (2009) 14–19. doi:10.1016/j.msea.2008.08.050.
- [53] S. A. Jones, M. J. Kaufman, Phase equilibria and transformations in intermediate titanium aluminum alloys, *Acta Metallurgica et Materialia* 41 (1993) 387–398. doi:10.1016/0956-7151(93)90069-5.
- [54] S. R. Dey, A. Hazotte, E. Bouzy, Crystallography and phase transformation mechanisms in TiAl-based alloys – A synthesis, *Intermetallics* 17 (2009) 1052–1064. doi:10.1016/j.intermet.2009.05.013.
- [55] E. Gamsjäger, Y. Liu, M. Rester, P. Puschnig, C. Draxl, H. Clemens, G. Dehm, F. D. Fischer, Diffusive and massive phase transformations in Ti–Al–Nb alloys – Modelling and experiments, *Intermetallics* 38 (2013) 126–138. doi:10.1016/j.intermet.2013.03.001.

- [56] A. Denquin, S. Naka, Phase transformation mechanisms involved in two-phase TiAl-based alloys—II. Discontinuous coarsening and massive type transformation, *Acta Materialia* 44 (1996) 353–365. doi:10.1016/1359-6454(95)00168-6.
- [57] G. Wegmann, R. Gerling, F.-P. Schimansky, Temperature induced porosity in hot isostatically pressed gamma titanium aluminide alloy powders, *Acta Materialia* 51 (2003) 741–752. doi:10.1016/S1359-6454(02)00465-2.
- [58] S. Tammam-Williams, P. J. Withers, I. Todd, P. B. Prangnell, Porosity regrowth during heat treatment of hot isostatically pressed additively manufactured titanium components, *Scripta Materialia* 122 (2016) 72–76. doi:10.1016/j.scriptamat.2016.05.002.
- [59] DIN EN ISO 6892-1: 2017-02-Metallic materials - Tensile testing - Part 1: Method of test at room temperature, 2017.
- [60] D. Wimler, J. Lindemann, H. Clemens, S. Mayer, Microstructural Evolution and Mechanical Properties of an Advanced γ -TiAl Based Alloy Processed by Spark Plasma Sintering, *Materials* 12 (2019) 1523. doi:10.3390/ma12091523.
- [61] M. Todai, T. Nakano, T. Liu, H. Y. Yasuda, K. Hagihara, K. Cho, M. Ueda, M. Takeyama, Effect of building direction on the microstructure and tensile properties of Ti-48Al-2Cr-2Nb alloy additively manufactured by electron beam melting, *Additive Manufacturing* 13 (2017) 61–70. doi:10.1016/j.addma.2016.11.001.
- [62] V. Imayev, R. Imayev, G. Salishchev, On two stages of brittle-to-ductile transition in TiAl intermetallic, *Intermetallics* 8 (2000) 1–6. doi:10.1016/S0966-9795(99)00065-5.
- [63] H. Jabbar, J.-P. Monchoux, M. Thomas, F. Pyczak, A. Couret, Improvement of the creep properties of TiAl alloys densified by Spark Plasma Sintering, *Intermetallics* 46 (2014) 1–3. doi:10.1016/j.intermet.2013.10.019.
- [64] Y.-W. Kim, Microstructural evolution and mechanical properties of a forged gamma titanium aluminide alloy, *Acta Metallurgica et Materialia* 40 (1992) 1121–1134. doi:10.1016/0956-7151(92)90411-7.
- [65] U. Fröbel, F. Appel, Strain ageing in γ (TiAl)-based and α_2 (Ti₃Al) titanium aluminides, *Intermetallics* 14 (2006) 1187–1193. doi:10.1016/j.intermet.2005.11.031.
- [66] J. Bieske, M. Franke, M. Schloffer, C. Körner, Microstructure and properties of TiAl processed via an electron beam powder bed fusion capsule technology, *Intermetallics* 126 (2020) 106929. doi:10.1016/j.intermet.2020.106929.
- [67] V. Razumovskiy, W. Ecker, D. Wimler, F. D. Fischer, F. Appel, S. Mayer, C. Helmut, An atomistic view on oxygen, antisites and vacancies in the γ -TiAl phase *Acta Materialia: under evaluation*, *Computational Materials Science* (2021).
- [68] M. Kasthuber, T. Klein, B. Rashkova, I. Weißensteiner, H. Clemens, S. Mayer, Phase transformations in a β -solidifying γ -TiAl based alloy during rapid solidification, *Intermetallics* 91 (2017) 100–109. doi:10.1016/j.intermet.2017.08.017.
- [69] H. Gabrisch, A. Stark, F.-P. Schimansky, L. Wang, N. Schell, U. Lorenz, F. Pyczak, Investigation of carbides in Ti–45Al–5Nb–xC alloys ($0 \leq x \leq 1$) by transmission electron microscopy and high energy-XRD, *Intermetallics* 33 (2013) 44–53. doi:10.1016/j.intermet.2012.09.023.

- [70] E. Schwaighofer, B. Rashkova, H. Clemens, A. Stark, S. Mayer, Effect of carbon addition on solidification behavior, phase evolution and creep properties of an intermetallic β -stabilized γ -TiAl based alloy, *Intermetallics* 46 (2014) 173–184. doi:10.1016/j.intermet.2013.11.011.
- [71] C. Scheu, E. Stergar, M. Schober, L. Cha, H. Clemens, A. Bartels, F.-P. Schimansky, A. Cerezo, High carbon solubility in a γ -TiAl-based Ti–45Al–5Nb–0.5C alloy and its effect on hardening, *Acta Materialia* 57 (2009) 1504–1511. doi:10.1016/j.actamat.2008.11.037.
- [72] A. Menand, A. Huguet, A. N´erac-Partaix, Interstitial solubility in γ and α_2 phases of TiAl-based alloys, *Acta Materialia* 44 (1996) 4729–4737. doi:10.1016/S1359-6454(96)00111-5.
- [73] L. Wang, H. Gabrisch, U. Lorenz, F.-P. Schimansky, A. Schreyer, A. Stark, F. Pyczak, Nucleation and thermal stability of carbide precipitates in high Nb containing TiAl alloys, *Intermetallics* 66 (2015) 111–119. doi:10.1016/j.intermet.2015.07.001.
- [74] K.-D. Liss, A. Bartels, A. Schreyer, H. Clemens, High-Energy X-Rays: A tool for Advanced Bulk Investigations in Materials Science and Physics, *Textures and Microstructures* 35 (2003) 219–252. doi:10.1080/07303300310001634952.
- [75] P. D. Nellist, S. J. Pennycook, The principles and interpretation of annular dark-field Z-contrast imaging, in: P. W. Hawkes (Ed.), *Advances in imaging and electron physics*, Vol. 113 of *Advances in Imaging and Electron Physics*, Academic Press, San Diego and San Francisco, 2000, pp. 147–203. doi:10.1016/S1076-5670(00)80013-0.
- [76] S. Banerjee, P. Mukhopadhyay, *Phase transformations: Examples from titanium and zirconium alloys*, Vol. 12 of *Pergamon materials series*, Elsevier, Amsterdam and Oxford, 2007.
- [77] R. V. Ramanujan, P. J. Maziasz, C. T. Liu, The thermal stability of the microstructure of γ -based titanium aluminides, *Acta Materialia* 44 (1996) 2611–2642. doi:10.1016/1359-6454(95)00402-5.
- [78] P. Maziasz, R. Ramanujan, C. Liu, J. Wright, Effects of B and W alloying additions on the formation and stability of lamellar structures in two-phase γ -TiAl, *Intermetallics* 5 (1997) 83–95. doi:10.1016/S0966-9795(96)00070-2.
- [79] T. Klein, B. Rashkova, D. Holec, H. Clemens, S. Mayer, Silicon distribution and silicide precipitation during annealing in an advanced multi-phase γ -TiAl based alloy, *Acta Materialia* 110 (2016) 236–245. doi:10.1016/j.actamat.2016.03.050.
- [80] T. Klein, M. Schachermayer, F. Mendez-Martin, T. Schöberl, B. Rashkova, H. Clemens, S. Mayer, Carbon distribution in multi-phase γ -TiAl based alloys and its influence on mechanical properties and phase formation, *Acta Materialia* 94 (2015) 205–213. doi:10.1016/j.actamat.2015.04.055.
- [81] W. H. Tian, M. Nemoto, Effect of carbon addition on the microstructures and mechanical properties of γ -TiAl alloys, *Intermetallics* 5 (1997) 237–244. doi:10.1016/S0966-9795(96)00086-6.
- [82] U. Christoph, F. Appel, R. Wagner, Dislocation dynamics in carbon-doped titanium aluminide alloys, *Materials Science and Engineering: A* 239-240 (1997) 39–45. doi:10.1016/S0921-5093(97)00558-3.
- [83] F. Appel, P. A. Beaven, R. Wagner, Deformation processes related to interfacial boundaries in two-phase γ -titanium aluminides, *Acta Metallurgica et Materialia* 41 (1993) 1721–1732. doi:10.1016/0956-7151(93)90191-T.

